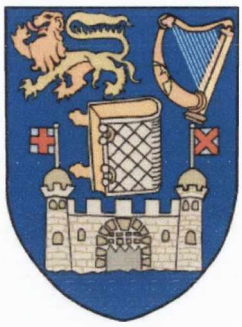

Highly Conductive, Transparent and Flexible Networks of Quasi 1-Dimensional Metallic Nanostructures

By

Philip E. Lyons

A thesis submitted for the degree of

Doctor of Philosophy

in the University of Dublin

School of Physics,

Trinity College Dublin,

2011

Declaration

I declare that the work in this thesis has not been previously submitted as an exercise for a degree to this or any other university.

The work described herein is entirely my own, except for the assistance mentioned in the acknowledgements and the collaborative work mentioned in the list of publications.

I agree that Trinity College Library may lend or copy this thesis on request.

to my grandparents, parents, brother and sisters.

Thank you

"There's this tremendous mess, of waves all over in space,

which is the light bouncing around the room, and going from one thing to the other...

And it's all really there!

But you gotta stop and think about it, about the complexity to really get the pleasure,

The inconceivable nature of nature!"

- *Richard P. Feynman*

Abstract

Direct current conductivity and morphological characterization has been performed on a wide range of films made from bundled single wall carbon nanotubes, produced by a selection of commercial suppliers. The conductivity increases with increasing nanotube graphitization but decreases with increasing film porosity, P, and mean bundle diameter, <D>. Computational studies show that the network conductivity is expected to scale linearly with the number density of inter-bundle junctions. A simple expression is derived to relate the junction number density to the porosity and mean bundle diameter. Plotting the experimental network conductivities versus the junction number density calculated from porosity and bundle diameter shows an approximate linear relationship. Such a linear relationship implies that the conductivity scales quadratically with the nanotube volume fraction, reminiscent of percolation theory. More importantly it shows the conductivity to scale with $<D>^{-3}$. Well-defined scaling with diameter and porosity allows the calculation of a specific conductivity expected for films with porosity of 50% and mean bundle diameter of 2 nm. This predicted specific conductivity scales well with the level of nanotube graphitization. Single wall carbon nanotubes synthesized by the arc-discharge method (Iljin Nanotech Ltd.) and HiPCO method (Carbon Nanotechnologies Inc.) exhibited the highest DC conductivities with values of 2.62×10^5 Sm^{-1} and 1.67×10^4 Sm^{-1} respectively.

Flexible, transparent, and very conducting thin composite films consisting of poly(3,4-ethylenedioxythiophene):poly(styrenesulfonate), filled with both arc discharge and HiPCO SWNTs, at high loading level, have been prepared. The films are of high optical uniformity. The arc discharge nanotube filled composites were significantly more conductive, demonstrating DC conductivities of $> 10^5$ Sm^{-1} for mass fractions > 50 wt%.

The ratio of DC to optical conductivity was higher for composites with mass fractions of 55-60 wt% than for nanotube-only films. For an 80 nm thick composite, filled with 60 wt% arc discharge nanotubes, this conductivity ratio was maximized at $\sigma_{DC}/\sigma_{Op} = 15$. This translates into transmittance (550 nm) and sheet resistance of 75 % and 80 Ω/□, respectively. These composites were electromechanically very stable, showing < 1 % resistance change over 130 bend cycles.

Aqueous dispersions of silver nanowires were used to prepare thin, flexible, transparent, conducting films. The nanowires are of length and diameter close to 6.5 μm and 85 nm respectively. At low thickness, the films consist of networks but appear to become bulk-like for mean film thicknesses above ~160 nm. These films can be very transparent with optical transmittance reaching as high as 92% for low thickness. The transmittance (550 nm) decreases with increasing thickness, consistent with an optical conductivity of 6472 Sm^{-1}. The films are also very uniform; the transmittance varies spatially by typically < 2 %. The sheet resistance decreases with increasing thickness, falling below 1 Ω/□ for thicknesses above 300 nm. The DC conductivity increases from 2×10^5 Sm^{-1} for very thin films before saturating at 5×10^6 Sm^{-1} for thicker films. Similarly, the ratio σ_{DC}/σ_{Op} increases with increasing thickness from 25 for the thinnest films, saturating at ~500 for thicknesses above ~160 nm. This is one of the highest conductivity ratio ever observed for nanostructured films and is matched only by aligned copper nanowire grids and doped metal oxide films. These nanowire films are electromechanically very robust, with all but the thinnest films showing no change in sheet resistance when flexed over > 1000 cycles. Such results make these films ideal as replacements for indium tin oxide as transparent electrodes. Films with optical transmittance and sheet resistance of 85 % and 13 Ω/□ respectively were prepared. This is very close to that displayed by commercially available indium tin oxide.

Acknowledgements

First and foremost I would like to thank my supervisor, Prof. Jonathan N. Coleman. He has managed to perfect the art of supervision by mixing solid direction, advice and when necessary, reassurance with a very approachable and fun attitude. Very special thanks go to Dr. Sukanta De. Not only has he been a constant source of advice and help in the laboratory but he somehow managed to proof read this too and I shudder to think of the mistakes I would have made in both without his input.

This research was carried out as part of collaborative project with Hewlett Packard, whose research staff have been nothing but helpful and supportive through the last four years. Many thanks to Vittorio, Jerome, Kev, Richard, Graeme, Liz and Anna, who had to sit through even more meetings than I did. There were a number of different groups working on this project and I was fortunate to end up working with a number of very helpful, positive and talented scientists who contributed to this research. To each I owe a very large "thank you". Evelyn Doherty completed, with help from Jerome, all the electromechanical measurements reported in this thesis. Not only did she contribute much to this thesis, but she has been a good friend too. I would also like to thank Prof. Werner Blau for his support. The atomic force microscopy work reported in this thesis was completed by Peter Nirmalraj. He has always been helpful, friendly and ready for a discussion. Many thanks to Peters supervisor, Prof. John Boland, who has been a driving force in the HP project, helping all the students get to where they needed to be. Many thanks are owed to Luiz Pereira and Dr. Mauro Ferreira who completed the computational work on nanotube networks. As I am by no means a chemist, I had on many occasion the need for chemical enlightenment. My thanks to Dr. Amro Satti and Prof. Yurii Gun'ko for

providing such enlightenment and for putting up with my constant surprise visits to the office.

I must thank the technical and administrative staff that made sure everything ran smoothly and were helpful and friendly doing it. In the School of Physics I would like to thanks John Kelly, Jemmer, Ken, Safety Joe, Dave, Pat, Gordon, Gillian, Una, Rebecca, Robbie, Samantha and Chris Smith. In CRANN I have Lia, Jacqueline, Tracey and Jen to thanks for all the help with conferences, fees and all the stuff I don't like to deal with. I would like to thank Des for his all-around help and friendliness. I would also like to thank Chris Keely for initially letting me fool around in the MI lab and also for his work in managing the HP project. The CMA staff was and are very helpful and accommodating and I'm very grateful for that. Thanks to Neal, Clodagh, Anthea, Leona, Amanda and Colin. I think over the last four years I think I must have used more acetone than any other person in the college. Thanks to Marcus and Colm in the Hazardous Materials facility for always getting me what I needed. Thanks to the Materials Ireland staff, Ramesh, Trevor and Eddie, for allowing the use of the lab throughout the years.

Very big thanks to the members, old and new, of the Coleman and Blau groups who have made this journey a treat. They are a welcoming and fun bunch to work with and I hope I will be there for another few Gluhwein parties. In no particular order thanks to Valeria, Anna, Fiona, Yenny, Umar, Shane, Helen, Chris K, Zhenyu, Rickard, Darren, Niall, Paula, Denise, Karen, Marguerite, Mustafa, Paul, and the new kids on the block Brian, Pete, Ronan, Arlene, and finally Sophie who started out being a helpful and fun summer student and ended up being even more help and fun as a post grad.

Along the way I received much help from summer students and so I would like to thank Tom Quinlan, Ming, Aleksey, Sebastien D, Thom Higgins, Abhiti, Sebastien C, and Alain.

Finally I would like to express my appreciation and gratitude to those who made this possible. To my grandparents, Ernest and Elizabeth Lyons and William and Esther Dunne, and especially to my parents Trevor and Jennifer. They have always done their best to provide for me, allowing me to try and educate myself as best as I could, and more importantly, supported me in all my endeavours, of which this thesis has been the most challenging. Thank you, I'll get a job soon, I promise!

Table of contents

Chapter 1 : Motivation and Thesis outline

1.1 Motivation

The success of mankind at becoming the dominant species on this planet can be attributed to our ability to utilise and control the materials available. Since the very beginning we have used stone and wood to provide shelter and tools. By 10000 BC[1] we had, through these advancements, developed agriculture which provided us with a firm base for social, economic and technological advancement. The extraction and use of metal was a milestone in the exploitation of natural materials but it is only since the birth of modern science in the 16th century that humans began to explore and explain the natural world in a quantitative way. The study of materials has always been of importance to society. Indeed, modern day materials science has its roots in the ancient 'art' of metallurgy and man's desire to control the properties of materials. The modern day field can be traced back to the late 19^{th} and early 20^{th} century when industrial demands created a need to not only use materials but to understand their properties. This understanding has given us an unprecedented control over materials in both development and applications and is the reason behind the current level of technology.

One of the biggest areas in technology today is electronic visual displays. The original televisions and computer monitors were based on cathode ray tubes but have recently been replaced by devices designed to be, amongst other things, slimmer with a larger screen area. For many years the race for improvement lay in the fields of size, definition and colour range. We have achieved screens the size of pool tables (Panasonics

150" 'Life Screen' plasma television) and developed high definition and high dynamic range displays[2] but one area that will be key for the development of possible future displays is flexibility and mechanical robustness. These displays, which include plasma, liquid crystal and light emitting diode cells, require transparent electrodes. Currently the materials of choice are metal doped oxides such as indium tin oxide (ITO).[3] This oxide, while providing excellent optical and electrical properties,[4] is very brittle and can crack easily resulting in barriers to electrical conduction.[5,6] Couple this problem with the rising cost of indium[7] and the high temperature processes required to form the oxide, and it becomes obvious that a more robust and cheaper alternative must be found.

The discovery of Fullerenes and other related structures in the 1980's and 90's,[8,9] along with development of technology enabling examination of such small objects, has presented the world with an interesting and very large range of new possibilities. In particular, quasi 1-Dimensional structures, such as carbon nanotubes and silver nanowires, present an appealing possibility for transparent electrode materials.[10,11] Networks of such structures would not only provide electrical conduction and optical transparency due to the tubes and wires intrinsic properties but also a mechanical edge as the individual components would have a degree of freedom and ductility. The motivation behind this thesis is to understand the electrical conductivity in such networks and use this understanding to control the relevant parameters, resulting in the formation and characterisation of highly conductive, transparent and flexible networks based on quasi 1-Dimensional metallic nanostructures.

1.2 Thesis Outline

Chapter 2 - Theory and characterisation methods. This chapter will begin with a discussion on direct current and optical conductivity. Ohms law will be introduced and a classical expression for conductivity derived. The interaction of light with matter will be discussed with emphasis on metals. The transmittance of a thin metal film will be related to the films sheet resistance. The theory and experimental setup used for observing some relevant spectroscopic phenomena will be discussed. Techniques for measuring electrical conductivity will be presented. Finally, the theory and operation of the scanning electron microscope and atomic force microscope, useful tools for imaging 1-Dimensional nanostructures, will be presented.

Chapter 3 – Materials and background will begin with an introduction into the industry standard for a transparent conductor, Indium Tin Oxide. Quasi 1-Dimensional nanostructures will be introduced, concentrating on carbon nanotubes and silver nanowires. The production, structure, properties and applications of said nanostructures will be presented. This will be followed by a brief section discussing electrically conducting polymers. Specifically, an overview of the synthesis and properties of Poly(3,4-ethylenedioxythiophene) poly(styrenesulfonate) (PEDOT:PSS) will be given.

Chapter 4 - The relationship between network morphology and conductivity in carbon nanotube films.[12] A large number of networks prepared using commercially available carbon nanotubes have been prepared and characterised. The network connectivity, described by the inter-nanotube junction density, will be shown to control the network conductivity. Furthermore, the specific conductivity of the nanotube networks will be shown to scale with a spectroscopic metric describing the crystalline purity of the carbon nanotubes. This will demonstrate that the properties of both the nanotubes and the network are important in preparing high conductivity films.

Chapter 5 - Transparent, conductive and flexible films based on carbon nanotubes.[13,14] Highly conductive, transparent and flexible films prepared from carbon nanotubes have been prepared. This chapter will present a method to produce highly conductive and uniform thin films of carbon nanotubes. The optical and electrical properties will be presented, concentrating on the optical uniformity and electromechanical stability. Furthermore, the addition of such networks to a conducting polymer matrix will show an increase in the desired properties, leading to some of the most conducting polymer composites known.

Chapter 6 - Silver Nanowire Networks as Flexible, Transparent, Conducting Films: Extremely High DC to Optical Conductivity Ratios.[15] Thin networks of silver nanowires have been fabricated. This chapter presents the preparation and characterisation of thin films prepared using silver nanowires. The films will be shown to be of high quality and uniformity, displaying sheet resistance and visible region optical transmittance values which make them applicable as flexible, transparent electrodes.

Chapter 7 – Conclusions and future work. A summary of the main results will be given. This will be followed by experimental conclusions. Future work will then be discussed.

Chapter 8 – Appendix. A list of relevant publications is outlined.

1.3 References

1 Ofer Bar-Yosef, "The Natufian Culture in the Levant, Threshold to the Origins of Agriculture," Evolutionary Anthropology: Issues, News and Reviews 6 (5), 159-177 (1998).

2 David E. Mentley, "State of Flat-Panel Display technology and Future Trends," Proceeding of the IEEE 90 (4), 453-459 (2002).

3 Ji Cui, Anchuan Wang, Nikki L. Edleman, Jun Ni, Paul Lee, Neal R. Armstrong, and Tobin J. Marks, "Indium Tin Oxide Alternatives - High Work Function Transparent Conducting Oxides as Anodes for Organic Light-Emitting Diodes," Advanced Materials 13 (19) (2001).

4 Sang-Mo Kim, You-Seung Rim, Min-Jong Keum, and Kyung-Hwan Kim, "Study on the electrical and optical properties of ITO and AZO thin film by oxygen gas flow rate," Journal of Electroceramics 23 (2-4), 341-345 (2008).

5 Y. Leterrier, L. Medico, F. Demarco, J. -A. E. Manson, U. Betz, M. F. Escola, M. Kharrazi Olsson, and F. Atamny, "Mechanical integrity of transparent conductive oxide films for flexible polymer-based systems," Thin Solid Films 460 (1-2), 156-166 (2004).

6 Z. Chen, B. Cotterell, and W. Wang, "The fracture of britttle thin films on compliant substrates in flexible displays," Engineering Fracture Mechanics 69 (5), 597-603 (2002).

7 Aurelien Du Pasquier, Husnu Emrah Unalan, Alokik Kanwal, Steve Miller, and Manish Chhowalla, "Conducting and transparent single-wall carbon nanotube electrodes for polymer-fullerene solar cells," Applied Physics Letters 87 (203511) (2005).

8 H. W. Kroto, J. R. Heath, S. C. O'Brien, R. F. Curl, and R. E. Smalley, "C_{60}: Buckminsterfullerene," Nature 318, 162-163 (1985).

9 Sumio Ijima, "Helical microtubules of graphitic carbon," Nature 354, 56-58 (1991).

10 Zhuangchun Wu, Zhihong Chen, Xu Du, Jonathan M. Logan, Jennifer Sippel, Maria Nikolou, Katalin Kamaras, John R. Reynolds, David B. Tanner, Arthur F. Hebard, and Andrew G. Rinzler, "Transparent, Conductive Carbon Nanotube Films," Science 305 (2004).

11 Jung-Yong Lee, Stephen T Connor, Yi Cui, and Peter Peumans, "Solution-Processed Metal Nanowire Mesh Transparent Electrodes," Nanoletters 8 (2), 689-692 (2008).

12 Philip E. Lyons, Sukanta De, Fiona Blighe, Valeria Nicolosi, Luiz Felipe C. Pereira, Mauro S. Ferreira, and Jonathan N. Coleman, "The relationship between network morphology and conductivity in nanotube films," Journal of Applied Physics 104 (4) (2008).

13 Sukanta De, Philip E. Lyons, Sophie Sorrel, Evelyn M. Doherty, Paul J. King, Werner J. Blau, Peter N. Nirmalraj, John J. Boland, Vittorio Scardaci, Jerome Joimel, and Jonathan N. Coleman, "Transparent, conductive and flexible thin films based on extremely conductive polymer-nanotube composites," ACS Nano 3 (3), 714-720 (2009).

14 Evelyn M. Doherty, Sukanta De, Philip E. Lyons, Aleksey Shmeliov, Peter N. Nirmalraj, Vittorio Scardaci, Jerome Joimel, Werner J. Blau, John J. Boland, and Jonathan N. Coleman, "The spatial uniformity and electromechanical stability of transparent, conductive films of single walled nanotubes," Carbon 47, 2466-2473 (2009).

15 Sukanta De, Thomas M. Higgins, Philip E. Lyons, Evelyn M. Doherty, Peter N. Nirmalraj, Werner J. Blau, John J. Boland, and Jonathan N. Coleman, "Silver Nanowire Networks as Flexible, Transparent, Conducting Films: Extremely High DC to Optical Conductivity Ratios," ACS Nano 3 (7), 1767-1774 (2009).

Chapter 2 : Theory and experimental techniques

In this chapter the relevant theory and experimental techniques will be outline. This thesis ultimately is concerned with the electronic and optical conduction in very thin metallic films composed of 1-Dimensional nanostructures. To this end the chapter will begin with an introduction to some relevant electronic and optical theory. Then the experimental techniques employed, including electrical, optical and microscopy measurements, will be introduced and a brief account of the theory and operation of each will be presented.

2.1 Optical and direct current conductivity

In this thesis the performance of transparent and conducting films are rated by using a figure of merit based on the optical and direct current (DC) conductivities. Both are determined by the response of electrons to an applied electric field, for optical conductivity the electric field is time varying with a high frequency i.e. light waves, while for direct current conductivity it is static as for an applied voltage.

The idea of the direct current conductivity is a relatively simple concept. The electric field created by a non-oscillating direct current voltage source connected to metal acts to accelerate the charge carriers through the medium. As they propagate through the

medium they suffer collisions due to defects in the crystal structure of the metal, the static positive ion array and other electrons. A materials resistance arises from collisions causing the electron drift velocity, v_d, to decay to zero exponentially with a time constant τ. The equation describing the acceleration of electrons under an applied electric field $\boldsymbol{E}$ at a given time, t, is given by[1]

$$m_e\left(\frac{d\mathbf{v}}{dt}+\frac{\mathbf{v}_d}{\tau}\right)=-e\mathbf{E}-e\mathbf{v}\times\mathbf{B} \qquad (2.1)$$

m_e is the effective mass of the electron, $\boldsymbol{v}$ is the electron velocity, e is the charge of an electron ($1.602\text{x}10^{-19}$C) and $\boldsymbol{B}$ is the magnetic field. For a direct current field the solution to Equation 2.1 has the form

$$\mathbf{v}_d=-\frac{e\tau}{m_e}\mathbf{E} \qquad (2.2)$$

The constant of proportionality between the $|\mathbf{v}_d|$ and $|\mathbf{E}|$ is called the carrier mobility given by

$$\varsigma=+\frac{e\tau}{m_e} \qquad (2.3)$$

The current density, $\boldsymbol{J}$, is the induced current per area (Amperes/ meter^2, Am^{-2}) created by the application of an electric field, $\boldsymbol{E}$ with units of Newtons per Coulomb, NC^{-1}. It is simply given be $n(-e)\mathbf{v}_d$ where n is the electron density. It follows that

$$\mathbf{J}=\frac{ne^2\tau}{m_e}\mathbf{E} \qquad (2.4)$$

The current density is related to the electric field by the direct current conductivity, σ_{DC}, according to Ohm's Law which states[1]

$$\mathbf{J} = \sigma \mathbf{E} \qquad (2.5)$$

And so

$$\sigma_{DC} = \frac{ne^2\tau}{m_e} = ne^2\varsigma \qquad (2.6)$$

The conductivity, with units of Siemens per meter (Sm^{-1}), gives a measure of the ability of a material to transport electric charge. This equation shows the DC conductivity is proportional to the number of electrons per volume available for conduction and the average distance an electron travels between collisions, described by the time constant τ.

This thesis is concerned with electronic conduction in networks of carbon nanotubes and silver nanowires. In such a network the individual components can be considered as randomly orientated conductive 1-Dimensional structures. Current can flow because of junctions between adjacent wires or tubes, creating an electrical pathway through the medium. These junctions create a potential barrier to the tunnelling of electrons between components, resulting in an associated resistance. And so, the conductivity of the individual components as well as the number of junctions per volume with junction resistance, R_J, will both have a role to play in the conduction process. The resistance associated with a junction can be measured using experimental tools such as the atomic force microscope[2] and for carbon nanotubes this can reach values of up to MΩ. The electronic connectivity of carbon nanotube bundles were investigated by Nirmalraj *et al.*[3] In this study they were able to either increase or decrease the mean junction resistance by either annealing the sample or treating it with acid. The network conductivity of the films subjected to different treatments scaled very well with the inverse of the mean junction resistance showing that the conductivity of a 1-Dimensional nanostructure network with large R_J is critically dependent on the junction resistance and nanotube/wire connectivity.

The optical conductivity, σ_{OP}, describes how a material responds to an *alternating* electric field. Light is a high frequency electromagnetic vibration in which electric and magnetic fields oscillate in phase perpendicular to each other, along the x and y planes respectively with the wave vector directed along the z-direction. A monochromatic plane light wave, traveling with velocity c, which is both time (t) and spatially (**r**) dependent, can be described in terms of the wave-vector, $\boldsymbol{q}$, the angular frequency, ω, and the maximum amplitude, $\boldsymbol{E}_0$, by[4]

$$\mathbf{E}(\mathbf{r},t) = \mathbf{E}_0 \exp\{i(\mathbf{q} \cdot \mathbf{r} - \varpi t)\} \qquad (2.7)$$

In a vacuum the wave is in its simplest form as there is no dissipation or any other complications. If a medium is subjected to an alternating electric field such as that present in a light wave then a redistribution of the charge in the medium occurs. This can create dipoles and magnetic moments, changes in polarization and induced current as the time varying electric and magnetic fields distort the bound charges. In an absorbing medium the wave attenuates due to damping by the bound charges. The current density, $\boldsymbol{J}$, arising as a result from the motions of the electrons in the applied field can be described by Ohm's law (Equation 2.5), showing that current density is proportional to the electric field, $\boldsymbol{E}$, with the materials conductivity, σ, defining their ratio.

The complex refractive index, $\hat{N}$, is a function describing the response of a medium to an alternating electric field and consists of the real (n) and imaginary (k) components.

$$\hat{N} = n + ik \qquad (2.8)$$

As a wave advances through a medium the amplitude of the electric field is decreased by a factor of $exp\{-2\pi k/n\}$[5] per wavelength of the light in the medium. The decrease in amplitude is dependent on the imaginary part of the refractive index which is also known

as the extinction coefficient. The real refractive index and extinction coefficient, are completely determined from the materials real conductivity σ_1, the real dielectric constant, ε_1, which gives a measure of how much resistance a material gives to the formation of an electric field (measured in Farads/meter, F/m) and the real part of the permeability, μ_1, which describes the materials ability to support the formation of a magnetic field (units of Henry per meter, Hm^{-1}). The dielectric constant is given by[5]

$$\hat{\varepsilon} = \varepsilon_1 + i\varepsilon_2 \qquad (2.9)$$

where ε_2 is the imaginary part of the dielectric constant and ε_1 and ε_2 are given by[5]

$$\varepsilon_1 = 1 - \frac{4\pi\sigma_2}{\omega} \qquad (2.10)$$

and

$$\varepsilon_2 = \frac{4\pi\sigma_1}{\omega} \qquad (2.11)$$

The refractive index and extinction coefficient can be expressed as

$$n^2 = \frac{\mu}{2}\left\{\left[\varepsilon_1^{\,2} + \left(\frac{4\pi\sigma}{\omega}\right)^2\right]^{1/2} + \varepsilon_1\right\} \qquad (2.12)$$

$$k^2 = \frac{\mu}{2}\left\{\left[\varepsilon_1^{\,2} + \left(\frac{4\pi\sigma}{\omega}\right)^2\right]^{1/2} - \varepsilon_1\right\} \qquad (2.13)$$

In terms of n and k, the dielectric constant, the permeability, μ_1, and real conductivity are given by

$$n^2 - k^2 = \varepsilon_1\mu_1 \qquad (2.14)$$

$$2nk = \frac{4\pi\mu_1\sigma_1}{\varpi} \qquad (2.15)$$

The complex wave-vector is given by

$$\mathbf{q} = \hat{q}\mathbf{n}_q \qquad (2.16)$$

Where $\boldsymbol{n}_q$ is the direction of propagation and

$$\hat{q} = \frac{\omega}{c}\hat{N} = \frac{n\omega}{c} + i\frac{k\omega}{c} \qquad (2.17)$$

The real part of the wave-vector expresses the travelling wave while the imaginary part takes into account the attenuation of the wave as described by k. In a metal there is a characteristic length scale over which an electromagnetic wave decreases by a factor of $1/e$ and is known as the skin depth, δ_0.

$$\delta_0 = \left[\frac{c^2}{2\pi\omega\mu_1\sigma_1}\right] \qquad (2.18)$$

This is related to the absorption coefficient, α, by

$$\delta_0 = \left(\frac{\alpha}{2}\right)^{-1} \qquad (2.19)$$

where

$$\alpha = \frac{4\pi k}{\lambda_0} \qquad (2.20)$$

Rearranging Equation 2.15 for k and substituting into Equation 2.20 we see that

$$\alpha = \frac{4\pi\sigma_1\mu_1}{nc} \qquad (2.21)$$

This equation shows that as the optical conductivity increases so does the absorption coefficient and the wave attenuates strongly in the medium and reduces the transmitted components of an incident electromagnetic wave.

A material requires a large DC conductivity and high transmittance in order to perform as a transparent electrode. Unfortunately a high conductivity also results in a large absorption coefficient, reducing the transmittance of the material. To reduce the absorption of light in an absorbing material the thickness must be reduced to very small dimensions. The thinnest material known is Graphene, a sheet of carbon atoms which are bonded in a 2-dimensional honeycomb type lattice. Due to linear energy dispersion at high symmetry points in the Brillouin zone, or Dirac points, electrons and holes can be described as zero effective mass particles by the Dirac equation.[6] Coupling the exciting electronic properties with visible transparency and chemical and mechanical robustness makes Graphene a very promising material for photonics and optoelectronics.[7] Quantum theory shows that materials with finite dimensions, such as Graphene, exhibit quantised conductance G_0, with a value of[8]

$$G_0 = \frac{2e^2}{h} = 7.748 \times 10^{-5} S \qquad (2.22)$$

Isolated single layers of Graphene exhibit a conductiance of $2G_0$,[9] even when the carrier concentration tends to zero.[10] This shows the maximum conductance of a graphene sheet is 15.49×10^{-5}S. Relating this 2-dimensional property to the 3-dimensional equivalent can be done by dividing by the thickness of one flake, ~0.35nm. This results in a conductivity value of $4.4 \times 10^{5} Sm^{-1}$, a very low conductivity when compared to that of bulk metals ($\sim 10^{7} Sm^{-1}$) The optical conductivity of Graphene is the given by the universal constant $e^2 / 4\hbar$.[11] The transmittance of a single Graphene layer can be calculated by applying Fresnel equation in the thin film limit giving[12]

$$T = (1 + 0.5\pi\xi)^{-2} \approx 1 - \pi\xi \approx 97.7\% \qquad (2.23)$$

The symbol ξ represents the fine structure constant which is a fundamental constant describing the coupling in electromagnetic interactions. It has the form[12]

$$\xi = \frac{G_0}{\pi \in_0 c} \approx \frac{1}{137} \qquad (2.24)$$

This shows that the transmittance of a Graphene layer is frequency independent and only depends on the fine structure constant, resulting in a single layer absorbing 2.3% of incident light. This is a significantly large value for a layer of material only one atom thick, with a few layers of Graphene absorbing nearly 10 % of incident light with a thickness of ~1nm.

These fundamental limits to the performance of Graphene in terms of conductivity and transmittance have been discussed by De *et al.*[13] In their report the authors rated optical and conductivity results reported for networks of Graphene flakes. They argue that undoped, pristine mono- and few layer-Graphene networks should exhibit a maximum optical and direct current (DC) conductivity ratio of 2.55, far below the value required for application in even the most basic transparent electrode roles. The authors reported a large variation in conductivity ratios from the literature and have concluded that the main reason for the spread of values was due to variation in DC conductivity caused by morphological effects such as changes in porosity. This limit to the conductivity and transmittance extends only to pristine un-doped Graphene as Equation 2.22 is only appropriate when the Fermi level is at the Dirac point.[10] By applying a gate voltage or doping, the Fermi level can be shifted and the conductivity is related to the level of doping by[9] $\sigma_{DC} = ne\varsigma$ where e is the charge on an electron, n is the carrier (electron or hole) density and ζ is the carrier mobility. Unintentional substrate induced doping by has been reported[14-17] but for doping to create the minimum conductivity required for transparent

electrode purposes a value of $n\zeta > 1.3 \times 10^{16} V^{-1} s^{-1}$ must be realised. Graphene has been shown to exhibit carrier concentrations as high as $n = 3 \times 10^{12} cm^{-2}$ when n-doped by a poly-vinyl alcohol coating.[14] Although Graphene's carrier mobility is reduced when placed in contact with a substrate, values of $\zeta = 4 \times 10^{4} cm^{-2} V^{-1} s_{-1}$ are thought to be attainable.[18] If the transmittance is not changed upon doping then the values given above for the carrier concentration and mobility would lead to a sheet resistance comparable to Indium Tin Oxide accompanied by a transmittance of 91%,[11] making it a very applicable material in the role of transparent electrodes.

2.2 *Electronic conduction in thin metallic films*[1,19]

The phenomenon of current flow has been of interest since the 18th century but it wasn't until 1827 that a quantitative description was published by Georg Ohm in his paper "*Die galvanische Kette, mathematisch bearbeitet*" (The galvanic circuit investigated mathematically).[20] Ohm's Law describes the relationship between the voltage, V, applied between two points of a metallic body and the current, I, flowing through it and takes the form

$$V = IR \qquad (2.25)$$

where R is the resistance and is dependent on the conductivity and sample size and independent of the current. For a conductor which conductivity, σ, and length and cross sectional area, L and A, respectively the resistance is

$$R = \frac{1}{\sigma} \frac{L}{A} \qquad (2.26)$$

Substituting into Equation 2.25 gives

$$V = \frac{JL}{\sigma} \qquad (2.27)$$

where

$$\boldsymbol{J} = \frac{I}{A} \qquad (2.28)$$

is the current density. Using the relation, formulated by Kirchoff, between voltage, V, and electric field, $\boldsymbol{E}$, inside the conductor, $\boldsymbol{E}=V/L$, we arrive at one of the most common forms of Ohm's Law, given earlier in Equation 2.5.

$$\mathbf{J} = \sigma \mathbf{E} \qquad (2.5)$$

When investigating the electrical properties of thin uniform films the resistance is often given by a 2-Dimensional quantity known as the sheet resistance R_s. From Equation 2.26 we have

$$R = \frac{1}{\sigma}\frac{L}{A} = \frac{1}{\sigma}\frac{L}{Wd} \qquad (2.29)$$

where W and d are the width and thickness which make up the cross sectional area A of the sample. The resistivity is simply the reciprocal of the conductivity. Grouping the resistivity and thickness together results in

$$R = \frac{\rho}{t}\frac{L}{W} = R_S\frac{L}{W} \qquad (2.30)$$

This gives the expression for sheet resistance

$$R_S = \frac{RW}{L} \qquad (2.31)$$

And finally, linking the conductivity to the sheet resistance using Equations 2.29 and 2.31 gives

$$R_S = \frac{1}{\sigma_{DC} d} \qquad (2.32)$$

The sheet resistance is a quantity having units of Ohms (Ω). However, this is confusing as it implies that the sheet resistance is equivalent to the bulk resistance. In order to avoid confusion the units of sheet resistance are given as Ohms per square (Ω/□) because measuring the resistance of a square sample gives a direct measurement of the sheet resistance, regardless of the squares dimension. Sheet resistance is particularly useful when investigating thin films. Generally, any thin conducting films used in electronic applications will have a uniform thickness to ensure no variation in the resistance. If this is the case then the sheet resistance can be measured simply and directly using a surface probe electrical measurement, resulting in a measure of the sample's resistance without requiring knowledge of the materials thickness.

2.3 Interaction of light with matter[4,21]

Of all the senses available to humans, sight is one of the most important. The interaction of light with matter produces a range of effects which help us navigate and understand this complex world. Optical processes and applications have long been of interest in the research and development of different technologies and the understanding and control of this interaction is essential in the field of optoelectronics.

Light can interact with matter in whole range of ways, producing a similarly large range of effects. These interactions can be condensed in to three main groups, reflection, propagation and absorption. The level at which these processes occur for a certain medium defines how they behave optically. An incident photon can be reflected from the surface atoms of a material, such as the case for many metals. Others may

propagate through the medium with a lower velocity, resulting in a change in the direction of propagation, known as refraction. If the photon has the same frequency as certain transition frequencies of the atom, then they can be absorbed, which reduces the intensity of beam as it propagates and as such controls the materials transmittance. Photons may also be scattered by sample atoms in which case they can be re-emitted with the same frequency (Rayleigh scattering) or different frequency (inelastic scattering). In certain materials luminescence occurs in which the incident photon raises an atom to higher energy level only to have it spontaneously emit light with a lower frequency at a later time. In the case of transparent electrodes for visual displays it would be beneficial for the material to exhibit low reflection, refraction and absorption resulting in a high visible transmittance.

2.3.1 The Beer-Lambert Law

The Beer-Lambert law describes the exponential relationship relating the absorption of light to the properties of the material through which the light is passing. Although the relationship is attributed to Johann Lambert, a Swiss physicist who published a book entitled *Photometria* in 1760, the law was first discovered by Pierre Bouger, a French mathematician. In 1729, thirty years before Lambert, Bouger published *Essai d'optique sur la gradation de la lumière* in which he discussed the loss of light after passing through a given distance in the earth's atmosphere. Bougers's and Lambert's findings were further expanded by the German physicist August Beer, who published a book entitled *Einleitung in die höhere Optik* in 1854. In his work he expanded on the initial exponential law in order to investigate the absorption of liquids, relating absorption to the concentration of the liquid under investigation.

The Beer-Lambert law can be derived by considering a beam of light propagating along the z-direction and incident normal to a thin slice of material with thickness dz. The material is considered to consist of absorbing particles and the slice is assumed to be thin enough that no particles overlap when viewed from the z-direction. The intensity, measured in lumens/m^2, of the incident light is reduced upon travelling through the material due to the interaction of photons with the particles, which depends on the absorption cross-section, φ, and the concentration of particles in the thin slice in N. The change in intensity, dI_z, from the initial intensity I_z, can be written as

$$dI_z = -I_z \varphi N dz \qquad (2.33)$$

which has a negative sign to account for the reduced intensity. The solution is obtained by integrating both sides of which yields

$$I_z = -\varphi N z + C \qquad (2.34)$$

where C is a constant. For a real slice of material with thickness d, measured in meters, the intensity before propagation is I_0 and after propagation is I_t which gives

$$Ln(I_d) - Ln(I_0) = -\varphi dN \qquad (2.35)$$

The transmittance, T, is defined[22] as the amount of incident light that propagates through the sample and is a simple fraction and so

$$T = \frac{I_t}{I_0} = e^{-\varphi dN} \qquad (2.36)$$

The absorbance of a medium is defined[22] as

$$A' = -log_e(T) \qquad (2.37)$$

and thus

$$A' = \varphi dN = \alpha' \qquad (2.38)$$

where α' is the extinction coefficient of the material which describes the extent that the intensity of a beam of light is reduced when passing through a certain medium and has units of m^{-1}.

Modifying the expression to remove the natural logarithm gives

$$A = -\text{Log}\left(\frac{I_z}{I_0}\right) = \frac{\alpha' \text{d}}{2.303} = \alpha d = \varsigma c d \qquad (2.39)$$

This gives a measure of the absorption of light after passing through a sample with thickness d, of concentration, c (in moles), and molar absorption coefficient, ς, which is a quantity which describes the level of absorption of a certain wavelength of light as it passes through a certain medium and has units of m^2/mol.

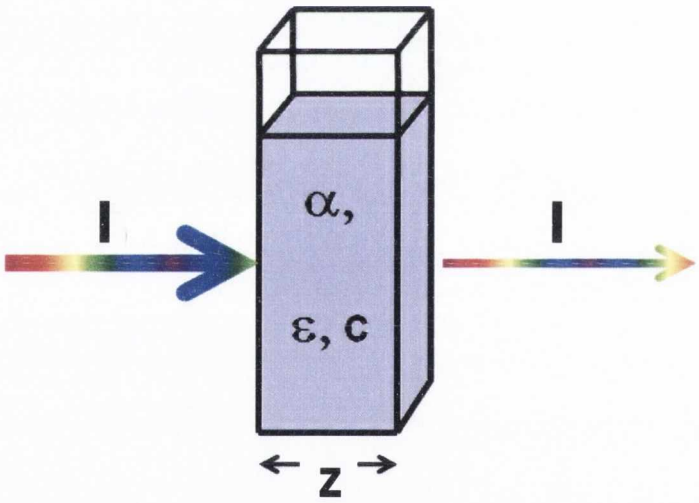

Figure 2.1 *Schematic representation of a Beer-Lambert law measurement. A sample with absorption coefficient α, or equivalently a molar absorption coefficient* **ε** *and concentration c is irradiated with a beam of light with intensity I_0, transmitting a beam with intensity I_z. The measurement of I as a function of wavelength enables the calculation of the sample absorbance from Equation 2.37*

This is a very useful analytical tool as it allows the calculation of the sample concentration or molar absorption coefficient by spectroscopic methods. Figure 2.1 is a schematic representation of an absorption measurement.

2.3.2 The interaction of light with thin metallic films[4]

Consider a plane wave incident, with wavelength λ_0, from a vacuum into a plane isotropic material at normal incidence. The medium is considered to have an infinite thickness. The incident wave, with subscript *i,* propagating along the N_{qi} direction, has an electric field strength (E_i) and magnetic field strength (H_i), at position r and time t, given by

$$\mathbf{E}_i = \mathbf{E}_{0i} \exp\left\{i\left(\mathbf{q}_i \bullet \mathbf{r} - \varpi_i t\right)\right\} \qquad (2.7)$$

$$\mathbf{H}_i = \mathbf{n}_{qi} \times \mathbf{E}_i \qquad (2.40)$$

Here q_i is the incident wave-vector, and ω is the frequency of the oscillating electromagnetic field. One part of the electric and magnetic field enters the medium while the other is reflected off the surface. The portion that enters the medium are written as

$$\mathbf{E}_t = \mathbf{E}_{0t} \exp\left\{i\left(\mathbf{q}_t \bullet \mathbf{r} - \varpi_t t\right)\right\} \qquad (2.41)$$

$$\mathbf{H}_t = \left(\frac{\varepsilon_1}{\mu_1}\right)^{\frac{1}{2}} \mathbf{n}_{qt} \times \mathbf{E}_t \qquad (2.42)$$

While the portion that is reflected from the surface are written as

$$\mathbf{E}_r = \mathbf{E}_{0r} \exp\left\{i\left(\mathbf{q}_r \bullet \mathbf{r} - \varpi_r t\right)\right\} \qquad (2.43)$$

$$\mathbf{H}_r = \mathbf{n}_{qr} \times \mathbf{E}_r \qquad (2.44)$$

Due to the boundary conditions the amplitudes of the incident (E_{0i}, H_{0i}), transmitted (E_{0t}, H_{0t}) and reflected (E_{0r}, H_{0r}) waves related by

$$E_{0t} = E_{oi} + E_{0r} \qquad (2.45)$$

$$H_{0t} = H_{0i} - H_{0r} \qquad (2.46)$$

From Maxwell's equations[23] we obtain

$$\hat{N}E_{0t} = E_{0i} - E_{0r} \qquad (2.47)$$

The symbol $\hat{N}$ denotes the complex refractive index given by $\hat{N} = n + ik$, which is a combination of the real refractive index n and the extinction coefficient k. Combining this with Fresnel' formulae[24] for transmission and reflection coefficients ($\hat{t}$ and $\hat{r}$ respectively) we find

$$\hat{r} = \frac{E_{0r}}{E_{0i}} = \frac{1-\hat{N}}{1+\hat{N}} \qquad (2.48)$$

$$\hat{t} = \frac{E_{0t}}{E_{0i}} = \frac{2}{1+\hat{N}} \qquad (2.49)$$

with a phase change upon reflection[4] of

$$\phi_r = \arctan\left\{\frac{2(k)}{1-n^2-k^2}\right\} \qquad (2.50)$$

The reflectivity, R, is defined as the ratio of the time averaged energy flux reflected from the surface, S_r, to the incident flux S_i. They are expressed[4] as the Poyntig vectors

$$S_r = \frac{c}{4\pi}\left|\mathbf{E}_{0r} \times \mathbf{H}_{0r}\right| \qquad (2.51)$$

$$S_i = \frac{c}{4\pi}\left|\mathbf{E}_{0i} \times \mathbf{H}_{0i}\right| \qquad (2.52)$$

Substituting the electric and magnetic fields given by Equations 2.7, 2.37-2.41 into these Poyntig vectors yields

$$R = \frac{S_r}{S_i} = \frac{|E_{0r}|^2}{|E_{0i}|^2} = |\hat{r}|^2 = \left|\frac{1-\hat{N}}{1+\hat{N}}\right|^2 = \frac{(1-n)^2+k^2}{(1+n)^2+k^2} \qquad (2.53)$$

Similarly, the transmission, T, can be expressed as

$$T = \frac{S_t}{S_i} = \sqrt{\varepsilon_1}\frac{|E_{0t}|^2}{|E_{0i}|^2} = \sqrt{\varepsilon_1}|\hat{t}|^2 = \frac{4n}{(1+n)^2+k^2} = 1-R \qquad (2.54)$$

where ε_1 is the real part of the complex dielectric constant of the medium $\hat{\varepsilon}$ which is made up of the real and imaginary, ε_2, dielectric constants . The square root of ε_1 is equal to the real part of the complex refractive index, n. $\hat{\varepsilon}$, ε_1 and ε_2 are related by

$$\hat{\varepsilon} = \varepsilon_1 + i\varepsilon_2 \qquad (2.55)$$

The dielectric constant connects the electric field strength $\boldsymbol{E}$ and the electric displacement $\boldsymbol{D}$ by

$$\mathbf{D} = \hat{\varepsilon}\mathbf{E} \qquad (2.56)$$

Up until now we have considered the transmittance of a normally incident plane wave through a medium with infinite thickness. This thesis is concerned with thin films and so we must look at the transmission of a single layer with finite thickness. This is done by considering a wave incident on the surface of the film which is split into reflected and transmitted parts. Due to the presence of a second interface, the back of the film, there will be a similar division each time the wave strikes an interface (Figure 2.2). The total

transmitted wave is then obtained by summing the multiply-reflected and multiply-transmitted components.

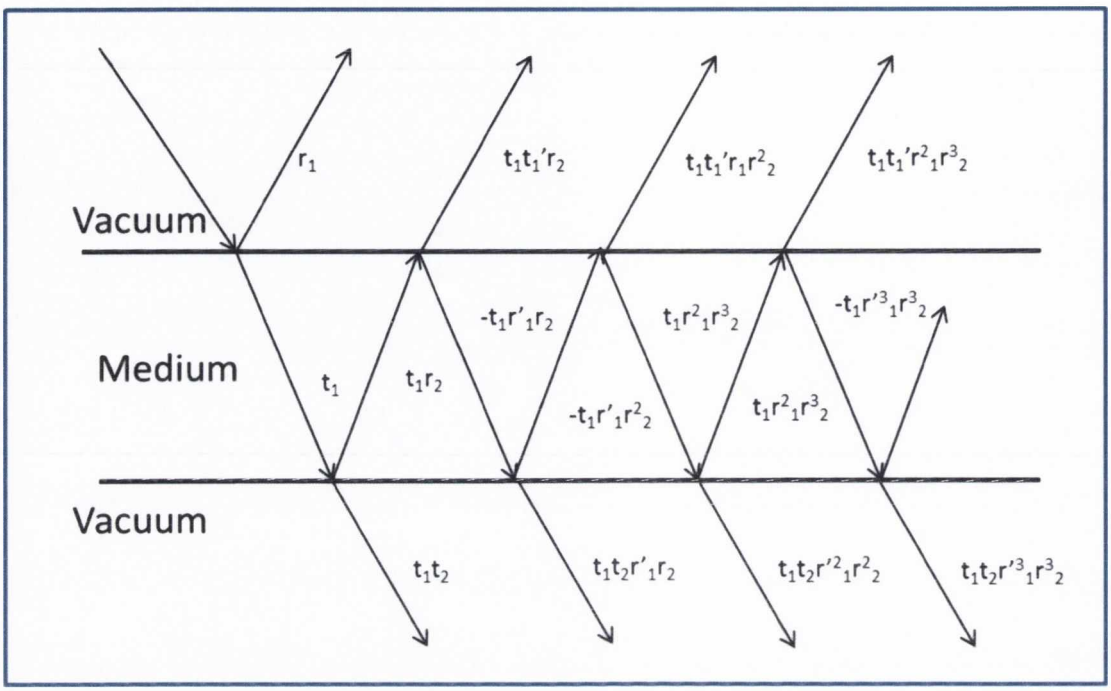

Figure 2.2 *Schematic representation of the multiple reflections and transmissions of light propagating through a thin layer in vacuum. The angle of incidence is depicted as being non-normal for illustrative purposes.*

For a single layer the Fresnel coefficients of propagation from vacuum to the medium are given by $\hat{r}_1$ and $\hat{t}_1$. The corresponding coefficients of propagation from the medium back into the vacuum are given by $\hat{r}_2'$ and $\hat{t}_2'$.

The successive amplitudes of the waves reflected back into the vacuum are given by $\hat{r}_1, \hat{t}_1\hat{t}_1'\hat{r}_2, -\hat{t}_1\hat{t}_1'\hat{r}_1\hat{r}_2^2, \hat{t}_1\hat{t}_1'\hat{r}_1^2\hat{r}_2^3, \ldots\ldots\ldots$. And the transmitted values are $\hat{t}_1\hat{t}_2, -\hat{t}_1\hat{t}_2\hat{r}_1\hat{r}_2, \hat{t}_1\hat{t}_2\hat{r}_1^2\hat{r}_2^2, \ldots\ldots\ldots$. The phase change upon traversing the film is expressed as

$$\beta = \frac{2\pi\hat{N}t}{\lambda_0} \qquad (2.57)$$

The phase change upon reflection is

$$\phi_r = \arctan\left\{\frac{-2k}{1-n^2-k^2}\right\} \qquad (2.58)$$

The attenuation of the wave as it propagates through the medium is described by the absorption coefficient which has the form, given earlier

$$\alpha = \frac{4\pi k}{\lambda_0} \qquad (2.59)$$

Substituting these equations into the summation of the transmitted wave components the final expression for the reflectivity and transmittance for a medium with finite thickness, R_f and T_f, are given by[4]

$$R_f = R\frac{\left(1-e^{-\alpha d}\right)^2 + 4e^{-\alpha d}\sin^2\beta}{\left(1-Re^{-\alpha d}\right)^2 + 4Re^{-\alpha d}\sin^2(\beta+\phi_r)} \qquad (2.60)$$

$$T_f = \frac{\left[\left(1-R\right)^2 + 4R\sin^2\phi_r\right]e^{-\alpha d}}{\left(1-Re^{-\alpha d}\right)^2 + 4Re^{-\alpha d}\sin^2\left(\beta+\phi_r\right)} \qquad (2.61)$$

For cases when the incident wavelength is greater than the film thickness the interference term in Equation 2.61 ($4Re^{-\alpha d}\sin^2(\beta+\phi_r)$) can be neglected. Substituting the expression for ϕ_r into Equation 2.58 the transmittance can then be written as[4]

$$T_f = \frac{\left(1-R\right)^2\left(1+k^2/n^2\right)e^{-\alpha d}}{1-R^2e^{-2\alpha d}} \qquad (2.62)$$

For optically very thin layers ($nd \ll \lambda$) the terms αd and β are very small and therefore the reflection R_f is close to zero. The transmission through the medium is then given by[4]

$$T_f \approx (1-R)^2 \exp\left(-\frac{4\pi kd}{\lambda_0}\right) = (1-R)^2 \exp\{-\alpha d\} \qquad (2.63)$$

However, in the case of a very thin metallic film the transmittance given by Equation 2.61 can be simplified by relating the real and imaginary refractive index and dielectric constant in Equations 2.14 and 2.15, giving

$$T_f = \frac{4}{4 + 8\varepsilon_2 \pi / \lambda_0 + \left(\varepsilon_1^2 + \varepsilon_2^2\right) 4\pi^2 d^2 / \lambda_0^2} \qquad (2.64)$$

The imaginary part of the dielectric constant is related to the optical conductivity and the impedance of free space, Z_0=377Ω, by[4]

$$\varepsilon_2 = \frac{\sigma_{Op} Z_0 \lambda}{2\pi} \qquad (2.65)$$

Multiplying this equation above and below by $\lambda_0 d$ gives

$$\frac{2\pi\varepsilon_2 d}{\lambda} = \sigma_{OP} Z_0 d \qquad (2.66)$$

If $\varepsilon_1^2 \ll \varepsilon_2^2$, which is the case for metals, then substitution of Equation 2.66 into 2.64 yields

$$T_f = \left(1 + \frac{Z_0 \sigma_{OP} d}{2}\right)^{-2} \qquad (2.67)$$

In the case of transparent electrodes it is beneficial to be able to link the sheet resistance, R_s, and the transmittance, T_f.

Rearranging Equation 2.32 for d and substituting into Equation 2.67 gives

$$T_f = \frac{1}{\left(1 + \frac{Z_0}{2R_s}\frac{\sigma_{op}}{\sigma_{dc}}\right)^2} \qquad (2.68)$$

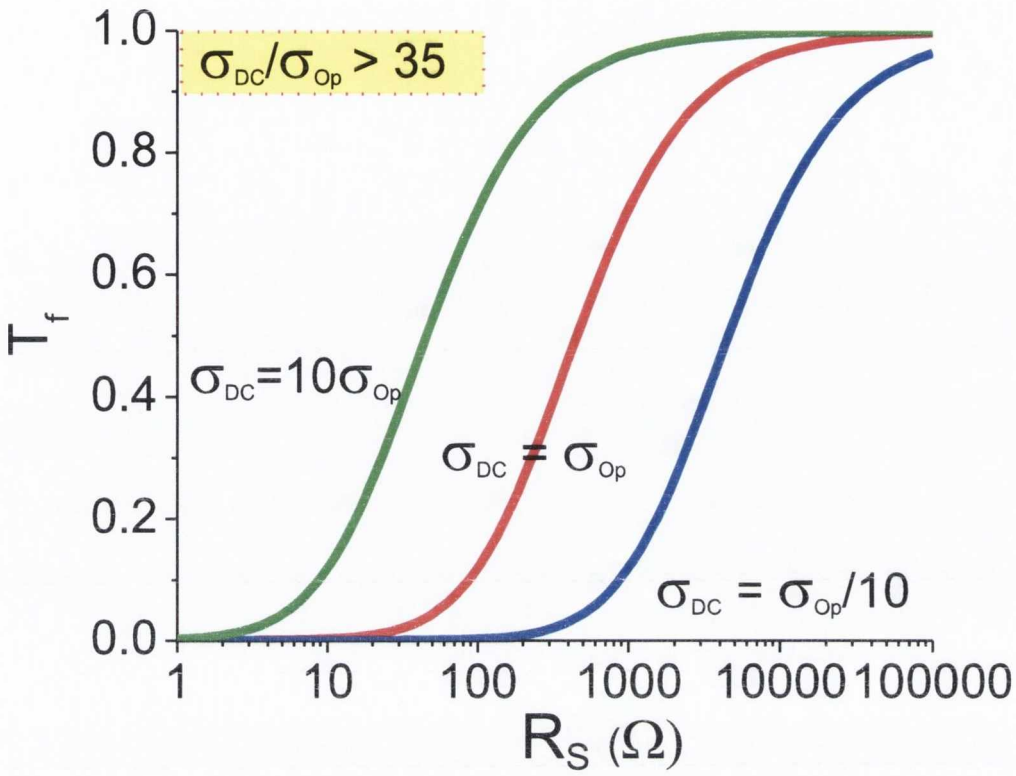

Figure 2.3 *Theoretical plot of transmittance versus sheet resistance for three different ratios of σ_{DC}/σ_{Op}, calculated using Equation 2.68. For transmittance and sheet resistance values necessary for integration in devices as a transparent electrode the ratio of the direct current conductivity, σ_{DC}, to the optical conductivity σ_{Op} must be maximised, resulting in a shift of the plotted curve to the top left.*

This equation shows that the value of the ratio σ_{dc}/σ_{op} for a given value of transmittance and sheet resistance can be used as a figure of merit for transparent conductive films as high values of transmittance and low values of sheet resistance, necessary for device applications, correspond to larger ratio values. It is important to note however, that Equation 2.68 is only a construction used only to relate the transmittance and sheet resistance of a thin metallic films in such a way that results in a convenient figure of

merit. Both σ_{DC} and R_s are inter-dependent on the film thickness as described by Equation 2.31 and as such Equation 2.68 is a convoluted, empirical expression which does not describe any underlying physical processes. Instead it allows the performance of a transparent conductor, in terms of R_s and T_f, to be numerically ranked by the dimensionless ratio of σ_{dc}/σ_{op} and visually represented in a graph of T_f against R_s, such as the graph in Figure 2.3.

In order to be considered for transparent conductor (TC) purposes, a material must possess both high visible region transmittance and high electrical conductivity. High visible region transmittance is a critical factor when designing visual displays based on devices such as light emitting diodes (LED) and plasma cells. In both display types, TCs are used as display electrodes,[25,26] controlling current flow in individual pixels, while allowing the transmission of the emitted light. Ideally the material should possess, along with high transmittance, a flat visible region absorption profile.[27] When incorporating a candidate TC into devices it would be advantageous in terms of patterning and production to have very thin films in order to keep topographical deviations to a minimum,[28] while at the same time keeping transmittance high. The reduction in the thickness of a conducting film will have the adverse effect of increasing the sheet resistance, which should be counteracted by maximising the conductivity. For example, solar cell modules suffer electrical losses due the resistance of the TC resulting in a decrease in device efficiency of 15-25% for the more cost effective devices.[29] Rowell and McGehee[30] calculated the fractional loss in efficiency of a solar cell due to TC resistance using a simple model of the Joule heating loss in the TC layer. They calculated that for a device with optimal width and TC film thickness, an efficiency of >80% can only be attained by a TC thin film with a sheet resistance of < 10Ω/□ and a transmittance of > 90%.[30] Other display-applicable devices such as organic light emitting diodes (OLEDs) also suffer power loses due to the resistance of TC layers.[27] Tests on separate OLED devices incorporating ITO and SWNT

thin films with respective sheet resistances of 20Ω/□ and 200Ω/□ as electrodes showed that the total light output was reduced by two orders of magnitude when using the more resistive film.[27] Although a lower sheet resistance is preferable, most technology platforms can function with $R_s \leq 100\Omega/\square$ and as such the minimum sheet resistance and transmittance requirement is often quoted as $R_s \leq 100\Omega/\square$ and $T \geq 90\%$,[31,32] which, when factored into Equation 2.68, gives a value of $\sigma_{DC}/\sigma_{Op} \geq 35$. This can be considered the minimum value required for a material to be used as a transparent electrode.

It is interesting to note that a value of transmittance has been related to both the absorption coefficient and the optical conductivity. The Beer Lambert Law includes a thickness term which can be related to the sheet resistance by manipulating Equation 2.31 and converting the conductivity to resistivity, giving

$$d = \frac{1}{\sigma_{DC} R_S} = \frac{\rho}{R_S} \qquad (2.69)$$

Relating this measure of d to the transmittance T gives

$$T = \exp\left(\frac{-\alpha\rho}{R_S}\right) \qquad (2.70)$$

In order to determine the applicability of Equations 2.68 and 2.70, a Taylor expansion of transmittance versus sheet resistance can be conducted by

$$e^x = 1 + x + \frac{x^2}{2!} + \frac{x^3}{3!} ..... \qquad (2.71)$$

and

$$(1+x)^\alpha = 1 + \alpha x + \frac{\alpha^2 x^2}{2!} + \frac{\alpha^3 x^3}{3!} ..... \qquad (2.72)$$

These expansions coincide up to the first order for

$$\alpha\rho = \frac{Z_0}{2} \cdot \frac{\sigma_{Op}}{\sigma_{DC}} \qquad (2.73)$$

This can be seen graphically in Figure 2.4, showing the equivalency of describing the transmittance by both the extension of the Beer-Lambert Law and the relationship in Equation 2.68. In both cases the slope of the curves can be used as a figure of merit for transparent conductors, allowing comparison of the optical and properties of different thin films. Using the Beer-Lambert law, the figure of merit is $\alpha\rho$, which results in a figure of merit with units of Ohms whereas the figure of merit, σ_{Op}/σ_{DC}, results in a dimensionless quantity.

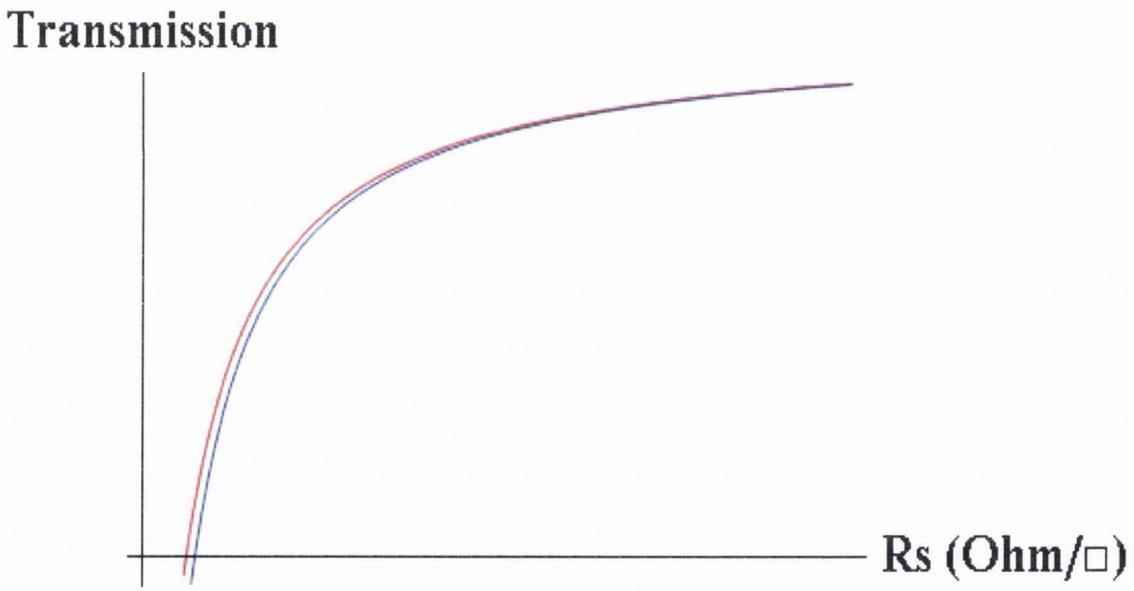

Figure 2.4 *Theoretical plot of Equation 2.65 (red line) and Equation 2.67 (blue line).*

As such, σ_{Op}/σ_{DC} (or more intuitively σ_{DC}/σ_{Op} as an increase in this ratio corresponds with an improvement in the optical and electrical properties) is used as a figure of merit in this work to describe relative performance of transparent and conductive films.

2.4 *Experimental techniques*

2.4.1 UV-Vis-NIR Transmittance and absorbance spectrophotometry[22,33]

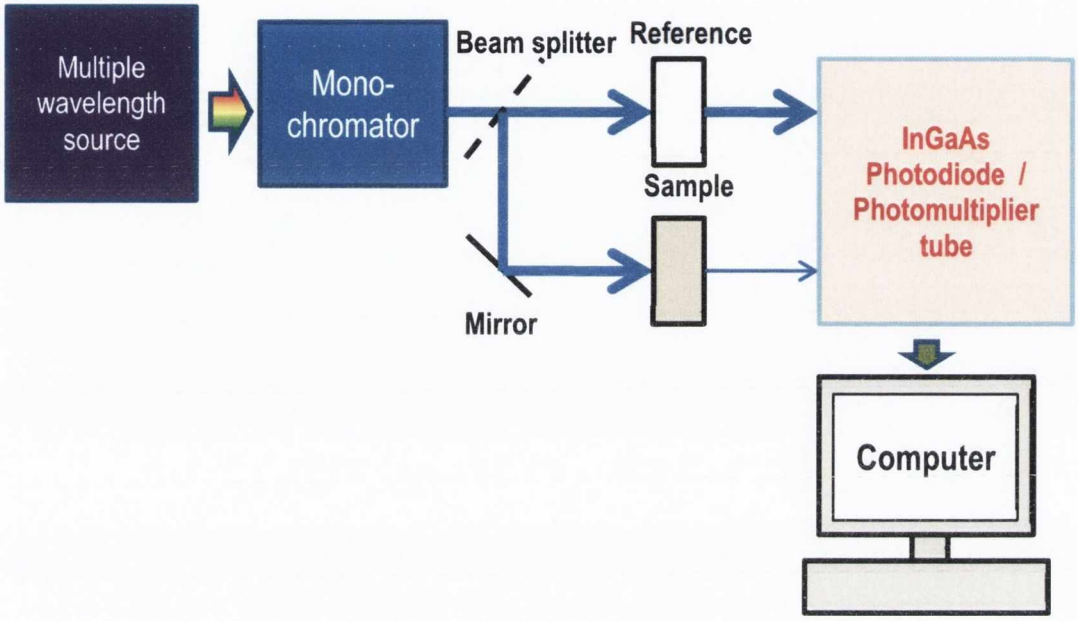

Figure 2.5 *Schematic representation of the UV-Vis-NIR absorption/transmittance spectrophotometer used in this work*

Spectrophotometry is the study of the interaction of electromagnetic radiation with matter over a range of wavelengths. UV-Vis-NIR refers to the ultraviolet-visible-near infrared section of the electromagnetic spectrum which is used in this type of spectroscopy. In this work a Varian Cary 6000i UV-Vis-NIR spectrophotometer with a spectral window of 175 - 1800 nm was used to analyse SWNT aqueous dispersions as well as measure the visible transmittance of SWNT, SWNT/PEDOT and AgNW thin films. A schematic diagram of the device is shown in Figure 2.5.

In this device light sources, including a Xenon lamp, Tungsten halogen and deuterium arc source, provide a broad range of wavelengths. This source is collimated by

the entrance slit to the monochromator which separates the light source into its individual wavelengths. This is done is such a way as to ensure only one wavelength is exiting the monochromator at any one time. The single wavelength beam is split into two equal intensity beams by a beam splitter. One beam is passed through a reference cell while the other is passed through the sample in question. These beams are then detected using a photomultiplier tube and an InGaAs photodiode. This information is interpreted using the Beer-Lambert Law and a measure of how much light is absorbed / transmitted can be deduced. This allows for a wavelength dependent measure of the absorption/transmittance and through it insight into the optical processes occurring in the sample.

2.4.2 White light flat-bed transmittance maps

Wavelength dependant optical transmittance measurements can be achieved by using a transmittance spectrophotometer. However this technique is limited as it does not gather information about the spatial optical uniformity. For a component to be integrated into an optoelectronics device the optical properties are generally required to be homogenous and even throughout its entirety.

In this work an Epson Perfection V700 Photo flat-bed transmission scanner was adapted for this purpose. The scanner has a bit depth of 48 bits per pixel and a spatial resolution of 6400 dpi. The output was calibrated using a number of neutral density filters allowing for position dependant white light transmittance measurements. From this a transmittance map of the sample can be created with a spatial resolution of 4 μm. From these maps a mean and standard deviation value can be calculated and used as a measure of the spatial uniformity of transparent films.

2.4.3 Electrical Measurement: 2- and 4- lead characterisation[34]

Measurement of resistance and calculation of conductivity is of upmost importance in developing new electronic components. Generally this involves connecting electrical contacts to a sample with known dimensions and applying a voltage. The resultant current flow is measured and the resistance, determined using Ohm's Law, can be converted easily into direct current conductivity.

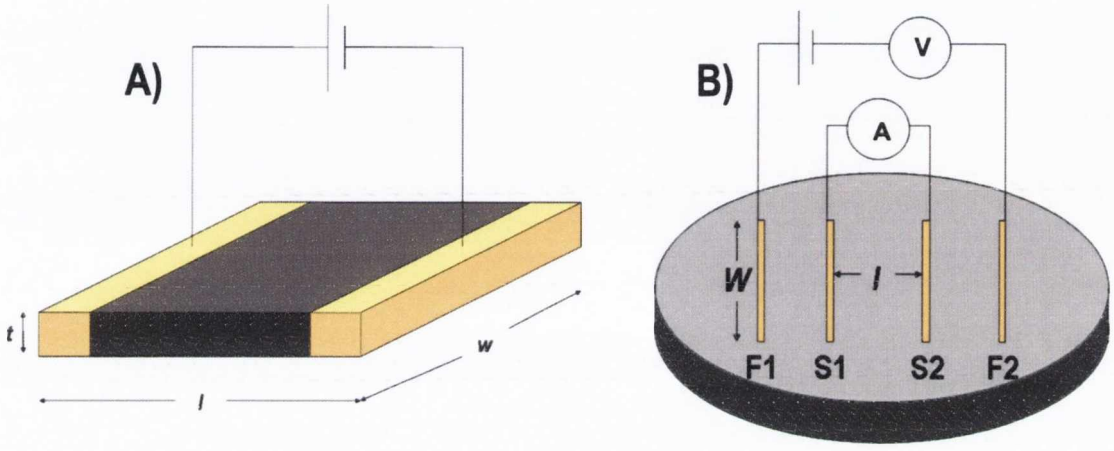

Figure 2.6 *Schematic representation of 2-point and 4-point probe measurements. A) 2-point probe measurements are performed by contacting a sample with metal electrodes and measuring the sample resistance as a function of length. B) 4-point measurements are performed after depositing metal contacts on the sample surface. Force probes F1 and F2 are used to apply a potential while source probes S1 and S2 measure the resultant current flow. Sheet resistance values are calculated using the sample width, w, and length, l.*

For thick, conductive samples a 2-lead probe resistance measurement (Figure 2.6 A) is used as it results in current flow throughout the entirety of the sample. In this measurement metal electrodes are applied to the ends of a strip of the material. Electrical leads are attached and the resistance is measured. By shortening the sample and reapplying

electrodes a number of times a plot of voltage versus length can be obtained. The resistance, R, is related to the length of the sample by

$$R = \frac{l}{\sigma A} + R_c \qquad (2.74)$$

where l and A are the sample length and cross sectional area respectively, R is the measured resistance and R_c is contribution to the measured resistance from the leads used to connect the sample to the measuring device along with a contact resistance between the electrode and sample. The conductivity can then be calculated from the slope of the resultant linear plots. The unwanted resistance contribution, R_c, can be minimised by using highly conductive leads that are glued to the sample with a conductive paint, such as silver paint.

As the dimensions of a sample are reduced the relative contribution to the overall resistance from the contact resistance increases and can result in very inaccurate measurements. In order to change this, the 4-lead technique is used.[35] This technique involves applying four collinear leads to the surface, two force leads and two sense leads (Figure 2.6 B). Specifically, in this method four equidistant, collinear silver wire contacts were fixed onto the film surface using silver paint. The electrodes were then connected to a Keithley 2400 source meter to measure the current-voltage behaviour of the sample.

A potential is applied through the force leads (F1 and F2) resulting in current flow across the sample. As a current is passed through the sample via the outer probes it sets up an electrical potential gradient, and the resulting difference in potential between the two inner sense probes (S1 and S2) is measured with a high-impedance voltmeter. The current (I) creates a voltage drop R_xI, where R_x is the resistance of the sample. The lead and contact resistances of the force leads cause a voltage drop given by $R_{F1}I$ and $R_{F2}I$ respectively, where R_{F1} and R_{F2} are the resistances of the force leads, including the contact resistance. The sense leads measure the overall voltage drop, with contributions from the

sample in question along with the connections i.e. $R_{F1}I + R_xI + R_{F2}I$. However, the sense leads measure the voltage drop associated with the sense leads, $R_{S1}I'$ and $R_{S2}I'$, where I' is the current in the voltmeter measuring the voltage drop across the sense leads and R_{S1} and R_{S2} are the overall resistances of the sense leads and their associated contact resistance. In total, the voltmeter connected across the sense leads measures the voltage drop, $R_{S1}I' + R_x(I+I') + R_{S2}I'$. Due a large impedance in the sense lead circuit $I' << I$ and so the error in the voltage due to Ohmic potential-drops across the sense leads is negligible. This ensures that the measured difference in potential is equal to the difference in potential across the sample. From this measurement and knowledge of the samples dimension the sheet resistance can be calculated.

In the field of semiconductor devices a well-known method of determining the sheet resistance of an approximately two-dimensional is the Van der Pauw method. In 1958 Leo Van der Pauw outlined a method of determining the resistivity of a disc with arbitrary shape,[36] although symmetrical samples result in a reduced measurement error. In this method four small electrical contacts (M, N, O, P) are placed around the circumference a sample that possesses uniform thickness and no isolated holes. Current, I_{MN}, is caused to flow along the circumference of the sample using contacts M and N and the voltage, V_{OP}, across the opposite edge (contacts O and P) is measured. The resistance $R_{MN,OP}$, can be determined from Ohms Law and a similar measurement can produce the resistance $R_{NO,PM}$. The Van der Pauw formula,

$$e^{-\pi R_{MN,OP}/R_S} + e^{-\pi R_{NO,PM}/R_S} = 1 \qquad (2.75)$$

can be rearranged to the form

$$R_S = \frac{\pi}{ln2}\frac{R_{MN,OP}+R_{NO,PM}}{2} f\left(\frac{R_{MN,OP}}{R_{NO,PM}}\right) \qquad (2.76)$$

where f is a correction factor based on the ratio $R_{MN,OP}/ R_{NO,PM}$.

The Van der Pauw variation of the 4-lead resistance measurement is the 4-point probe method.[35] In this method the co-linear leads are replaced by four equally spaced metal point contact probes, all having the same finite radius. These contacts, with inter-probe distance *d*, are pressed against the sample surface and generally these tips are spring mounted to avoid damage to the sample surface, although they can still be detrimental to very thin films like the films investigated in this thesis. The sample area must be very large compared to the inter-probe spacing. The sheet resistance a semi-infinite thin sheet with thickness *t* can be calculated from current and voltage measurements of the sample using the expression

$$R_S = 2\pi t d \frac{V}{I} \qquad (2.77)$$

2.4.4 Resonant Raman spectroscopy[37-39]

Raman spectroscopy is a technique used to study the change in frequency of a photon after interaction with a material.[40] For simplicity, consider a monochromatic wave of light propagating in the *z*-direction with an oscillating electric field interacting with a diatomic molecule. The amplitude electric field, $\boldsymbol{E}_x$, at a given time *t* can be written as

$$\mathbf{E}_x = \mathbf{E}_x^0 \cos(2\pi \nu_o t) \qquad (2.78)$$

Were $\boldsymbol{E}_x^o$ is the maximum amplitude of the electric field and ν_0 is the frequency. The natural vibration of the molecule is ν_v and the normal vibration vector, as a function of time, can be written as

$$\mathbf{q}_v = \mathbf{q}_v^0 \cos(2\pi \nu_v t) \qquad (2.79)$$

A dipole moment, $\boldsymbol{\varphi}$, is induced when the monochromatic light interacts with the molecule and can be expressed in terms of the polarizability tensor of the molecule, ψ.

$$\boldsymbol{\varphi} = \psi \mathbf{E} \qquad (2.80)$$

The induced dipole will oscillate and emit light at three different frequencies which can be determined by expanding the polarizability tensor as a Taylor series in the normal vibration vector as follows:

$$\psi = \psi^0 + \left(\frac{d\psi}{d\mathbf{q}_v}\right)\mathbf{q}_v + \ldots\ldots \qquad (2.81)$$

Upon substitution of Equation 2.78 and 2.79 the dipole moment can be expressed as

$$\boldsymbol{\varphi} = \mathbf{E}_x^0 \psi^0 \cos(2\pi\nu_0 t) + \mathbf{E}_x^0 \left(\frac{d\psi}{d\mathbf{q}_v}\right)_0 \mathbf{q}_v^0 \left\{\cos\left[2\pi(\nu_0 - \nu_v)t\right] + \cos\left[2\pi(\nu_0 + \nu_v)t\right]\right\} \qquad (2.82)$$

The three frequencies of scattered light are ν_o, $(\nu_o - \nu_v)$, and $(\nu_o + \nu_v)$. The scattering process which results in no change in frequency is known as Rayleigh scattering. The other two scattering processes, which result in a shifted frequency by an amount equal to the natural frequency of the molecular vibration, are collectively known as Raman scattering. The light which has been scattered with lower energy, $(\nu_o - \nu_v)$, gives rise to Stokes peaks, while the light scattered with higher frequency, $(\nu_o + \nu_v)$, causes Anti-Stokes peaks in the Raman spectrum.

Typically, Raman spectra are plotted with intensity (arbitrary units) against the shift in wavelength, or Raman shift, $\tilde{\nu}$, with units cm^{-1}. The Raman shift is calculated by

$$\tilde{\nu} = \frac{1}{\lambda_0} - \frac{1}{\lambda_v} \qquad (2.83)$$

Were λ_0 and λ_v are the wavelengths of the incident and scattered light effectively. If the Raman spectrum is plotted in this way then the Rayleigh line will have a zero Raman shift value and the peaks in the spectra will correspond to a Raman active vibrational mode. A vibrational mode will only be Raman active if the rate of change of the

polarizability tensor, ψ, with respect to the molecular normal vibration vector has a non-zero value i.e.

$$\left(\frac{d\psi}{d\mathbf{q}_v}\right) \neq 0 \qquad (2.84)$$

In a molecule with a centre of symmetry, a change in polarizabilty occurs when the centre of symmetry is retained and thus symmetrical vibrations are Raman active. As such, symmetry considerations and group theory are useful tools in determining Raman active modes.

The particular type of Raman spectroscopy implemented in this work is known as Resonance Raman spectroscopy.[38] In Resonance Raman spectroscopy the energy of the incident radiation or the scattered radiation coincides with an electronic transition in the investigated species, allowing investigation into otherwise weak Raman active modes. This enhances the vibration modes associated with the excited electronic transition and the scattering intensity is increased, in some cases by up to 10^5,[40] which provides more spatially specific spectra as only a few molecules experience the increase in scattering.

Resonance Raman spectroscopy is particularly suited to the study of carbon based materials and much work has been done in the area Resonance Raman spectroscopy of carbon nanotubes[41] and Graphene.[42] The Raman spectral features of Graphene and carbon nanotubes will be discussed in the following chapter.

Raman spectroscopy is named after the Indian scientist C. V Raman, who along with K. S. Krishnan, first reported inelastic scattering of monochromatic light in 1928.[43] Two soviet scientist, G. S. Landsberg and L. I. Mandelshtam, had discovered the effect earlier than Raman and Krishnan but unfortunately published their results at a slightly later time.[44] Since then technology advancements have improved the accuracy and ease of use of Raman spectrometers.

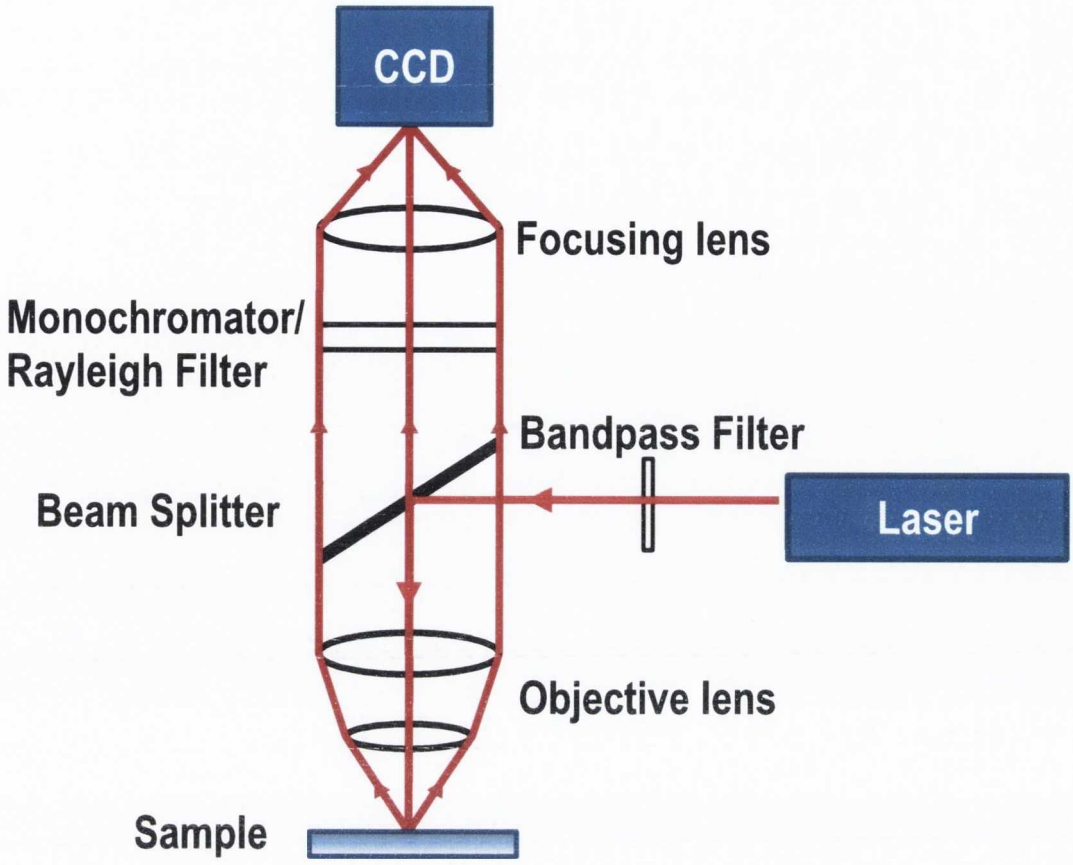

Figure 2.7 *Schematic representation of fundamental components in a Raman spectrometer.*

A basic Raman spectrometer is outline in Figure 2.7. A laser is used to provide a monochromatic, coherent and micron sized light beam. After passing through a bandpass filter to ensure monochromaticity, the beam is focused on the surface of the sample. The reflected light is passed through a Rayleigh scattering filter to reduce its contribution as it is statistically the dominant process and then a variable monochromator. The filtered light is then collected by a CCD camera linked to a computer resulting in a spectrum consisting of the variation of inelastic scattering intensity with changing wavenumber, which is the difference between the excitation wavelength and the scattered wavelength. The scattering intensity is related to the polarizability of the molecule, or the tendency of the electron cloud or charge distribution to be distorted by an external electromagnetic field. Some

specific Raman techniques include time-resolved Raman scattering, which monitors a chemical or physical process over a set time period giving information about the evolution of the system, and surface enhance Raman spectroscopy which enhances Raman scattering due to adsorbed molecules on a metallic surface.

2.4.5 Scanning electron microscopy[45,46]

Traditionally a microscope is an instrument which allows the visual study of small objects by using multiple lenses to focus the light from a sample area into the eye or other light collector. Fundamentally this is based on the interaction of the visible region of the electromagnetic spectrum (300 nm < λ < 800 nm) with the object in question and as such has a theoretical limit, with white light, of ~ 0.3 μm.[45] In scanning electron microscopy (SEM) high energy electrons are produced in a vacuum by a number of possible processes which have, depending on the accelerating voltage, wavelengths of the order of 10^{-9} – 10^{-13} m. The electrons are focused into a beam which is raster scanned across the surface of a metallic sample resulting in the backscattering of electrons and other emissions. Detection of these electrons can be used to form an image of the surface with a resolution as low as a couple of nanometers

Generally electrons are produced by two main sources. Thermionic emission of electrons from the surface of a metal is caused when a sufficiently large voltage is applied across a suitable metal electrode. The emission current is dependent on the temperature and work function of the metal with tungsten (W) being a common choice. Another route, that doesn't require such high temperatures, is field emission. A very strong electric field applied to the surface of metals can cause the emission of electrons. This technique is in many ways preferable to thermionic emission due to a lower temperature and, depending on the filament work function and shape, the ability to be performed using relatively low

voltages. These phenomena are the basis for an electron gun which accelerates the emitted electrons to high energies (between < 1 keV and ~30 keV). The electron beam is then passed through a number of electric or magnetic field condenser lenses which focus the beam into a nanometre sized spot on the surface of the sample. A tear shaped interaction volume extends into the body of the sample and it is in this volume that the majority of electron perturbing processes such as inelastic and elastic scattering occur. Inelastic collisions between electrons and surface atoms can result in the emission of secondary electrons from the K-shell of the sample atom. This process only results emission of electrons very close to the impinging electron beam which makes it a favourable and common way to image surfaces at high resolution. Electrons can be elastically scattered from the sample atoms and a small fraction are back scattered. These can be collected and used to gather information on the contrast between chemical composition from the different degrees elemental species backscatter electrons.

In this work two SEMs were used, a Hitachi S-4300 and a Zeiss Ultra. The S-4300 is cold field emission based microscope with an accelerating voltage capability of 0.5 – 30 kV. It is fitted with secondary electron and x-ray detector and has a resolution of 1.5 nm at 15 kV. The Ultra has a thermal field emission electron source with an accelerating voltage range of 0.02 – 30 kV and a resolution of 0.8 nm at 15 kV. It is equipped with a high efficiency in-lens secondary electron detector allowing very detailed topological imaging.

2.4.6 Atomic force microscopy[47,48]

Atomic force microscopy (AFM) images surfaces through the measured repulsive or attractive forces experienced by a solid probe when in close proximity with the surface. The deflection of a piezoelectric cantilever equipped with a sharp probe at its tip is

measured by a reflected laser, schematically shown in Figure 2.8. As the tip is brought close to the surface it first experiences an attractive force due to the Leonard-Jones type potential and as the distance decrease down to atomic levels the force turns repulsive as the Pauli exclusion principle prohibits the tip and surface electrons from occupying the same state and space. This enables three main imaging modes, contact, non-contact and tapping modes.

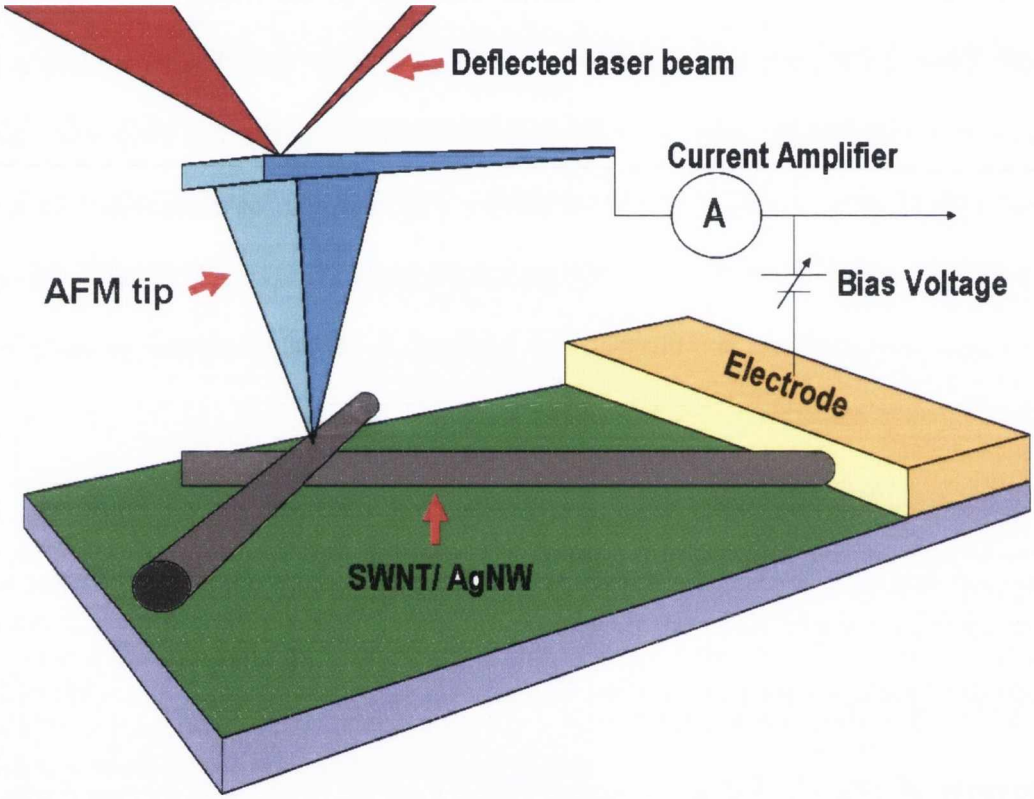

Figure 2.8 *Schematic diagram of the operation of an AFM, specifically in the conductive mode.*

In the contact mode the tip is raster scanned across the area of interest. The tip is kept close enough to the surface to experience the repulsive exclusion force. Due to the steep potential gradient when the tip is in contact with the surface the force experienced by the tip varies greatly with small distances and any deflection of the tip as it moves across

the surface is measured by a deflected laser beam. The amount of deflection of the cantilever can be related to the force experienced by the tip once the spring constant of the cantilever is known. Under certain circumstance this can result in atomically resolved images, however, because the tip is in contact with the sample surface, scratching and damage to both tip and surface can occur. Non-contact mode is less destructive as the tip is held 50 – 150 angstroms above the surface.

The close proximity of the tip results in attractive van der Waals forces which are measured and converted in a topographic image. Although this is less intrusive the measured force is quite weak and as such the resolution is not as high when using optical detectors. By monitoring the frequency of vibration of the cantilever any changes can be correlated with a change of force and so can be used to image to a higher resolution in non-contact mode.

As both contact and non-contact modes have disadvantages in certain areas a third, intermediate, mode is used. An external piezoelectric device actuates the cantilever to a set frequency which is monitored as the probe traverses the surface. The amplitude of vibration is set at 10 – 100 nm and when the tip comes close to the surface the change in the experienced force dampens the vibration. This is measured and by keeping the oscillation amplitude constant the distance between surface and probe is measured providing a surface map of the sample. This mode has less of an impact than contact mode and can provide good resolution.

Normal AFM imaging techniques are limited to topographical and mechanical information without gleaning much information about the electronic properties of the sample under investigation. An AFM technique which is quite useful in the study of nanoscale metallic systems is conductive atomic force microscopy (C-AFM). By coating the tip in a conducting material, a chromium/platinum coating was used in this work, the

probe can essentially become a nano-electronic contact. When the probe is held at ground and a direct current bias (0.2 mV to 2 V) is applied to the sample (Figure 2.8) any contact between the two results in current flow which is recorded. In conjunction with measuring the current flow, the AFM can create a topographic map allowing the superimposition of the two images and the investigation into local electronic conduction. This is very useful for investigating 1-Dimensional nanostructure and has been used to study the electronic properties of individual carbon nanotube bundles deposited on an insulating substrate.[2,49,50] Nirmalraj *et al*,[3] Fujiwara *et al*[51] and Stadermann *et al*[52] have used the technique to investigate the conductance of carbon nanotube networks. They showed that the resistance measured jumped dramatically at SWNT bundle junctions and that when the measured resistance jump was used to calculate the network conductivity from suggested model[53] the results agreed well with experiment.[3]

2.5 References

1 J. R. Hook and H. E. Hall, *Solid State Physics*. (Wiley, 1991).

2 M. Stadermann, S. J. Papadakis, M. R. Falvo, Q. Fu, J. Liu, Y. Fridman, J. J. Boland, R. Superfine, and S. Washburn, "Exponential decay of local conductance in single-wall carbon nanotubes," Physical Review B **72** (245406) (2005).

3 Peter N. Nirmalraj, Philip E. Lyons, Sukanta De, Jonathan N. Coleman, and John J. Boland, "Electrical Connectivity in Single-Walled Carbon Nanotube Networks," Nano Letters **9** (11), 3890-3895 (2009).

4 Martin Dressel and George Gruner, *Electrodynamics in Solids*. (Cambridge University Press, Cambridge, 2002).

5 M. Dressel and G. Gruner, *Electrodynamics of Solids: Optical Properties of Electrons in Matter*. (Cambridge University Press, Cambridge, 2002).

6 P. A. M. Dirac, "The quantum theory of the electron," Proceedings of the Royal Society London A **117** (610-624) (1928).

7 F. Bonaccorso, Z. Sun, T. Hasan, and A. C. Ferrari, "Graphene photonics and optoelectronics," Nature Photonics **4** (9), 611-622 (2010).

8 J. H. Davies, *The physics of low-dimensional semiconductors*. (Cambridge University Press, 1998).

9 K. S. Novoselov, A. K. Geim, S. V. Morozov, D. Jiang, M. I. Katsnelson, I. V. Grigorieva, S. V. Dubonos, and A. A. Firsov, "Two-dimensional gas of massless Dirac fermions in graphene," Nature **438** (7065), 197-200 (2005).

10 A. K. Geim and K. S. Novoselov, "The rise of graphene," Nat Mater **6** (3), 183-191 (2007).

11 R. R. Nair, P. Blake, A. N. Grigorenko, K. S. Novoselov, T. J. Booth, T. Stauber, N. M. R. Peres, and A. K. Geim, "Fine Structure Constant Defines Visual Transparency of Graphene," Science **320** (5881), 1308 (2008).

12 A. B. Kuzmenko, E. van Heumen, F. Carbone, and D. van der Marel, "Universal Optical Conductance of Graphite," Physical Review Letters **100** (11), 117401 (2008).

13 Sukanta De and Jonathan N. Coleman, "Are There Fundamental Limitations on the Sheet Resistance and Transmittance of Thin Graphene Films?," ACS Nano **4** (5), 2713-2720 (2010).

14 Peter Blake, Paul D. Brimicombe, Rahul R. Nair, Tim J. Booth, Da Jiang, Fred Schedin, Leonid A. Ponomarenko, Sergey V. Morozov, Helen F. Gleeson, Ernie W. Hill, Andre K. Geim, and Kostya S. Novoselov, "Graphene-Based Liquid Crystal Device," Nano Letters **8** (6), 1704-1708 (2008).

15 K. S. Novoselov, A. K. Geim, S. V. Morozov, D. Jiang, Y. Zhang, S. V. Dubonos, I. V. Grigorieva, and A. A. Firsov, "Electric Field Effect in Atomically Thin Carbon Films," Science **306** (5696), 666-669 (2004).

16 Keun Soo Kim, Yue Zhao, Houk Jang, Sang Yoon Lee, Jong Min Kim, Kwang S. Kim, Jong-Hyun Ahn, Philip Kim, Jae-Young Choi, and Byung Hee Hong, "Large-scale pattern growth of graphene films for stretchable transparent electrodes," Nature **457** (7230), 706-710 (2009).

17 Alfonso Reina, Xiaoting Jia, John Ho, Daniel Nezich, Hyungbin Son, Vladimir Bulovic, Mildred S. Dresselhaus, and Jing Kong, "Large Area, Few-Layer Graphene Films on Arbitrary Substrates by Chemical Vapor Deposition," Nano Letters **9** (1), 30-35 (2008).

18 Xuesong Li, Yanwu Zhu, Weiwei Cai, Mark Borysiak, Boyang Han, David Chen, Richard D. Piner, Luigi Colombo, and Rodney S. Ruoff, "Transfer of Large-Area Graphene Films for High-Performance Transparent Conductive Electrodes," Nano Letters **9** (12), 4359-4363 (2009).

19 Neil W. Ashcroft and N. David Mermin, *Solid State Physics*. (Saunders College Publishing, 1976).

20 G. S. Ohm, "Die galvanische Kette, mathematisch bearbeitet", (T. H. Reimann, Berlin, 1827).

21 Mark Fox, *Optical Properties of Solids*. (Oxford University Press, 2001).

22 Peter Atkins and Julio De Paula, *Physical Chemistry*. (Oxford University Press, 2002).

23 James Clerk Maxwell, "A Dynamical Theory of the Electromagnetic Field," Philosophical Transactions of the Royal Society of London **155**, 459-512 (1865).

24 O. S. Heavens, *Optical properties of thin solid films*. (Dover publications Inc., New York, 1991).

25 J. P. Boeuf, "Plasma display panels: physics, recent developments and key issues," Journal of Physics D: Applied Physics **36** (6), R53 (2003).

26 Yoon-Heung Tak, Ki-Beom Kim, Hyoung-Guen Park, Kwang-Ho Lee, and Jong-Ram Lee, "Criteria for ITO (indium-tin-oxide) thin film as the bottom electrode of an organic light emitting diode," Thin Solid Films **411** (1), 12-16 (2002).

27 Hu Liangbing and et al., "Flexible organic light-emitting diodes with transparent carbon nanotube electrodes: problems and solutions," Nanotechnology **21** (15), 155202 (2010).

28 Roy G. Gordon, "Criteria for choosing transparent conductors," MRS Bulletin **32** (2007).

29 A. V. Shah, H. Schade, M. Vanecek, J. Meier, E. Vallat-Sauvain, N. Wyrsch, U. Kroll, C. Droz, and J. Bailat, "Thin-film Silicon Solar Cell Technology," Prog. Photovolt: Res. Appl. **12**, 113-142 (2004).

30 Michael W. Rowell and Michael D. McGehee, "Transparent electrode requirements for thin film solar cell modules," Energy & Environmental Science **4** (1), 131-134 (2011).
31 Hong-Zhang Geng, Ki Kang Kim, Kang Pyo So, Young Sil Lee, Youngkyu Chang, and Young Hee Lee, "Effect of Acid Treatment on Carbon Nanotube-Based Flexible Transparent Conducting Films," Journal of the American Chemical Society **129** (7758) (2007).
32 Young-Bae Park, Liangbing Hu, George Gruner, Glen Irvin, and Paul Drzaic, "37.4: Late-News Paper: Integration of Carbon Nanotube Transparent Electrodes into Display Applications," SID Symposium Digest of Technical Papers **39** (1), 537-540 (2008).
33 Agilent Technologies,(10/21/2010)"Cary 6000i preliminary performance data",14/03/2011 http://www.chem.agilent.com/Library/specifications/Public/si-0188.pdf
34 Dieter K. Schroder, *Semiconductor Material and Device Characterization*. (John Wiley & Sons, Inc., New Jersey, 2006).
35 Siegmar Roth and David Carroll, *One-Dimensional Metals*. (Wiley-VCH, Weinhem, 2004).
36 L. J. Van der Pauw, "A method of measuring specific resistivity and Hall effect of discs of arbitrary shape," Philips Research Reports **13** (1), 1-9 (1958).
37 Michael J. Pelletier, *Analytical Applications of Raman Spectroscopy*. (Blackwell Publishing, 1999).
38 Bernhard Schrader, *Infrared and Raman Spectroscopy*. (VCH Publishers, Inc., 1995).
39 Maher S. Amer, *Raman Spectroscopy, Fullerenes and Nanotechnology*. (Royal Society of Chemistry, 2010).
40 J. R. Ferraro and K. Nakamoto, *Introductory Raman Spectroscopy*. (Academic Press Inc., San Diego, 1994).
41 M. S. Dresselhaus, G. Dresselhaus, A. Jorio, A. G. Souza Filhob, and R. Saito, "Raman spectroscopy on isolated single wall carbon nanotubes," Carbon **40** (12), 2043-2061 (2002).
42 A. C. Ferrari, J. C. Meyer, V. Scardaci, C. Casiraghi, M. Lazzeri, F. Mauri, S. Piscanec, D. Jiang, K. S. Novoselov, S. Roth, and A. K. Geim, "Raman Spectrum of Graphene and Graphene Layers," Physical Review Letters **97** (18) (2006).
43 C. V. Raman and K. S. Krishnan, "A New Type of Secondary Radiation," Nature **121**, 501-502 (1928).
44 G. S. Landsherg and L. I. Mandelstam, "Uber die Lichtzerstrenung in Kristallen," Zeitschrift fur Physik **50**, 769 (1928).
45 Ian M. Watt, *The principles and practice of electron microscopy*. (Cambridge University Press, Cambridge, 1997).
46 Joseph Goldstein, *Scanning electron microscopy and X-ray microanalysis*. (Springer, 2003).
47 C. Julian Chen, *Introduction to Scanning Tunneling Microscopy*. (Oxford University Press, 1993).
48 Massimiliano Di Ventra, *Introduction to Nanoscale Science and Technology*. (Kluwer Academic Publishers, 2004).
49 Akihiko Fujiwara, Ryosuke Iijima, Kenji Ishii, Hiroyoshi Suematsu, Hiromichi Kataura, Yutaka Maniwa, Shinzo Suzuki, and Yohji Achiba, "Local current density detection of individual single-wall carbon nanotubes in a bundle," Applied Physics Letters **80** (11) (2002).
50 Pedro J. de Pablo, Maria T. Martinez, Jaime Colchero, Julio Gomez-Herrero, Wolfgang K. Maser, Ana M. Benito, Edgar Munoz, and Arturo M. Baro,

"Mechanical and Electrical Properties of Nanosized Contacts on Single-Walled Carbon Nanotubes," Advanced Materials **12** (8) (2000).

51 A. Fujiwara, R. Iijima, H. Suematsu, H. Kataura, Y. Maniwa, S. Suzuki, and Y. Achiba, "Local electronic transport through a junction of SWNT bundles," Physica B **323**, 227-229 (2002).

52 M. Stadermann, S. J. Papadakis, M. R. Falvo, J. Novak, E. Snow, Q. Fu, J. Liu, Y. Fridman, J. J. Boland, R. Superfine, and S. Washburn, "Nanoscale study of conduction through carbon nanotube networks," Physical review B **69** (201402(R)) (2004).

53 Philip E. Lyons, Sukanta De, Fiona Blighe, Valeria Nicolosi, Luiz Felipe C. Pereira, Mauro S. Ferreira, and Jonathan N. coleman, "The relationship between network morphology and conductivity in nanotube films," Journal of Applied Physics **104** (4) (2008).

Chapter 3: Materials

3.1 Introduction

The purpose of this chapter is to introduce the materials used throughout this research. Single wall carbon nanotubes (SWNTs), Silver nanowires (AgNWs) and the electrically conducting polymer poly(3,4-ethylenedioxythiophene) doped with poly(styrenesulfonate) (PEDOT:PSS) all exhibit interesting and indeed very useful properties. This chapter will act as an introduction to these materials, providing a broad overview of the structure, properties and synthesis while indicating the relevant advantages offered by these materials as well as problems associated with them. It is the hope that this information will persuade the reader that these nanomaterials are a viable choice in the pursuit of conductive, transparent and more importantly, flexible electrodes.

3.2 Indium tin oxide

Certain metallic oxides have been known for a long time to display both electrical conductivity and optical transparency. Badeker[1] reported conducting and transparent thin films of cadmium oxide prepared by thermal oxidation of sputtered cadmium films as far back as 1907. Since then, semiconducting oxide films have attracted a lot of investigation due to the many possible applications of transparent conductors.[2] One of the main areas of interest is the use of transparent conductors in flat panel displays. Unlike cathode ray tubes,

flat panel displays require a conducting, transparent material with the industry standard being indium tin oxide (ITO).

Indium tin oxide is name given to tin-doped indium oxide films. Indium oxide (In_2O_3) is a doped n-type semiconductor, typically consisting of ~90% In_2O_3 and ~10% SnO_2. ITO has a cubic bixbyte structure, the same crystal structure as undoped-bulk In_2O_3.[3] The nature of ITOs electrical conductivity is still highly contentious.[4] Doping In_2O_3 with SnO_2 replaces In^{3+} with Sn^{4+}, injecting charge carriers into the lattice and partially filling the conduction band.[5] It has been proposed that oxygen vacancies create an impurity band which overlaps the conduction band, creating a degenerate semiconductor,[6] and recent work has shown that hydrogen atoms at interstitial or oxygen defect sites can create shallow donor states in both In_2O_3 and SnO_2, both of which contribute to the electrical conductivity.[4] Early measurements indicated a direct band gap of ~3.75eV using optical methods, with lower energy forbidden transitions occurring at 2.619eV.[7] Recent studies have set an upper limit on the fundamental band gap of ITO at 2.9eV with the optical band gap having an energy of 3.75eV.[8] Due to this, ITO exhibits strong absorption above 4eV[5] with lower energy absorption related to scattering by tin atoms and grain boundaries.[5]

ITO thin films are always polycrystalline and optimised deposition can result in films which display conductivities as high as 1.2×10^5 S/m,[9] with a carrier concentration and Hall mobility of $1.38 \times 10^{21} cm^{-3}$ and $53.5 cm^2(V\ s)^{-1}$) respectively.[9] This high electrical conductivity is accompanied by a visible region transmittance > 80% as well as high infrared reflectance.[9] These electrical and optical properties make ITO a suitable material for rigid transparent conductor roles.[2] However, due to ITO's crystalline nature, thin films of the material crack during tension and compression,[10] showing large increases in the resistance of the samples.[11,12] This mechanical instability, along with the scarcity of Indium[5] renders ITO unsuitable for the next generation of flexible displays.

3.3 Carbon Nanotubes

3.3.1 Carbon

Carbon, it could be argued, is perhaps the most important element in existence. Due to its accommodating electronic structure it can, and does, form the basis of a vast array of chemical compounds.[13] Indeed, this ability allowed the formation of the earliest and simplest organisms which in turn evolved into life as we know it today. This argument is based on the fact that carbon has four valence electrons with an isolated electron configuration of $1s^2 2s^2 2p^2$ which allows for each carbon atom to bond with up to four other atoms.[14] Not only does this create the possibility of very complex and multiple component molecules but also, due to the carbon atoms' ability to share electrons between them in strong π-bonds, facilitates very stable two dimensional structures.[15]

Carbon has an electron configuration of $1s^2 2s^2 2p^2$ which would suggest that a maximum of two electrons are required to fill the valence energy level. However, these orbitals experience hybridisation in which the lower energy $2s^2$ shell mixes with the $2p$-orbitals to create hybrid orbitals with relative directionality. This essentially convert's carbon from a species with two half-filled orbitals into one that can have a maximum of four and so allowing it to bond to up to 4 other atoms. These hybrid orbitals allow carbon to exist in a number of different allotropes, whose properties depends on the orientation of these hybrid bonds.

Probably the best known carbon allotrope is diamond. This crystalline material consists of carbon atoms covalently bonded to four other carbon atoms through sp^3 hybridized σ-bonds in a tetrahedral arrangement. The identical bonds in this lattice (shown in Figure 3.1) result in diamond being extremely strong, making it very useful in industry. Its other properties include high thermal conduction, high optical dispersion[16] as well as a wide band gap making it an electrical insulator.[15]

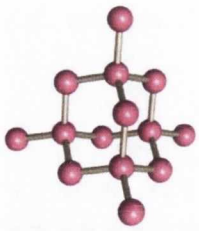

Figure 3.1 *Crystalline structure of diamond showing the tetrahedral sp^3 hybridised bonds.*

The most energetically favourable and common allotrope of carbon is known as graphite.[15] In this arrangement, sheets of strongly bound atoms are weakly held together in layers by van der Waals forces. In each individual layer every carbon atom is bonded to its three nearest neighbours through σ-bonds of the sp^2 hybrid orbitals. The hybridisation of these orbitals results in a lone *2p* orbital perpendicular to the plane of the sheet which overlaps above and below the sheet with neighbouring *2p* orbitals to form a delocalised bonding state, known as π-states, and the anti-bonding π^*-states. This bonding network then interacts weakly with other sheets to form a three dimensional layered structure (Shown in Figure 3.2). The physical properties of graphite, including electrical conductivity, are highly anisotropic due to these layers confining it applications.[15]

A single layer of graphite, called Graphene, was thought impossible to isolate due to thermal fluctuations which make it energetically favourable for two dimensional crystallites to rearrange themselves into 3-D structures.[17] However, Graphene has been epitaxially grown on certain substrates, the first report of which dates back to 1966 when chemical vapour deposition was used by Karu *et al*[18] to grow mono- and few-layer Graphene on transition metal substrates. In 1976 Isett *et al*[19] reported the formation of mono-layer Graphene on the surface of Ni(111) via annealing induced segregation of carbon. The structure of mono-layer Graphene on the surface of Ni(111) were determined by Rosei *et al*[20] and later re-evaluated by Gamo *et al*[21] in 1997. However, these epitaxially

grown Graphene films are not considered isolated as interaction with the substrate alters the electronic structure of Graphene and hence measurement of its electronic properties have proven elusive.

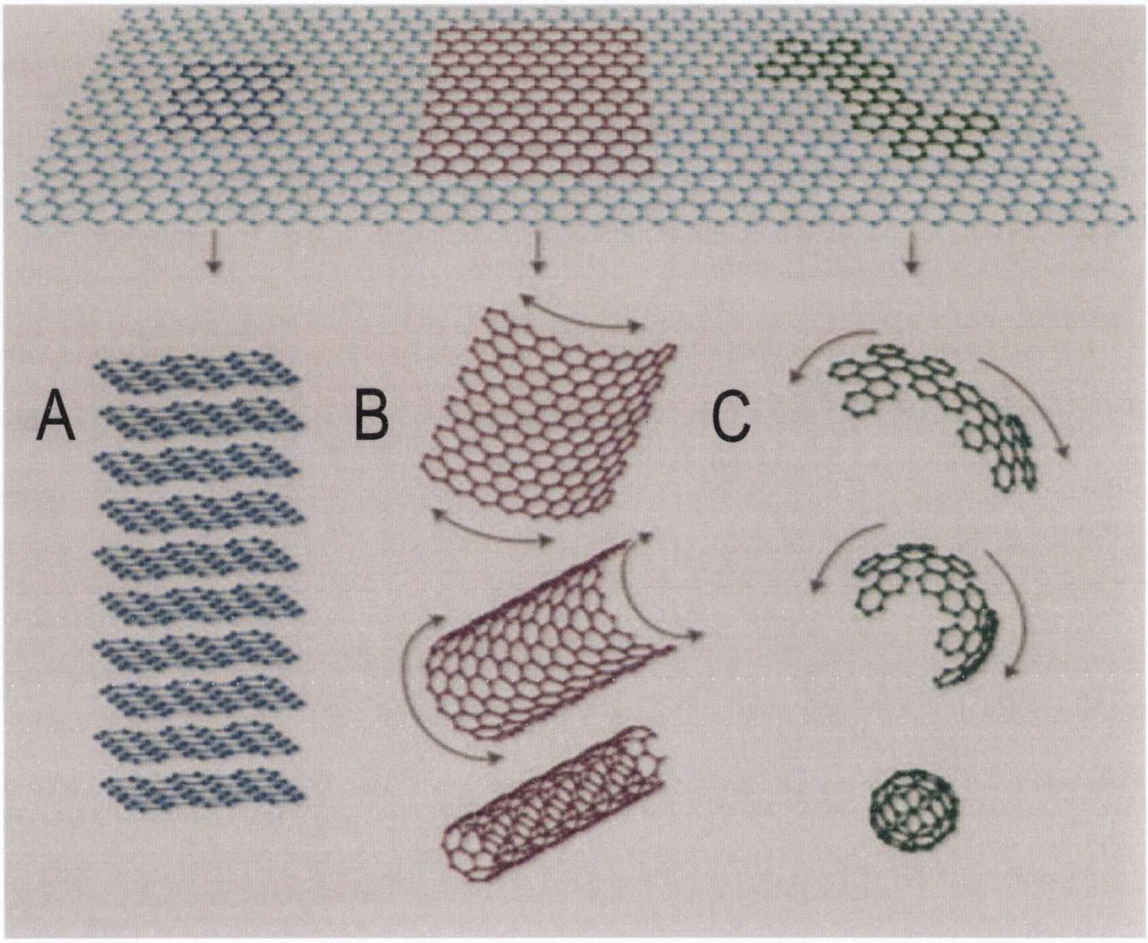

Figure 3.2 *Figure showing how an individual graphene sheet can play the role of building block for different carbon allotropes. A) Graphite occurs when graphene sheets are stacked together. B) Rolled into a cylinder the sheet becomes a single wall carbon nanotube. C) Graphene can be wrapped into a ball, giving birth to large variety of Fullerenes. (Image reproduced from Nat. Mat. 6, 183-191(2007))*

In 2004 the first example of an isolated single layer was demonstrated by Novoselov *et.al*[22] via mechanical cleaving using scotch tape and other routes have been

demonstrated such as liquid phase exfoliation.[23] In particular, Hernandez *et al*[24] demonstrated a solvent based method of exfoliating individual, defect free, Graphene sheets from bulk graphite. This work was built on by Kahn *et al*[25]. In their report the authors outlined a process for exfoliating graphite in solvents using low power sonication to produce high concentration (1.2 mg/ml) dispersions of Graphene, with flake lengths above 1 μm. In similar work Lotya *et al*[26] reported exfoliation of Graphene from graphite in water/surfactant solutions which resulted in a large percentage of mono- (~3 %) and few-layer (~40 %) Graphene flakes. Lotya *et al*[27] went on to improve their surfactant-stabilised Graphene dispersions, producing up to 20 % mono-layer Graphene sheets with an average length and width of ~1 μm and 400 nm respectively. Such techniques have given researchers the chance to investigate Graphene's extraordinary properties with the focus being on its electronic nature. In an isolated Graphene flake the unhybridized π- and π^*- states mentioned above give rise to a valence and conduction band in the band structure which meet at two points in the Brillouin zone which lie at the Fermi level. Since there is no energy gap between the two bands and the density of states vanishes to zero at the Fermi level Graphene is sometimes referred to as a zero gap semi-conductor.[28]

The Graphene hexagonal lattice is the buildings block for a host of novel and interesting structures. In 1985 Kroto *et al*[29] were investigating the conditions for the formation of atomic carbon clusters in the atmospheres of giant red stars. This resulted in the discovery of the Buckminsterfullerene, the first member of the new carbon allotrope family, the Fullerenes, to be studied and characterised. Where diamond is a three dimensional crystalline structure and graphite is essentially stacked two dimensional crystals, fullerenes are hollow balls, tubes or ellipsoids consisting entirely of carbon. For example, the Buckminsterfullerene has a molecular formula of C_{60} and a truncated icosahedron structure consisting of twenty hexagons and twelve pentagons (Shown in Figure 3.2 C). However, the history of the specific class of Fullerene, the carbon nanotube,

dates back over 50 years when the first carbon nanotube-like structures were seen in 1952 by Radushkevich and Lukyanovich who published clear images of 50 nanometre diameter tubes made of carbon in the Soviet *Journal of Physical Chemistry*.[30] Due to the journal being in Russian and the lack of access to soviet journals caused by the cold war the discovery went largely unnoticed. In 1976 Oberlin *et al*[31] studied the carbon nanofibres produced by the pyrolysis of benzene using electron microscopy. In their report they showed an image of a nano-scale tube of carbon but unfortunately the resolution as not sufficient to confirm the presence of a graphitic structure. In 1991 Ijima reported the formation of coaxial helical tubes of graphitic sheets in the soot of an arc-discharge reactor.[32] These tubes, which have become known as carbon nanotubes, can consist of multiple concentric layers, called multiwall carbon nanotubes (MWNT), dual layer, called double wall carbon nanotubes or a lone layer, shown in Figure 3.2 B, called single wall carbon nanotubes (SWNT) which were separately reported in 1993, by Ijima[33] in the NEC corporation and Bethune *et al*[34] in the IBM research division. Carbon nanotubes hold great interest and promise in the field of nanotechnology due to their extraordinary properties. The structure and properties of carbon nanotubes will be the focus for the next section of this chapter.

3.3.2 Structure of Single Wall Carbon Nanotubes

To form a single wall carbon nanotube, a single graphene sheet must be rolled to form a seamless cylinder, the dimensions of which lie in the nanometer scale for the diameter and from micrometer to centimetre in length, giving them extremely high aspect ratios. This tube can be closed at each end by a hemispherical cap composed of hexagonally bonded carbon atoms with pentagonal defects.

The joining of the ends of a vector connecting any two crystallographic equivalent points will produce a nanotube with specific orientation. The crystal lattice translation vectors $\vec{a}_1$ and $\vec{a}_2$, depicted in Figure 3.1.3, can be linearly combined to give the chiral vector $\vec{c}_h$.

$$\vec{c}_h = n\vec{a}_1 + m\vec{a}_2 \qquad (3.1)$$

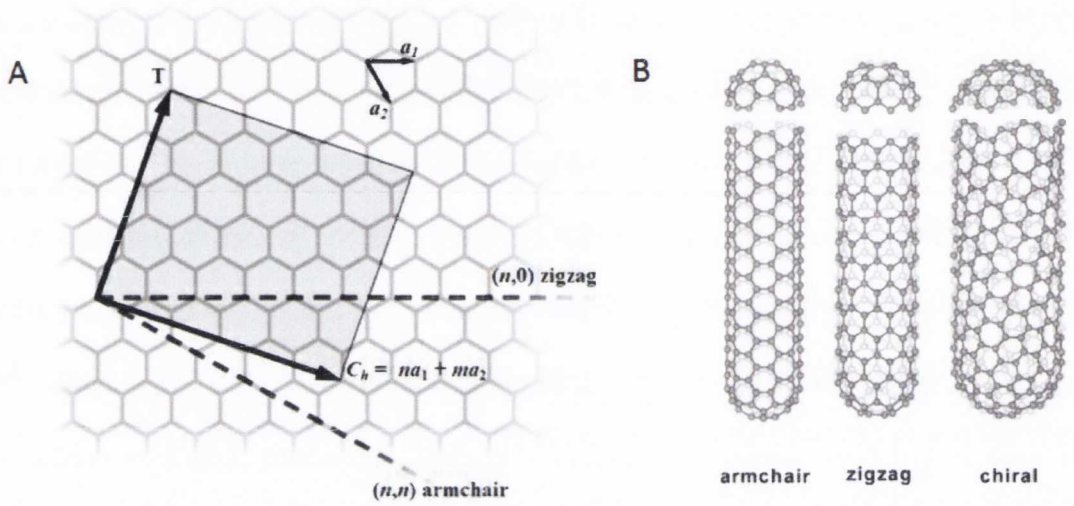

Figure 3.3 *A) Figure representing the translation vectors $\vec{a}_1$ and $\vec{a}_2$ and the wrapping or chiral vector $\vec{c}_h$, here defined as $\overrightarrow{OA}$. In this example the (5, 2) chiral vector is shown. B) Representative models of the three main nanotube groups, armchair, zigzag and chiral.*

The indices (n, m) are integers which describe the nanotubes crystallographic 'finger print' or chirality.[35] Although there a large number of possibilities in the variation of chiralities, limits do exist due to strain energies associated with the bending of the sp^2 bonds between adjacent carbon atoms and the diameter tends to lie around 1.5 nm.[15] The diameter of a nanotube can be determined if the chirality is known as the diameter is simply given by L/π where L is the circumferential length and

$$L = |c_h| = \sqrt{c_h . c_h} = a\sqrt{n^2 + m^2 + nm} \qquad (3.2)$$

And so

$$d = \left(a\sqrt{n^2 + m^2 + nm}\right)/\pi \qquad (3.3)$$

Although there are a host of chiralities, two distinct combinations of integer indices gives achiral nanotubes (see Figure 3.13 B). These are (n, 0) and (n,n), sometimes referred to as zigzag and armchair tubes respectively because of the pattern associated with the carbon carbon bonds along the chiral vector $\vec{c}_h$. These special cases correspond to a chiral angle, θ, of 0° for the zigzag and 30° for the armchair. All other wrapping vectors with a chiral angle in the range $0 \leq \theta \leq 30°$ are referred to as chiral.

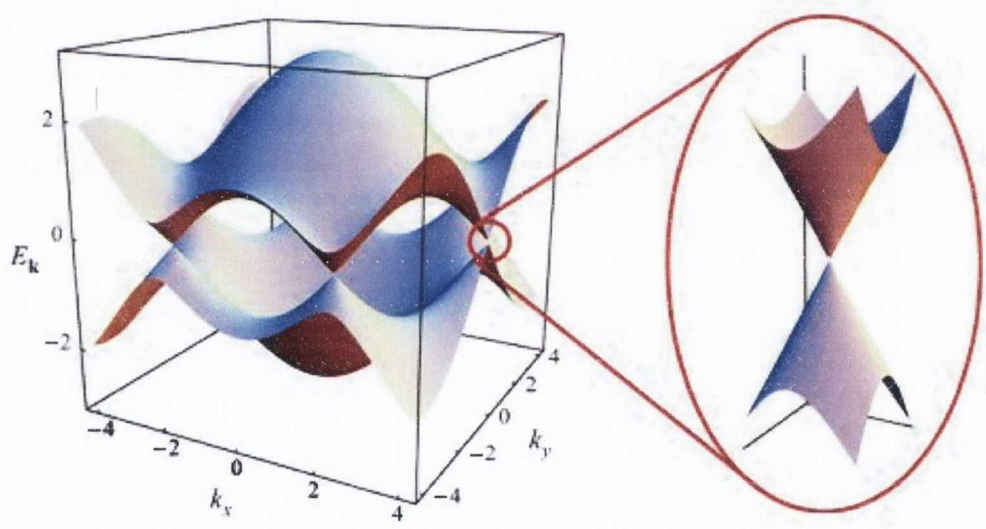

Figure 3.4 *Valence band and conduction band dispersion in the first brillouin zone of a single graphene layer. (Image reproduced from J. Phys.: Condens. Matter* 21 323201 (2009))

3.3.3 Electronic properties of Single Wall Carbon Nanotubes

Since a nanotube consists of rolled graphene it is instructive to first consider the electronic structure of a sheet of graphene in the x-y plane. In this system each carbon

atom has three sp^2 hybrid σ–bonds to neighbouring resulting in a hexagonal 'chicken wire' structure. This leaves a lone electron in the p_z orbital of each atom. These combine and result in the π and π^* states. Due to the high number of atoms involved in this extended π system and the exclusion principle, the states are split to form π and π * bands. There are two electrons per hexagonal unit and this means that the lower p band is completely filled. The energy dispersion of graphene in the first Brillouin zone can be calculated using a tight binding method[35] and is shown in Figure 3.14 showing that at the high symmetry K point the π and π * states are tangent to each at the Fermi level.

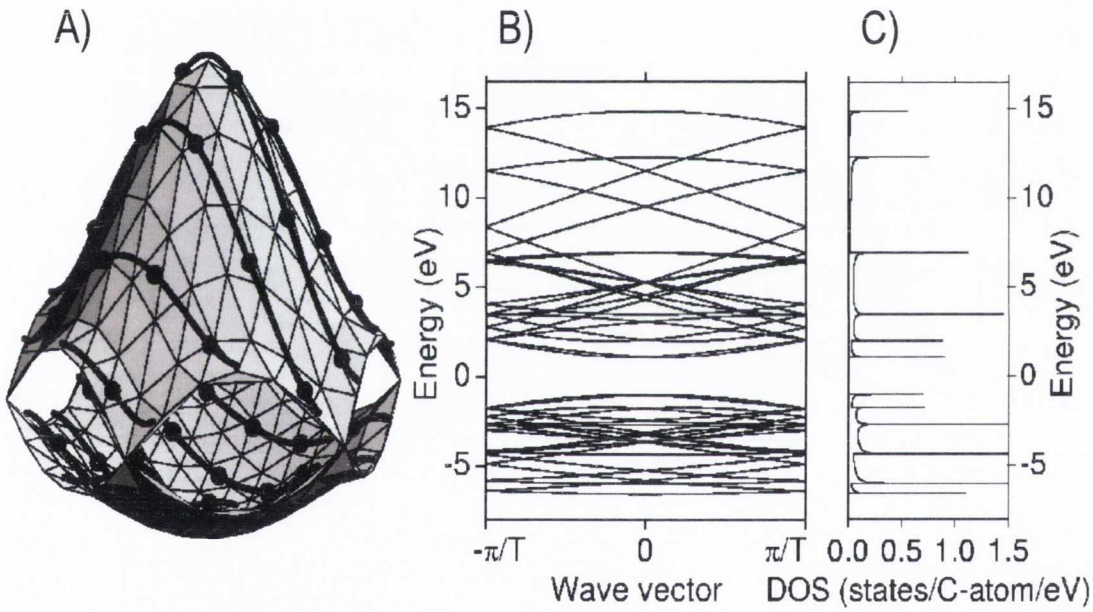

Figure 3.5 *A) The conduction and valence bands of the graphene layer in the 1st Brillouin zone calculated according to the π -band nearest-neighbor tight-binding model. The cutting lines of the zone folding scheme for the (4, 2) nanotube are shown as dashed lines.[36] B) Band diagram for the (4, 2) nanotube obtained by zone-folding from A). C) Density of electronic states for the band diagram shown in B).(Image reproduced from Physics Reports 409 (2), 47-99 (2004))*

So far the electronic structure of an unrolled nanotube has been discussed, but to understand the properties of carbon nanotube the consequences of rolling the graphene sheet must be addressed. In the above treatment, Born-von Karman periodic boundary conditions apply,[37] $\vec{k}.\vec{r} = 2\pi j$, where $\vec{k}$ is the electron wavevector, j is an integer and $\vec{r}$ is any lattice translation vector. In reciprocal space the spacing of k states with respect to the number of states, N, and parallel to $\vec{r}$ is given by

$$\frac{dk_r}{dN} = \frac{2\pi}{|\vec{r}|} \qquad (3.4)$$

If the graphene sheet is assumed to be infinitely long, $|\vec{r}|$ is infinitely large and so the spacing between k states in infinitely small in any direction. When you roll up a graphene sheet to form a nanotube $|\vec{r}|$ along the tube axis in infinite but along the circumference of the tube the boundary condition becomes $\vec{k}.\vec{c}_h = 2\pi j$. Since the chiral vector is usually only tens of nanometers long the k states along $\vec{c}_h$ are discrete. The allowed k states of a nanotube are restricted to lines within the first Brillouin zone parallel to the tube axis. The allowed wave vectors of the nanotube in reciprocal space can be mapped onto the first brillouin zone of graphene (Figure 3.1 A).[36] Through this restriction the energy dispersion can be obtained and an example of a (4, 2) nanotube is shown in Figure 3.1 A. As shown in Figure 3.14 B there is a gap between the conduction and valence bands everywhere in the Brillouin zone except the K points and unless the vector $\vec{K}$, connecting the zone centre and zone edge is allowed, the nanotube will have a bandgap. The curvature of the bonds along the circumferential direction are slightly distorted resulting is degeneracy of the K-point in the direction of $\vec{K}$. As a consequence the only truly metallic zero bandgap nanotubes are those having n = m or when n is a multiple of 3.[15]

This metallic / semiconducting variation is apparent when describing the density of states (DOS) of the nanotube from their individual energy dispersions. When looking at the DOS energy dependence a non-zero value is seen for metallic nanotubes, whereas semiconducting tubes exhibit a zero DOS.[38] The 1-Dimensional nature of nanotubes also gives rise to important singularities called *van Hove* singularities[15] which appear at band minimums where the bands overlap. Furthermore these singularities have energy gaps which are directly related to the chiral vector and hence the nanotube diameter. Since the gaps are structure dependent and can result in sharp optical transitions the DOS plays an important role in the spectroscopy study of carbon nanotubes.[15]

3.3.4 Resonant Raman spectroscopy of Graphene and Carbon Nanotubes

As graphene is the building block of the Fullerene family, including carbon nanotubes, it is instructive to first consider its Raman spectrum. There are three sharp peaks in the Raman spectra of graphene, the *G*-band (~1580cm$_{-1}$), the *D*-band (~1360cm^{-1}) and the *2D*-band (~2700cm^{-1}).[39,40] The doubly degenerate E_{2g} mode at the Brillouin zone centre gives rise to a sharp peak in the Raman spectrum at ~1580cm^{-1}.[41] This so-called *G*-band is due to the first order mode arising from in-plane longitudinal and transverse lattice vibrations.[41] The *G*-band position increases as the Fermi energy increases when graphene is doped[42-44] due to a non-adiabatic breakdown of the Kohn anomaly.[45] The *G*-band full width at half maximum increases with increasing Fermi energy as phonons are restricted from decaying to electron-hole pairs due to the Pauli exclusion principle.[42,45]

The peak at ~1360cm^{-1}, which is due to an in plane A_{1g} zone edge mode,[41] is called the *D*-band and is a dispersive second order process which only becomes active with the introduction of defects to the graphene sheet, either crystal edges or lattice defects.[39,41]

The second order of the *D* peak is known as the *2D* peak and is attributed to a two phonon fourth order scattering process.[46,47] Due to double resonance, this peak changes in position with varying excitation energies.[46] This peak can be used to discern the number of graphene layers in a sample.[47] Unlike a single graphene layer, which has a single *2D* peak, a multilayers of graphene exhibit a *2D* peak with four components, D_{1B}, D_{1A}, D_{2A} and D_{2B} because the electronic interaction between layers splits the π and π^* bands into four bands.[39] As the number of layers is increased from a bilayer the relative contribution of the D_1 peaks is reduced and after five layers the spectra is a near match to that of bulk graphite.[39] Furthermore, the *2D* peak intensity can give information about the doping level.[42,48] The *2D* peak position increases for *p* doping while it decreases for *n* doping[42] and as the doping level increases the intensity of the *D* band decreases.[48]

The typical Raman spectra of carbon nanotubes displays number of key features, including the radial breathing modes (RBM) of the NTs (~ 200 cm^{-1}), the D-band (~ 1300 cm^{-1}), the G-band (~ 1570 cm^{-1}), and the 2D-band (~ 2600 cm^{-1}). The RBM is a first order phonon mode in which the carbon atoms move coherently in the radial direction, perpendicular to the nanotube axis, which stretches the carbon-carbon bonds. The frequency of the RBM is inversely proportional to the SWNTs diameter, and can be used to assign the chirality of the investigated nanotube.[49] The D- band is a peak attributed to defect induced disorder in the crystal lattice.[50] The D-band is a second order one-phonon resonance mode[46] which disappears in perfect crystal lattices.[50,51] The G-band is a first order phonon mode associated with the vibration of the two carbon atoms in the nanotube unit cell. It results from two vibrational modes, in-plane vibrations along the nanotube axis (longitudinal optical mode , LO) as well as in-plane vibrations along the circumferential direction of the nanotube (transvers optical mode, TO).[52] The G-band consists of two main peaks attributed to the axial and circumferential vibrations, the G^+ and G^- peaks.[53] For semiconducting nanotubes the G+ and G- bands are assigned to the LO and TO vibrational

modes respectively, the opposite of metallic nanotubes in which the G^+ and G^- bands are assigned to the TO and LO respectively.[52] The 2D-band peak is due to two-phonon second order scattering process.[46] For individual SWNTs, both metallic and semiconducting, the 2D peak is a 2-peak structure and information about the chirality can be determined.[54]

3.3.5 Physical properties of Single Wall Carbon Nanotubes

The crystal structure and unique electronic properties of carbon nanotubes give rise to a number of very advantageous physical properties. As discussed previously, the sp^2 hybrid bonding regime give rise to a delocalised π electron system. Theoretical calculations[55] have shown that in contrast to other metallic wires, the electrons experience an effective disorder averaged over the tube circumference, leading to electron mean free paths that increase with diameter. Single wall carbon nanotubes have a theoretical current density[56] of 4×10^9 A/cm^2 which is three orders of magnitude larger than copper. The carbon atoms found in a nanotube lattice are strongly bonded. These bonds are quite stiff and result in high longitudinal sound velocity (~ 20 Kms^{-1}) and very good thermal conduction (1750 – 5800 Wm^{-1}K^{-1}).[15]

Nanotubes exhibit a very high Young's modulus and strength while being relatively light weight with a low density of 1500 Kg/m^3, much lower than that of steel (~ 7800 Kg/m^3). Theoretical calculations[57] predict a Young's modulus of the order of 1000 GPa which has been confirmed indirectly and directly. Lourie *et al*[58] used Raman spectroscopy to monitor the shift in position of the 2D band during cooling-induced compressive deformation of SWNTs embedded in an epoxy matrix and were able to calculate a Young's modulus value of 3000 GPa from a thermal stress model. Krishnan *et al*[59] used transmission electron microscopy to measure the freestanding room temperature vibrations of a range of SWNT. From this an average value for the Young's modulus of SWNTs was

calculated to be 1250 GPa. These values are superior even to Kevlar (130 GPa) making carbon nanotubes one of the stiffest materials known. They also exhibit strengths of between 50 and 100 GPa which is extremely high when compared to even the best steel (~ 5.5 GPa). Nanotubes have also shown to be able to withstand very high bending radii and kinks[60] which, and along with their electronic properties, make them remarkably suitable as network components in flexible electronics.

3.3.6 Synthesis and production of Single Wall Carbon Nanotubes

Carbon nanotubes can be synthesised using a number of different routes with four main techniques dominating the field. These are arc discharge,[32] laser ablation,[61] chemical vapour deposition (CVD)[62] and gas phase catalytic growth.[63]

Arc discharge involves passing a current between two graphite electrodes causing the vaporisation of the carbon anode to a buffer gas.[32] Gas phase catalytic growth involves passing CO gas dosed with an iron-cobalt catalyst through a heated reactor, resulting in nanotubes growth on the reactor walls. The CVD process is quite similar to gas phase catalytic growth. It involves preparing a substrate with metal catalysts before placing it in a high temperature chamber. A carrier gas and carbon source gas are then passed over the substrate, causing the growth of nanotubes at the metal catalyst covered substrate as opposed to the reactor wall.[62] Laser ablation nanotubes are created when a pulsed laser sublimates a graphitic target at high temperature chamber while an inert gas is bled into the chamber. The carbon vapour condenses on cooler parts of the reactor where they can be collected.[61] As the two main nanotube types used in this work were prepared using arc-discharge and gas phase catalytic growth these will be discussed in more detail.

Multiwall nanotubes were first found in the soot produced by the arc-discharge method.[32] In an inert atmosphere a DC voltage is applied across two closely spaced (~ 1

mm) graphite electrodes. This voltage induces a dielectric breakdown of the gas between the electrodes allowing current flow via an electric arc which produces very high (~3000 °C) temperatures. The vaporisation of the graphite from the anode produces nanotube growth on the cathode. This technique allows control over production of SWNT or MWNT by doping the anode with metal catalyst such as Fe, Co, Ni, Y or Mo, while at the same time controlling the diameter of the tubes by using different inert gases (He, Ar) and pressures.

The gas phase catalytic growth technique involves decomposing an organometallic precursor at high temperature in an inert environment.[63,64] Organometallic compounds are sublimated or evaporated and fed into a high temperature (900-1200°C) inert gas furnace. When the molecules decompose, the metal species coalesce into nanoparticles which act as catalysts for the growth of nanotubes. The decomposition supplies initial amounts of carbon for the growth and other carbon containing gases such as acetylene, methane, hexane etc are supplied to increase the carbon source. The specific variation of the gas phase catalytic growth technique used to produce some of the SWNTs employed in this research is known as HiPCO® (High pressure carbon monoxide). In this process $Fe(CO)_5$ is used to produce iron nanoparticles that act as nucleation sites for the transformation of high pressure carbon monoxide into carbon which subsequently form the nanotubes.[65]

3.3.7 Separation and dispersion of Single Wall Carbon Nanotubes

So far the nanotubes that have been considered have been isolated single tubes. Unfortunately individual nanotubes are difficult to obtain. Due to the delocalised π system residing on both the inner and outer surface of the tube they exhibit very strong *van der Waals* attraction.[66] This causes the nanotubes to aggregate into ropes, or bundles, as they are commonly known. The diameter and length of the bundles can reach tens of

nanometers while the length is dependant only on the constituent nanotube's length. This agglomeration has a number of property degrading consequences. Since individual adjacent nanotubes in a bundle are bound by low energy dipole interactions they can experience slipping along the tube axis which can reduce their mechanical properties appreciably. Nirmalraj *et al*[67] used conductive atomic force microscopy to measure the resistance associated with the junction of nanotube bundle in a disordered network. It was shown that as the diameter increased the junction resistance increased directly showing a need to de-bundle nanotubes for any conductive network applications.

Production of nanotubes results in a mixture of semiconducting and metallic nanotubes and consequently any bundle arising from such a mixture will have poorly defined electronic properties. This blurring of the electronic structure negates any contribution from the required nanotubes. It would be beneficial to be able to separate metallic and semiconducting nanotubes in order to obtain the required properties for a certain technology platform and a lot of research has been conducted in order to reach this goal.[68] Different approaches to the separation of nanotubes include size-exclusion or ion-exchange chromatography[69-73] and electrophoresis.[74-78] Zheng *et al*[29] used DNA to assist with the dispersion of nanotubes. After dispersion, ion exchange chromatography was used to separate nanotubes with different chiralities, allowing the separation of metallic and semiconducting nanotubes. Krupe *et al*[31] demonstrated separation of metallic and semiconducting nanotubes using electrophoresis. In their experiment an applied electric field induced dipoles in solvent suspended nanotubes. With the metallic tubes having a larger electric dipole they migrated along the electric field gradient resulting in the deposition of metallic nanotubes on the electrode. While this technique was able to isolate a collection of nanotubes with 80 % exhibiting a metallic structure, the mass of nanotubes purified was only 0.1 % of the initial value and as such this technique is not suitable for large scale processing.

Perhaps the most promising separation method is based on density gradient ultracentrifugation (DGU).[79-84] In this method the different buoyant densities of different nanotube structures in exploited. The buoyant density of a given nanotube is related to the mass per volume, with the volume depending on the nanotube diameter. As discussed earlier, the electronic structure of carbon nanotubes is critically dependant on their diameter and so this technique facilitates the separation of semiconducting and metallic SWNTs.

Individual nanotubes can be separated from bundles via ultrasonication in an aqueous surfactant solution.[80] The nanotube dispersions can then be centrifuged at a very high revolutions per minute (RPM), known as ultracentrifugation, in a density gradient medium. The centripetal forces resulting from ultracentrifugation separate the nanotubes according to their buoyant densities, with nanotubes remaining in the fraction of the density gradient that matches their buoyant density. This allows the collection of separated nanotubes with Arnold *et al*[80] reporting a narrow diameter distribution in which > 97 % of the SWNT had diameters within a 0.02 nm range. A hydrodynamic model describing the separation of surfactant-suspended SWNTs in a density gradient medium was developed by Nair *et al*[85], showing that the effective densities of the suspended SWNT depends on the number of adsorbed surfactant molecules on each nanotube. Using DGU, Green *et al*[81] produced transparent and conductive thin films of predominately metallic SWNTs. Their results showed that using metallic SWNTs, an increase in conductivity of ~5.6 was obtainable. Further, they showed control over the colour of the film by using different diameter metallic SWNT. On the other hand, Nougaret *et al*[86] fabricated field effect transistors from separated semi-conducting SWNTs, showing the potential of electronically separated SWNTs in important devices.

While this is an important step in the utilisation of these unique molecules, aggregation is the tallest hurdle in the race to fully exploit the very useful properties of

carbon nanotubes. With this in mind a large amount of work has been done to tackle the problem.[23] A number of routes have been reported to isolate individual nanotubes in the liquid phase and a brief overview of these will be presented below.

The use of acids, covalent functionalization, macromolecules, surfactants and certain solvents have all yielded exfoliation of nanotubes to a certain degree, each with their own advantages and drawbacks. Very high concentrations (~80 mg/ml) of SWNTs have been reported when dispersed in superacids.[87-89] Superacids are those with acidity greater than that of pure sulphuric acid such as Fluoroantimonic acid ($HSbF_6$) and Fluorosulfuric acid (FSO_3H). These acids induce protonation of the SWNT side wall, altering the tubes electronic properties and eliminating *van der Waals* interactions between individual tubes. Instead an electrostatic double layer is formed from the protons and the acid supplied counterions, preventing the SWNTs from aggregating. Even though this has resulted in high dispersion concentrations, the use of superacids can damage the SWNT lattice and is unattractive for any large scale industrial processing.

It has been shown that functional groups can be covalently attached to the side walls of carbon nanotubes.[90,91] This can help the dispersability of nanotubes in a number of ways. In some cases the stabilization is due to steric considerations. Interacting groups on separate nanotubes, when in close proximity, lower the systems entropy and hence increase the free energy of the system, promoting repulsion between individual tubes. In other cases the functional groups provide electrostatic stabilisation, Zhao *et al*[92] functionalized SWNT with Poly(aminobenzene sulfonic acid) (PABS) and polyethylene glycol (PEG), achieving SWNT concentrations of up to 5 mg/ml in water. High quality dispersions of functionalised SWNTs were reported by Amiran *et al.*[93] In this study a number of functionalized SWNT types were exfoliated in common solvents to high levels with an average bundle diameter of 5-6 nm occurring at a concentration as high as 1 mg/ml. Other chemical routes include the formation of charge transfer complexes. Reduction with alkali

metals forms a carbon nanotube salt which can result in a true solution of nanotubes in certain organic solvents with a concentration of up to 4.2 mg/ml reported.[94]

A large range of macro molecules have reportedly exfoliated nanotubes. Star *et al*[95] and Coleman *et al*[96] have shown that polymers such as PmPV and mpNV can be non-covalently attached to the nanotube side wall assisting exfoliation. Biomolecules such as DNA, synthetic oligonucleotides and peptides have also exhibited the ability to exfoliate nanotubes.[97-100] This occurs by non-covalent attachement of the biomolecules to the nanotube, and in the case of DNA this can take on a helical form. Cathcart *et al* [101] reported spontaneous debundling of nanotubes in DNA. This is important for the implementation of carbon nanotubes in biological systems where they have shown promise as artificial muscles, sensors and other applications.[102,103]

One of the main attractions to using macromolecules such as DNA and surfactants is the ability of using water as the dispersing medium. This is highly advantageous for the large scale processing and implementation of carbon nanotubes. The use of surfactants to disperse and isolate nanotubes has been extensively researched.[104-107] Surfactants are amphiphile organic molecules possessing a hydrophobic chain capped with a hydrophilic head and the most commonly used surfactants are sodium dodecyl sulphate (SDS), sodium dodecylbenzene sulphonate (SDBS) and sodium cholate (SC). These molecules can induce a surface charge which attracts counterions from the liquid. This attraction forms micelles around the nanotubes which, due to the Coulomb repulsion arising from the double layer, separate and stabilizes the nanotubes.[23]

It would be beneficial to be able to disperse SWNTs in the liquid phase without the need for macromolecular stabilization or chemical treatment as this would simplify any processing required. Organic solvents such as N,N-dimethylformamide (DMF),[108] N-methyl-2-pyrrolidone (NMP)[109] and other amide[110] and organic solvents[111] have been used

to produce stable dispersions of SWNTs. Ausman *et al*[109] suggested that successfull solvents require high electron pair donicity, low hydrogen bond donation parameter and high solvatochromic parameters. Giordani *et al*[112] reported a large population (~ 70 %) of individual SWNTs dispersed in NMP at a concentration of 0.004 mg/ml which were stable for weeks. Bergin *et al*[113] exfoliated up to 40 % individual SWNT in γ-butyrolactone, known in some circles as liquid ecstasy. Bergin *et al* also reported on the spontaneous exfoliation of SWNTs in NMP with athermal solubility. The ability of solvents to disperse SWNT has been shown to correlate well with the Hansen solubility parameters and is related to the SWNT and solvent surface tension.[114] Although certain questions still need to be answered about the mechanism involved, this provides a route to the provision of a host of solvents theoretically capable of dispersing SWNTs to a high quality. Through this advancement, hopefully, varied and interesting application of SWNTs will be realised.

3.4 Silver Nanowires

3.4.1 Structure of Silver Nanowires

Silver, atomic number 47, is a transition metal and one of the so called 'noble' metals. Bulk silver, a precious metal with a face centred cubic crystal structure (Figure 3.1, is of interest in many areas. Its malleable nature and high optical reflectivity combined with the highest thermal conductivity of any metal and the highest electrical conductivity[37] of any element makes it a desirable material for many applications. It has long been used to make jewellery and other decorative items but a low contact resistance and excellent electrical properties has made it an important material in electronics. It is reasonably inert and does not oxidise under normal conditions, it does however, react with sulphur to produce silver sulphide which tarnishes the surface and as a result can limit the use of silver in certain situations.

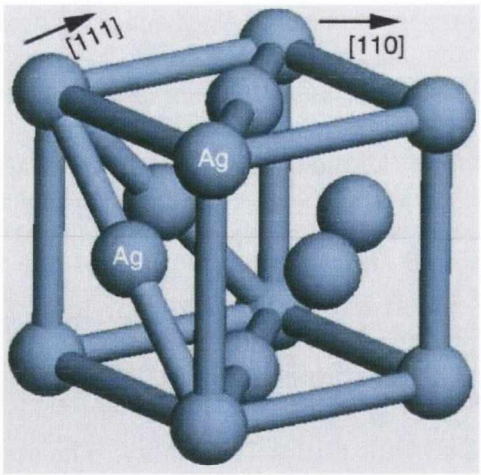

Figure 3.6 *Face centred cubic lattice found in silver. The [1,1,1] and [1,1,0] crystal directions are shown for illustrative purposes.*

Due to its high thermal (429 $Wm^{-1}K^{-1}$ @300K)[115] and electrical conductivity (6.3 x 10^7 Sm^{-1})[115], silver is a promising material in the development of nanometre sized wires. Silver nanowires are of great interest as interconnects and other roles in nanoscale electronic devices[116] and for forming thin networks for electrode purposes.[117] Silver nanowires (AgNWs), unlike carbon nanotubes, are solid crystalline structures. Their lengths can range from hundreds of nanometres up to tens of microns and diameters as low as 0.4 nm have been reported[118] with the upper limit lying were nano ends and micro begins. Like the bulk material, silver nanowires exhibit a face centred cubic structure (shown in Figure 3.1) with Sun *et al*[119] reporting a lattice constant of ~4.08 Å which is very close to the accepted value (~4.09 Å). The nanowire axis crystallinity and hence the exterior side walls and end facets have been shown to vary depending on the synthesis type and conditions. Hong *et al*[118] reported monocrystalline silver nanowires with very low diameter of 0.4 nm while Nielsch *et al*[120] grew thicker (~50nm) monocrystalline structures. They both displayed the [1,1,0] crystal orientation along the wire length and [2,2,0] perpendicular to the wire axis but the atomically thin wires exhibited some lattice

distortion due to the low dimensionality. Others[119,121] reported bicrystal nanowires, with a mean diameter of 38 nm, that were twinned along the [1,1,1] crystal direction which is the most stable orientation in a face centred cubic lattice.

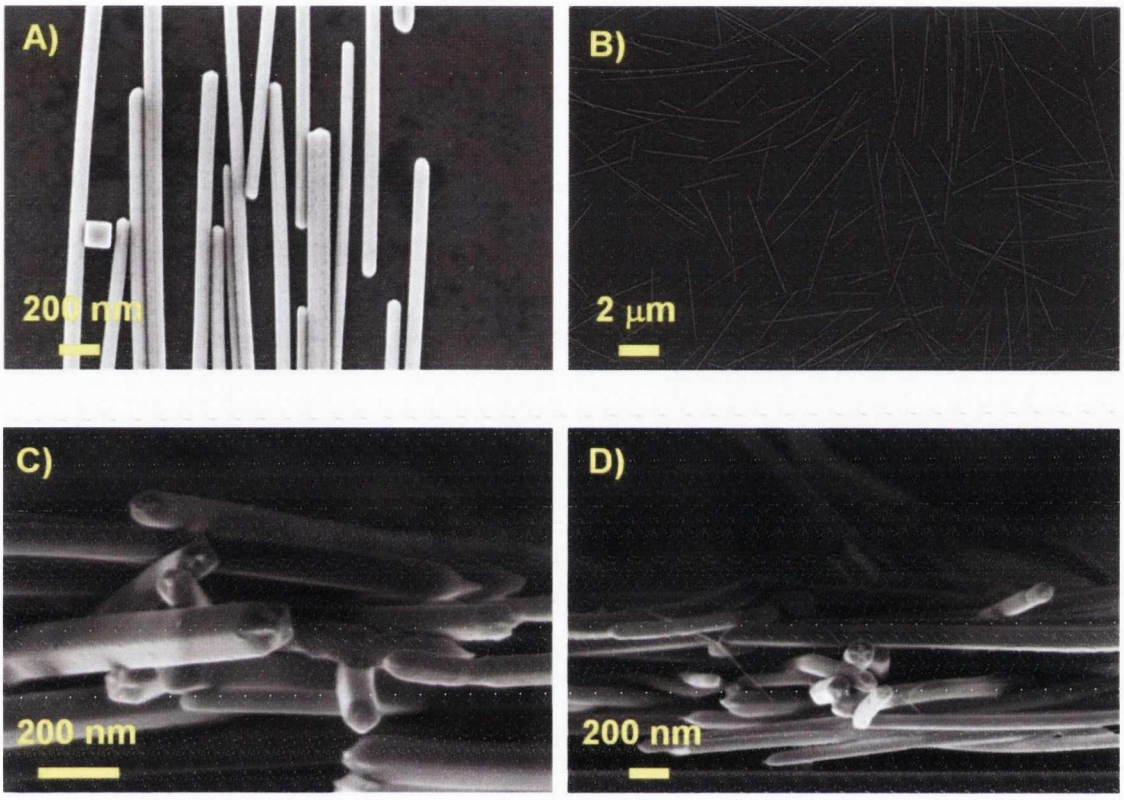

Figure 3.7 *Example SEM images of the silver nanowires used in this work. A) High magnification shows the uniform diameter of each nanowire as well as the triangular wire ends. Note the cubic silver nanoparticle, a remnant from the synthesis reaction B) Lower magnification shows the long straight structure of these nanowires. C) and D) Side view of a nanowire network clearly shows the fivefold symmetry described.*

The preference to form the [1,1,1] twin has been reported by many groups[122-125] and can result in a cyclic penta-twinned structure. In this structure five identical crystal wires are twinned along the [1,1,1] crystal face forming a structure with a pentagonal cross section and with [1,0,0] sidewalls. This diversity in the grown structures may result in

varying properties and nanowire reactivities enabling control over the required nanowire features.

3.4.2 Electronic and Optical properties of Silver Nanowires

In a silver atom the closed atomic orbitals up to $4p^6$ are tightly bound to the ion core and as such can be neglected when considering silvers energy band structure.[37] This leaves eleven electrons in the silver primitive cell which form a number of energy bands. The higher energy bands are known as *s*-bands which spread over a broad range.[126] They overlap the lower energy *d*-band complex at the high symmetry point, *W*, in the first brillouin zone.[126] The *d*-band complex lies very low in energy, lower than other noble metals, and inhibits interband optical transitions which gives rise to silvers lack of colour. Bulk silver displays a very high electrical conductivity which, being an intrinsic property should remain constant as the size of the material is reduced. However, as the dimensions are reduced down to nanometer sizes the electron mean free path is hindered due to the increasing confinement. At room temperature the electron mean free path in silver is 52 nm [37], meaning that, statistically an electron will travel 52 nm before a scattering event. On average the length of AgNWs can vary between a few and tens of micrometers, but the diameter can decrease down to few-atom thickness. Reaching a dimension comparable to the electron mean free path results in an increase in surface scattering events, interrupting and scattering the electrons and severely reducing conductivity.[127] Zhang *et al*[128] showed that the resistivity of silver films increases dramatically once the thickness is reduced below the electron mean free path and reached a conductivity value a quarter of the bulk value when the thickness was reduced to ~ 39 nm (assuming an even distribution of elastic and in-elastic collisions). For a silver nanowire with a diamater of 50nm at a temperature of 4.2 K Graff *et al*[122] measured a conductivity of 6.1×10^5 Sm^{-1} which is two orders of

magnitude lower than that of bulk silver. Decreasing the nanowires diameter down to 15 nm, Park *et al*[129] recorded conductivities of 5 x 10^4 Sm^{-1} for DNA-templated nanowires. Interestingly, copper nanowires with a width of 50 nm have been shown[130] to exhibit a conductivity of 3.3 x 10^3 Sm^{-1} after an anneal stage which reorders the nanowire crystal structure to a lower energy configuration.

This decrease in nanowire conductivity with diameter becomes even more apparent once the critical dimension nears the Fermi wavelength, $\lambda_F = 2\pi/k_F$, where k_F is the Fermi wavevector. Under these conditions the conductance becomes quantized in units of $G_0=2e^2/h$ due to confinement of the transverse modes.[131] This has been reported by Zhao *et al*[132] For AgNWs with seven atoms per cross section they calculated the conductance to have peaks at 1 G_0, 2.6 G_0 and 4 G_0 which agrees well with the experimental results obtained by Rodrigues *et al*[133] who investigated the transport properties of different atomically structured nanowires.

The reduction in dimension of materials can change the optical properties of materials due to a number of phenomena. One of the most pronounced effects is the coherent excitation of the nearly free electrons in the conduction band which result in plasmons, quantized oscillations of the free electron density. Silver nanowires exhibit transverse and longitudinal plasmon resonance. These plasmons result from the coherent coupling of the surface states with incident electromagnetic waves with wavelengths greater than the wire dimension. In the case of nanowires the diameters are generally < 100 nm and this results in a transverse plasmon with a wavelength of 410 nm[127] while the longitudinal plasmon oscillation can be tuned by varying the length, vanishing to zero at long lengths. The surface plasmons result from a strong coupling which is enhanced by the end facets of the nanowire. These acts as scattering centres which helps compensate any momentum difference between the incident photon and the silver plasmon modes. It has

been shown[134] that radially symmetric AgNWs allow the propagation of surface plasmons quite well even when subjected to a bend radius of 4 □m. Inter-nanowire Plasmon coupling was observed and a Plasmon propagation length was found to be > 3 □m. Ditlbacher *et al*[125] reported on Plasmon propagation in chemically grown AgNWs. It was found that the Plasmon propagation lengths reached ~10 μm and the end facets exhibited a reflectivity of ~25% making the wires applicable as Fabry-Perot resonantors. The optically excited surface plasmons can therefore be created, guided and controlled, making silver nanowires very interesting in the fields of nanoscale plasmonics and quantum optics.[135]

3.4.3 Physical properties of Silver Nanowires

In the bulk regime the ratio of surface atomic species to those in the interior is very small. As the dimensions decrease this ratio increases and for nano-dimensioned wires this ratio is very large. Another result of decreasing the material size is a reduction in the relative number of defects in the bulk, with some nanowires showing exceptional crystallinity and surface structure.[127] As a consequence the physical properties of materials vary due to size effects with mechanical properties generally increasing with reduced dimension. The first reported mechanical results for silver nanowires was by Li *et al.*[136] They used a nanoindenter to probe an AgNW with a diameter of 42 nm and found the elastic modulus to be 88 GPa which lies close to the accepted value of 76 GPa.[137]. In work completed by Cuenot *et al*[30] the elastic modulus of silver nanowires as a function of nanowire diameter was investigated using atomic force microscopy. It was found that for diameter > 70 nm the measured values were independent of diameter with a value averaging around the accepted value. As the diameter was decreased there was an increase in the eleastic modulus. The elastic modulus was nearly twice the value of the bulk (140 GPa) for a naowire with a diameter of 30 nm. The wires exhibited no structural change

when the diameter was reduced and the increase in modulus was explained by surface tension effects. Wu *et al*[138] measured an average elastic modulus of 102 GPa for silver nanowires with diameters between 22 and 35 nm. Furthermore, they showed that an annealing step increases the yield strength to a value of 7.3 GPa while the elastic modulus didn't change. This yield strength is considerably higher than bulk silver (55 MPa). This increase in mechanical properties is advantageous when considering the use of silver nanowires in nanodevices.

The thermal conductivity of silver is exceptionally high and exceeds that of any other metal.[115] Theoretical calculations have shown[139] that as the diameter of metallic wires is reduced to the thermal conductivity increases dramatically due to an increase in surface scattering. In other calculations the thermal conductivity was seen to degrade at diameters in the range of 500 nm, reducing to half the bulk value when the diameter reached the electron mean free path length scale.[140] The thermal conductivities of individual silicon nanowires were measured by Li *et al*[141] and were over two orders of magnitude lower than the bulk value. They also observed a deviation from the Debye T^3 law[142] for the lowest diameter (22 nm) wire, indicating that processes other than surface scattering affect the thermal conductivity in such confining structures. To the best of my knowledge no experimental measurement on the thermal conductivity of individual AgNWs has been reported but it is expected that such a decrease in the thermal conductivity would follow the behaviour exhibited by copper nanowires.

3.4.4 Synthesis and production of Silver Nanowires

The synthesis of silver nanowires generally falls into three main categories, physical[133] and electrodeposition[143] and chemical.[144] The chemical route will be given more attention as the silver nanowires used in this work were produced in this fashion.

Electrodeposition involves reducing silver ions from an electrolyte solution which collect on the circuit cathode and form nanowires. Generally this procedure relies of physical confinement in order to direct the silver growth. For example Chakravorty *et al*[143] prepared silver nanowires with diameter ~2 nm and lengths of ~ 2 mm by electrically reducing silver ions from a silver nitrate solution in the pores of a polyvinyl alcohol membrane. In another case[145] aluminium and alumina film were used as templates to grow nanowires in an electrochemical bath. These wires exhibited good monodispersity and lengths of up to 30 mm with diameters ranging from 180 – 400nm for the aluminium templated growth and 25 – 40 nm for the alumina template nanowires. The same authors also reported on monocrystalline silver nanowires using a similar technique and alumina membranes as the growth channel.[120]

Chemical routes to the synthesis of AgNWs usually involve the chemical reduction of silver ions from an electrolyte solution at the interface of a seed or template material.[146] In some cases this is achieved by using membranes with nanosized pores similar to electrodeposition as demonstrated by Barbic *et a.l*[144] In this synthesis a gold film was evaporated onto one side of a polycarbonate membrane which was then immersed in a commercially available Ag-ion-containing amplification solution. This resulted in the spontaneous reduction of silver at the gold interface and the subsequent nanowire growth in the membrane pores. In a similar scheme Zhang *et al*[147] used aluminium oxide templates to grow Ag nanotubes with diameters ranging between 25 and 60 nm. A derivative of templated chemical growth was used by Hong *et al*[148] to grow extraordinarily thin monocrystalline AgNWs. In their setup they used ultraviolet radiation to increase the reduction rate of silver nitrate in the pores of self assembled arrays of calix[4]hydroquinone nanotubes. The nanowires produced were stable in ambient atmosphere and aqueous environments, something which is not often reported for such thin metal nanowires.

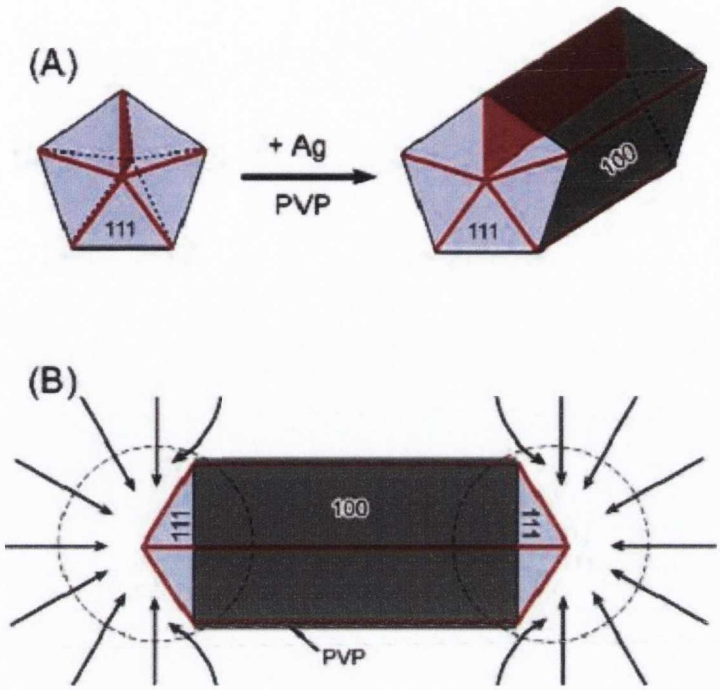

Figure 3.8 *Schematic representation of the growth of silver nanowires by the soft solution process. A) A fivefold symmetrical silver nanoparticle act as a nucleation sites, specifically at the twin planes (red lines). The [1,0,0] side surface interacts strongly with the PVP molecules, passivating the side surface and constricting growth to the [1,1,1] capped ends. B) Nanorods grow into longer nanowires with addition of material to the [1,1,1] end faces by Oswald ripening process.* [123]

One of the most investigated AgNW synthesis method is known as soft solution processing.[119,121,123,149] In this scheme metal nanoparticles act as seeds for the nucleation and growth of nanowires fuelled by the reduction of silver nitrate. Wet chemical synthesis of silver nanorods and nanowires of controllable aspect ratio was reported by Jana *et al*[150] in 2001. Silver seeds with a diameter of ~4 nm were used as nucleation sites for the reduction of silver nitrate by ascorbic acid in the prescene of the cationic surfactant cetrimonium bromide (CTAB). This surfactant acted as a template for AGNW growth. Sun *et al*[119] were able to control the growth of AGNWs using poly(vinyl pyrrolidone) (PVP)

and other surfactants as stabilisers in the platinum nanoparticle seeded growth of AGNWs by the reduction of silver nitrate by ethylene glycol. This produced bi-crystalline nanowires with aspect ratios as high as 1000. The same group reported further on the growth mechanism of multiply twinned nanowires[123] which were discussed in the section dedicated to the structure of AGNWs. They found that the wires produced were bound by [1,0,0] crystal faces on the side of the wires and [1,1,1] facets at the wire ends. These crystal surfaces were shown to have very different reactivities to dithiol molecules causing the passivation of the sidewall with PVP molecules.

This essentially blocks the sidewall from further growth forcing nucleation on the [1,1,1] end faces then further growth by Oswald ripening. This process has been developed to use a number of capping and control agents over the last couple of years so much so that it is the subject of a review in Reviews on Advanced Materials Science by Zhang *et al.*[151] Both Murphy *et al*[146] and Zheng *et al*[124] reported synthesis of AGNWs without the use of surfactant template or nanoparticle seeds by the reduction of silver nitrate using sodium citrate. This resulted in the formation of a mixture of nanoparticles, rods and wires. The nanowires were then separated from other structures by centrifugation. In both cases the wires had diameters of between 30 and 50 nm. Both nanowire samples showed the same structure as that reported by Sun *et al*[123], that of a fivefold symmetrical twinned crystal discussed earlier. A novel method was pioneered by Braun *et al.*[152] In their work a single DNA molecule was used as a template scaffold in the formation of AGNWs by reduction of silver nitrate. This process was accommodated by ion exchange between Ag^{+} and Na^{-} from the DNA strand, creating nanometre aggregates which facilitated further deposition. The wires, which had a thickness of ~100 nm and a length of ~12 □m, were seen to consist of 30 -50 nm diameter grains. Silver coating was performed after attaching the DNA strand to gold electrodes, allowing the electrical characteristics of the nanowire to be investigated. They showed non-Ohmic features which was suggested to arise from inter-grain resistance.

3.5 Electrically conducting polymers

Organic polymers have an important place in product manufacturing. They can possess high malleability, tuneable physical properties and good chemical resistance which make them very useful in a host of applications. They have proven so versatile that plastics have replaced wood, metal, ceramics and other materials in many of their traditional roles. For the most part organic polymers show electrically insulating properties which has limited their applications in the electronics industry to structural components. In 1978 H. Shiakawa of the Tokyo Institute of technology and A. Heeger and A. MacDiarmid of the University of Pennsylvania published a paper in the Journal of the American Chemical Society reporting the synthesis of highly conducting films of derivatives of polyacetylene $(CH)_x$.[153] This work caused huge interest as the many possibilities of conducting plastics were imagined and they received the Nobel Prize in Chemistry in 2000 for "their discovery and development of conductive polymers".

The electrically conducting mixture of the polymers Poly(3,4-ethylenedioxythiophene) and poly(styrenesulfonate) (PEDOT:PSS) was used in this work and its properties and synthesis will be discussed below. This polymer mixture has high conductivity, optical transparency and a good film forming ability which makes it very applicable in the field of transparent electrodes.

3.5.1 *PEDOT: PSS electronic and physical properties*

The electronic conductivity of certain polymers arises from their bonding scheme.[15] Polymers contain repeating units, called monomers, which are joined to form large chain-like molecules. Generally the carbon atoms in the backbone of such molecules are covalently bonded by sp^3 hybridized σ-bonds. In this scheme the valence electrons are tightly bound with low mobility and as such do not contribute to electrical conduction.

However, the unique electronic structure of carbon allows it to form sp^2 hybrid orbitals which can overlap in neighbouring carbon atoms to form sp^2 bonded polymer backbones, known as conjugated polymers. In this situation there exists a single electron per carbon atom in a p-state orthogonal to the three σ-bonds. An illustration of sp^2 bonding scheme is shown in Figure 3.1 Overlap of adjacent p-states form a delocalised π-bond system along the length of the chain giving rise to an electronic band. If the bond length of the single and double were identical this would lead to metallic transport properties. However, Peierls instability[154] splits this band into 2 sub-bands, the valence and conduction band. The completely full valence band is separated from the empty conduction band by an energy gap, making the material a semiconductor. For example PEDOT has a band gap in the range of 1.5-1.6 eV.[155] The electronic properties of conductive polymers can be changed by doping the material by oxidation or reduction. This injects charge carriers, electrons or holes, shifting the Fermi level of the material and allowing conduction.

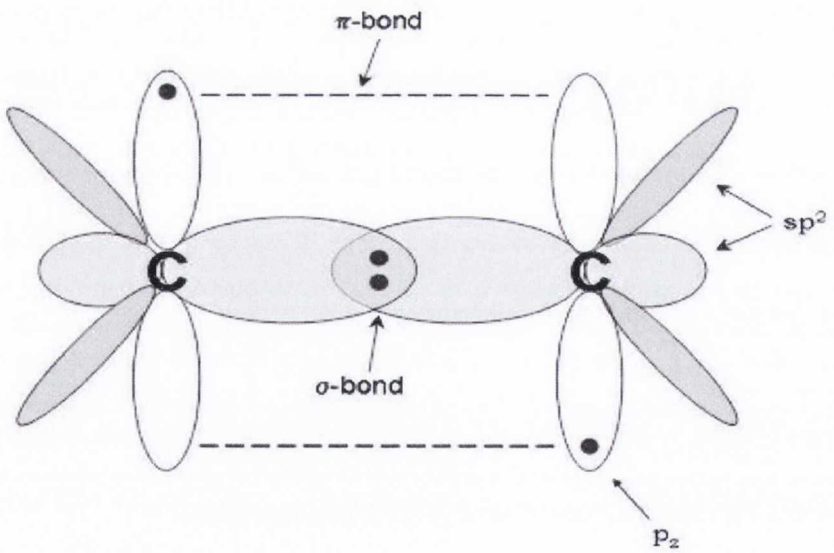

Figure 3.9 *Graphic illustration of covalent bonds in a conjugated system. Alternating double-single carbon-carbon σ-bonds make up the polymer back bone. The p-states, here shown in the z-direction, overlap to form π-bonds.*

Poly(3,4-ethylenedioxythiophene) is a conjugated polymer based on a monomer consisting of a sulphur containing five membered ring (shown in Figure 3.1 A). In its neutral state PEDOT exhibits relatively high electrical conductivity of up to 4 x 10^3 Sm^{-1}. PEDOT also exhibits good thermal stability, with continuous degradation occurring at 150 °C and complete decomposition at 390 °C.[156] Due to a bandgap of ~1.5 eV which peaks at 2 eV PEDOT absorbs strongly in the middle of the visible spectrum giving it a dark blue colour.[155]

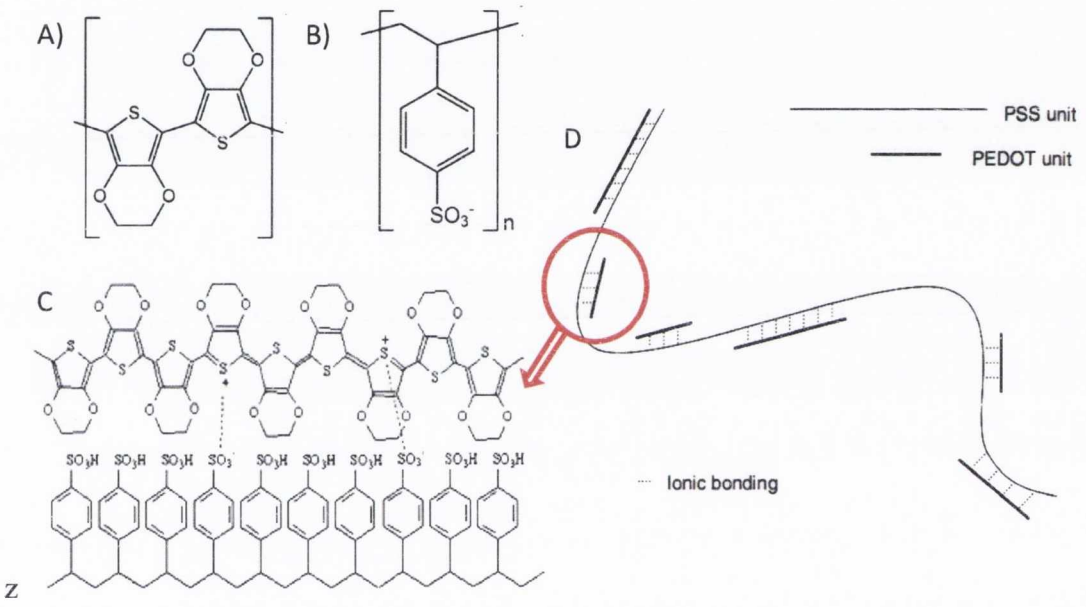

Figure 3.10 *Chemical structure of A) the PEDOT monomer 3,4-ethylenedioxythiophene and B) the PSS monomer styrenesulfonate. C) Polymerization of PEDOT in the presence of PSS results in a salt like chemical structure. D) Visual representation of the PEDOT:PSS structure proposed by Kirchmeyer and Reuter (Image partially adapted from "PEDOT as a Conductive Polymer." (Taylor and Francis, 2010)).*

Like most semiconducting polymers PEDOT can be repeatedly doped and dedoped to both the n- and p-states.[155] This increases the conductivity up to ~ 2 x 10^4 Sm^{-1} and unlike most other conducitng polymers the absorption maximum shifts to 0.6 eV rendering

PEDOT nearly transparent in the visible spectrum.[155] Thin films of doped PEDOT show good stability and as such have received much attention as components in many technologies. There is interest in applying PEDOT as electrodes in capacitors,[157] as antistatic and electrostatic coatings and due to the option to repeatedly doped and de-doped it is off interest to electrochromic applications.[155]

However, on its own, PEDOT is insoluble[157] and as such is very difficult to process rendering it inapplicable to many technologies. This hurdle is addressed by polymerizing PEDOT in the presence of a water soluble polyelectrolyte Poly(styrene sulfonate) (PSS).[157] This molecule is a sulfonated polystyrene with a monomer structure of that shown in Figure 3.1 B. In the PEDOT:PSS mixture part of the PSS sulfonyl group is deprotnated leaving a negative charge while the PEDOT chain carries a positive charge. It has been proposed that PEDOT exists as chain comprising 16-18 monomer units which are bound to much large PSS chains.[158] They form a salt like complex which allows the dispersion of PEDOT:PSS in an aqueous emulsion which can be processed with ease.

Although the addition of PSS allows the application of PEDOT:PSS via an aqueous emulsion it also results in reduced electrical properties. In chemically polymerized PEDOT:PSS there is an excess of PSS which coated nanometre sized particles of PEDOT:PSS. Any deposition, be it spin coating, drop casting etc, results in a film of PEDOT:PSS domains with dimensions of varying size, a typical length/width would be ~25nm, that are separated by layers of PSS. This dielectric gap results in a tunnelling barrier which decreases the conductivity.[159] In the case of the PEDOT:PSS used in this work (Clevios™ P) the electrical conductivity can be tailored by varying the PEDOT:PSS ratio and does not exceed 1 x 10^3 Sm^{-1}. Work has been carried out to investigate the morphological affect has on PEDOT:PSS film conductivity. It has been reported that the addition of high boiling point solvents and certain polar solvents to the PEDOT:PSS dispersion results in conductivity increase.[159] This has tentatively been explained by

swelling of the polymer nanoparticles and a reduced PSS surface layer and resulted in three orders of magnitude increase in the conductivity.[160] Other effects such as conformational changes to the PEDOT chains and screening effects between PEDOT and PSS due to polar solvents have also been suggested in work that ,after treatment with ethylene glycol, resulted in a conductivity of 2 x 10^4 Sm^{-1}.[161] Along with high visible transmissivity and good stability PEDOT:PSS's properties have made it a material of interest in the areas of transparent electrodes for use in devices such as OLEDs, [162]

3.5.2 *PEDOT: PSS synthesis*

The synthesis of PEDOT can be obtained through two main routes. These are oxidative chemical polymerization and electrochemical polymerization.[155] Ethylene dioxythiophene monomers can be polymerized by chemical reduction using ferrous oxidising agents.[163] These normally include ferric chloride ($FeCl_3$) and ferric tosylate ($Fe(CH_3C_6H_4SO_2)_3$). This produces black, insoluble powder which can be reduced to its neutral state with the use of hydrazine in acetonitrile. In order to synthesize PEDOT:PSS EDOT monomers are polymerizes in an aqueous solution of poly(styrenesulfonate) using sodium persulfate ($Na_2S_2O_8$) as an oxidising agent, producing a dark blue aqueous emulsion.[155]

Electrochemical oxidation of PEDOT requires the presence of EDOT monomers and tetraethylammonium perchlorate (Et_4NClO_4) in propylene carbonate ($C_4H_6O_3$) or acetonitrile (CH_3CN). This can be advantageous as the experimental setup required results in the ability to form thin films on the working electrode and is very controllable. In order to synthesis PEDOT:PSS an electrochemical oxidation polymerization can be conducted in an aqueous solution of poly(styrenesulfonate) (PSS).[155]

3.6 Transparent conductors based on nanomaterials

A replacement for current transparent conductive electrodes has long been sought as mechanical and production problems with the doped oxide standards render them unlikey to be used in next generation displays and devices. Much work has been done in developing networks for nanostructures, such as carbon nanotubes, for application as transparent electrodes and is the subject of a review published in 2006.[164] There have been many reports on the different methods of fabricating and improving the properties nanostructured network and a brief overview of the field will be given in this section. The emphasis will fall on films constructed from single wall carbon nanotubes with silver nanowires and graphene receiving some attention.

In 2004 researchers in the Departments of Physics and Chemistry in the University of Florida reported the fabrication of transparent and conductive single wall carbon nanotube films. In their work Wu *et al*[34] demonstrated deposition of homogenous SWNT films by vacuum filtration onto a filter membrane. The filter membranes were dissolved in solvents which allowed transfer of the films to a substrate for electrical and optical characterisation. A film with a thickness of 50 nm showed exhibited a sheet resistance of 30Ω/□ with a transmittance of > 70%. They used their films to fabricate an electric field-activated optical modulator, showing the applicability of SWNT transparent films in certain electronic roles. Kaempgen *et al*[25] reported the production of transparent single wall nanotube films by a simple spray technique. The deposited films showed a transmittance value of 90% with a sheet resistance of 1kΩ/□ which did not vary under mechanical stress, including folding. Spray deposition also was used by Artukovic *et al*[24] in 2005. They incorporated these films in the production of flexible transistors which showed promising results, however they suggested that improved network properties would result in a better device performance. Another example of SWNT thin film

fabrication was developed by Zhou *et al*[27] and reported in 2006. They deposited CNT films on alumina filter membranes from which they were successful at lifting the entire film off with an electrostatic elastomer stamp made from polydimethylsiloxane (PDMS). The network was then transferred to a substrate by using heat to thermally release the network from the surface of the stamp. This novel method had the added attraction that the PDMS stamp shape could be easily changed, allowing the easy patterning of SWNT films. Films prepared this way showed a low *Rs* of ~120Ω/□ combined with a relatively high transmittance of ~80%. Carbon nanotube thin films were incorporated into the architecture of an organic light emitting diode display as transparent electrodes by Zhang *et al*[18]. Using an elastomer stamp, they transferred the films, deposited by vacuum filtration, to both glass and polymer substrate and patterned the film with O_2 plasma. The devices showed good stability and lifetime, however the brightness and current density were much lower than similar devices based on indium tin oxide electrodes which the authors suggested was a result of a lower work function of the nanotubes. The surface roughness, critical for incorporating these films in devices, was greater than that of ITO by a factor of three. Hence the authors suggested improvements in network morphology and intrinsic nanotube conductivity are required for the exploitation of SWNTs in such roles.

As nanotube networks are essentially an ensemble of 1-Dimesional wires it can be expected that as the thickness is decreased there is a point below which conducting pathways through the film as lost. This phenomenon is described by percolation theory and was investigated for carbon nanotubes by Hu *et al*[69]. The sheet resistance was measured as a function of the network density and good agreement with theory was observed. The same group went on to study the effect of nanotube aspect ratio on the network conductivity. In their report Hecht *et al*[26] described the relationship between network conductivity and the constituent tube length and diameter. By controlling the bundle length using high power sonication they were able to deposit films with similar bundle diameters but with varying

bundle length. From their data they determined the conductivity to scale with the bundle length as $\sigma_{DC} \sim L^{1.46}$. They also argue that the conductivity should scale with the diameter as D^{-n} where $0<n<2$, showing the importance of working with long, thin nanotube bundles.

The effect of acids on the electronic structure of carbon nanotubes was investigated by Graupner *et al*[165] in 2003. Treatment of thick nanotube networks with a number of Brønsted acids produced p-doped nanotubes, shifting the Fermi level closer to the valence band, however they did not report on the conductivity of their treated films. In an attempt to decrease the sheet resistance of transparent SWNT films by taking advantage of such doping, Geng *et al*[19] subjected their films to a 12 M nitric acid bath. They observed an increase in conductivity by a factor of ~2.5 with no appreciable change to the transmittance. However, this increase was associated with the removal of residual surfactant used in the dispersion process as opposed to chemical doping of the tubes. The same authors went on to investigate the effect of different surfactants on the optical properties of CNT films.[104] Residual surfactant from the dispersion process was seen to suppress certain optical transitions, namely the S11, S22 and M11 peaks. The films were then treated with nitric acid to remove the surfactant and restore the peaks. This treatment caused an increase in both the optical and DC conductivity with the acid treated films displaying a conductivity ratio $\sigma_{DC}/\sigma_{Op}=25.3$, a result close to the required value of 35. Bromine (Br) doping of carbon nanotubes was reported by Fanchini *et al*[21]. After chemical etching of the nanotubes, the authors were able to introduce one Bromine atom for every twenty Carbon atoms in the hexagonal lattice by treatment with phosphorous tribromide (PBr_3). The electronegative Bromine sites lowered the Fermi level and produced an acceptor peak which resulted in a conductivity increase. In a similar report, Parekh *et al*[20] demonstrated a fivefold increase in conductivity upon treatment with nitric acid and thionyl chloride ($SOCL_2$) which caused the nanotubes to be functionalised with chlorine and acyl chloride groups. The conductivity increase was attributed to a shift in the Fermi

energy which, although smaller than the shift that occurs with Bromine functionalization, still has a measurable effect. Although acid treatment has been shown in many cases to cause an increase in the film conductivity it is in many ways an undesirable means to an end as residual ions can be detrimental to some materials used in display devices.

Other routes to transparent electrodes based on carbon nanotubes have revolved around the addition of a conducting polymer. Ham *et al*[76] used spin coating and bar rolling on dispersion based on a number of single wall carbon nanotube types mixed with PEDOT:PSS to prepare transparent films. These films displayed a sheet resistances in the range of kΩ coupled with a transmittance > 70%. Moon *et al*[77] dispersed acid treated SWNTs and MWNTs in a PEDOT aqueous solution. They deposited transparent films using the bar coating method which proved to be robust and flexible and exhibited optimised values of sheet resistance and transmittance of 247 Ω/□ and 84.7 % respectively. A large scale method of preparing SWNT/PEDOT:PSS composite films was demonstrated by Mustonen *et al*[78] in 2007. They deposited conductive patterns using an inkjet printer and a film with a transmittance of ~90% was accompanied by a sheet resistance of ~10kΩ/□. In order to take advantage of the existence of metallic nanotubes Wang *et al*[73] isolated metallic SWNTs by selective interaction of poryphins with semiconducting nanotubes. The authors then proceeded by preparing both PEDOT:PSS/metallic SWNT composites and deposited films by spraying. These composites displayed better properties than a mixed nanotube composite control with sheet resistances reaching ~300Ω/□ for a transmittance of ~82%. Flexible organic light-emitting diodes were fabricated using a PEDOT:PSS/SWNT composite as the anode by Wang *et a.l*[166] These devices demonstrated a lower turn on voltage and higher luminous intensity than those using ITO as the anode. Carbon nanotubes and their composites have been shown to exhibit respectable values of conductivity and optical transmittance,[167] particularly in the case of acid treated films.[168]

However, as the race for transparent, flexible and conductive films speeds up, other options will need to be investigated in order to determine the most suitable material.

Individual silver nanowires (AgNWs) have shown very high conductivities[122] and pioneering work done by Lee *et al*[70] in 2008 demonstrated very large σ_{DC}/σ_{Op} conductivity ratios for random networks of AgNWs. They produced nanowires using a soft solution synthesis which displayed an average length and diameter of 8.7 μm and 103 nm respectively. By drop casting solutions of AgNWs onto transparent substrates and annealing at a low temperature to remove residual surfactant, sheet resistance and transmittance measurements showed a maximised value of 16Ω/□ and 86%, which corresponds to a conductivity ratio value of σ_{DC}/σ_{Op}~150. Using these networks they fabricated simple organic photovoltaic cells which, along with being flexible, exhibited a 19 % higher photocurrent than a similar device fabricated using ITO as the electrode. Their report showed that silver nanowires, unlike carbon nanotubes, are relatively easy to process and even at such an early stage, rival ITO in the conductivity and transmittance.

Graphene has drawn much attention since its discovery in 2004.[22] Due to its 2-Dimensional shape and unique electronic structure it has been considered as promising transparent conducting material[169] and in 2008 a number of groups reported on the use of Graphene in such a capacity.[170-172] Like carbon nanotubes, Graphene is not easily dispersed and due to this there is a substantial barrier to its application.[24] It has been shown however, that oxidised Graphene, which has considerably poorer electrical properties,[173] can be suspended more readily.[174] Once the Graphene oxide has been deposited in a layer or film it can be reduced through chemical treatment and other methods to return it to its conducting state.[175] Eda *et al*[175] reported on a method of depositing uniform Graphene oxide films from solution by vacuum filtration followed by a transfer to a suitable substrate. After transfer and filter membrane dissolution the Graphene oxide were

chemically reduced by hydrazine vapour and anneal in nitrogen at 200°C. Although this method showed the ability to form very thin and transparent films the associated sheet resistance was very high, in the kΩ range. A dip coating method of producing Graphene oxide films was demonstrated in the Max Planck Institute by Wang *et al*[72]. The film coating process was followed by a 1100°C anneal in argon and/or hydrogen. A post-reduction film with a 10 nm thickness exhibited a transmittance (1000nm) and sheet resistance of 70.7% and 1.8kΩ respectively. They used these films to prepare a thin film transistor which showed a power conversion efficiency of 0.26% which was lower than that of a standard control device. Wu *et al*[74] spin coated functionalised Graphene films onto quartz slides. They then reduced the samples by high temperature vacuum annealing. For a 7 nm film they reported a sheet resistance and transmittance (550 nm) of 80Ω/□ and 82% respectively, a considerable improvement on previous reports. They incorporated these reduced Graphene films into organic light-emitting diodes and the resultant devices showed comparable current densities, luminance and external quantum efficiencies to those of an ITO based control device.

3.7 References

1 K. Bädeker, "Über die elektrische Leitfähigkeit und die thermoelektrische Kraft einiger Schwermetallverbindungen," Annalen der Physik **327** (4), 749-766 (1907).

2 Minami Tadatsugu, "Transparent conducting oxide semiconductors for transparent electrodes," Semiconductor Science and Technology **20** (4), S35 (2005).

3 H. L. Hartnagel, A. L. Dawar, A. K. Jain, and C. Jagadish, *Semiconducting transparent thin films*. (Institute of Physics Publishing, Bristol, 1995).

4 P. D. C. King, R. L. Lichti, Y. G. Celebi, J. M. Gil, Vil, atilde, R. C. o, H. V. Alberto, J. Piroto Duarte, D. J. Payne, R. G. Egdell, I. McKenzie, C. F. McConville, S. F. J. Cox, and T. D. Veal, "Shallow donor state of hydrogen in In_{2}O_{3} and SnO_{2} : Implications for conductivity in transparent conducting oxides," Physical Review B **80** (8), 081201 (2009).

5 I. Hamberg and C. G. Granqvist, "Evaporated Sn-doped In[sub 2]O[sub 3] films: Basic optical properties and applications to energy-efficient windows," Journal of Applied Physics **60** (11), R123-R160 (1986).

6 Radhouane Bel Hadj Tahar, Takayuki Ban, Yutaka Ohya, and Yasutaka Takahashi, "Tin doped indium oxide thin films: Electrical properties," Journal of Applied Physics **83** (5), 2631-2645 (1998).

7 R. L. Weiher and R. P. Ley, "Optical Properties of Indium Oxide," Journal of Applied Physics **37** (1), 299-302 (1966).

8 Aron Walsh, Juarez L. F. Da Silva, Su-Huai Wei, ouml, C. rber, A. Klein, L. F. J. Piper, Alex DeMasi, Kevin E. Smith, G. Panaccione, P. Torelli, D. J. Payne, A. Bourlange, and R. G. Egdell, "Nature of the Band Gap of In_{2}O_{3} Revealed by First-Principles Calculations and X-Ray Spectroscopy," Physical Review Letters **100** (16), 167402 (2008).

9 Akio Suzuki, Tatsuhiko Matsushita, Takanori Aoki, Akihito Mori, and Masahiro Okuda, "Highly conducting transparent indium tin oxide films prepared by pulsed laser deposition," Thin Solid Films **411** (1), 23-27 (2002).

10 Zhong Chen, Brian Cotterell, and Wei Wang, "The fracture of brittle thin films on compliant substrates in flexible displays," Engineering Fracture Mechanics **69** (5), 597-603 (2002).

11 Y. Leterrier, L. Médico, F. Demarco, J. A. E. Månson, U. Betz, M. F. Escolà, M. Kharrazi Olsson, and F. Atamny, "Mechanical integrity of transparent conductive oxide films for flexible polymer-based displays," Thin Solid Films **460** (1-2), 156-166 (2004).

12 Evelyn M. Doherty, Sukanta De, Philip E. Lyons, Aleksey Shmeliov, Peter N. Nirmalraj, Vittorio Scardaci, Jerome Joimel, Werner J. Blau, John J. Boland, and Jonathan N. Coleman, "The spatial uniformity and electromechanical stability of transparent, conductive films of single walled nanotubes," Carbon **47** (10), 2466-2473 (2009).

13 Antoinette M. Mannion, *Carbon and its Domestication*. (Springer, 2006).

14 Loretta Jones and Peter Atkins, *Chemistry: Molecules, Matter and Change*. (W. H. Freeman, 2000).

15 Massimiliano Di Ventra, Stephane Evoy, and James R. Heflin, *Introduction to nanoscale science and technology*. (Kluwer Academic Publishers, 2004).

16 George E. Harlow, *The Nature of Diamonds*. (Cambridge University Press, Cambridge, 1997).

17 A. K. Geim, "Graphene: Status and Prospects," Science **324** (2009).

18 Alexander E. Karu and Michael Beer, "Pyrolytic Formation of Highly Crystalline Graphite Films," Journal of Applied Physics **37** (5), 2179-2181 (1966).

19 L. C. Isett and J. M. Blakely, "Segregation isosteres for carbon at the (100) surface of nickel," Surface Science **58** (2), 397-414 (1976).

20 R. Rosei, M. De Crescenzi, F. Sette, C. Quaresima, A. Savoia, and P. Perfetti, "Structure of graphitic carbon on Ni(111): A surface extended-energy-loss fine-structure study," Physical Review B **28** (2), 1161 (1983).

21 Y. Gamo, A. Nagashima, M. Wakabayashi, M. Terai, and C. Oshima, "Atomic structure of monolayer graphite formed on Ni(111)," Surface Science **374** (1-3), 61-64 (1997).

22 K. S. Novoselov, A. K. Geim, S. V. Morozov, D. Jiang, Y. Zhang, S. V. Dubonos, I. V. Grigorieva, and A. A. Firsov, "Electric Field Effect in Atomically Thin Carbon Films," Science **306** (2004).

23 Jonathan N. Coleman, "Liquid-Phase Exfoliation of Nanotubes and Graphene," Advanced Functional Materials **19**, 3680-3695 (2009).

24 Yenny Hernandez, Valeria Nicolosi, Mustafa Lotya, Fiona M. Blighe, Zhenyu Sun, Sukanta De, I. T. McGovern, Brendan Holland, Michele Byrne, Yurii K. Gun'Ko, John J. Boland, Peter Niraj, Georg Duesberg, Satheesh Krishnamurthy, Robbie Goodhue, John Hutchison, Vittorio Scardaci, Andrea C. Ferrari, and Jonathan N.

Coleman, "High-yield production of graphene by liquid-phase exfoliation of graphite," Nat Nano **3** (9), 563-568 (2008).
25 Umar Khan, Arlene O'Neill, Mustafa Lotya, Sukanta De, and Jonathan N. Coleman, "High-Concentration Solvent Exfoliation of Graphene," Small **6** (7), 864-871 (2010).
26 Mustafa Lotya, Yenny Hernandez, Paul J. King, Ronan J. Smith, Valeria Nicolosi, Lisa S. Karlsson, Fiona M. Blighe, Sukanta De, Zhiming Wang, I. T. McGovern, Georg S. Duesberg, and Jonathan N. Coleman, "Liquid Phase Production of Graphene by Exfoliation of Graphite in Surfactant/Water Solutions," Journal of the American Chemical Society **131** (10), 3611-3620 (2009).
27 Mustafa Lotya, Paul J. King, Umar Khan, Sukanta De, and Jonathan N. Coleman, "High-Concentration, Surfactant-Stabilized Graphene Dispersions," ACS Nano **4** (6), 3155-3162 (2010).
28 A. K. Geim and K. S. Novoselov, "The Rise of Graphene," Nature Materials **6**, 183-191 (2007).
29 Alexandre Mantovani Nardes, Eindhoven University of Technology, 2007.
30 M. S. Dresselhaus, G. Dresselhaus, R. Saito, and A. Jorio, "Raman spectroscopy of carbon nanotubes," Physics Reports **409** (2), 47-99 (2004).
31 R. Saito, M. Fujita, G. Dresselhaus, and M. S Dresselhaus, "Electronic structure of chiral graphene tubules," Applied Physics Letters **60** (18) (1992).
32 Sumio Ijima, "Helical microtubules of graphitic carbon," Nature **354**, 56-58 (1991).
33 Sumio Iijima and Toshinari Ichihashi, "Single-shell carbon nanotubes of 1-nm diameter," Nature **363**, 603-605 (1993).
34 D. S. Bethune, C. H. Klang, M. S. de Vries, G. Gorman, R. Savoy, J. Vazquez, and R. Beyers, "Cobalt-catalysed growth of carbon nanotubes with single-atomic-layer walls," Nature **363**, 605-607 (1993).
35 R. Saito, *Physical Properties of Carbon Nanotubes*. (World Scientific Publishing Company, 1998).
36 G. G. Samsonidze, R. Saito, A. Jorio, M. A. Pimenta, A. G. Souza Filho, A. Grüneis, G. Dresselhaus, and M. S. Dresselhaus, "The concept of cutting lines in carbon nanotube science," Journal of Nanoscience and Nanotechnology **3** (6), 431-458 (2003).
37 Neil W. Ashcroft and N. David Mermin, *Solid State Physics*. (Harcourt Brace College Publishers, Orlando, 1976).
38 A. Loiseau, P. Launois-Bernede, P. Petit, S. Roche, and J.-P. Salvetat, *Understanding Carbon Nanotubes: From basics to applications*. (Springer, 2006).
39 A. C. Ferrari, J. C. Meyer, V. Scardaci, C. Casiraghi, M. Lazzeri, F. Mauri, S. Piscanec, D. Jiang, K. S. Novoselov, S. Roth, and A. K. Geim, "Raman Spectrum of Graphene and Graphene Layers," Physical Review Letters **97** (18) (2006).
40 Andrea C. Ferrari, "Raman spectroscopy of graphene and graphite: Disorder, electron-phonon coupling, doping and nonadiabatic effects," Solid State Communications **143** (1-2), 47-57 (2007).
41 F. Tuinstra and J. L. Koenig, "Raman Spectrum of Graphite," The Journal of Chemical Physics **53** (3) (1970).
42 A. Das, S. Pisana, B. Chakraborty, S. Piscanec, S. K. Saha, U. V. Waghmare, K. S. Novoselov, H. R. Krishnamurthy, A. K. Geim, A. C. Ferrari, and A. KSood, "Monitoring dopants by Raman scattering in an electrochemically top-gated graphene transistor," Nat Nano **3** (4), 210-215 (2008).
43 Simone Pisana, Michele Lazzeri, Cinzia Casiraghi, Kostya S. Novoselov, A. K. Geim, Andrea C. Ferrari, and Francesco Mauri, "Breakdown of the adiabatic Born-Oppenheimer approximation in graphene," Nat Mater **6** (3), 198-201 (2007).

44 Jun Yan, Yuanbo Zhang, Philip Kim, and Aron Pinczuk, "Electric Field Effect Tuning of Electron-Phonon Coupling in Graphene," Physical Review Letters **98** (16), 166802 (2007).
45 Michele Lazzeri and Francesco Mauri, "Nonadiabatic Kohn Anomaly in a Doped Graphene Monolayer," Physical Review Letters **97** (26), 266407 (2006).
46 C. Thomsen and S. Reich, "Double Resonant Raman Scattering in Graphite," Physical Review Letters **85** (24), 5214 (2000).
47 D. M. Basko, "Theory of resonant multiphonon Raman scattering in graphene," Physical Review B **78** (12), 125418 (2008).
48 C. Casiraghi, "Doping dependence of the Raman peaks intensity of graphene close to the Dirac point," Physical Review B **80** (23), 233407 (2009).
49 A. Jorio, R. Saito, J. H. Hafner, C. M. Lieber, M. Hunter, T. McClure, G. Dresselhaus, and M. S. Dresselhaus, "Structural (n, m) Determination of Isolated Single-Wall Carbon Nanotubes by Resonant Raman Scattering," Physical Review Letters **86** (6), 1118 (2001).
50 F. Tuinstra and J. L. Koenig, "Raman spectum of Graphite," Journal of Chemical Physics **53**, 1126-1130 (1970).
51 K. Sato, R. Saito, Y. Oyama, J. Jiang, L. G. Cançado, M. A. Pimenta, A. Jorio, Ge G. Samsonidze, G. Dresselhaus, and M. S. Dresselhaus, "D-band Raman intensity of graphitic materials as a function of laser energy and crystallite size," Chemical Physics Letters **427** (1-3), 117-121 (2006).
52 Stefano Piscanec, Michele Lazzeri, J. Robertson, Andrea C. Ferrari, and Francesco Mauri, "Optical phonons in carbon nanotubes: Kohn anomalies, Peierls distortions, and dynamic effects," PHYSICAL REVIEW B **75** (3), 035427 (2007).
53 A. Jorio, A. G. Souza Filho, G. Dresselhaus, M. S. Dresselhaus, A. K. Swan, Uuml, nl, M. S., B. B. Goldberg, M. A. Pimenta, J. H. Hafner, C. M. Lieber, and R. Saito, "G-band resonant Raman study of 62 isolated single-wall carbon nanotubes," PHYSICAL REVIEW B **65** (15), 155412 (2002).
54 M. S. Dresselhaus, G. Dresselhaus, A. Jorio, A. G. Souza Filho, and R. Saito, "Raman spectroscopy on isolated single wall carbon nanotubes," Carbon **40** (12), 2043-2061 (2002).
55 C. T. White and T. N. Todorov, "Carbon nanotubes as long ballistic conductors," Nature **393** (1998).
56 Seunghun Hong and Sung Myung, "Nanotube Electronics: A flexible approach to mobility," Nature Nanotechnology **2**, 207-208 (2007).
57 E. Hernández, C. Goze, P. Bernier, and A. Rubio, "Elastic Properties of C and $B_xC_yN_z$ Composite Nanotubes," Physics Review Letters B **80**, 4502-4505 (1998).
58 O. Lourie and H. D. Wagner, "Evaluation of Young's modulus of carbon nanotubes by micro-Raman spectroscopy," Journal of Materials Research **13** (9) (1998).
59 A. Krishnan, E. Dujardin, T.W. Ebbesen, P. N. Yianilos, and M. M. J. Treacy, "Young's modulus of single-walled nanotubes," Physical Review B **58** (20) (1998).
60 Sumio Ijima, Charles Brabec, Amitesh Maiti, and Jerzy Bernholc, "Structural flexibility of carbon nanotubes," Journal of Chemical Physics **104** (5) (1995).
61 T. Guo, P. Nikolaev, A. Thess, D. T. Colbert, and R. E. Smalley, "Catalytic growth of single-walled manotubes by laser vaporization " Chemical Physics Letters **243** (1-2), 49-54 (1995).
62 Alan M. Cassell, Jeffrey A. Raymakers, Jing Kong, and Hongjie Dai, "Large Scale CVD Synthesis of Single-Walled Carbon Nanotubes," Journal of Physical Chemisty B **103**, 6484-6492 (1999).
63 M. José-Yacamán, M. Miki-Yoshida, L. Rendón, and J. G. Santiesteban, "Catalytic growth of carbon microtubules with fullerene structure," Applied Physics Letters **62** (657) (1993).

64 Pavel Nikolaev, Michael J. Bronikowski, R. Kelley Bradley, Frank Rohmund, Daniel T. Colbert, K. A. Smith, and Richard E. Smalley, "Gas-phase catalytic growth of single-walled carbon nanotubes from carbon monoxide," Chemical Physics Letters **313**, 91-97 (1999).

65 Michael J. Bronikowski, Peter A. Willis, Daniel T. Colbert, K. A. Smith, and Richard E. Smalley, "Gas-phase production of carbon single-walled nanotubes from carbon monoxide via the HiPco process: A parametric study," Journal of Vacuum Science & Technology A **19** (1800) (2001).

66 Andreas Thess, Roland Lee, Pavel Nikolaev, Hongjie Dai, Pierre Petit, Jerome Robert, Chunhui Xu, Young Hee Lee, Seong Gon Kim, Andrew G. Rinzler, Daniel T. Colbert, Gustavo E. Scuseria, David Tománek, John E. Fischer, and Richard E. Smalley, "Crystalline Ropes of Metallic Carbon Nanotubes," Science **273** (5274), 483-487 (1996).

67 Peter N. Nirmalraj, Philip E. Lyons, Sukanta De, Jonathan N. Coleman, and John J. Boland, "Electrical Connectivity in Single-Walled Carbon Nanotube Networks," Nano Letters **9** (11), 3890-3895 (2009).

68 Mark C. Hersam, "Progress towards monodisperse single-walled carbon nanotubes," Nat Nano **3** (7), 387-394 (2008).

69 Ming Zheng, Anand Jagota, Michael S. Strano, Adelina P. Santos, Paul Barone, S. Grace Chou, Bruce A. Diner, Mildred S. Dresselhaus, Robert S. Mclean, G. Bibiana Onoa, Georgii G. Samsonidze, Ellen D. Semke, Monica Usrey, and Dennis J. Walls, "Structure-Based Carbon Nanotube Sorting by Sequence-Dependent DNA Assembly," Science **302** (5650), 1545-1548 (2003).

70 Michael S. Strano, Ming Zheng, Anand Jagota, G. Bibiana Onoa, Daniel A. Heller, Paul W. Barone, and Monica L. Usrey, "Understanding the Nature of the DNA-Assisted Separation of Single-Walled Carbon Nanotubes Using Fluorescence and Raman Spectroscopy," Nano Letters **4** (4), 543-550 (2004).

71 Ming Zheng and Ellen D. Semke, "Enrichment of Single Chirality Carbon Nanotubes," Journal of the American Chemical Society **129** (19), 6084-6085 (2007).

72 Ming Zheng, Anand Jagota, Ellen D. Semke, Bruce A. Diner, Robert S. McLean, Steve R. Lustig, Raymond E. Richardson, and Nancy G. Tassi, "DNA-assisted dispersion and separation of carbon nanotubes," Nat Mater **2** (5), 338-342 (2003).

73 G. S. Duesberg, J. Muster, V. Krstic, M. Burghard, and S. Roth, "Chromatographic size separation of single-wall carbon nanotubes," Applied Physics A: Materials Science & Processing **67** (1), 117-119 (1998).

74 Daniel A. Heller, Rebecca M. Mayrhofer, Seunghyun Baik, Yelena V. Grinkova, Monica L. Usrey, and Michael S. Strano, "Concomitant Length and Diameter Separation of Single-Walled Carbon Nanotubes," Journal of the American Chemical Society **126** (44), 14567-14573 (2004).

75 A. Vetcher Alexandre and et al., "Fractionation of SWNT/nucleic acid complexes by agarose gel electrophoresis," Nanotechnology **17** (16), 4263 (2006).

76 Stephen K. Doorn, Michael S. Strano, Michael J. O'Connell, Erik H. Haroz, Kristy L. Rialon, Robert H. Hauge, and Richard E. Smalley, "Capillary Electrophoresis Separations of Bundled and Individual Carbon Nanotubes," The Journal of Physical Chemistry B **107** (25), 6063-6069 (2003).

77 Woo-Jae Kim, Monica L. Usrey, and Michael S. Strano, "Selective Functionalization and Free Solution Electrophoresis of Single-Walled Carbon Nanotubes: Separate Enrichment of Metallic and Semiconducting SWNT," Chemistry of Materials **19** (7), 1571-1576 (2007).

78 Stephen K. Doorn, Robert E. Fields, Hui Hu, Mark A. Hamon, Robert C. Haddon, John P. Selegue, and Vahid Majidi, "High Resolution Capillary Electrophoresis of

Carbon Nanotubes," Journal of the American Chemical Society **124** (12), 3169-3174 (2002).

79 Michael S. Arnold, Samuel I. Stupp, and Mark C. Hersam, "Enrichment of Single-Walled Carbon Nanotubes by Diameter in Density Gradients," Nano Letters **5** (4), 713-718 (2005).

80 Michael S. Arnold, Alexander A. Green, James F. Hulvat, Samuel I. Stupp, and Mark C. Hersam, "Sorting carbon nanotubes by electronic structure using density differentiation," Nat Nano **1** (1), 60-65 (2006).

81 Alexander A. Green and Mark C. Hersam, "Colored Semitransparent Conductive Coatings Consisting of Monodisperse Metallic Single-Walled Carbon Nanotubes," Nano Letters **8** (5), 1417-1422 (2008).

82 Anton V. Naumov, Oleg A. Kuznetsov, Avetik R. Harutyunyan, Alexander A. Green, Mark C. Hersam, Daniel E. Resasco, Pavel N. Nikolaev, and R. Bruce Weisman, "Quantifying the Semiconducting Fraction in Single-Walled Carbon Nanotube Samples through Comparative Atomic Force and Photoluminescence Microscopies," Nano Letters **9** (9), 3203-3208 (2009).

83 Alexander Green, Matthew Duch, and Mark Hersam, "Isolation of single-walled carbon nanotube enantiomers by density differentiation," Nano Research **2** (1), 69-77 (2009).

84 Alexander L. Antaris, Jung-Woo T. Seo, Alexander A. Green, and Mark C. Hersam, "Sorting Single-Walled Carbon Nanotubes by Electronic Type Using Nonionic, Biocompatible Block Copolymers," ACS Nano **4** (8), 4725-4732 (2010).

85 Nitish Nair, Woo-Jae Kim, Richard D. Braatz, and Michael S. Strano, "Dynamics of Surfactant-Suspended Single-Walled Carbon Nanotubes in a Centrifugal Field," Langmuir **24** (5), 1790-1795 (2008).

86 L. Nougaret, H. Happy, G. Dambrine, V. Derycke, J. P. Bourgoin, A. A. Green, and M. C. Hersam, "80 GHz field-effect transistors produced using high purity semiconducting single-walled carbon nanotubes," Applied Physics Letters **94** (24), 243505-243503 (2009).

87 Virginia A. Davis, Lars M. Ericson, A. Nicholas G. Parra-Vasquez, Hua Fan, Yuhuang Wang, Valentin Prieto, Jason A. Longoria, Sivarajan Ramesh, Rajesh K. Saini, Carter Kittrell, W. E. Billups, W. Wade Adams, Robert H. Hauge, Richard E. Smalley, and Matteo Pasquali, "Phase Behaviour and Rheology of SWNTs in Superacids," Macromolecules **37**, 154-160 (2004).

88 Sivarajan Ramesh, Lars M. Ericson, Virginia A. Davis, Rajesh K. Saini, Carter Kittrell, Matteo Pasquali, W. E. Billups, W. Wade Adams, Robert H. Hauge, and Richard E. Smalley, "Dissolution of Pristine Single Walled Carbon Nanotubes in Superacids by Direct Protonation," Journal of Physical Chemisty B **108** (26), 8794-8798 (2004).

89 P. K. Rai, R. A. Pinnick, A. N. Parra-Vasquez, V. A Davis, H. K. Schmidt, R. H. Hauge, R. E. Smalley, and M. Pasquali, "Isotropic-nematic phase transition of single-walled carbon nanotubes in strong acids," Journal of the American Chemical Society **128** (2), 591-595 (2006).

90 S. Banerjee, T. Hemraj-Benny, and S. S. Wong, "Covalent Surface Chemistry of Single-Walled Carbon Nanotubes," Advanced Materials **17** (1), 17-29 (2005).

91 S. Niyogi, M. A. Hamon, H. Hu, B. Zhao, P. Bhowmik, R. Sen, M. E. Itkis, and R. C. Haddon, "Chemistry of Single-Walled Carbon Nanotubes," Accounts of Chemical Research **35** (12), 1105-1113 (2002).

92 Bin Zhao, Hui Hu, Aiping Yu, Daniel Perea, and Robert C. Haddon, "Synthesis and Characterization of Water Soluble Single-Walled Carbon Nanotube Graft Copolymers," Journal of the American Chemical Society **127** (22), 8197-8203 (2005).

93 Johnny Amiran, Valeria Nicolosi, Shane D. Bergin, Umar Khan, Philip E. Lyons, and Jonathan N. Coleman, "High quality dispersions of functionalized single walled nanotubes at high concentration," Physocal Chemistry C **112** (10), 3519-3524 (2008).

94 Alain Pénicaud, Philippe Poulin, Alain Derré, Eric Anglaret, and Pierre Peti, "Spontaneous Dissolution of a Single-Wall Carbon Nanotube Salt," Journal of the American Chemical Society **2005** (127), 1 (2005).

95 Dr. Alexander Star, Prof. J. Fraser Stoddart, David Steuerman, Mike Diehl, Akram Boukai, Dr. Eric W. Wong, Dr. Xin Yang, Sung-Wook Chung, Dr. Hyeon Choi, and Prof. James R. Heath, "Preparation and Properties of Polymer-Wrapped Single-Walled Carbon Nanotubes," Angewandte Chemie International Edition **40** (9), 1721-1725 (2001).

96 Jonathan N. Coleman, Alexander Fleming, Stefanie Maier, Sean O'Flaherty, Andrew I. Minett, Mauro S. Ferreira, Stefan Hutzler, and Werner J. Blau, "Binding Kinetics and SWNT Bundle Dissociation in Low Concentration Polymer–Nanotube Dispersions," Journal of Physical Chemisty B **108** (11), 3446-3450 (2004).

97 Naotoshi Nakashima, Shingo Okuzono, Hiroto Murakami, Tonau Nakai, and Kenichi Yoshikawa, "DNA Dissolves Single-walled Carbon Nanotubes in Water," Chemistry Letters **32** (5) (2003).

98 J. Marguerite Hughes, Helen Cathcart, and Jonathan N. Coleman, "Dispersion and Exfoliation of Nanotubes with Synthetic Oligonucleotides: Variation of Dispersion Efficiency and Oligo-Nanotube Interaction with Base Type," Journal of Physical Chemisty C **114** (27), 11741-11747 (2010).

99 Vasiliki Zorbas, Alfonso Ortiz-Acevedo, Alan B. Dalton, Mario Miki Yoshida, Gregg R. Dieckmann, Rockford K. Draper, Ray H. Baughman, Miguel Jose-Yacaman, and Inga H. Musselman, "Preparation and Characterization of Individual Peptide-Wrapped Single-Walled Carbon Nanotubes," Journal of the American Chemical Society **126** (23), 7222-7227 (2004).

100 Valeria Nicolosi, Helen Cathcart, Alan R. Dalton, Damian Aherne, Gregg R. Dieckmann, and Jonathan N. Coleman, "Spontaneous Exfoliation of Single-Walled Carbon Nanotubes Dispersed Using a Designed Amphiphilic Peptide," Biomacromolecules **9**, 598-602 (2008).

101 Helen Cathcart, Susan Quinn, Valeria Nicolosi, John M Kelly, Werner J Blau, and Jonathan N Coleman, "Spontaneous Debundling of SWNTs in DNA based Dispersions," Journal of Physical Chemisty C **111** (66-74) (2007).

102 A. Bianco and M. Prato, "Can Carbon Nanotubes be Considered Useful Tools for Biological Applications?," Advanced Materials **15** (20), 1765-1768 (2003).

103 Ray H. Baughman, "Materials Science: Playing Nature's Game with Artificial Muscles," Science **308** (5718), 63-65 (2005).

104 Hong-Zhang Geng, Dae Sik Lee, K iKang Kim, Gang Hee Han, Hyeon Ki Park, and Young Hee Lee, "Absorption spectroscopy of surfactant-dispersed carbon nanotube film: Modulation of electronic structures," Chemical Physics Letters **455**, 275-278 (2008).

105 Olga Matarredona, Heather Rhoads, Zhongrui Li, Jeffrey H. Harwell, Leandro Balzano, and Daniel E. Resasco, "Dispersion of Single-Walled Carbon Nanotubes in Aqueous Solutions of the Anionic Surfactant NaDDBS," Journal of Physical Chemisty B **107**, 13357-13367 (2003).

106 Zhenyu Sun, Valeria Nicolosi, David Rickard, Shane D Bergin, Damian Aherne, and Jonathan N Coleman, "Quantitative evaluation of surfactant stabilized single walled carbon nanotubes: Dispersion quality and its correlation with zeta potential," Journal of Physical Chemistry C **112** (29), 10692-10699 (2008).

107 S. D Bergin, V. Nicolosi, H. Cathcart, M. Lotya, D. Rickard, Z. Sun, W. J. Blau, and J. N. Coleman, "Large Populations of Individual Nanotubes in Surfactant-Based Dispersions without the Need for Ultracentrifugation," Journal of Physical Chemistry C **112** (4), 972-977 (2008).

108 Jie Liu, Michael J. Casavant, Michael Cox, D. A. Walters, P. Boul, Wei Lu, A. J. Rimberg, K. A. Smith, Daniel T. Colbert , and Richard E. Smalley, "Controlled deposition of individual single-walled carbon nanotubes on chemically functionalized templates," Chemical Physics Letters **303**, 125-129 (1999).

109 Kevin D. Ausman, Richard Piner, Oleg Lourie, and Rodney S. Ruof, "Organic Solvent Dispersions of Single-Walled Carbon Nanotubes: Toward Solutions of Pristine Nanotubes," Journal of Physical Chemistry B **104** (38), 8911-8915 (2000).

110 Brian J. Landi, Herbert J. Ruf, James J. Worman, and Ryne P. Raffaelle, "Effects of Alkyl Amide Solvents on the Dispersion of Single-Wall Carbon Nanotubes," Journal of Physical Chemistry B **108** (44), 17089-17095 (2004).

111 Jeffrey L. Bahr, Edward T. Mickelson, Michael J. Bronikowski, Richard E. Smalley, and James M. Tour, "Dissolution of small diameter single-wall carbon nanotubes in organic solvents?," Chemical Comminication, 193-194 (2001).

112 Silvia Giordani, Shane D. Bergin, Valeria Nicolosi, Sergei Lebedkin, Manfred M. Kappes, Werner J. Blau, and Jonathan N. Coleman, "Debundling of Single-Walled Nanotubes by Dilution: Observation of Large Populations of Individual Nanotubes in Amide Solvent Dispersions," Journal of Physical Chemistry B **110** (15708) (2006).

113 Shane D. Bergin, Valeria Nicolosi, Silvia Giordani, Antoine de Gromard, Leslie Carpenter, Werner J. Blau, and Jonathan N. Coleman, "Exfoliation in ecstasy: liquid crystal formation and concentration-dependent debundling observed for single-wall nanotubes dispersed in the liquid drug g-butyrolactone," Nanotechnology **18** (45) (2007).

114 Shane D. Bergin, Zhenyu Sun, David Rickard, Philip V. Streich, James P. Hamilton, and Jonathan N. Coleman, "Multicomponent Solubility Parameters for Single-Walled Carbon Nanotube−Solvent Mixtures," ACS Nano **3** (8), 2340-2350 (2009).

115 *CRC Handbooko of Chemistry and Physics*. (CRC Press, Florida, 2011).

116 A. I. Yanson, G. Rubio Bollinger, H. E. van der Brom, N. Agrait, and J. M. van Ruitenbeek, "Formation and manipulation of a metallic wire of single gold atoms," Nature **395**, 783-785 (1998).

117 Sukanta De, Thomas M. Higgins, Philip E. Lyons, Evelyn M. Doherty, Peter N. Nirmalraj, Werner J. Blau, John J. Boland, and Jonathan N. Coleman, "Silver nanowire networks as flexible, transparent, conducting films: Extremely high DC to optical conductivity ratios," ACS Nano **3** (7), 1767-1774 (2009).

118 Byung Hee Hong, Sung Chul Bae, Chi-Wan Lee, Sukmin Jeong, and Kwang S. Kim, "Ultrathin Single-Crystalline Silver Nanowire Arrays Formed in an Ambient Solution Phase," Science **294** (2001).

119 Yugang Sun, Byron Gates, Brian Mayers, and Younan Xia, "Crystalline Silver Nanowires by Soft Solution Processing," Nano Letters **2** (2), 165-168 (2002).

120 G. Sauer, G. Brehm, S. Schneider, K. Nielsch, R. B. Wehrspohn, J. Choi, H. Hofmeister, and U.Gosele, "Highly ordered monocrystalline silver nanowire arrays," Journal of Applied Physics **91** (5) (2002).

121 Yugang Sun, Yadong Yin, Brian T. Mayers, Thurston Herricks, and Younan Xia, "Uniform Silver Nanowires Synthesis by Reducing AgNO3 with Ethylene Glycol in the Presence of Seeds and Poly (Vinyl Pyrrolidone)," Chemical Materials **14**, 4736-4745 (2002).

122 A. Graff, D. Wagner, H. Ditlbacher, and U. Kreibig, "Silver Nanowires," The European Physical Journal D **34**, 263-269 (2005).
123 Yugang Sun, Brian Mayers, Thurston Herricks, and Younan Xia, "Polyol Synthesis of Uniform Silver Nanowires: A Plausible Growth Mechanism and the Supporting Evidence," Nano Letters **3** (7), 955-960 (2003).
124 Shu-Hong Zhang, Zhi-Yuan Jiang, Zhao-Xiong Xie, Xin Xu, Rong-Bin Huang, and Lan-Sun Zheng, "Growth of Silver Nanowires from Solutions: A Cyclic Penta-twinned-Crystal Growth Mechanism," Journal of Physical Chemisty B **109**, 9416-9421 (2005).
125 Harald Ditlbacher, Andreas Hohenau, Dieter Wagner, Uwe Kreibig, Michael Rogers, Ferdinand Hofer, Franz R. Aussenegg, and Joachim R. Krenn, "Silver Nanowires as Surface Plasmon Resonators," Physical Review Letters **95**, 257403 (2005).
126 G. Fuster, J. M. Tyler, N. E. Brener, J. Callaway, and D. Bagayoko, "Electronic structure and related properties of silver," Physical Review B **42** (12), 7322 (1990).
127 Guozhong Cao, *Nanostructure and Nanomaterials*. (Imperial College Press, London, 2004).
128 W. Zhang, S. H. Brongersma, O. Richard, B. Brijs, R. Palmans, L. Froyen, and K. Maex, "Influence of the electron mean free path on the resistivity of thin metal films," Microelectronic Engineering **76**, 146-152 (2004).
129 Sung Ha Park, Matthew W. Prior, Thomas H. LaBean, and Gleb Finkelstein, "Optimized fabrication and electrical analysis of silver nanowires templated on DNA molecules," Applied Physics Letters **89**, 033901 (2006).
130 Jin Onuki, Khyoupin Khoo, Yasushi Sasajima, Yasunori Chonan, and Takashi Kimura, "Journal of Applied Physics," 108 **044302** (2010).
131 R. Landauer, "Conductance determined by transmission: probes and quantised constriction resistance," Journal of Physics: Condensed Matter **1** (43), 8099 (1989).
132 Jijun Zhao, Calin Buia, Jie Han, and Jian Ping Lu, "Quantum transport properties of ultrathin nanowires," Nanotechnology **14**, 501-504 (2003).
133 V. Rodrigues, J. Bettini, A. R. Rocha, L. G. C. Rego, and D. Ugarte, "Quantum conductance in silver nanowires: Correlation between atomic structure and transport properties," Physical Review B **65** (153402) (2002).
134 Aric W. Sanders, David A. Routenberg, Benjamin J. Wiley, Younan Xia, Eric R. Dufresne, and Mark A. Reed, "Observation of Plasmon Propagation, Redirection, and Fan-Out in Silver Nanowires," Nano Letters **6** (8), 1822-1826 (2006).
135 A. V. Akimov, A. Mukherjee, C. L. Yu, D. E. Chang, A. S. Zibrov, P. R. Hemmer, H. Park, and M. D. Lukin, "Generation of single optical plasmons in metallic nanowires coupled to quantum dots," Nature **450** (06230) (2007).
136 Xiaodong Li, Hongsheng Gao, Catherine J. Murphy, and K. K. Caswell, "Nanoindentation of Silver Nanowires," Nano Letters **3** (11), 1495-1498 (2003).
137 Michael F. Ashby and D.R.H. Jones, *Engineering Materials 1, Third Edition: An Introduction to Properties, Applications and Design*. (Butterworth-Heinemann, Oxford, 1998).
138 Bin Wu, Andreas Heidelberg, XiaoMing Sun, John E. Sader, YaDong Li, and John J. Boland, "Microstructure-Hardened Silver Nanowires," Nano Letters **6** (3), 468-472 (2006).
139 Lu Xiang, Gu Ji-Hua, and Chu Jun-Hao, "Thermal Conductivity of Metallic Wires," Chinese Physics **10** (3), 1009-1963 (2001).
140 Derek Stewart and Pamela M. Norris, "Size effects on the thermal conductivity of thin metallic wires: Microscale implications," Microscale Thermophysical Engineering **4**, 89-101 (2000).

141 Deyu Li, Yiying Wu, Philip Kim, Li Shi, Peidong Yang, and Arun Majumdar, "Thermal conductivity of individual silicon nanowires," Applied Physics Letters **83** (14) (2003).
142 P. Debye, "Zur Theorie der spezifischen Waerme," Annalen der Physik (Leipzig) **39** (4) (1912).
143 S. Bhattacharrya, S. K. Saha, and D. Chakravorty, "Nanowire formation in a polymeric film," Applied Physics Letters **76** (26), 3896-3898 (2000).
144 Mladen Barbic, Jack J. Mock, D. R. Smith, and S. Schultz, "Single crystal nanowires prepared by the metal amplification method," Journal of Applied Physics **91** (11) (2002).
145 Jinsub Choi, Guido Sauer, Kornelius Nielsch, Ralf B. Wehrspohn, and Ulrich Gosele, "Hexagonally Arranged Monodisperse Silver Nanowires with Adjustable Diameter and High Aspect Ratio," Chemistry of Materials **15**, 776-779 (2003).
146 K. K. Caswell, Christopher M. Bender, and Catherine J. Murphy, "Seedless, Surfactantless Wet Chemical Synthesis of Silver Nanowires," Nano Letters **3** (5), 667-669 (2003).
147 Shu-Hong Zhang, Zhao-Xiong Xie, Zhi-Yuan Jiang, Xin Xu, Juan Xiang, Rong-Bin Huang, and Lan-Sun Zheng, "Synthesis of silver nanotubes by electroless deposition in porous anodic aluminium oxide templates," Chemical Comminication, 1106-1107 (2004).
148 Byung Hee Hong, Sung Chul Bae, Chi-Wan Lee, Sukmin Jeong, and Kwang S. Kim, "Silver Nanowire Arrays Formed in Ambient Solution Phase," Science **294** (2001).
149 Y. Sun and Y. Xia, "Large-Scale Synthesis of Uniform Silver Nanowires Through a Soft, Self-Seeding, Polyol Process," Advanced Materials **14** (11), 833-837 (2002).
150 Nikhil R. Jana, Latha Gearheart, and Catherine J. Murphy, "Wet chemical synthesis of silver nanorods and nanowires of controllable aspect ratio," Chemical Communications, 617-618 (2001).
151 Guangqing Yan, Li Wang, and Lei Zhang, "Recent Research Progress on Preparation of Silver Nanowires by Soft Solution Method, Preparation of Gold Nanotubes and Pt Nanotubes from Resultant Silver Nanowires and their Applications in Conductive Adhesive," Reviews on Advanced Materials Science **24**, 10-25 (2010).
152 Erez Braun, Yoav Eichen, Uri Sivan, and Gdalyahu Ben-Yoseph, "DNA-templated assembly and electrode attachment of a conducting silver wire," Nature **39**, 775-778 (1998).
153 C. K. Chiang, M. A. Druy, S. C. Gau, A. J. Heeger, E. J. Louis, A. G. MacDiarmid, and H. Shirakawa Y. W. Park, "Synthesis of Highly Conducting Films of Derivatives of Polyacetylene $(CH)_x$," Journal of the American Chemical Society **100** (3) (1978).
154 R. E. Peierls, *Quantum Theory of Solids*. (Oxford University Press, Oxford, 1955).
155 Qibing Pei, Guido Zuccarello, Markus Ahlskog, and Olle Inganas, "Electrochromic and haighly stable poly(3,4-ehtylenedioxythiophene) switches between opaque blue-blak and transparent sky blue," Polymer **35** (7), 1347-1351 (1994).
156 A. N. Aleshin, R. Kiebooms, and A. J. Heeger, "Metalli conductivity of highly doped poly(3,4-ethylenedioxythiophene)," Synthetic Metals **101**, 369-370 (1999).
157 J. C. Carlberg and O. Inganäs, "Poly(3,4-ethylenedioxythiophene) as Electrode Material in Electrochemical Capacitors," Journal of the Electrochemical Society **144** (4), L61-L64 (1997).
158 Stephan Kirchmeyer, Andreas Elschner, Knud Reuter, and Wilfried Lovenich, *PEDOT as a Conductive Polymer*. (Taylor and Francis, 2010).

159 S. K. M. Jönsson, J. Birgerson, X. Crispin, G. Greczynski, W. Osikowicz, A. W. Denier van der Gon, W. R. Salaneck, and M. Fahlman, "The effects of solvents on the morphology and sheet resistance in poly(3,4-ethylenedioxythiophene)-polystyrenesulfonic acid (PEDOT-PSS) films," Synthetic Metals **139** (1), 1-10 (2003).

160 Henry J. Snaitha, Henry Kenricka, Marco Chiesaa, and Richard H. Friend, "Morphological and electronic consequences of modifications to the polymer anode 'PEDOT:PSS' " Polymer **8** (29), 2573-2578 (2005).

161 Jianyong Ouyang, Qianfei Xu, Chi-Wei Chu, Yang Yang, Gang Li, and Joseph Shinar, "On the mechanism of conductivity enhancement in poly(3,4-ethylenedioxythiophene):poly(styrene sulfonate) film through solvent treatment," Polymer **45**, 8443-8450 (2004).

162 W. H. Kim, G. P. Kushto, H. Kim, and Z. H. Kafafi, "Effect of Annealing on the Electrical Properties and Morphology of a Conducting Polymer used as an Anode in Organic Light-Emitting Devices," Journal of Polymer Science Part B: Polymer Physics **41** (21), 2522-2528 (2003).

163 L. Groenendaal, F. Jonas, D. Freitag, H. Pielartzik, and J. R. Reynolds, "Poly(3,4-ethylenedioxythiophene) and Its Derivatives: Past, Present, and Future," Advanced Materials **12** (7), 481-494 (2000).

164 N. M. R. Peres, "The transport properties of graphene," Journal of Physics: Condensed Matter **21**, 323201 (2009).

165 Sang N. Kim, Zhengtang Luo, and Fotios Papadimitrakopoulos, "Diameter and Metallicity Dependent Redox Influences on the Separation of Single-Wall Carbon Nanotubes," Nano Letters **5** (12), 2500-2504 (2005).

166 Zhihong Chen, Xu Du, Mao-Hua Du, C. Daniel Rancken, Hai-Ping Cheng, and Andrew G. Rinzler, "Bulk Separative Enrichment in Metallic or Semiconducting Single-Walled Carbon Nanotubes," Nano Letters **3** (9), 1245-1249 (2003).

167 Wei Wang, K. A. Shiral Fernando, Yi Lin, Mohammed J. Meziani, L. Monica Veca, Li Cao, Puyu Zhang, Martin M. Kimani, and Ya-Ping Sun, "Metallic Single-Walled Carbon Nanotubes for Conductive Nanocomposites," Journal of the American Chemical Society **130** (4), 1415-1419 (2008).

168 J. S. Moon, J. H. Park, T. Y. Lee, Y. W. Kim, J. B. Yoo, C. Y. Park, J. M. Kim, and K. W. Jin, "Transparent conductive film based on carbon nanotubes and PEDOT composites," Diamond and Related Materials **14** (11-12), 1882-1887.

169 Jonathan K. Wassei and Richard B. Kaner, "Graphene, a promising transparent conductor," Materials Today **13** (3), 52-59 (2010).

170 Peter Blake, Paul D. Brimicombe, Rahul R. Nair, Tim J. Booth, Da Jiang, Fred Schedin, Leonid A. Ponomarenko, Sergey V. Morozov, Helen F. Gleeson, Ernie W. Hill, Andre K. Geim, and Kostya S. Novoselov, "Graphene-Based Liquid Crystal Device," Nano Letters **8** (6), 1704-1708 (2008).

171 Héctor A. Becerril, Jie Mao, Zunfeng Liu, Randall M. Stoltenberg, Zhenan Bao, and Yongsheng Chen, "Evaluation of Solution-Processed Reduced Graphene Oxide Films as Transparent Conductors," ACS Nano **2** (3), 463-470 (2008).

172 Alexander A. Green and Mark C. Hersam, "Solution Phase Production of Graphene with Controlled Thickness via Density Differentiation," Nano Letters **9** (12), 4031-4036 (2009).

173 Inhwa Jung, Matthew Pelton, Richard Piner, Dmitriy A. Dikin, Sasha Stankovich, Supinda Watcharotone, Martina Hausner, and Rodney S. Ruoff, "Simple Approach for High-Contrast Optical Imaging and Characterization of Graphene-Based Sheets," Nano Letters **7** (12), 3569-3575 (2007).

174 Sasha Stankovich, Dmitriy A. Dikin, Richard D. Piner, Kevin A. Kohlhaas, Alfred Kleinhammes, Yuanyuan Jia, Yue Wu, SonBinh T. Nguyen, and Rodney S. Ruoff,

"Synthesis of graphene-based nanosheets via chemical reduction of exfoliated graphite oxide," Carbon **45** (7), 1558-1565 (2007).
175 Goki Eda, Giovanni Fanchini, and Manish Chhowalla, "Large-area ultrathin films of reduced graphene oxide as a transparent and flexible electronic material," Nat Nano **3** (5), 270-274 (2008).

Chapter 4 : The relationship between network morphology and conductivity in carbon nanotube films[1]

4.1 Introduction and background

The relationship between transparency and sheet resistance for thin conducting films is controlled by the ratio of direct current conductivity (σ_{DC}) to optical conductivity (σ_{OP})[2], such that high values of σ_{DC}/σ_{OP} correspond to the required properties. The value of σ_{OP} for typical NT films depends on the film density and tends to be close to 1.7 x 10^4 Sm^{-1} at 550 nm^3. Thus, in order to optimise the properties of transparent electrodes, the DC conductivity of NT films must be maximised. Currently the best conductivities reported have been ~ (5-6) x 10^5 Sm^{-1}. [4,5] To achieve this the minimum industry requirements, it can be calculated that the film conductivity must exceed 7 x 10^5 Sm^{-1} [6]. Thus, procedures must be developed to improve the conductivity of even the best NT films. A number of chemical routes have been demonstrated to achieve this, namely, via chemical doping[7] and functionalisation[8]. However, NT films with conductivity exceeding 7 x 10^5 Sm^{-1} have not been reported as yet. In order to produce such conductive films, it will be necessary to fully understand the factors controlling the conductivity of NT films.

Unlike the optical conductivity, the DC conductivity is limited by the tunnelling of electrons from tube to tube (or more realistically from bundle to bundle).[9] Thus the overall

DC conductivity will depend critically on the number of conductive paths through the film and the typical number of inter-bundle junctions encountered on a given path. These parameters, and so the DC conductivity, are intimately linked to the network morphology. Very little work has been done on the effect of the morphological properties of the NT films on the conductivity. NT films are always porous and always consist of networks of bundles, not individual NTs. The porosity tends to vary from film to film as does the bundle size. Thus, any attempt to maximise the DC conductivity must be preceded by optimisation of the morphological properties of the film.

In this chapter we explore whether the conductivity is solely limited by the inter-NT junction resistance or if it is affected by the properties of the NTs themselves. In addition, we attempt to determine how the network properties affect the ultimate film conductivity. By measuring bulk DC conductivity of NT films made from a range of different NT types, we demonstrate that the film conductivity increases with increasing NT graphitisation. In addition, the conductivity decreases both with increasing film porosity and with increasing bundle size. Using experiment and computer modelling, we show that the conductivity scales approximately with the inter-NT junction density that we derive in terms of porosity and bundle diameter. Finally, we introduce the "specific conductivity", which we show scales with the Raman G/D ratio, emphasising that the properties of the NTs themselves and not just the network properties are important for high conductivity films.

4.2 Experimental procedure

Different types of single wall NTs (SWNTs), double wall NTs (DWNTs) and functionalised SWNTs were purchased from seven commercial producers, as shown in Table 4.1, and used as supplied. Dispersions of NTs were prepared in different solvents[10,11]

and surfactant solutions[12] by stepwise sonication using a high power ultrasonic processor model GEX600 (129W and 60kHz) and a low-power ultrasonic bath (model Ney Ultrasonic). These dispersions were produced at a starting concentration of 0.444 mg/ml in the appropriate solvent by sonicating for 3 minutes using the ultrasonic tip processor. The initial dispersions were then diluted to a concentration of 0.08 mg/ml and subjected to another minute of high power tip sonication, followed by 4 hours in a low-power ultrasonic bath. Finally the dispersions were sonicated by ultrasonic tip processor for 0-15 minutes, depending on the tube type. In contrast to other NT types, films from HiPCO SWNT in N-methyl-pyrrolidone (NMP) were prepared using dispersions sonicated at a range of sonication times: 0, 2, 4 and 6 minutes.

NT films were prepared by filtering 150ml of each dispersion through a porous polyvinylidene fluoride (PVDF) filtration membrane (Millipore, Durapore membrane filters, 0.45 μm pore size). The deposited NT films were washed with 250 ml of de-ionized water followed by 50ml acetone and dried under vacuum at room temperature for 12 hours. The dried films, with an average thickness of 20 μm, were peeled off the filter membrane and cut into strips with an average width of 2.25 mm for detailed characterisation.

The resistance was measured as a function of strip length by a two lead method[13]. This is done by applying painted silver electrodes to the ends of a strip, measuring the resistance, cutting the end off, reapplying the electrode and re-measuring the resistance. This was repeated a number of times to give a set of eight to ten resistance (R) and length (L) values allowing the conductivity to be calculated from $\sigma=L/RA$ where A is the cross sectional area.

Supplier	Nanotube type (functional groups in brackets)	Carbon Purity (%)	Solvent
Iljin Nanotechnologies	Arc-discharge SWNTs	70-80	SDS/H_2O
Carbon Nanotechnologies Inc.	HiPCO SWNT's	>90	NMP,DMF
Nanocyl	CCVD SWNT's	>70	NMP
	CCVD DWNT's	>90	NMP
Elicarb, Thomas Swan & Co. Ltd.	As prepared CVD SWNT's	>70	NMP
	Annealed CVD SWNT's	>90	NMP
SouthWest Nanotechnologies Inc.	CoMoCAT® SWNTs	>90	NMP
Nanolab	CVD DWNTs	-	NMP
Carbon Solutions Inc.	As prepared Arc Discharge SWNTs	60-85	NMP
	P2-SWNT (Low level -COOH)	80-100	NMP,DMF
	P3-SWNT (High level -COOH)	80-100	NMP,DMF
	P5-SWNT (Octadecylamine)	85-95	Chloroform
	P7-SWNT (Polyethyleneglycol)	85-95	H_2O
	P8-SWNT (m-polyaminobenzene sulfonic acid)	85-95	H_2O

Table 4.1 *Commercial NT suppliers and the NT types used in this work. Also shown are the NT purities as given by the suppliers' website and the solvents used. NB the purity quoted is the fraction of the material in the form of NTs.*

The graphitisation of the NTs after processing into films was investigated using Raman spectroscopy with an excitation wavelength of 633 nm (Horiba Jobin Yvon, LabRam HR Series). For each film, Raman measurements were made on five different regions of the films. In all cases these spectra were similar for a given film. The five spectra were then averaged to give a final representative Raman spectrum. The film density

was measured by carefully weighing the films using a microbalance and measuring the dimensions using a digital micrometer. The porosity of the films was calculated using the measured density of the films and the accepted density of SWNTs (1500 kg/m^3). The average bundle diameters of the deposited films were measured using field emission scanning electron microscopy (SEM) (Zeiss Ultra) operated with an acceleration of 5kV (resolution ~ 4 nm). In all cases the mean diameters were significantly larger than the instrumental resolution.

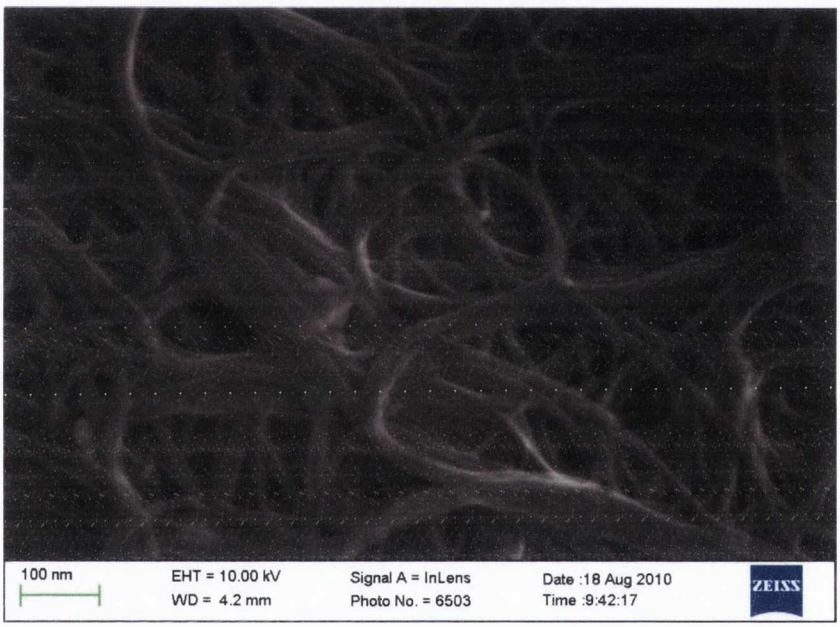

Figure 4.1 *SEM image of the surface of a film prepared from Iljin SWNTs in SDS/H_2O. This image is representative of all the carbon nanotube films made in this study.*

4.3 Results

Direct current (DC) conductivity measurements were made for all NT films. The bulk conductivity was calculated by measuring the film resistance as a function of strip length[13]. The advantage of this method is that it results in a well-defined potential in these (relatively thick and in some cases relatively resistive) films, guaranteeing current flow

throughout the bulk of the film. In all cases the resistance scaled linearly with film length as predicted by Ohm's law. The conductivity is then obtained from the slope of the resistance / length curve while the contact resistance is obtained from the intercept. In all cases the contact resistance was close to zero. The conductivity of the films ranged from 2.08×10^2 Sm^{-1} for the film of Nanocyl SWNT dispersed in NMP up to 2.62×10^5 Sm^{-1} for the film of arc-discharge Iljin SWNTs dispersed in an aqueous solution of sodium dodecyl sulphate (SDS). Notably, the carboxylic acid functionalised P3 SWNTs (Carbon solution Inc.) dispersed in DMF displayed a reasonably high conductivity (1.3×10^4 Sm^{-1}) despite their high levels of functionalisation. This is probably because their –COOH functionalities are thought to be predominately at the tube ends[14] and so have limited effect on charge transport through the tube bodies.

Skakalova *et al.*[15] reported the conductivity for Bucky-paper prepared from HiPCO SWNT dispersed in sodium dodecyl sulphate (SDS) solution to be 5.5×10^4 Sm^{-1}, quite similar to our result (1.67×10^4 Sm^{-1}) for the film of HiPCO SWNTs dispersed in DMF. However, much higher values for conductivity of thin NT films of up to 6×10^5 Sm^{-1}, have been reported[4] which is comparable to the conductivity of the Iljin SWNT film prepared. The difference between these values is most likely due to differences in film morphology as will be discussed below.

Two main factors control charge transport through NT films, the conductivity of the tubes themselves and the ability of the carriers to tunnel from tube to tube. To simplify matters we neglect variations in metal / semiconductor populations and ignore effects of slightly different diameter distributions for different tube types. Within these approximations the conductivity of the NTs themselves is controlled by the structural and chemical defect population associated with a given tube type[16]. We justify this assumption by noting that in all cases the networks are made up of bundles, not individual NTs. Current flow in bundles is thought to be predominately through the metallic NTs.[17] We

expect that the effective conductivity of these metallic NTs is strongly affected by their defect content[16]. The rate of tunnelling across a given bundle-bundle junction is controlled by the junction width and the electronic properties of the constituent tubes and so the mean tunnelling rate is controlled by the statistics of the distribution of junctions.[18] This is not something that is easy to control for a given sample of NTs. However, the number of junctions that a carrier must traverse, on average, when travelling through a NT film depends on how the NTs/ bundles are arranged within the film i.e. the network morphology. For our purposes, we can describe the film morphology using two parameters, the porosity and the mean bundle diameter. These parameters then determine the junction population in these networks. Thus, in order to investigate the factors controlling the conductivity of NT films we quantify the porosity and the mean bundle diameter by density measurements and SEM, respectively. In addition, we probe the level of defects in each tube type by Raman spectroscopy.

Raman spectroscopy is one of the most widely used techniques to characterise SWNTs. Shown in Figure 4.2 are the Raman spectra of three selected films, each displaying a number of key features, including the radial breathing modes (RBM) of the NTs (~ 200 cm^{-1}), the D-band (~ 1300 cm^{-1}), the G-band (~ 1570 cm^{-1}), and the 2D-band (~ 2600 cm^{-1}). For our purposes we are interested in the G- and D-bands. The relative intensity of the former is generally associated with the level of perfection of the hexagonal lattice.[19] For samples containing only NTs, the relative intensity of the D-band is related to the presence of disorder in the tube.[20] However, un-purified NT samples also have a contribution to the D-band from non-NT carbonaceous impurities. In all cases, the tubes used in this work have been purified by the manufacturer. The quoted purity values are given in Table 4.1, where available, and in the vast majority of cases exceed 80 %. While it is prudent to treat manufacturers purity figures with caution, examination of SEM images have not shown significant quantities of impurities in any case. Thus we associate the D-

band of our Raman spectra with imperfections to the hexagonal lattice of the NTs. Then, by measuring the ratio between the G-band and the D-band intensities I_G/I_D we have an approximate metric for the perfection of the hexagonal lattice.[20] These ratios varied from 23.2 for well graphitised tubes (Arc-discharge Iljin SWNT in SDS/H_2O) down to 3.2 for very defective tubes (Carbon Solutions P7 SWNT in H_2O)

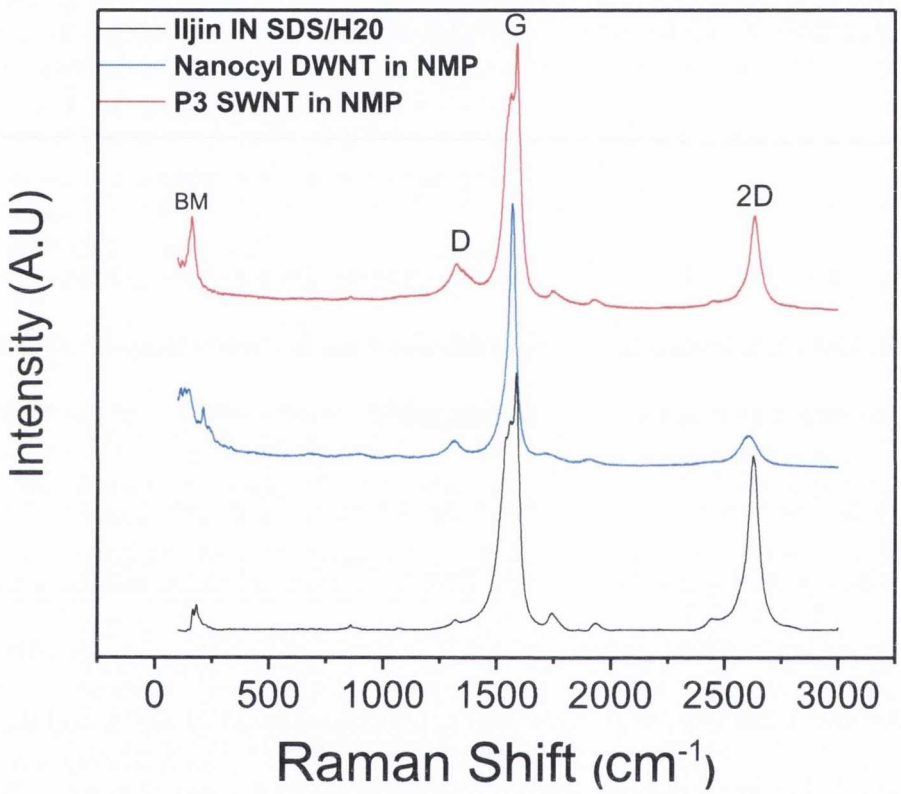

Figure 4.2 *Typical Raman spectra for three of the film types used in this study*

The average bundle diameters in the films were measured using SEM. A scanning electron micrograph for the film of Iljin SWNT prepared using SDS based dispersions is shown in Figure 4.1. This image is typical of NT films in general. The mean bundle diameter for this sample was ~ 12 nm. The average bundle diameter varied between 10 nm

(Carbon Solutions P3 SWNTs in DMF) and 21 nm (Carbon Solutions P2 SWNTs in NMP). As can be clearly seen from Figure 4.1, NT based films tend to be quite porous[21]. The porosity of the films P was calculated from the density of the films ρ_{film} and the density of NT ρ_{NT} using[21] $P=(1 - \rho_{film}/\rho_{NT})$. The porosity of the SWNT films varied greatly from 42 % (South Western Nanotechnologies Inc. SWNT in NMP) to 76 % (Nanocyl SWNT in NMP). The porosity of the functionalised SWNTs exhibited a smaller variation, ranging between 48 % (Carbon Solutions P3 SWNTs in NMP) and 66 % (Carbon Solutions P7 SWNTs in water). It should be noted that the porosity is of course related to the NT volume fraction by $V_f=1 - P$. Both parameters will be used in this work.

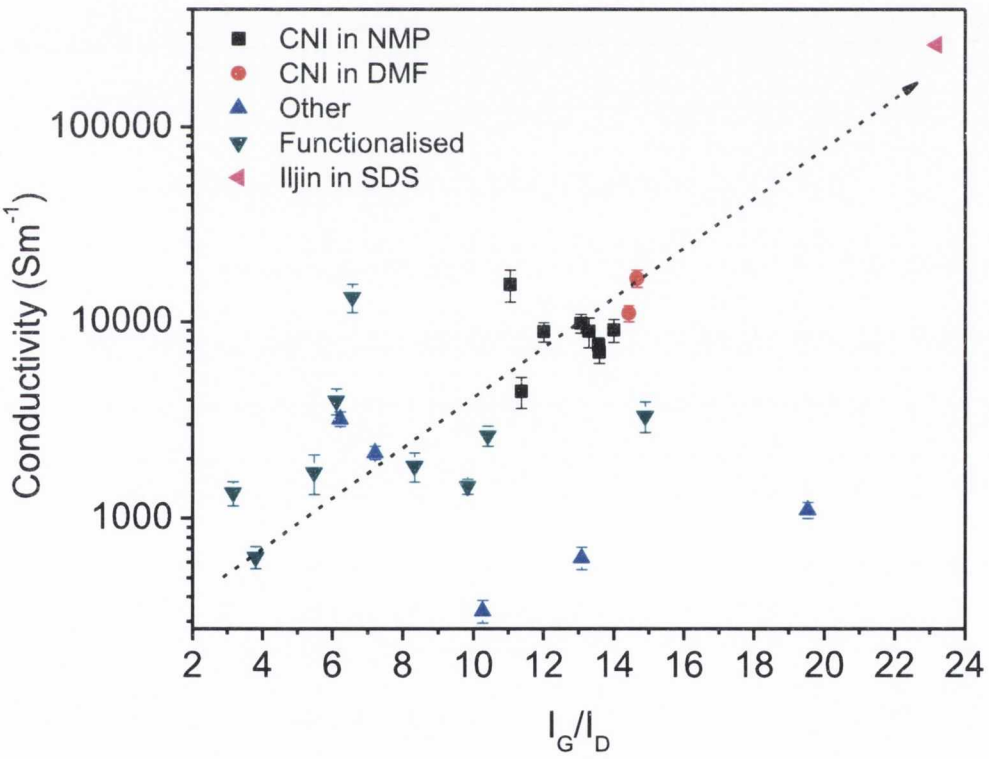

Figure 4.3 *Raman ratio showing scaling (dashed line) of conductivity with nanotube graphitisation.*

As discussed above, the conductivity of NT films should be dependent on two main physical aspects, the NT structure (graphitisation) and the film morphology. Using the ratio of Raman G–band (I_G) to D–band (I_D) intensities as a proxy for structural perfection, a graph of the film conductivity as a function of I_G/I_D was plotted (shown in Figure 4.3). While the data points are quite scattered, it is clear that the conductivity tends to be larger for films made from tubes with higher I_G/I_D *i.e,* higher structural perfection. This is unsurprising as the conductivity of individual NTs has been shown [16] to be heavily dependent on the presence of defects in the graphitic structure. These defects can include pentagons, heptagons, vacancies, dopants, or functional groups that all act to alter the electronic structure of the perfect tubes.

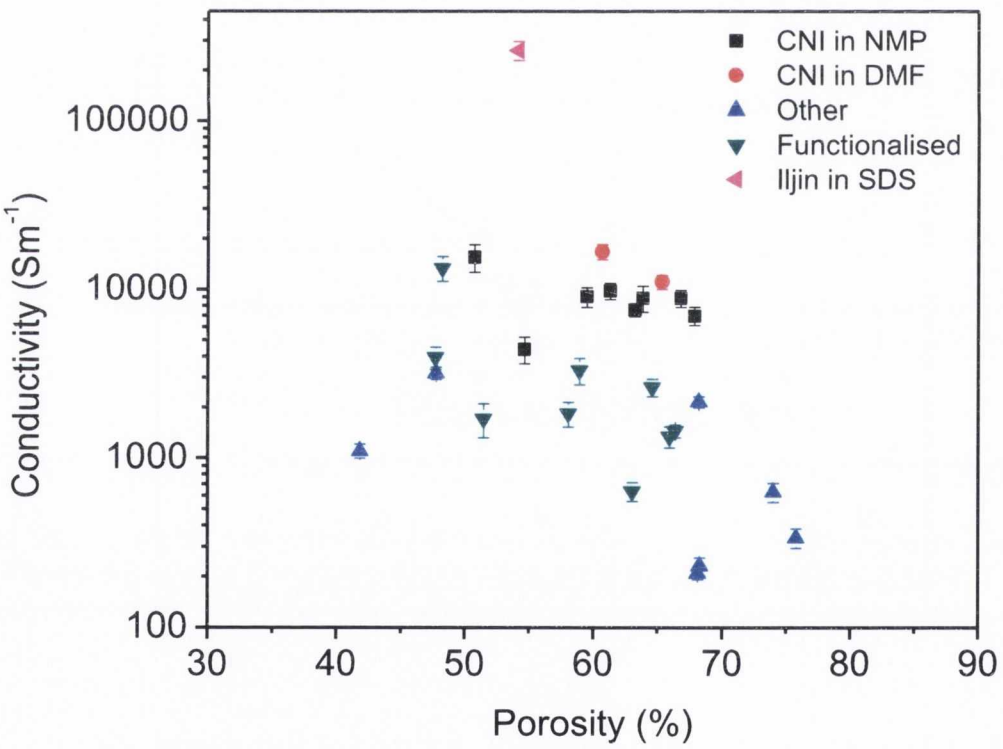

Figure 4.4 *Film conductivity as a function of film porosity showing a decrease in conductivity for more porous films.*

The film morphology can be determined by porosity and the average bundle diameter. The film conductivity was plotted as a function of porosity (shown in Figure 4.4). While the data displays some scatter, the trend of decreasing conductivity with increasing porosity is clear. Qualitatively, this makes sense as a sparse network (more porous) would certainly be expected to be less conductive.

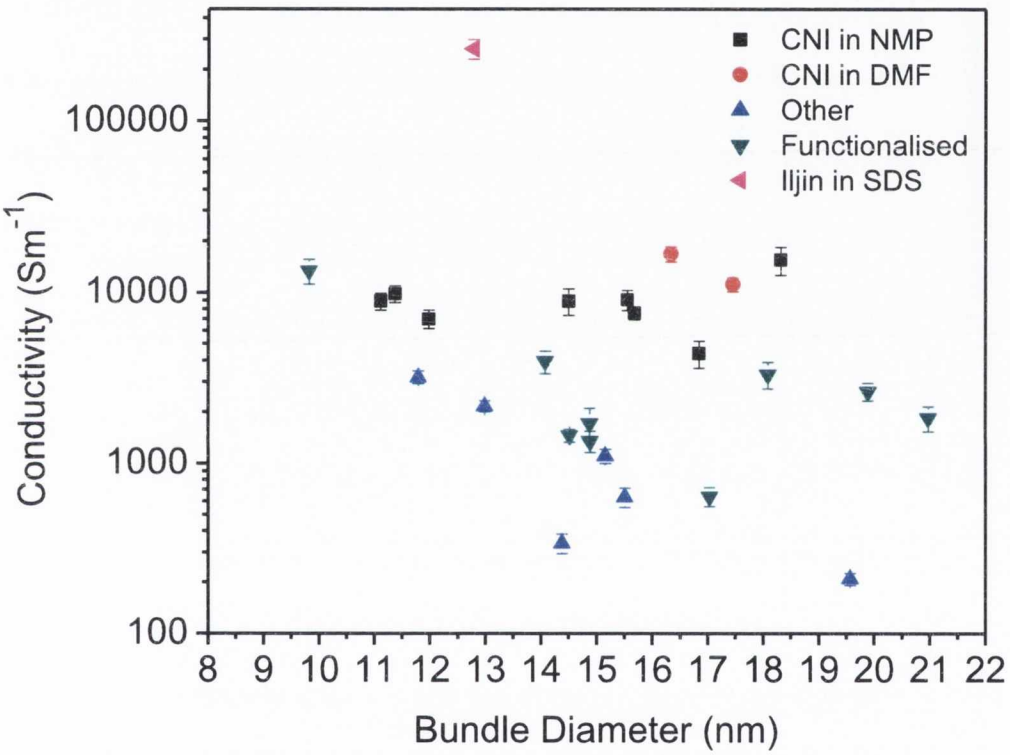

Figure 4.5 *Film conductivity as a function of bundle diameter showing higher conductivity for more exfoliated films.*

Figure 4.5 shows a plot of conductivity versus mean bundle diameter. Again, while some scatter is observed, the trend is clear with the conductivity decreasing steadily as the bundle diameter increases. This latter phenomenon is not unexpected. Hecht *et al.*[22] predicted in 2006 that the conductivity of thin NT films should scale approximately as

$1/D^2$, as a result based on an analysis of the dependence of the number of junctions in a system on the level of bundling.[22]

4.4Discussion

4.4.1 Inter-bundle junction density and bundle connectivity

However, any more detailed analysis of the conduction process would have to consider the number of conducting pathways through the film. This is less straightforward and would require detailed knowledge of the arrangement of bundles within the film. It can be postulated that the number of conductive paths is related to the number density of inter-NT junctions. This is a quantity that is much easier to calculate. An estimate of the number of junctions per unit volume of film N_j can be obtained by calculating the number of bundles per unit volume and multiplying by half the mean number of junctions per bundle $\langle\theta\rangle/2$. The number of bundles per unit volume is related to the film density and the mean bundle diameter $\langle D\rangle$ giving

$$N_J = \frac{\langle\theta\rangle}{2}\frac{\rho_{film}/\rho_{NT}}{\pi\langle D\rangle^2\langle L\rangle/4} = \langle\theta\rangle\frac{2(1-P)}{\pi\langle D\rangle^2\langle L\rangle} \qquad (4.1)$$

Where $\langle L\rangle$ is the mean bundle length and $\langle\alpha\rangle$ is the mean number of junctions per bundle. Using $\langle\theta\rangle/2$ accounts for double counting of junctions.

Estimating $\langle\theta\rangle$ is slightly less straightforward. A cylindrical shell of thickness $\langle D\rangle$ surrounding a test bundle (diameter $\langle D\rangle$) was considered as a simple example. It is then necessary to estimate how many bundles (diameter $\langle D\rangle$) intersect this shell under circumstances similar to those within a NT network. To start, an estimate of the volume of intersection of an arbitrary bundle within the shell is made. While the volume of

intersection for two cylinders (diameters $\langle D \rangle$ and $3\langle D \rangle$) under these circumstances ($\langle D \rangle$ < cylinder axis separation < $2\langle D \rangle$) can be calculated, the result is not a simple analytic function[23]. However it can be shown numerically that the volume of intersection scales with $\langle D \rangle^3$. It is assumed that the mean volume of intersection is just $V_{int}=\kappa\langle D \rangle^3$ (κ is assumed to be invariant with bundle diameter and film porosity). The measured density of the film is then used to estimate the total mass (associated with intersecting bundles) contained within the shell divided by the mass per volume of intersection ($M_{int}=\rho_{NT}\ \kappa\ \langle D \rangle^3$). It is approximated that every bundle intersecting the shell is *in contact* with the test bundle. This means that the number of junctions per bundle is just the number of bundles within the shell so

$$\langle \theta \rangle \approx \frac{\rho_{film}}{\rho_{NT}} \frac{8\pi \langle L \rangle}{4\kappa \langle D \rangle} = (1-P)\frac{2\pi \langle L \rangle}{\kappa \langle D \rangle} \qquad (4.2)$$

However not all the bundles intersecting the shell are actually in contact with the test bundle. To account for this, it is assumed (see below) that Equation 4.2 is correct *within a constant factor*. This allows Equation 4.2 to be rewritten as

$$\langle \theta \rangle \approx \beta(1-P)\frac{\langle L \rangle}{\langle D \rangle} \qquad (4.3)$$

Where all constants ar[1]e consolidated in a single constant β.

To test the veracity of this approach numerical simulations to model the connectivity of a conducting network formed by a large number of rods were performed.[a] Because the network is inherently disordered, fluctuations in the network connectivity must be accounted for by considering a truly disordered network made of randomly distributed finite-sized one-dimensional rods contained within a box of side *2L x 2L x 4L*,

[a]The computational simulations reported in this thesis were performed by Luiz F. C. Pereira and Dr. Mauro Ferreira of the School of Physics, Trinity College Dublin

where L is the rod length. The rods are assumed to be identical with diameter D, length L and aspect ratio (AR) defined as $AR=L/D$. The volume fraction of rods V_f is related to the porosity P by $V_f=1 - P$ and is easily obtained by calculating the volume occupied by the rods within a sampling cubic box or arbitrary size.

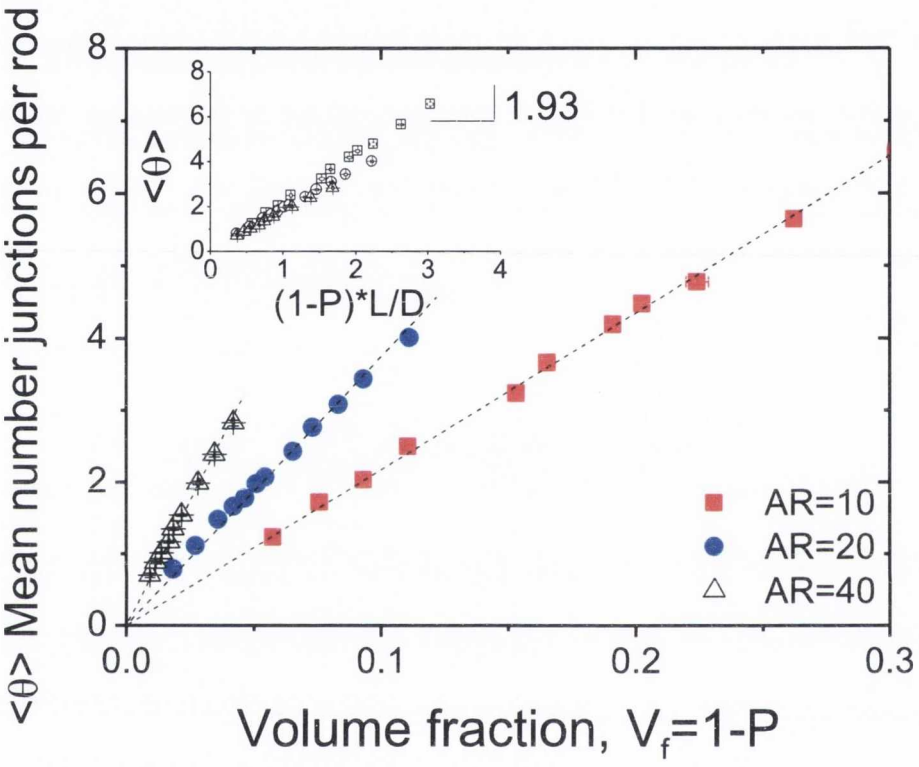

Figure 4.6 *Computer simulations of properties of random networks of rods (a) Calculations of mean number of junctions per rod ‹θ› as a function of volume fraction for three different aspect ratios. Inset: mean number of junctions per rod as a function of volume fraction times the aspect ratio showing universal scaling as predicted by Equation 4.3.*

The connectivity of the network can be calculated by looking at the shortest distance between rods within the sampling box. If the shortest distance between two rods is less than the rod diameter, it can be assumed they are connected. By counting over all

possible pairs within the box the connectivity of the network can be mapped. This approach allows the number of junctions per rod, $\langle\theta\rangle$, to be calculated. It should be noted that statistical significance is only achieved after several configurations of disorder which allows calculation of the dispersions in the volume fraction and in the mean number of connections per rod, respectively.

As predicted by Equations 4.2 and 4.3, the calculated value of $\langle\theta\rangle$ increases linearly with the volume fraction V_f, with an increase rate which depends on the AR of the rods (see Figure 4.6 inset). When plotted as a function of the product $V_f x\ L/D$ (Figure 4.6 inset), $\langle\theta\rangle$ grows linearly along the same straight line for all aspect ratios, confirming the veracity of Equation 4.3. By comparison of the measured slope of Figure 4.6 (inset) with Equation 4.3, a value β can be estimated giving $\beta \approx 1.93$. The calculated values of β can be used to show that $\langle\theta\rangle$ ranges 54 to 124 junctions/μm of bundle length for the P2-NMP and HiPCO-NMP samples, respectively. It should also be pointed out that β (and hence κ) is invariant with bundle diameter and volume fraction. Combining Equations 4.1 and 4.3 an expression for the number of junctions per unit volume is obtained

$$N_J \approx \frac{2\beta}{\pi}\frac{(1-P)^2}{\langle D^3\rangle} = \frac{2\beta}{\pi}\frac{V_f^2}{\langle D^3\rangle} \qquad (4.4)$$

were $(1 - P)=V_f$, the NT volume fraction. The junction number was calculated to vary from 1.8 x 10^{22} m^{-3} for Nanocyl SWNT in NMP to 3.7 x 10^{23} m^{-3} for the P3 SWNT in DMF.

4.4.2 Relationship between network conductivity and NJ

As discussed above, the network conductivity is expected to depend on both the NT conductivity and the network morphology. However, if the NTs themselves are much less

resistive than the junctions it could be expected that the network properties dominate the network conductivity. In this scenario, the network conductivity would be expected to scale approximately with N_j.

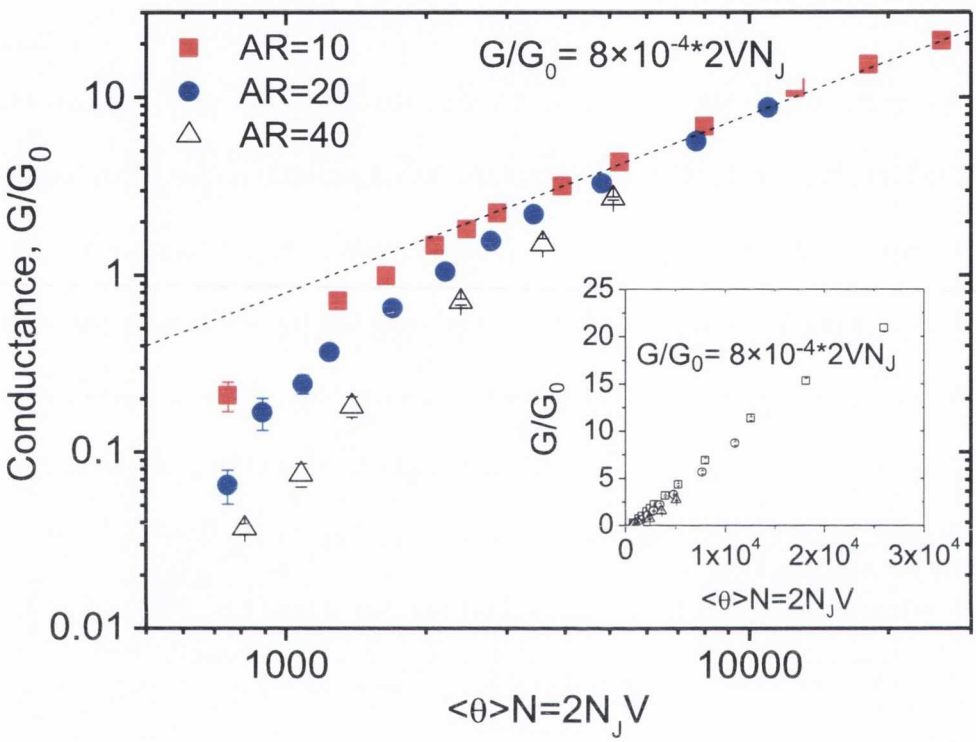

Figure 4.7 *Calculations of the conductance of a network of N rods as a function of the number of junctions per rod, ‹θ›, times N, ‹a›N, for three different aspect ratios. G is expressed in units of (G_0) where G_0 is the junction conductance. The fact that all curves asymptotically approach the dashed line (linear scaling) shows that the conductance scales with the number of junctions per unit volume, N_J, where N_j=‹θ›N/2V, with V as the volume of the box containing the rods. Inset: The same data shown on a linear-linear plot. The dotted line represents $G/G_0 = 8\times10^{-4}N_J$.*

Numerical simulations can be used to investigate the relationship between the network conductivity and the number of junctions per unit volume, N_j. How the

conductance, G, of the disordered networks scales with the mean number of connections per rod $\langle\theta\rangle$ can be investigated once the scaling of the average connectivity and volume fraction is known. When calculating $\langle\theta\rangle$ (Figure 4.7) the connectivity of the networks can be mapped, identifying which tubes are connected and how they are distributed across the film. By enclosing this network in a sampling box the number of tubes intersecting opposite sides can be estimated. These pairs of opposite sides can be considered as electrodes. The box size used was $2L \times 2L \times 4L$ with the electrodes being placed on opposing $2L \times 2L$ faces (L being the rod length). A large number of conducting NTs were used to model nodes connected by resistors of resistance R_0 (conductance $G_0=1/R_0$). The resistors were used to represent the barrier experienced by charge carriers in attempting to hop between neighbouring tubes.

Upon defining the network the equivalent resistance (and hence conductance) between two arbitrary nodes can be calculated. Calculations were carried out for boxes with different number of nodes and hence different number of nanotubes, N. The largest calculation carried out was for a number of rods N=1860 such that $\langle\theta\rangle N$=26000. In order to achieve statistical significance all the results were obtained after averaging over several configurations of disorder. Calculations based on larger values of N were unattainable due to time restraints on computational power.

The calculations above show that, for each value of rod aspect ratio (AR), the conductance increases monotonically with $\langle\theta\rangle$ (Figure 4.8). To understand the relationship between the conductivity, as represented here by the network conductance and the number of junctions per volume N_j by noting the relationship

$$N_J = \frac{\langle\theta\rangle}{2}\frac{N}{V} \qquad (4.5)$$

Where N/V is the total number of rods per unit volume.

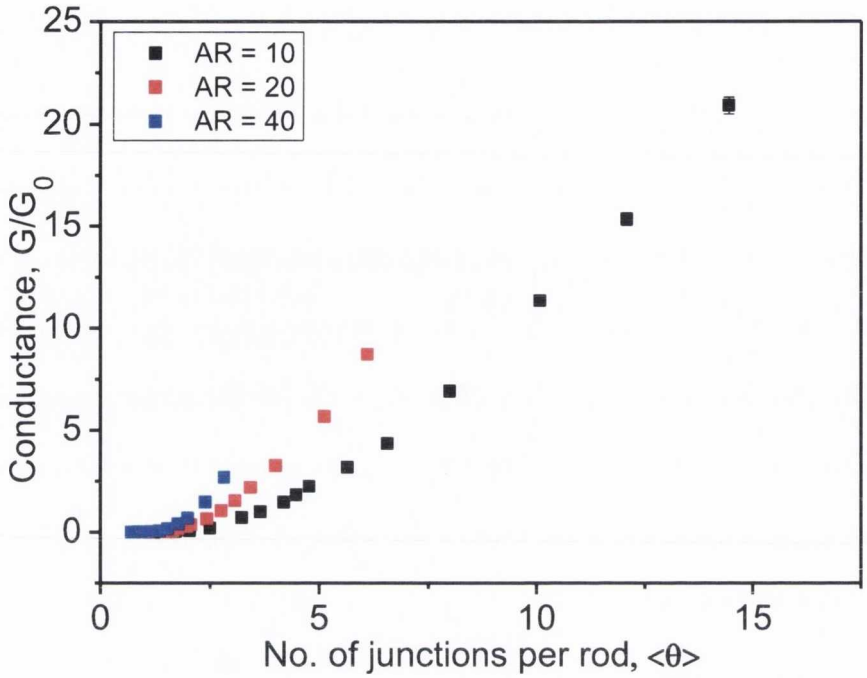

Figure 4.8 *Calculations of the conductance of a network of N rods as a function of the number of junctions per rod, ‹θ›, for three different aspect ratios. For each aspect ratio (AR) the network conductance increases monotonically with increasing‹θ›.*

The conductance is plotted in Figure 4.7 as a fraction of $\langle\theta\rangle N=2N_jV$ for three different rod aspect ratios. For each aspect ratio, the conductance increases with increasing $\langle\theta\rangle N$. While each curve is independent at low values of $\langle\theta\rangle N$, they come together for values of $\langle\theta\rangle N \approx 5000$ and subsequently appear to scale with the same linear trend. As the box volume V was constant in all cases, this strongly suggests that, for values of $\langle\theta\rangle N > 5000$, the network conductance scales linearly with N_j. Due to time constraints on computational time, data points with a large enough $\langle\theta\rangle N$ to show unambiguously that the data for each aspect ratio converge on the same straight line were not performed (calculations with $AR = 40$ are considerably more time consuming). However by plotting the high aspect ratio data

on a linear-linear curve (Figure 4.7 inset), it can be seen that the curves for each aspect ratio increase linearly with similar slopes, $G/G_0=8 \times 10^4 \times 2VN_j$. The lowest value of N_j of the experimental NT films was measured to be ~$1.8 \times 10^{22}m^{-3}$. Coupled with the size of the box used in the computation (taking $L > 1\mu m$), the realistic lower value for a network of $\langle\theta\rangle N=2N_jV$ can be estimated to be 1.8×10^5, well into the region where the data is expected to coalesce on the same straight line. Thus, in any real network, it can be confidently said that $G/G_0 \propto N_j$ for all aspect ratios. This linear relationship between network conductance G and N_j allows the conductivity (with reference to Equation (4.4)) to be written as

$$\sigma \approx \kappa \frac{(1-P)^2}{\langle D^3 \rangle} = \kappa \frac{V_f^2}{\langle D^3 \rangle} \qquad (4.6)$$

Where κ is a constant for a given tube type. Note that this expression scales as $1/\langle D^3\rangle$ not $1/\langle D^2\rangle$ as suggested previously by Hecht *et al*[22].

The experimental data was examined in order to ascertain any relationship between network conductivity and junction number density as seen in numerical studies discussed above. Shown in Figure 4.9 is a plot of σ versus N_j for each type of NT that was studied. An approximate linear scaling for the HiPCO-DMF and HiPCO-NMP NT films was observed. Additionally the majority of functionalised and all of the "other" NTs followed the same approximate linear trend. However, two problems are made clear: the conductivity of all the functionalised tubes does not scale well with N_j and the graph contains significant scatter. These two points will be addressed below.

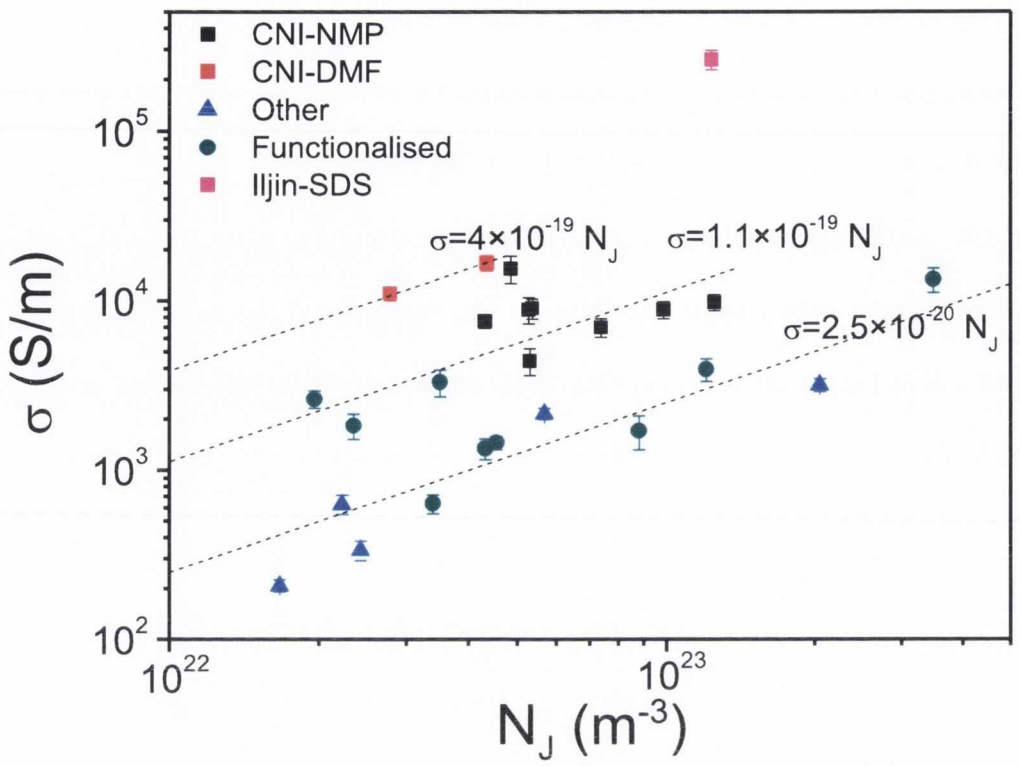

Figure 4.9 *Approximate scaling of conductivity with number density of inter-NT junctions. The dashed lines illustrate linear scaling as described by the attached equations.*

4.4.3 Effect of intrinsic nanotube properties

As described above, both modelling and experimental data suggest approximately linear scaling between network conductivity and the junction number density. However this can only occur if all the tubes have the same intrinsic conductivity. With reference to Figure 4.5, this is not the case. Thus, the effect on the film conductivity on variations in the intrinsic NT properties must be extracted. This was done by comparing the conductivities of all the networks studied in the absence of any morphological differences. The conductivities of each film were rescaled to represent the conductivity of a film whose

porosity and mean bundle diameter were fixed at specific values P_0 and D_0. This was done by combining the linearity of σ and N_j with Equation 4.4. Variations in this parameter are then due to intrinsic differences between tube types. This specific conductivity σ_0 was calculated from

$$\sigma_0 = \frac{\sigma}{N_J}\frac{2\beta}{\pi}\frac{(1-P_0)^2}{D_0^3} \qquad (4.7)$$

This method can also be used to estimate the maximum realistic conductivity values attainable by appropriate choice of P and $\langle D \rangle$. The porosity of NT films is very difficult to control so an average value of P_0=0.5 was chosen. Small bundle sizes are expected to lead to more conductive films so a realistic minimum values $\langle D_0 \rangle$=2nm was chosen. Using Equation 4.7 the specific conductivity was calculated to range from 4.8 x 10^5 Sm^{-1} for Nanocyl SWNT in NMP up to 1.5 x 10^7 Sm^{-1} for HiPCO dispersed in DMF. It should be pointed out that the upper end of this scale is more than twenty times as high as the most conductive NT film reported to date[4] which suggests that further improvements on the state of the art are possible. From Figure 4.3 it was shown that variations in the defect population in the NTs, determined by their I_G/I_D ratio, results in variations in the network conductivity. This means that the network conductivity should scale with the I_G/I_D ratio once morphological effects are negated.

From Figure 4.3 it is known that variations in the defect population and hence variation in the NT conductivity result in variations in the network conductivity. This means that when morphological effects are removed, the conductivity should scale with a parameter related to the conductivity of the individual NTs. Earlier, the Raman ratio I_G/I_D was used as a proxy for such a parameter.

Figure ***4.*** 4.10 shows a plot of specific conductivity versus Raman ratio.

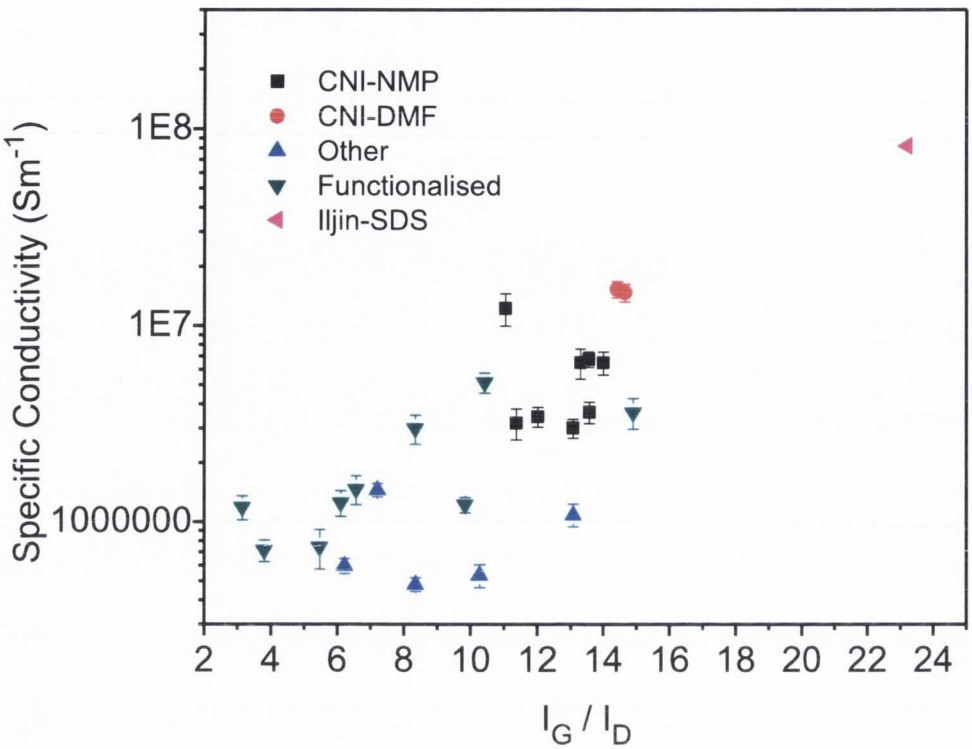

Figure 4.10 *Scaling of specific conductivity with the Raman ratio. The specific conductivity is the conductivity rescaled to represent the conductivity of a network produced from the same tubes but with mean bundle diameter ‹D› =2 nm and porosity P=0.5. This scaling demonstrates that the deviations from linearity in Figure 4.9 can be correlated to the level of graphitization of the NTs.*

Iljin SWNTs show very high purity and intrinsic conductivity and its corresponding data point lays in-line with the other samples. HiPCO NT samples are grouped strongly at the top right of the graph indicating relatively high levels of perfection and intrinsic conductivity. Conversely, the "other" tube types show a low specific conductivity irrespective of Raman ratio. Interestingly, the specific conductivity of the functionalised NTs scales exponentially with Raman ratio. This behaviour is most clear for this category because the base tubes are identical with the only variation being the type and

degree of functionalisation. In general it is clear that σ_0 scales very strongly with Raman ratio and hence the perfection of the NTs. While not surprising, this clearly shows that when morphological effects are removed the NT perfection controls the film conductivity.

This analysis shows that, in addition to depending on the conductivity of the individual NTs, the film conductivity depends on the morphological properties of the network, specifically the junction number density, which can be expressed in terms of P and $\langle D \rangle$. It must be emphasised that these results are semi-empirical. For example, Equation 4.6 makes no mention of tube length, even though Hecht *et al.*[22] showed that film conductivity does indeed scale with tube length. A length dependence *could* be found by a rigorous analysis of the relationship between conductivity and N_j, i.e., $\kappa=f(L)$. Nevertheless, the data presented in this work shows that high conductivity is achieved for lower porosity films and/or films produced from smaller bundles. This observation also explains why the HiPCO films investigated in this work have conductivities an order of magnitude below the best films from literature[24] and the Iljin film has conductivity comparable to the best films from literature as they have a very long length (~1-10 μm). High conductivity films are generally made from ultracentrifuged dispersions that consist mainly of individual NTs and very small bundles. This translates into low values of D and hence high conductivities. In this work, no attempt was made to fully exfoliate the NTs, resulting in large D values and so lower conductivities.

4.4.4 Estimation of inter-bundle resistance

According to Figure 4.7, the network conductance scales linearly with N_j. This scaling relationship can be written as $G=2N_jVNG_0m$, where m is the common slope found in. Figure 4.7. The data in Figure 4.7 was calculated using a box size of $2L \times 2L \times 4L$ with

the electrodes on opposing $2L \times 2L$ faces. The conductance G can be converted to conductivity σ and when the dimensions are taken into account $\sigma = 32mL^2G_0N_j$. This can be compared to the experimental data presented in Figure 4.9 remembering that the parameter L used to define the box size was set as equal to the rod length in all cases. While the bundle length in the films are not known it can be assumed that it is significantly larger than the NT length and $1\mu m < L < 50\mu m$ (HiPCO NT have $<L> \sim 0.8$ μm, while Iljin have $<L> \sim 3.5$ μm[25]). In the model, the NTs have zero resistance, meaning that the network conductivity was due only to the junctions. This approximation is most valid for the tubes / bundles with the highest intrinsic conductance. Thus, this model is most applicable to NT films consisting of either (1) larger bundles that are effectively metallic or (2) individual metallic-only nanotubes. From Figure 4.10 it can be seen that the network prepared from Iljin SWNT in SDS/H_2O had the highest intrinsic conductance. Figure 4.10 shows that $\sigma = 4 \times 10^{-19} N_j$. Comparing this with the equation above and noting that $m = 4 \times 10^4$, the interjunction resistance can be estimated as $70\ k\Omega < R_0 < 3.5 M\Omega$ from Figure 4.10. This value is smaller than that estimated by Stahl *et al.*[26] for the inter-tube coupling resistance in NT bundles. This is surprising as the inter-bundle junction resistance would be expected to exceed the intra-bundle tunnelling resistance. The reason for the discrepancy is not clear but it is unlikely to be due to the bundle length estimate as the bundle length is not expected to exceed 50μm in the NT films studied in this work.

4.4.5 Parallels with percolation

Finally it is worth noting that the relationship between conductivity and NT volume fraction expressed in Equation 4.6 is reminiscent of the standard percolation equation describing the conductivity of conductor-insulator composites[27] $\sigma = \sigma_0 (V_f - V_{f,crit})^t$, where σ_0 is a constant related to the conductivity of the conducting inclusions,[28] $V_{f,crit}$ is the

critical volume fraction above which the first conducting path through the sample is formed (the percolation threshold),[27] and t is the critical exponent.[27] the similarity becomes more marked when one realises that for NTs, the percolation threshold is generally in the range of 0.1 % - 1%[29-31] and so at the high volume fractions studied here, $V_f - V_{f,crit} \approx V_f$. More interestingly, in simple systems the critical exponent is thought to take the universal value of t=2.0 in three dimensions[27]. Taking these facts into account, the percolation equation becomes identical in form to Equation 4.6. However such similarities are deceptive. The percolation equation is only truly valid close to the percolation threshold which is not the case here. In addition, Equation 4.6 is derived from consideration of the density of junctions in a dense network, not a percolating system. However, the comparison is instructive nevertheless. In 2007 Blighe *et al.*[13] reported percolation-like behaviour with t=2.2±0.2 for very high volume fraction polymer-NT composites ($10\% < V_f < 45\%$) . This was cited as an example of percolation –like scaling, far from the percolation threshold, that is contrary to general expectations. However, the result obtained here suggests that the measured exponent may be more indicative of network behaviour, described by Equation (4.6), than percolation. In fact, the κ value associated with the data presented by Blighe *et al.*[13] can be back calculated. Using $\langle D \rangle$=13nm and σ_0=5 x $10^4 Sm^{-1}$ a value of κ=1.1 x $10^{-19} Sm^2$ was calculated, in good agreement with the range estimated above.

4.5 Conclusion

In conclusion the conductivity of NT films prepared using a large number of different tube types was measured. The films were characterised by Raman spectroscopy, SEM and density measurements which led to a calculation of the Raman G:D ratio, the

mean bundle diameter $\langle D \rangle$, and the film porosity P. It was found that the conductivity tended to increase in films made from less defective tubes. However the conductivity was lower for films that were either more porous or contained larger bundles. Computer simulations showed that the conductivity of a network of conducting rods should scale linearly with the inter-rod junction density. Expressions for the number of junctions per nanotube and the number density of junctions in terms of the porosity and mean bundle diameter were derived. Experimentally, approximate scaling of conductivity with the junction number density was observed. This allowed the calculation of a specific conductivity, i.e., the expected conductivity for a network of tubes with P=0.5 and $\langle D \rangle$=2nm. This specific conductivity tends to scale strongly with Raman ratio. This demonstrates that the properties of both the nanotubes and the network are important for high conductivity films. This work makes it clear that if highly conductive films are required, one needs to work with very conductive, defect-free NTs that have been extensively exfoliated and arranged into dense films.

4.6 References

1 Philip E. Lyons, Sukanta De, Fiona Blighe, Valeria Nicolosi, Luiz Felipe C. Pereira, Mauro S. Ferreira, and Jonathan N. Coleman, "The relationship between network morphology and conductivity in nanotube films," Journal of Applied Physics **104** (044302) (2008).

2 L. Hu, D. S. Hecht, and G. Gruner, "Percolation in Transparent and Conducting Carbon Nanotube Networks," Nano Letters **4** (12), 2513-2517 (2004).

3 B. Ruzicka and L. Degiorgi, "Optical and dc conductivity study of potassium-doped single-walled carbon nanotube films," Physical Review B **61** (4), 2468-2471 (2000).

4 Zhuangchun Wu, Zhihong Chen, Xu Du, Jonathan M. Logan, Jennifer Sippel, Maria Nikolou, Katalin Kamaras, John R. Reynolds, David B. Tanner, Arthur F. Hebard, and Andrew G. Rinzler, "Transparent, Conductive Carbon Nanotube Films," Science **305**, 1273-1276 (2004).

5 Hong-Zhang Geng, Ki Kang Kim, Kang Pyo So, Young Sil Lee, Youngkyu Chang, and Young Hee Lee, "Effect of Acid Treatment on Carbon Nanotube-Based Flexible Transparent Conducting Films," Journal of the American Chemical Society **129**, 7758-7759 (2007).

6 M. Dressel and G. Gruner, *Electrodynamics of Solids: Optical Properties of Electrons in Matter*. (Cambridge University Press, Cambridge, 2002).

7 Giovanni Fanchini, Husnu Emrah Unalan, and Manish Chhowalla, "Modification of transparent and conducting single wall carbon nanotube thin films via bromine functionalization," Applied Physics Letters **90** (092114) (2007).

8 Bhavin B. Parekh, Giovanni Fanchini, Goki Eda, and Manish Chhowalla, "Improved conductivity of transparent single-wall carbon nanotube thin films via stable postdeposition functionalization," Applied Physics Letters **90** (121913) (2007).

9 Elena Bekyarova, Mikhail E. Itkis, Nelson Cabrera, Bin Zhao, Aiping Yu, Junbo Gao, and Robert C. Haddon, "Electronic Properties of Single-Walled Carbon Nanotube Networks," Journal of the American Chemical Society **127** (16), 5990-5995 (2005).

10 Shane D. Bergin, Valeria Nicolosi, Silvia Giordani, Antoine de Gromard, Leslie Carpenter, Werner J. Blau, and Jonathan N. Coleman, "Exfoliation in ecstasy: liquid crystal formation and concentration-dependent debundling observed for single-wall nanotubes dispersed in the liquid drug γ -butyrolactone," Nanotechnology **18** (455705) (2007).

11 Silvia Giordani, Shane D. Bergin, Valeria Nicolosi, Sergei Lebedkin, Manfred M. Kappes, Werner J. Blau, and Jonathan N. Coleman, "Debundling of Single-Walled Nanotubes by Dilution: Observation of Large Populations of Individual Nanotubes in Amide Solvent Dispersions," Journal of Physical Chemistry B **110**, 5708-15718 (2006).

12 Jie Liu, Andrew G. Rinzler, Hongjie Dai, Jason H. Hafner, R. Kelley Bradley, Peter J. Boul, Adrian Lu, Terry Iverson, Konstantin Shelimov, Chad B. Huffman, Fernando Rodriguez-Macias, Young-Seok Shon, T. Randall Lee, Daniel T. Colbert, and Richard E. Smalley, "Fullerene Pipes " Science **280** (5367), 1253-1256 (1998).

13 Fiona M. Blighe, Yenny R. Hernandez, Werner J. Blau, and Jonathan N. Coleman, "Observation of Percolation-like Scaling – Far from the Percolation Threshold – in High Volume Fraction, High Conductivity Polymer- Nanotube Composite Films," Advanced Materials **19**, 4443–4447 (2007).

14 Bin Zhao, Hui Hu, and Robert C. Haddon, "Synthesis and properties of water-soluble single-walled carbon nanotube-polymer(*m*-aminobenzinesulfonic acid) graft copolymer," Advanced Functional Materials **14** (1), 71-76 (2004).

15 V. Skakalova, A. B. Kaiser, U. Dettlaff-Weglikowska, K. Hrncarikova, and S. Roth, "Effect of Chemical Treatment on Electrical Conductivity, Infrared Absorption, and Raman Spectra of Single-Walled Carbon Nanotubes," Journal of Physical Chemistry B **109**, 7174-7181 (2005).

16 H. Dai, W. Wong, and C. M. Lieber, "Probing Electrical Transport in Nanomaterials: Conductivity of Individual Carbon Nanotubes " Science **272** (523), 523 - 526 (1996).

17 M. Stadermann, S. J. Papadakis, M. R. Falvo, J. Novak, E. Snow, Q. Fu, J. Liu, Y. Fridman, J. J. Boland, R. Superfine, and S. Washburn, "Nanoscale study of conduction through carbon nanotube networks," PHYSICAL REVIEW B **69** (20), 201402 (2004).

18 Peter N. Nirmalraj, Philip E. Lyons, Sukanta De, Jonathan N. Coleman, and John J. Boland, "Electrical Connectivity in Single-Walled Carbon Nanotube Networks," Nano letters **9** (11), 3890-3895 (2009).

19 F. Tuinstra and J. L. Koenig, "Raman spectum of Graphite," Journal of Chemical Physics **53**, 1126-1130 (1970).

20 K. Sato, R. Saito, Y. Oyama, J. Jiang, L. G. Cançado, M. A. Pimenta, A. Jorio, Ge G. Samsonidze, G. Dresselhaus, and M. S. Dresselhaus, "D-band Raman intensity of graphitic materials as a function of laser energy and crystallite size," Chemical Physics Letters **427** (1-3), 117-121 (2006).

21 C. J. Frizzell, M. in het Panhuis, D. H. Coutinho, Jr. K. J. Balkus, A. I. Minett, W. J. Blau, and J. N. Coleman, "Reinforcement of macroscopic carbon nanotube structures by polymer intercalation: The role of polymer molecular weight and chain conformation," Physical Review B **72** (245420) (2005).

22 David Hecht, Liangbing Hu, and George Grüner, "Conductivity scaling with bundle length and diameter in single walled carbon nanotube networks," Applied Physics Letters **89** (133112) (2006).

23 J. Boersma, P. J. Doelder, and J. K. M. Jansen, "A volume Problem (M. K. Lewis)," SIAM Review **25** (1), 102-106 (1983).

24 T. M. Barnes, J. van de Lagemaat, D. Levi, G. Rumbles, T. J. Coutts, C. L. Weeks, D. A. Britz, I. Levitsky, J. Peltola, and P. Glatkowski, "Optical characterization of highly conductive single-wall carbon-nanotube transparent electrodes," PHYSICAL REVIEW B **75** (23), 235410 (2007).

25 Evelyn M.Doherty, Sukanta De, Philip E. Lyons, Aleksey Shmeliova, Peter N. Nirmalraj, Vittorio Scardaci, Jerome Joimel, Werner J. Blau, John J. Boland, and Jonathan N. Coleman, "The spatial uniformity and electromechanical stability of transparent, conductive films of single walled nanotubes," Carbon **47**, 2466-2473 (2009).

26 H. Stahl, J. Appenzeller, B. Lengeler, R. Martel, Ph. Avouris, Bin Zhao, Hui Hu, and Robert C. Haddon, "Investigation of the inter-tube coupling in single-wall nanotube ropes," Materials Science and Engineering C **15**, 291-294 (2001).

27 Amnon Aharony Dietrich Stauffer, *Introduction to percolation theory*. (Taylor & Francis, London, 2003).

28 M. Foygel, R. D. Morris, D. Anez, S. French, and V. L. Sobolev, "Theoretical and computational studies of carbon nanotube composites and suspensions: Electrical and thermal conductivity," Physical Review B **71** (104201) (2005).

29 E. J. Garboczi, K. A. Snyder, and J. F. Douglas, "Geometrical percolation threshold of overlapping ellipsoids," Physical Review E **52** (1), 819-828 (1995).

30 D. S. McLachlan, C. Chiteme, W. D. Heiss, and Junjie Wu, "The correct modelling of the second order terms of the complexAC conductivity results for continuum percolation media, using a single phenomenological equation," Physica B **338**, 256-260 (2003).

31 Rajagopal Ramasubramaniam, Jian Chen, and Haiying Liu, "Homogeneous carbon nanotube-polymer composites for electrical applications," Applied Physics Letters **83** (14), 2928-2930 (2003).

Chapter 5 : Transparent, conductive and flexible films based on carbon nanotubes

5.1 Introduction

In the previous chapter it was shown that the conductivity of thick carbon nanotubes films depends strongly on two factors. First it was shown that in order to obtain high conductivities, the constituent nanotube bundles must have a low diameter and be arranged in as dense a network as possible. This decrease in bundle diameter and porosity leads to a high inter-tube junction density, the parameter governing the ability of charge carriers to move through the network. Secondly it was shown that, once morphological factors have been taken into account, the network conductivity increases with the ratio of the G-band to D-band as measured by Raman spectroscopy.

However, the thick films investigated in the previous chapter are of little interest for optoelectronic applications as they are not transparent and for the most part are too resistive for many applications. Using the knowledge gleaned from the previous work, this chapter presents a process for fabricating thin, transparent and conductive carbon nanotube films. Furthermore, it will be shown that the addition of nanotubes to a conducting polymer matrix improves the optical and electrical properties.

5.2 Transparent, conductive and flexible films of single wall carbon nanotubes[1]

5.2.1 Introduction

Even though some of the networks prepared in the previous chapter displayed high conductivities (Iljin Nanotechnologies, Carbon Nanotechnologies Inc.) they are unsuitable for display electrodes due to their large thickness. In order to utilise carbon nanotube networks as display electrodes they must be thin enough to transmit light while keeping a high DC conductivity. There are two issues requiring attention in order to fabricate very thin films. The first is to address the issue of nanotube aggregation. The thick films investigated previously were prepared from a large volume of nanotube dispersion, making extensive exfoliation difficult due to the long preparation time. Dispersions used to prepare very thin films on the other hand pose no such problem due to the small volume required to prepare a film (assuming the concentration is fixed). This in turn should cause an increase in junction density in the network and a decrease in porosity, both of which have been shown to scale with increasing DC conductivity.[2] The second issue is the transfer of these thin films to a suitable substrate for both electrical and optical characterisation. Although a process for such a feat has already been developed[3], it is prudent to perfect this process when being used in the lab.

This section addresses these issues as well as showing characterisation of the electrical, optical and mechanical properties of thin films made from arc-discharge Iljin SWNTs dispersed in a number of aqueous surfactant solutions.

5.2.2 Experimental Method

One of the major problems in utilising the impressive electrical and mechanical properties of carbon nanotubes is their tendency to aggregate into large bundles. There has been a lot of work done to debundle nanotubes using acids[4,5], macromolecules and surfactants[6-9] and organic solvents[10,11]. Once the nanotubes are deposited on a filter membrane, the membrane itself must be removed by dissolution in organic solvents[3] in order to transfer the film to a substrate for characterisation. Mixed cellulose ester filter membranes (MF-Millipore Membrane, mixed cellulose esters, Hydrophilic, 0.025 μm, 47 mm) were used as they are soluble in many solvents. This renders any solvent based dispersion useless as they would destroy the membrane during filtration and so this work was limited to using aqueous solutions of surfactants as a nanotube dispersant.

Aqueous solutions of surfactants were prepared at a concentration of 5 mg/ml by overnight stirring. These solutions were used to make stock dispersions of both Iljin arc-discharge SWNTs (Iljin Nanotechnology) and HiPCO SWNTs (Carbon Nanotechnology Inc.) such that the mass ratio was 5:1 (nanotube concentration 5 mg/ml). Each dispersion was subjected to 5 minutes of high-power tip sonication (Vibra Cell CVX; 750W, 20 % 60 kHz), then placed in a sonic bath (Model Ney Ultrasonic) for 1h, and then subjected to another 5 min of high power sonication. They were then allowed to rest over night before being centrifuged at 5500 rpm for 90 min. The supernatant was carefully decanted and saved. The post-centrifuge nanotube concentration was determined from absorbance measurements (Cary 6000i).

To be able to prepare films of controllable thickness a metric of some sort must be determined. If we assume that the porosity of nanotube films doesn't deviate with reduced thickness then we can control the thickness by simply controlling the mass deposited. The film thickness, t, was calculated from the deposited mass per unit area, M/A, using M/A =

ρt, where ρ is the film density. While the density is not known for these thin films, it was shown in the previous chapter that the vast majority of thick films made form a range of nanotube types had densities between 450 and 700 kg/m^3 (nanotube networks tend to be very porous). Thus the density is taken as 570 ± 150 kg/m^3 accepting this will result in a ~25 % error in the nominal thickness and any dependant quantities such as DC or optical conductivity. Initially, HiPCO SWNT films with a thickness of ~100nm and 200nm were prepared by diluting the stock dispersions down to concentrations ranging between 10^{-1} mg/ml and 10^{-3} mg/ml in order to determine the concentration that resulted in the highest conductivity. This dilution was accomplised by addition of surfactant stock solution and 1 minute tip sonication. Electrical testing of the films showed that although there was only a small variation, a maximum DC conductivity was found for films prepared from dispersions with $C_{NT} = 0.005$ mg/ml.

Transferring the films deposited from the cellulose ester membranes entails washing the film after filtration with Millipore water and then rolling the film onto a pre-heated (~90°C) Polyethylene terephthalate (PET) sheet. Pressure is then applied for a set amount of time before dissolving the membrane away using acetone and methanol.

Problems with the film lifting off the PET during processing were addressed by varying the pressure applied during drying (290 gcm^{-2} down to 2.9 gcm^{-2}) and the drying times (2hrs @ 90^{0}C on a hot plate, 6hrs Room T in vacuum). The conductivity of the HiPCO SWNT films increased with decreasing pressure, but this was countered by a low adhesion of the film to PET resulting in the film being destroyed during the dissolving process. A value of 175 gcm^{-2} was chosen as it gave slightly lower conductivities but better adhesion and hence a better chance of a fully transferred film. While different setting times and temperatures affected the conductivity slightly, an optimum level of conductivity and film stability was seen with the 2hrs at 90^{0}C on a hot plate.

The membranes were initially dissolved by simply placing the film in four sequential baths of acetone followed by a final wash of methanol and then drying in air. The turbulence of the liquid bath caused damage to the fragile films, resulting in the film lifting of the PET. An initial exposure to acetone vapour was used before using liquid baths. The exposure to acetone stiffened the membrane and allowed liquid baths to be used with little damage to the film. The effect of the level of removal of MCE from the film surface on the conductivity was investigated by varying the exposure time to the solvent, the volume of solvent and the number of baths used. The conductivities of the films were similar, allowing us the use four 15min exposures to 500ml acetone followed by 15mins exposure to 500ml methanol.

As films of arc-discharge Iljin SWNTs produced the highest network conductivities in the previous study they were used for the remainder of work presented in this section. Films with a thickness of ~50 nm were prepared using the optimised technique discussed above with dispersions of aqeuous solutions of sodium dodecyl sulphate (SDS), sodium dodecylbenzene sulfonate (SDBS), lithium dodecyl sulphate (LDS),Sodium Cholate (SC) and Triton® X-100. We found the conductivities of these films to be (2.3×10^5, 2.1×10^5, 2.2×10^5, 1.9×10^5, 3.8×10^4 Sm^{-1}) respectively. We suggest that the deviation of the Triton results is due to lower dispersion quality and hence a poorer quality film. Due to their popularity, we chose to focus on SDBS and SDS for the remainder of this work.

A range of films were then fabricated with thicknesses ranging between 10 – 100 nm. Transmission scans were made using an Epson Perfection V700 photo flat-bed transmission scanner with a bit depth of 48 bits per pixel and a spatial resolution of 6400 dpi. The numerical output of the scanner was calibrated by scanning a range of neutral density filters. The resultant calibration curve was used to transform the output to represent transmittance. This results in a transmittance map with a transmittance value for every

pixel. Transmission maps were transformed into absorbance maps by applying $A = -\log T$ to each pixel. The mean and standard deviations of the transmittance or absorbance were calculated from the entire data set (i.e., from the entire set of pixel values). Scanning electron microscopy measurements were made using a Hitachi S-4300 field emission scanning electron microscope. Charging was avoided by transferring the nanotube film from cellulose membrane to a glass substrate coated with a thin gold/palladium film. Atomic force microscope images were obtained using a Dimension V AFM.[a] In order to extract the topography and conductance data simultaneously, the microscope was operated in the conductance imaging mode (C-AFM).[a] In this technique, the AFM tip acts like a mobile probe on the surface and is held at ground potential and a DC bias is applied to the sample. The *z* feedback signal is used to generate a normal contact mode AFM topographic profile, and the current passing between the tip and the sample is measured using a pre-amplifier to generate the conductance image. A bias voltage of 0.2 mV up to 1 V is applied to the electrode on the surface that drives current through the wires. A current range of 2 pA to1 μA can be detected by the pre-amplifier in the C-AFM module. For this purpose, a Cr/Pt-coated conductive tip with a force constant of 3 N/m and a resonant frequency of 75 kHz was employed. In all cases, the loading force employed during measurement was approximately 15 nN. (The tips were purchased from Budget Sensors, ElectriMulti 75.) Optical transmission spectra were recorded using a Cary Varian 6000i, with a sheet of PET used as the reference. Sheet resistance measurements were made using the four-probe technique with silver paste electrodes of dimensions and spacings typically of ~ millimetre in size and a Keithley 2400 sourcemeter. Electromechanical measurements were made using a Zwick Z0.5 Proline tensile tester.[c1] The AgNW film on PET was bent into a semi circle, which was constrained by the grips of the tensile tester. The film was connected via

[a] The AFM and C-AFM measurements were performed by Dr. Peter Nirmalraj of the School of Chemistry, Trinity College Dublin.

[b] The electromechanical measurements were performed by Evelyn Doherty of the School of Chemistry, Trinity College Dublin and Jerome Joimel of Hewlett Packard DIMO, Liffey Park Technology Campus, Barnhall Road, Leixlip, Co Kildare, Ireland.

two electrodes (attached to the grips) to a Keithley KE 2601. The bend radius was then defined by the distance between the grips. The inter-grip distance was then oscillated typically between 15 and 5 mm over many cycles. LabVIEW software recorded film resistance, inter-grip distance, and cycle number.

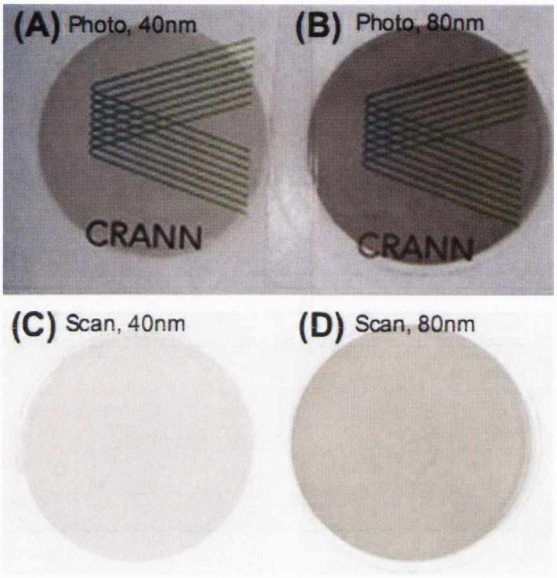

Figure 5.1 *Photographs of 40 and 80 nm thick Iljin SWNT films (SDS) respectively. (C) and (D) Optical white-Light transmission scans of the films pictured in (A) and (B).*

5.2.3 Results and discussion

Shown in Figure 5.1 A and B are photographs of films of Iljin SWNT (SDS) with thicknesses of 40 and 80 nm respectively. To investigate the optical quality of the films transmission scans of the same films (Figure 5.1 C and D) were made. These scans are effectively white light transmission maps of the films. Scans were performed with a spatial resolution of 4 μm (6400 dpi). The spatially averaged white light transmittances were 75% and 61% for the 40nm and 80nm films respectively. The uniformity of these films is given by the standard deviation of the transmittance, calculated over the entire film area, which were 0.9% and 1.1% for the 40nm and 80nm film respectively. The ratios of standard

deviation transmission to mean transmission for these films were 1.2% and 1.8% respectively. The low value of this quantity indicates the very high quality and optical uniformity of these films.

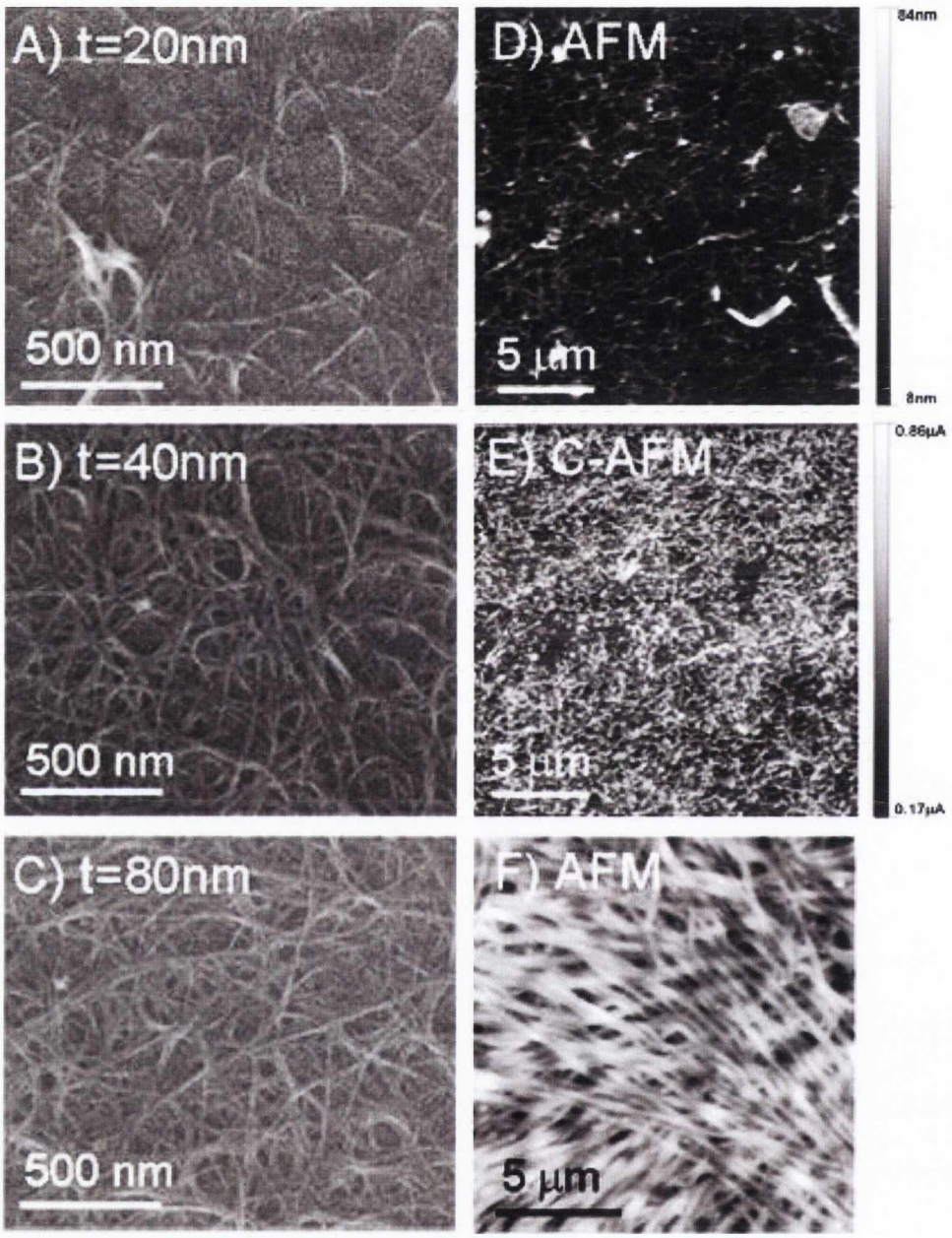

Figure 5.2 *(A–C) SEM images of selected nanotube films of various average film thickness. (D) An AFM image of the surface of a 10 nm thick Iljin/SDS film. (E) A conducting-AFM image of the same region pictured in (D). (F) An AFM image of analigned region of a 50 nm thick Iljin/SDS film.*

In order to characterise the film morphology, SEM micrographs of nanotube films with different thicknesses were recorded. This is important as nanotube film conductivities scale with bundle diameter and film density. Representative images for the SDS based films are shown in Figure 5.2 A–C for films of 20, 40 and 80 nm thickness. Such images are typical of SWNT networks and show a porous network. For all thicknesses, the mean bundle diameter was invariant at ~12 nm. In addition it appears as if the 20 nm thick film is less uniform than the thicker films, a point that will be discussed below.

The film morphology was further characterized by AFM and C-AFM. Shown in Figure 5.2 D is an AFM image of the surface of a 10 nm thick film of Iljin SWNTs prepared from SDS. It should be emphasised that this is an average thickness, calculated from a deposited mass per unit area of 5.5mg/m^2. As shall be seen below, considerable variations in local thickness are observed in this low thickness regime. In any case, a network similar to that in Figure 5.2 A can clearly be seen. Shown in Figure 5.2 E is a C-AFM current map of the area of the Iljin film shown in Figure 5.2 D. The current map of the Iljin film is similar to the topographical map in Figure 5.2 D showing a network of SWNT bundles from which current can flow out of the plane of the film. This is important as it shows that current can be gathered uniformly from all areas of the surface of these films. This is a critical property for any material with potential for use as an electrode. Interestingly, domains of aligned nanotube bundles (Figure 5.2 F) are sometimes seen. The formation of these regions may reflect the presence of a nematic phase of bundles in the dispersion.

For both SDS and SDBS films, the transmission spectra (Figure 5.3) were relatively featureless, displaying a slight dip around 700 nm which is associated with the presence of S22 optical transitions. Sharp transitions associated with van Hove singularities were not observed, probably due to broadening associated with nanotube aggregation[12]. In all cases

the transmittance decreased with increasing thickness, while the spectral profile remained invariant.

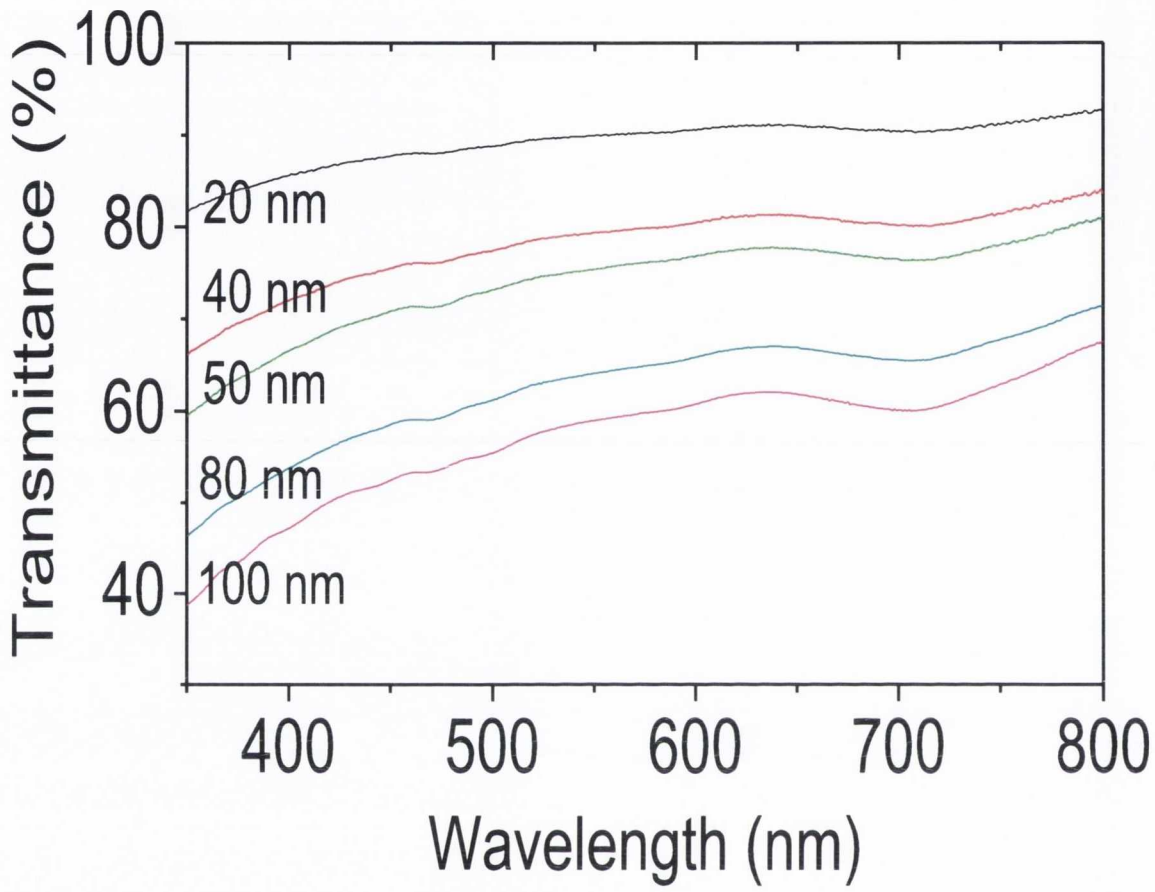

Figure 5.3 *Transmission spectra for Iljin SWNT films (SDS) of thicknesses between 20 nm and 100 nm.*

Shown in Figure 5.4 A is the transmittance, T, (λ = 550nm) as a function of film thickness, t. For both film types, T falls from ~ 95% for 10 nm thick films to ~ 60% for 100 nm thick films, with all data falling on the same line. By modelling the interaction of thin conducting films ($t << \lambda$) with light, the transmittance is related to the film thickness, t, by Equation 2.67 and has been fitted to the data in Figure 5.4 A as shown by the dotted line. This curve fits both data sets well giving σ_{Op} =1.7 ± 0.4 x 10^4 Sm^{-1} (λ = 550 nm), reasonably close to previously measured values of ~1.5 x 10^4 Sm^{-1} for thin films of both

Iljin SWNTs[13] and laser produced SWNT.[14] This agreement shows that our thickness calculation is reasonably accurate.

The measured sheet resistance for both surfactant types is shown in Figure 5.4 B as a function of film thickness, varying from ~3 kΩ/□ for t=10nm to 50-70 Ω/□ for t=100nm. It is immediately clear that the SDS based films are slightly less resistive than the SDBS based films. As shown by the dotted lines, both data sets scale well as $R_s = 1/\sigma_{DC}t$ for t>40 nm, suggesting the film morphology becomes thickness-invariant above this thickness.

The DC conductivity is shown in Figure 5.4 as a function of thickness. In line with the sheet resistance data, the conductivity is reasonably constant at higher values, but falls off below t=40 nm. The thicker films have conductivities (t>40 nm) of $\sigma_{DC} \approx 1.9 \pm 0.5 \times 10^5$ Sm^{-1} and $\sigma_{DC} \approx 2.3 \pm 0.5 \times 10^5$ Sm^{-1} for SDBS and SDS based films respectively. These conductivities are exceptionally high. The state-of-the-art for thin (un-doped) nanotube films is $\sigma_{DC} \approx 1.5 \times 10^5 Sm^{-1}$ which was measured for spray cast networks of Iljin SWNTs.[13] It is speculate that the high conductivity of these films is due to the length of these Iljin SWNTs.

AFM measurements were performed on sparse deposited networks. This allowed the measurement of bundle lengths. The lengths were measure to be between 1 and 10 μm with a mean and standard deviation of 3.5 μm and 2 μm respectively. For comparison purposes, the same measurements were carried out for sparse networks of HiPCO SWNTs prepared under similar conditions, measuring a mean and standard deviation of 0.8 μm and 0.4 μm respectively. As the conductivity of the nanotube films is expected to scale with bundle length,[15] L, as $\sigma \propto L^{1.7}$, the length of these tubes are believed to be an important factor contributing to the high conductivity of these films.

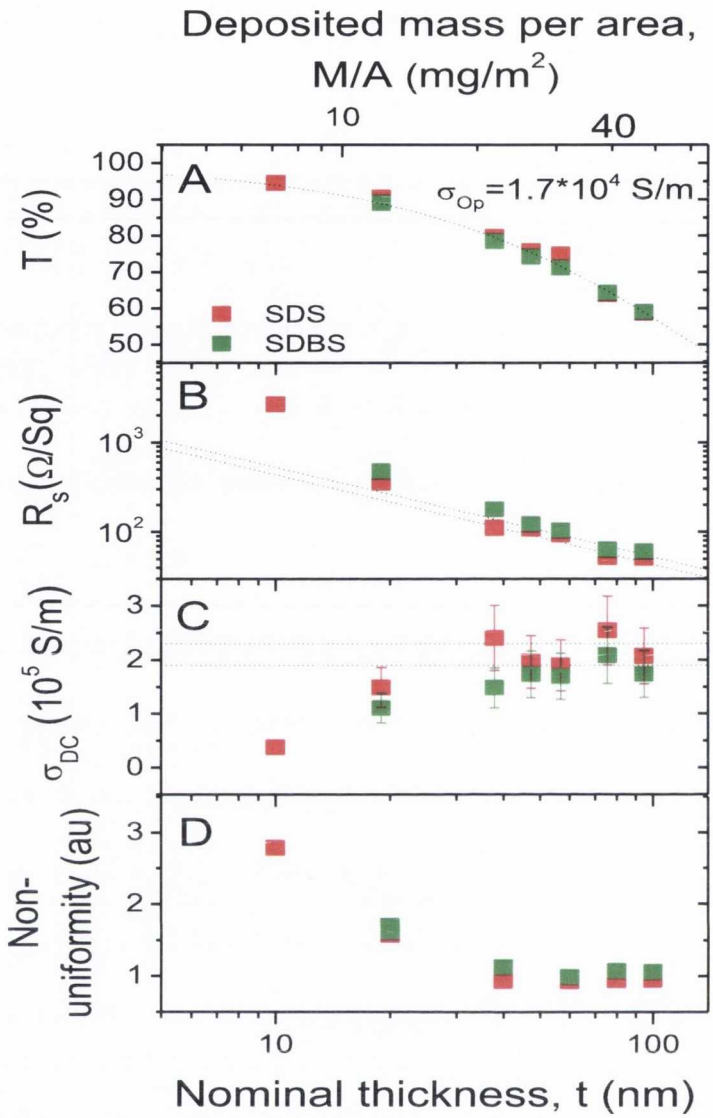

Figure 5.4 *Properties of nanotube films as a function of film thickness, t, for both SDS and SDBS films. A) Optical transmittance, measured at 550 nm. The dotted line is a fit to Equation 2.67, consistent with an optical conductivity of* 1.7×10^4 Sm^{-1}. *B) Sheet resistance. The dotted lines are fits to* $R_s = 1/(\sigma_{DC}t)$, *where* σ_{DC} *is the DC conductivity. The upper and lower curves are consistent with DC conductivities of* 1.9×10^5 Sm^{-1} *and* 2.3×10^5 Sm^{-1} *respectively. C) DC conductivity, calculated from* $R_s = 1/(\sigma_{DC}t)$. *The upper and lower dotted lines illustrate DC conductivities of* 2.3×10^5 Sm^{-1} *and* 1.9×10^5 Sm^{-1} *respectively. D) Film non-uniformity as defined by the standard deviation of local absorbance measured with a spatial resolution of 4* μm *(scan area 2mm×2mm).*

A number of recent papers have found a fall-off in conductivity at low thickness, similar to that observed here[16]. In very thin films, this can be attributed to percolation effects[17]. It is proposed that a network above the percolation threshold can be characterised by non-uniformities in a real nanotube density when measured on length scales similar to the mean nanotube length. This effect can be explored in more detail by measuring the local non-uniformity of the films as a function of thickness. This is done by recording transmission scans (pixel size 4 μm) of a number of the films discussed above. The resulting transmission maps is transformed into absorbance (A) maps using $A = -\log T$. According to the Beer-Lambert law, the absorbance is proportional to the number of absorbing objects per unit area. This means the absorbance map is a measure of the spatial distribution of nanotubes per 4 μm pixel.

The non-uniformity is defined here as the standard deviation of absorbance as measured over a 2 mm x 2 mm grid (500 x 500 pixels). A large degree of non-uniformity is associated with a high standard deviation. The data for non-uniformity versus sample thickness is plotted in Figure 5.4 D. It is clear from this data that the non-uniformity is constant for thicker films but increases sharply for films thinner than 40 nm. This increase in non-uniformity correlates almost exactly with the thickness below which the conductivity falls off. Thus, a percolated network becoming bulk-like can be observed by measuring the point when the uniformity becomes invariant with thickness.

The uniformity of these nanotubes films was investigated using spatially resolved transmission/absorbance measurements. However, it is noted that these results apply only to the type of films studied in this work i.e .those produced by vacuum filtration. A number of different techniques have been successfully demonstrated to produce nanotube films, spin coating, dip coating etc. It is likely that each of these techniques results in different degrees of uniformity.

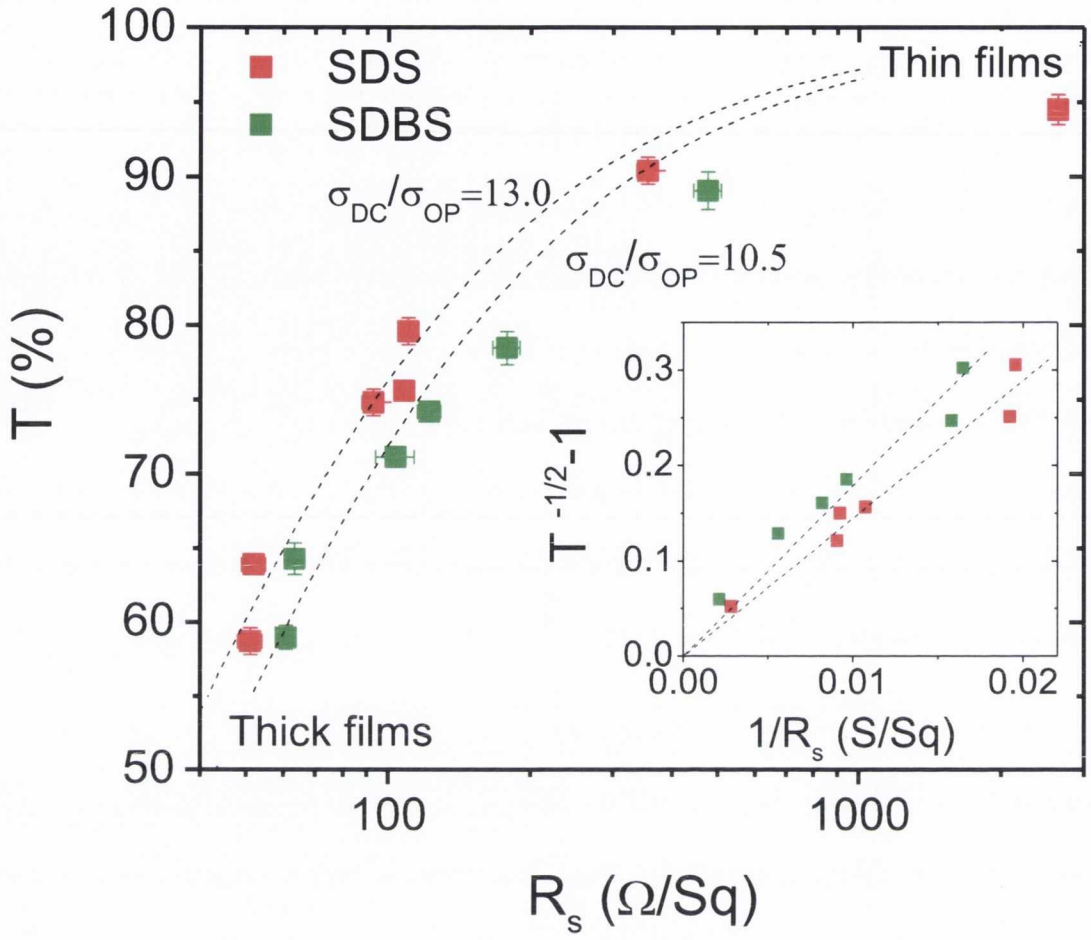

Figure 5.5 *Transparency as a function of sheet resistance for both SDS and SDBS films. The dotted lines are fits to Equation 2.68, consistent with σ_{DC}/σ_{Op} values of 13.0 and 10.5 for SDS and SDBS based films respectively. Inset: Transparency-sheet resistance data plotted to highlight the applicability of Equation 2.68.*

Shown in Figure 5.5 is the transmittance (λ =550 nm) plotted as a function of sheet resistance for both SDS and SDBS based films. Equation 2.68. has been fitted to the data for both film types as shown by the dashed lines. In the inset the data is re-plotted such that data following Equation 2.68 should follow a straight line, with the data showing good linearity. The fits give values of the conductivity ratio to be σ_{DC}/σ_{Op} = 13.0 and σ_{DC}/σ_{Op} =

10.5, reasonably consistent with the values for σ_{DC} and σ_{Op} calculated previously. These conductivity ratios are quite high. To my knowledge, the state-of-the-art T, R_s data for as-prepared nanotube films, such as those presented here, results in σ_{DC}/σ_{Op} =13–16.[18] The best results for as-prepared films produced from commercially available nanotubes have been for films of Iljin SWNTs, giving σ_{DC}/σ_{Op} = 10.1.[13] Thus the SDS data presented here is slightly ahead of the state-of-the-art for as-prepared films of commercially available SWNTs.

However, as mentioned above, industry requires $R_s \leq 100\ \Omega/\square$ coupled with $T \geq 90$ % (λ= 550 nm) for a material to qualify as an ITO replacement.[19] Using Equation 2.68, this means $\sigma_{DC}/\sigma_{Op} \geq 35$. As σ_{Op} is more or less fixed in these films, this means σ_{DC} must be increased by a factor of x2 – 2.5 to ~ 5 x 10^5 Sm^{-1} to meet industry requirements. The state-of-the-art as-prepared samples described above were improved by x2.5 by acid post-treatment, resulting in σ_{DC}/σ_{Op} = 26. However, this technique is problematic if the nanotube films are to be used as electrodes in OLEDs or organic solar cells, as the presence of small mobile counter-ions may poison the active layer. It would be favourable to develop a nonchemical method to increase σ_{DC}/σ_{Op}. There are two possibilities. The first is to prepare high volume fraction polymer-nanotube composite films using conducting polymer matrices. Such materials have recently been demonstrated, showing reduced σ_{Op} resulting in increased σ_{DC}/σ_{Op}.[20] Secondly, exfoliation of the nanotubes followed by film formation in such a way as to frustrate nanotube re-aggregation would result in films with smaller bundles. It has recently been suggested that the conductivity scales as $D^{-3.2}$. Thus, a decrease in bundle diameter by only a factor of x0.7 to ~15 nm would be enough to increase σ_{DC}/σ_{Op} by x2.8.

As mentioned above, these films have optical and electrical properties close to what is required to replace ITO. However, they are potentially even more useful as a flexible,

transparent, electrode material. Such a material is of considerable interest as an electrode in applications such as e-paper.[21] To test this, Iljin SWNT films on PET, made from SDS and SDBS at a number of thicknesses were prepared. In addition, a 60 nm thick ITO film was prepared for comparison. In each case the sheet resistance was monitored during bending with the nanotube film both in tension and in compression. The films were bent from an initial radius of curvature of 7.5 mm to a final radius of 2.5 mm before being relaxed. Shown in Figure 5.6 A is the sheet resistance versus radius of curvature during both the bending and release phase (note that the magnitude of the average strain felt by the film is plotted in the top axis[22]). As expected,[23,24] ITO fails catastrophically on tensile bending, with the sheet resistance increasing irreversibly by almost two orders of magnitude. In comparison, the sheet resistance of the SDS-based Iljin films (Figure 5.6 B–E) vary by < 1 % during both bend and release phases for films both in tension and compression. In contrast, while the SDBS film was very stable in tension, its sheet resistance varied significantly while bending in compression.

While these nanotube films are clearly relatively stable during one bend cycle, it is important to ascertain their stability over many bend cycles. Shown in Figure 5.6 F–J is the mean sheet resistance per cycle plotted versus cycle number for the same films examined in Figure 5.6 A–E. In Figure 5.6 F, cyclic test data for an ITO/PET film is shown. In this case to avoid immediate failure, the film was tested at much lower curvature with minimum bend radius on each cycle of only 20 mm. The sheet resistance of this film increased by a factor of x8 before failing around cycle 150. In contrast, the sheet resistance of the SDS-Iljin films fell by <5 % in compression and <2 % in tension over ~2000 cycles. The SDBS-Iljin films were similarly stable in tension but underwent a decrease in R_s of ~8 % when cycled in compression. Note that none of these nanotube films failed during these measurements. The number of cycles was limited by time constraints.

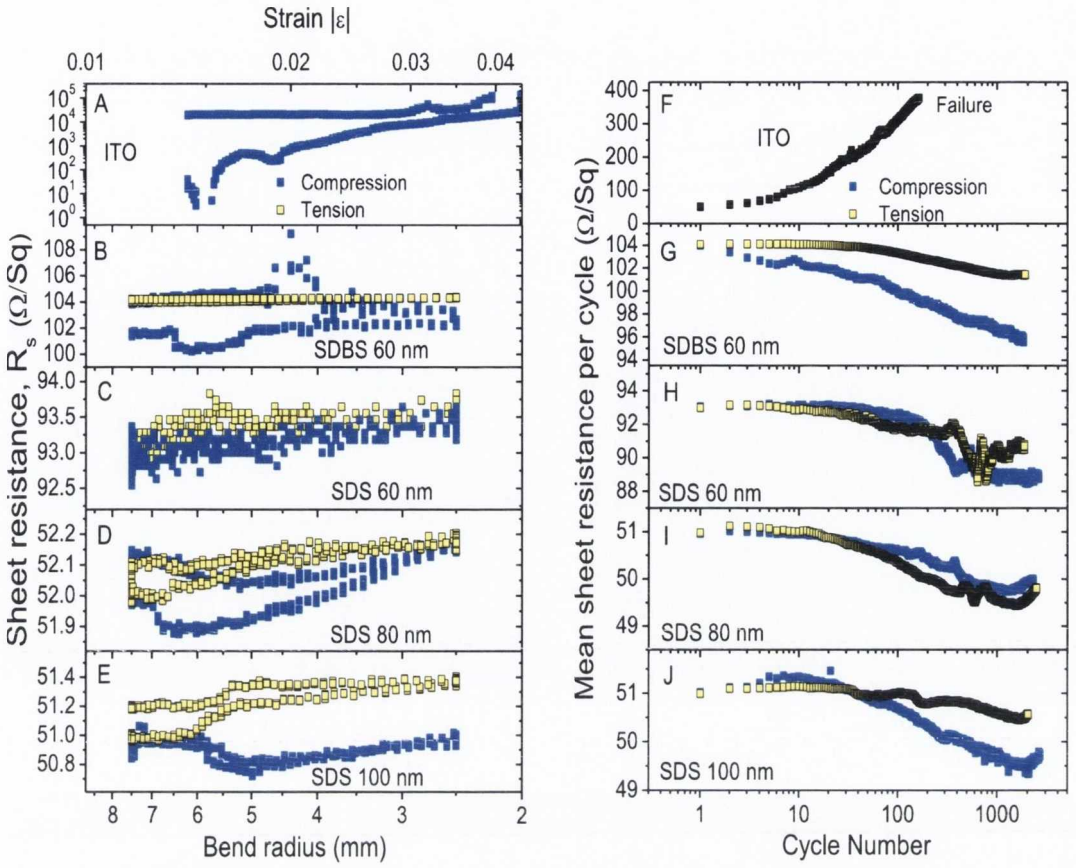

Figure 5.6 *Data showing the electromechanical stability of nanotube films. A-E) Sheet resistance of films of ITO and nanotubes (prepared from SDBS and SDS of different thicknesses) during a bend cycle where the bend radius is reduced from 7.5 mm to 2.5 mm before relaxing back to 7.5 mm. Shown on the top axis is the strain associated with these bend radii. The ITO sample was measured in compression only, while the nanotube samples were measured both in tension and compression. Note that ITO fails completely under these conditions with R_s remaining at ~3×10^4 Ω/□ when the sample was released (upper portion of curve). In contrast, the sheet resistance of the nanotube films vary by no more than 5%. F-J) Average sheet resistance per cycle for films identical to those in A-E) as a function of cycle number. For the nanotube films, each cycle was a bend-relaxation cycle as described above. However, to avoid failure on the first cycle, the ITO film was only bent to a radius of 20 mm. Note that while the ITO film failed after 160 cycles, the nanotube films were not observed to fail. Rather, the number of cycles was limited by time constraints.*

5.2.4 Conclusions

Thin, flexible nanotube films with DC conductivity surpassing the state of the art were prepared. Initial tests have shown that dispersing the nanotubes with the surfactant sodium dodecyl sulphate gives the most conductive films. It was found that the optical transmittance of SDS-prepared films scales with thickness as expected for a thin metallic film. Data analysis gives a value for the optical conductivity (λ=550 nm) of 1.7 x 10^4 Sm^{-1}, similar to previous measurements. For thicknesses above 40 nm, the in-plane conductivity is constant at ~2 x 10^5 Sm^{-1}. However, below 40 nm, the conductivity falls off rapidly. This behaviour correlates with measurements of the film non-uniformity which show films with t <40 nm to be significantly less uniform. Conductive AFM measurements show the current flow out of the film to be very uniform on length scales greater than ~2 μm. For films with t >40 nm the ratio of DC to optical conductivity was σ_{DC}/σ_{Op} = 13.0, leading to values of transmittance and sheet resistance such as T = 80 % and R_s =110 Ω/□ for the t = 40 nm film. The electromechanical stability of our films was characterised by monitoring the sheet resistance during bending. Sheet resistance was monitored during one bend-release cycle as a function of strain for films bent both in tension and in compression. In addition, the average resistance per cycle was monitored over many bend cycles. It was found that the resistance change was very small over the first cycle and typically <5 % and <2 % over >2000 cycles for films bent in compression and tension respectively. These results show that, pending a factor of x3 increase in conductivity, these materials may be suitable for use as an ITO replacement material.

5.3 Improving network conductivity by addition of a conducting polymer[20]

5.3.1 Introduction

To achieve a conductivity ratio $\sigma_{DC}/\sigma_{Op} \geq 35$ a DC conductivity of $\sigma_{DC} \sim 5.3 \times 10^5$ S/m is required. However, while nanotube films have displayed σ_{DC}/σ_{Op} ratios of up to 13 for as-prepared films[13] and up to 25 for acid-treated films[13], there is still a lot of work to be done in order to create a viable replacement for ITO. While acid-treated films have conductivity ratios approaching the target, these films may be unsuitable for organic light emitting diode (OLED) applications as the presence of residual mobile counter ions can poison the emissive layer. In addition, nanotube films tend to be relatively porous[2] and have significant surface roughenss[13], properties that can be detrimental to certain electrode applications. In many ways, it would be preferable to have a polymer-nanotube composite film as the electrode. However, such composites have traditionally had low conductivities,[25] typically < 10 S/m,[25] and so a low σ_{DC}/σ_{Op} ratio. Recently a number of papers have appeared which have broken this paradigm. This has happened in two ways. Blighe *et al.* demonstrated a filtration-based method to prepare very high volume fraction polymer-nanotube composite films.[26] Even while using an insulating matrix (polystyrene), these films demonstrated conductivities up to 10^4 Sm^{-1}. The other method has been to use conducting polymers as matrices.[27] While these composites prepared with small-ion-doped conducting polymers are unsuitable for use in applications such as OLEDs due to mobile counter ions, composites prepared from conducting polymers doped with large immobile counter-ions pose no such problem. Such a polymer is poly(3,4-ethylenedioxythiophene) doped with poly(styrenesulfonate) (PEDOT:PSS). Here the PEDOT chains are positively

charged, while the PSS chains are negatively charged. Recently[28-31] PEDOT has been combined with carbon nanotubes to produce composites with conductivities of up to ~ 7 x 10^4 S/m.[32] Such films displayed σ_{DC}/σ_{Op} ~ 9, which is impressive but could be improved upon. In this section, two previous approaches to prepare high volume fraction composites will be combined to prepare high volume fraction composites from SWNTs blended with PEDOT:PSS.

5.3.2 Experimental procedure

HiPCO SWNTs were purchased from Unidym (www.Unidym.com/), while Iljin arc discharge SWNTs were purchased from Iljin Nanotech Co., Ltd. (www.iljinnanotech.co.kr/). PEDOT:PSS was purchased from HC Stark under the tradename Baytron PH500 (www.hcstark.com). The PEDOT:PSS used in this work was purchased as a suspension of polymer nanoparticles, each a few tens of nanometers in diameter. Stock SWNT dispersion were prepared using the technique outlined earlier in this chapter. Briefly, an aqueous solution of sodium dodecyl sulphate was used to disperse SWNTs using high power sonication. Centrifugation was performed and the supernatant kept. Absorption spectroscopy was used to determine the concentration of the SWNT dispersion.

Nanotube-PEDOT:PSS composite dispersions were subsequently prepared by mixing the required volume of nanotube stock solution and PEDOT:PSS dispersion, keeping the partial nanotube concentration in the composite dispersion at 0.005 mg/mL. Note that no secondary dopant was added to the PEDOT:PSS. This composite dispersion was then subjected to 1 minute high-power sonication. The composite films were prepared by vacuum filtration using porous cellulose filter membranes (MF-Milliporemembrane, mixed cellulose esters, hydrophilic, 0.025 μm, 47 mm diameter). The films thicknesses

were controlled by the volume of dispersion filtered and hence the deposited nanotube mass. The deposited films were washed with 200 mL of Millipore water followed by a wet transfer (see previous section) to a polyethyleneterephthalate (PET) substrate using heat and pressure. The cellulose filter membranes were then removed by treatment with acetone vapour and subsequent acetone liquid baths followed by a methanol bath. The diameter of the films was 36 mm. The film thickness, t, was calculated from the deposited mass per unit area, M/A, using $M/A = \rho t$, where ρ is the film density. The film densities were estimated to be 600 – 900 kg/m^3 for mass fractions from 0.8 to 0.2. These values are estimated by calculating the weighted average values of the densities of porous nanotube films (~450 kg/m^3)[2] and PEDOT:PSS (~1000 kg/m^3). The thickness was estimated to be correct to within 10 %. This means that the DC and optical conductivities carry an error of 10 %. Transmission scans were made using an Epson Perfection V700 photo flat-bed transmission scanner. Scanning electron microscopy measurements were made using a Hitachi S-4300 field emission scanning electron microscope. Atomic force microscope images were obtained using a Veeco Nanoman AFM system. In order to extract the topography and conductance data simultaneously, the microscope was operated in the conductance imaging mode (C-AFM). In this technique, the AFM tip acts like a mobile probe on the surface and is held at ground potential, and a DC bias is applied to the sample. The z feedback signal is used to generate a normal contact mode AFM topographic profile, and the current passing between the tip and the sample is measured using a preamplifier to generate the conductance image. A bias voltage of 0.2 mV up to 1 V is applied to the electrode on the surface that drives current through the tubes. A current range of 2 pA to 1 μA can be detected by the preamplifier in the C-AFM module. For this purpose, a Cr/Pt coated conductive tip with a force constant of 3 N/m and a resonant frequency of 75 kHz was employed. In all cases, the loading force employed during measurement was approximately 15 nN. (The tips were purchased from Budget Sensors, ElectriMulti 75.)

Optical transmission spectra were recorded using a Varian Cary 6000i. In all cases, a sheet of PET was used as the reference. Sheet resistance measurements were made using the four-probe technique with silver electrodes of dimensions and spacings typically of ~ millimetres in size and a Keithley 2400 source meter. Electromechanical measurements were made using a Zwick Z0.5 Proline tensile tester. The composite films on PET were bent in to a semicircle, which was constrained by the grips of the tensile tester. The film was connected via two electrodes (attached to the grips) to a Keithley KE 2601. The bend radius was then defined by the distance between the grips. The inter-grip distance was then oscillated between typically 15 and 5mm over many cycles. LabVIEW software recorded film resistance, inter-grip distance, and cyclenumber.

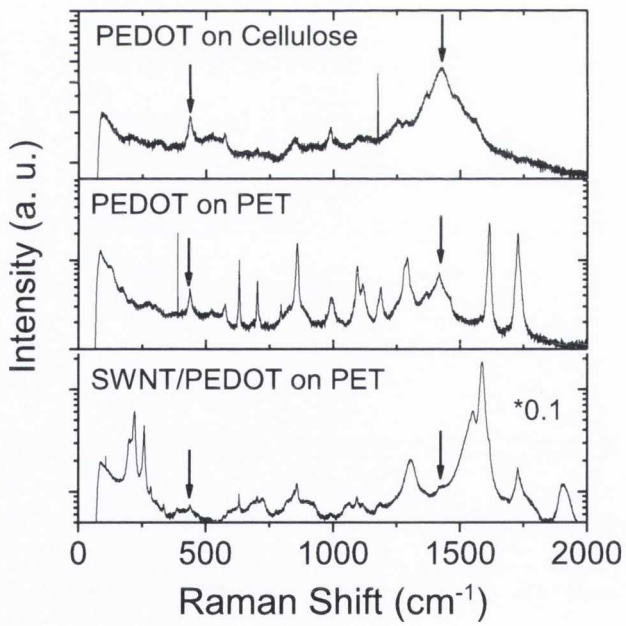

Figure 5.7 *Raman spectra of (top) a PEDOT:PSS film prepared by vacuum filtration on a cellulose filter, (middle) the same film after transfer to PET , and (bottom) an Iljin/PEDOT:PSS film prepared on a cellulose filter after transfer to PET.*

5.3.3 Results and Discussion

Composite films were prepared by vacuum filtration from aqueous dispersions with PEDOT:PSS as the matrix and both Iljin and HiPCO SWNTs as the filler. For both filler types, films containing a range of mass fractions from 20 to 100 % (nanotube only) were fabricated at a fixed nominal thickness, t = 50 nm. In addition, for a fixed mass fraction (55 wt% for HIPCO, 60 wt% for Iljin), films were prepared with a range of thicknesses. It is important to verify that the polymer nanoparticles are not lost through the filter but remain to form part of the composite film. To check this, we prepared PEDOT:PSS films on cellulose membrane filters before transferring to PET substrates. These films were electrically conductive, confirming the presence of PEDOT:PSS. In addition, Raman spectra (λ_{ex} = 633 nm) collected both on the filter and on PET showed the presence of PEDOT:PSS through its characteristic bands at 440 and 1420 cm^{-1} [33](see Figure 5.7, top and middle, arrows indicate the peaks). In addition, Raman spectra measured on Iljin / PEDOT:PSS composite films also showed the presence of these PEDOT:PSS bands. (NB these bands appear weak in the composite film due the relatively high intensity of the nanotube bands). Thus, it is believed that the polymer is retained on the filter to form composite films.

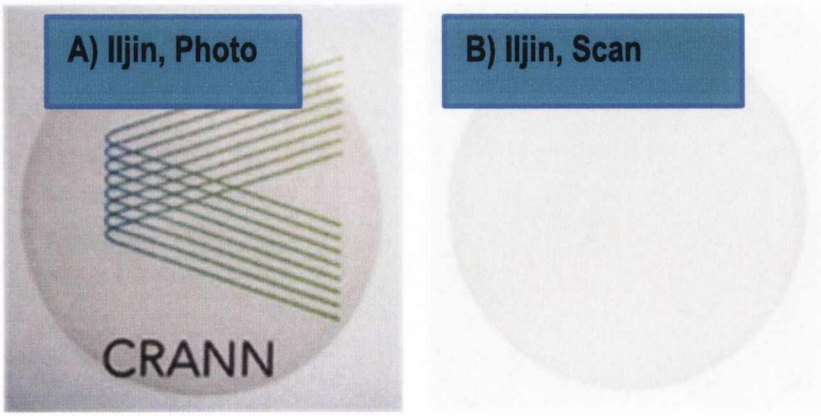

Figure 5.8 *A) Photo of a t = 60 nm, 60 wt% Iljin composite film. B) Transmission scan (150dpi) of the same film as A.*

A photograph of a typical composite film (60 wt% Iljin, thickness t = 60nm) is shown in Figure 5.8 A. The high film quality is immediately apparent. To explore this in more detail, transmission scans of the same film were made (Figure 5.8 B). This scan is effectively a white light transmission map of the film with a resolution of 160 μm (150 dpi). The spatially averaged white-light transmittance was 81 % for this film. The uniformity of the film is given by the standard deviation of the transmittance, calculated over the entire film area, which was 0.8 %. The ratio of standard deviation transmission to mean transmission was 1 %. The low value of this quantity indicates the very high quality and optical uniformity of these composite films.

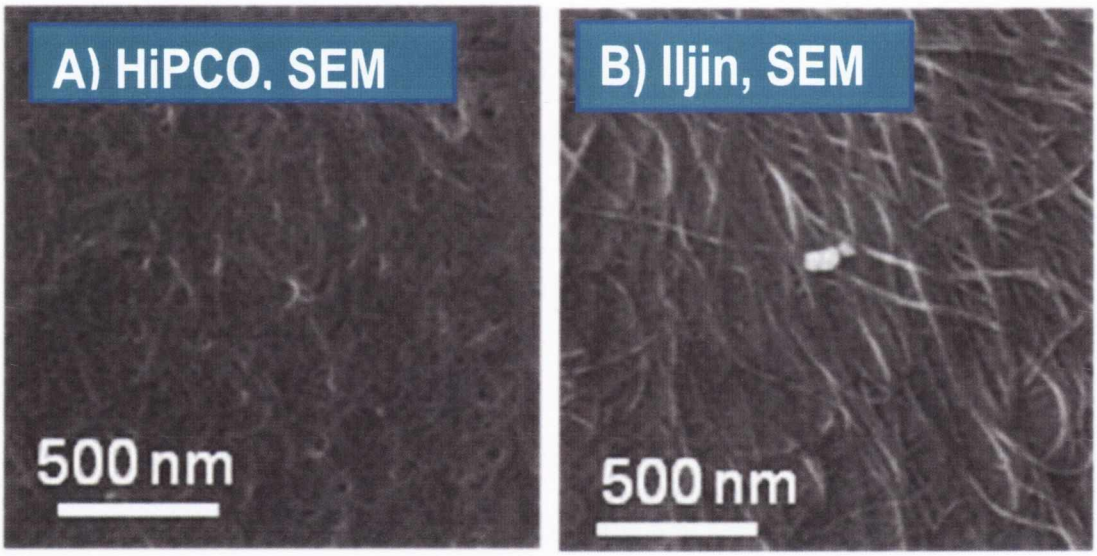

Figure 5.9 *SEM images of nominally 50nm thick SWNT/PEDOT:PSS composite films prepared using (A) HiPCO nanotubes (M_f = 55%) and (B) Iljin nanotubes (M_f = 60 %).*

Shown in Figure 5.9 A-B are representative SEM images of the surface of both HiPCO (M_f = 55 %, t = 50 nm) and Iljin (M_f = 60 %, t = 50 nm) based composites. For the HiPCO case, the network is hardly visible, appearing obscured by a polymer coating which

fills much of the networks free volume. For the Iljin composites, the polymer coating appears to be limited to a cylindrical shell surrounding the Iljin nanotubes. This disparity in coating may indicate differences between the surface energies of Iljin and HiPCO SWNTs or may simply be a reflection of differences in pore structure and / or size for the two film types. Nevertheless, both films have some free volume, making the surface of these films rough on the scale of tens of nanometers.

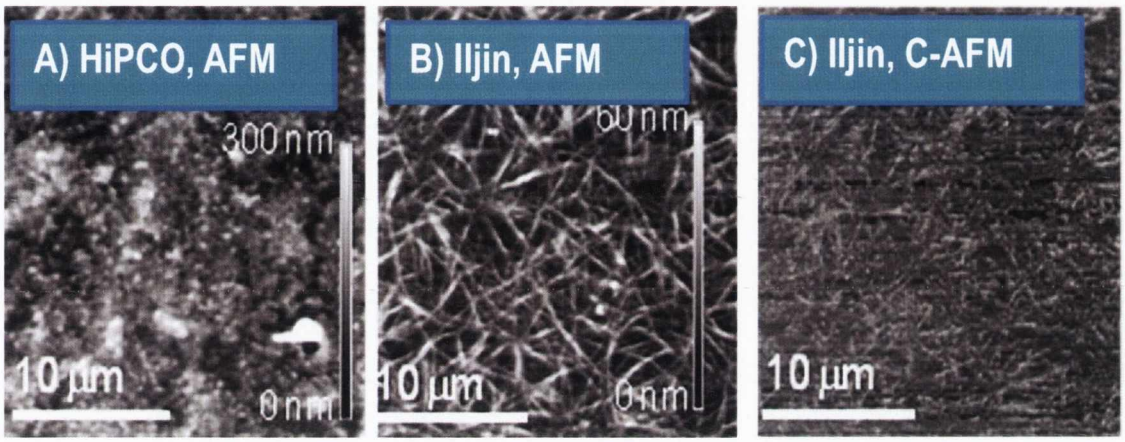

Figure 5.10 *AFM images of nominally 50 nm thick (A) HiPCO/PEDOT:PSS and (B) Iljin/PEDOT:PSS composite films. (C) Conductive AFM image of the same Iljin film area as B.*

Shown in Figure 5.10 A is an AFM image of the surface of the HiPCO composite film shown in Figure 5.9 A. The network is not resolved in this image due to the polymer coating. Note that considerable surface roughness can be seen in this image. For the Iljin composite, AFM images show a network of straight, well defined bundles (Figure 5.10 B). This network is considerably less rough than the HiPCO composite discussed above. Shown in Figure 5.10 C is a conductive AFM current map of the area of the Iljin composite shown in Figure 5.10 B. The current map of the Iljin film is very similar to the topographical map in Figure 5.10 B showing well defined polymer coated SWNT bundles

which act as current paths out of the plane of the film. This is important as it shows that current can be gathered uniformly from all areas of the surface of these films, a critical property for any material with potential for use as an electrode. Surprisingly, it was impossible to detect a C-AFM signal from the HiPCO based composites, perhaps due to the thick polymer coating.

These films were also characterised for both their electrical and optical transmission properties. For comparison, initially a 50nm thick film of PEDOT:PSS was characterised. This displayed optical transmittance (λ = 550 nm) of 93% and sheet resistance of 3.7MΩ/□, equivalent to a DC conductivity of 5S/m. This is in line with what we expect for PEDOT:PSS without secondary doping.[34] For the composite films, optical transmittance versus wavelength spectra were flat and reasonably featureless for both composite types (similar to previously published spectra[28], see Figure 5.3. In general, as the nanotube mass fraction increased, the transmittance decreased while the spectral shape remained unchanged. The transmittance at λ = 550 nm is shown plotted as a function of mass fraction in Figure 5.11 A for both composite types. In both cases, the data are similar, falling from 90 – 95 % for the 10 wt% sample to ~75 % for the 100 wt% sample. The sheet resistance, as measured on the same films, is shown in Figure 5.11 B In both cases, the sheet resistance falls slightly with increasing mass fraction. However, the Iljin composites are less resistive, falling to R_s ~140Ω/□ compared to a minimum value of ~ 450Ω/□ for the HiPCO composites. The nominal DC conductivity, σ_{DC}, as a function of nanotube mass fraction is shown in Figure 5.11 C and emphasises the higher conductivity associated with the Iljin composites, which reach a maximum value of 1.4 x 10^5 S/m compared to a maximum value of 4 x 10^4 S/m for the HiPCO composites. In both cases, the maximumin DC conductivity occurs for the nanotube-only film (100%). Interestingly, neither composite type faithfully follows percolation-like scaling, the general form of which is shown by the dotted line.

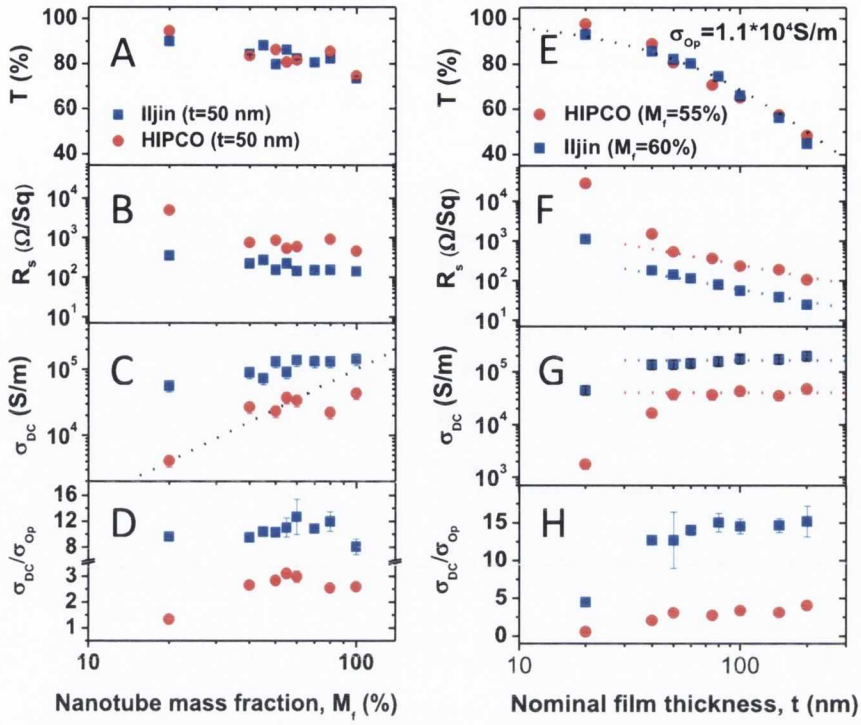

Figure 5.11 *Optical and electrical data for PEDOT:PSS-based composites filled with both HiPCO and Iljin SWNT. (A) Transmittance (λ = 550nm), (B) sheet resistance, and (C) DC conductivity as a function of nanotube mass fraction for films with nominal thickness of 50 nm. The dotted line in (C) illustrates quadratic behaviour expected for percolating nanotube networks. (D) Ratio of DC to optical conductivity as calculated from the sheet resistance/transmittance data using Equation 2.68 for both Iljin and HiPCO composites as a function of nanotube mass fraction. (E) Transmittance (550nm), (F) sheet resistance, (G) DC conductivity, and (H) ratio of DC conductivity to optical conductivity as a function of film thickness for films of mass fraction 55 % (HiPCO) and 60 % (Iljin). The dotted line in E is a fit to Equation 2.67. The dotted lines in F and G illustrate the behavior expected for bulk materials.*

In order to identify the optimum mass fraction for further studies, we use the data in Figure 5.11 A, B to calculate σ_{DC}/σ_{Op} as a function of M_f, using Equation 2.68. This is

shown in Figure 5.11 D for both composites. It is noted that σ_{DC}/σ_{Op} depends weakly on M_f, and appears to peak at 60 and 55 wt% for Iljin and HiPCO composites, respectively. This will be discussed in greater detail below.

With this in mind, films with mass fractions fixed at the optimized values (60 and 55 wt% for Iljin and HiPCO) for both composite types but with a range of nominal thicknesses from t = 20 to 200 nm were prepared. As before, for each film, the transmittance and sheet resistance were measured. Again, the transmittance spectra were relatively featureless. The transmittance at 550 nm was plotted as a function of nominal thickness in Figure 5.11 E. Both data sets fall on the same curve, with T decreasing as t is increased. For thin conducting films, the transmittance is related to the film thickness by Equation 2.67. and has been fitted to the data in Figure 5.11 E as shown by the dotted line. Both data sets can be very well fit by Equation 2.67, taking $\sigma_{Op} = (1.1 \pm 0.1) \times 10^4$ S/m (λ = 550nm). This value is significantly lower than that of $\sigma_{Op} = 1.5 \times 10^4$ S/m (λ = 550nm) found for neat films of SWNTs.[13,14] The sheet resistance data for the same films are shown in Figure 5.11 F. In both cases, R_s falls with increasing t, with the Iljin composites significantly less resistive. Both data sets are well fit by $\sigma_{DC} = 1/R_s t$, for t = 40 nm, suggesting the film morphology becomes thickness invariant above this thickness. The nominal conductivity is shown in Figure 5.11 G as a function of thickness. In line with the sheet resistance data, the conductivity is reasonably constant at higher values, falling off below t = 40 nm. These optimised films have mean conductivities (t > 40 nm) of σ_{DC} = $(1.65 \pm 0.2) \times 10^5$ and $(4.0 \pm 0.4) \times 10^4$ S/m for Iljin and HiPCO composites, respectively.

It is worth noting that these conductivities are extremely high even for composites with conducting matrices. Bulk composites prepared from SWNTs embedded in polyacrylonitrile have reached conductivities of 1.5×10^4 S/m.[27] Composites based on SWNTs embedded in PEDOT:PSS have also shown very high conductivities, reaching

values of ~7 x 10^4 S/m. However, to my knowledge, this work is the first to demonstrate composite conductivities greater than 10^5 S/m. There are two main reasons why such high conductivities were achieved. The first is that we use Iljin nanotechnology Inc. arc-discharge SWNTs, which are well known for their ability to form highly conductive nanotube films.[16] In fact, the state-of-the-art for nanotube films is for films prepared using Iljin SWNTs, displaying conductivities as high as 2 x 10^5 S/m.[16] The second reason is that, building on previous work,[26] it is possible to attain nanotube mass fractions far in excess of any others reported in the literature. It is this combination of highly conductive tubes at high mass fraction that gives such superlative properties.

The ratio σ_{DC}/σ_{Op} was calculated as a function of film thickness from the data in Figure 5.11 E-F using Equation 2.68. This data is shown in Figure 5.11 H and scales with thickness in a fashion similar to the DC conductivity. At thicknesses above 80 nm, σ_{DC}/σ_{Op} saturates close to values of 15 and 3.3 for the Iljin and HiPCO composites, respectively.

As described above, many applications require low sheet resistance coupled with high transparency. To this end, transmittance was plotted versus sheet resistance for all four data sets (fixed t, varying M_f, and fixed M_f, varying t, for both nanotube types) in Figure 5.12. For each tube type, both data sets (varying both t and M_f) fall close to the same curve as illustrated by the dotted lines. The Iljin data, however, is shifted to lower R_s, in line with their higher conductivities. The data has been fitted using Equation 2.68 in Figure 5.12 are consistent with σ_{DC}/σ_{Op} = 14.8 and 3.3 for the Iljin and HiPCO composites, respectively. These values are as expected from Figure 5.11 H. It is interesting that the data found by varying M_f for fixed t also falls on this line. This can be seen more clearly by plotting the data as $T^{-1/2}$-1 versus $1/R_s$ as shown in the inset of Figure 5.12. Here, data described by Equation 2.68 on a straight line. This is observed for all data (except for those films with the lowest values of t or M_f) with linearity illustrated by the dotted lines. This

shows that, not only are the films prepared by varying t described by Equation 2.68, but the films prepared by varying M_f are also. This is interesting as it shows that composites with different mass fractions of nanotubes tend to have similar values of σ_{DC}/σ_{Op}.

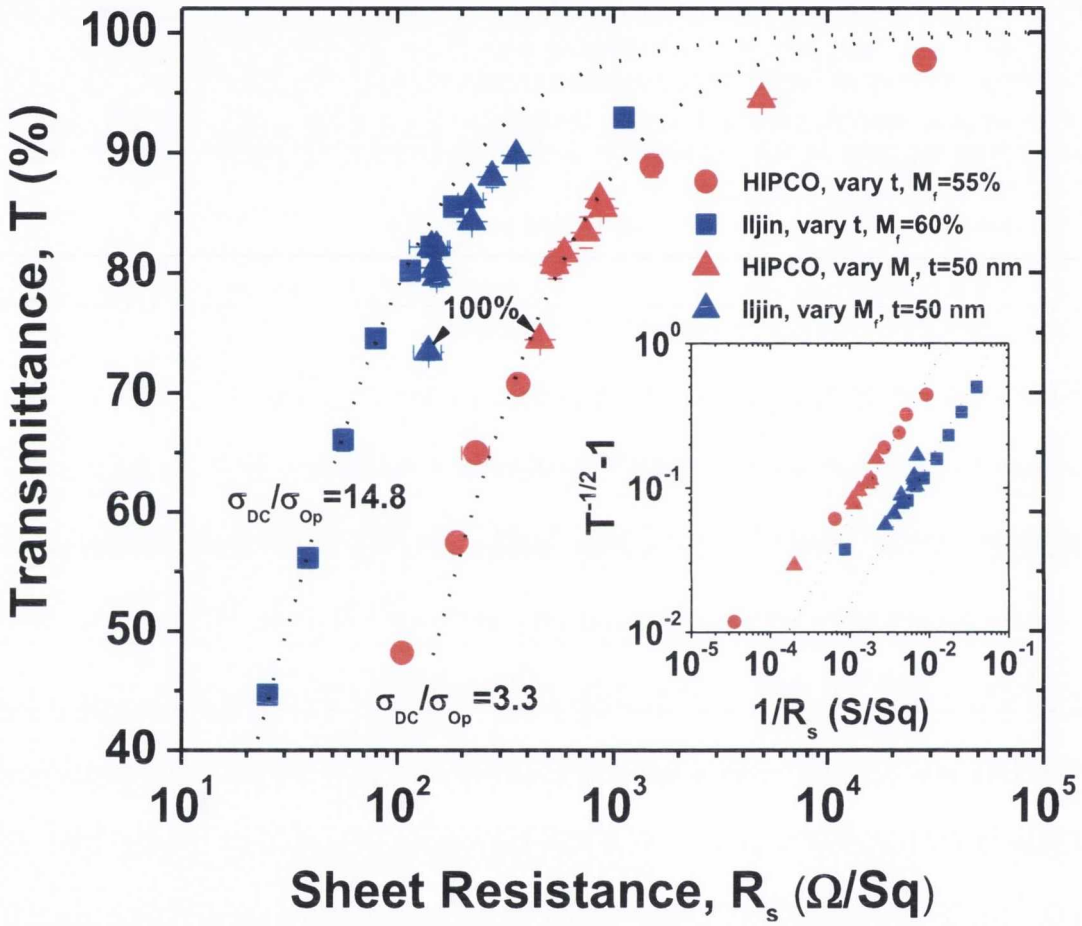

Figure 5.12 *Transmittance (λ = 550nm) plotted as a function of sheet resistance for all the samples measured in this work. The dotted lines are fits to Equation 2.68. Inset: Transmittance versus sheet resistance data plotted to emphasize how well these data are fitted by Equation 2.68. The dotted lines are equivalent to the fit lines in the main figure.*

Referring back to Figure 5.11 D it is noted that while σ_{DC}/σ_{Op} displays a clear peak for each composite, its overall dependence on M_f is very weak. Thus, σ_{DC}/σ_{Op} only varies between 8 and 15 for the Iljin networks and between 1 and 3 for the HiPCO networks over the entire range of mass fractions. This relative invariance suggests that reductions in the mass fraction, while resulting in a more open nanotube network, do not significantly change the network topology or connectivity.

Another interesting point is that the data for the nanotube-only films fall close to, but slightly below these trend-lines, illustrating their inferior properties. This is in contrast to the vast majority of polymer-nanotube composites where the electrical properties are significantly reduced by the presence of polymer layers, which act as tunnelling barriers, between adjacent nanotubes.[25,35] The fact that the electrical / optical properties of these composites are certainly not inferior but actually superior to the nanotube only films suggests that inter nanotube polymer layers do not significantly inhibit intertube electron transfer at nanotube junctions. It was proposed that this lack of tunnelling barriers, coupled with the reasonably low optical conductivity observed in composites, contributes to these high values of σ_{DC}/σ_{Op}. That σ_{DC}/σ_{Op} displays a peak when plotted versus mass fraction shows that the DC and optical conductivities scale differently with nanotube mass fraction. Thus, the balance between charge transport and light absorption is optimised at certain mass fractions (σ_{DC}/σ_{Op} = 12.7, M_f = 60 wt%, t = 60 nm). It is noted that this is higher than the value measured for Iljin-only films of the same thickness (σ_{DC}/σ_{Op} = 8.1, M_f = 100 wt%, t = 60nm).

Overall, the highest value was σ_{DC}/σ_{Op} = 15.0 ± 1.2 (Iljin, M_f = 60 wt%, t = 80 nm). This is significantly higher than both the highest published value of ~9 for simple polymer-nanotube composites[32] and the value of ~12 obtained for composites of lithium-doped SWNTs.[31] (In the previous two papers, σ_{DC}/σ_{Op} was not quoted. They were calculated from

published R_s, T data.) Note that the value of $\sigma_{DC}/\sigma_{Op} = 15.0 \pm 1.2$ is higher even than the highest value reported for undoped SWNT – only films ($\sigma_{DC}/\sigma_{Op} = 10.1$).[13] Only data for acid-treated SWNT networks have resulted in higher values ($\sigma_{DC}/\sigma_{Op} = 25$).[13]

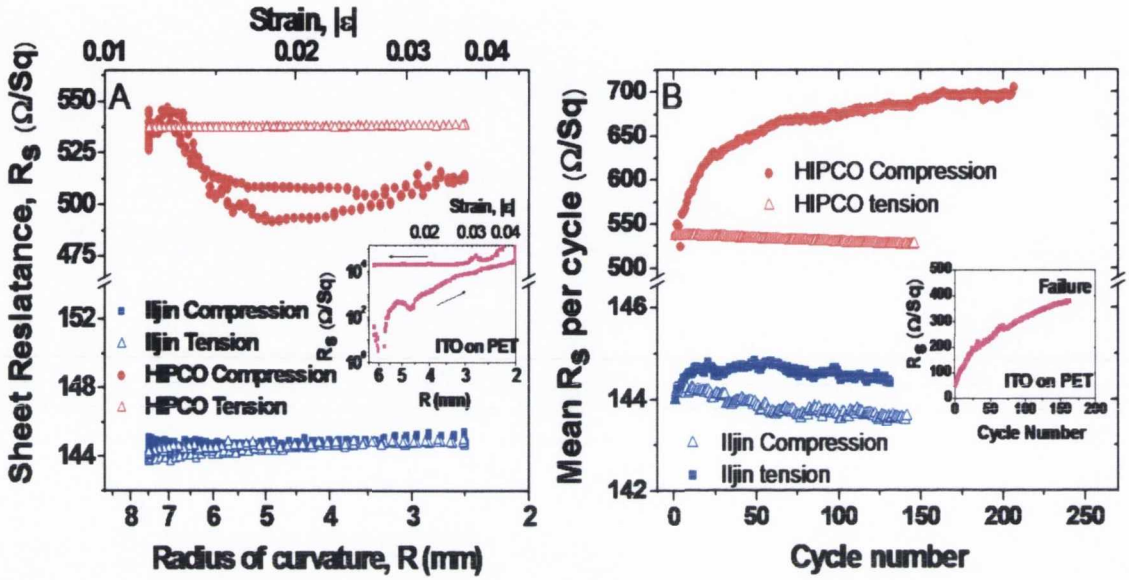

Figure 5.13 *Electromechanical measurements made on composites with t = 50 nm and M_f = 55 % (HiPCO) and M_f = 60 % (Iljin). (A) Sheet resistance versus radius of curvature for one bend/release cycle measured for films both in compression and intension. Inset: Results for a film of ITO on PET. (A) Mean sheet resistance per cycle as a function of cycle number for films in both tension and compression. Inset: Results for a film of ITO on PET.*

Finally, these composites are close to being a viable replacement for ITO and they are potentially even more useful as a flexible, transparent, electrode material. Such a material is of considerable interest as an electrode in applications such as e-paper.[21] To test this, composite films on PET using both Iljin and HiPCO nanotubes as filler (t = 50 nm, $M_{f,Iljin}$ = 60wt %, $M_{f,HiPCO}$ = 55 wt%) were prepared. In each case, the sheet resistance during bending was monitored with the composite film both in tension and in compression. The films were bent from an initial radius of curvature of 7.5 mm to a final radius of 2.5

mm before being relaxed. Shown in Figure 5.13 A is the sheet resistance versus radius of curvature during both the bending and release phases (note that the magnitude of the average strain[36] felt by the film is plotted in the top axis). From this data, it is clear that the sheet resistance of the Iljin-based composites varies by <1 % during both bend and release phases for films both in tension and in compression. In comparison, while the HiPCO films are very stable in tension, they undergo a reproducible reduction in resistance of ~10 % while bending in compression. For comparison purposes, shown in the inset is data taken for an ITO film sputtered onto PET that was subjected to the same test. It is clear that the ITO fails catastrophically on tensile bending, with the sheet resistance increasing irreversibly by almost 2 orders of magnitude.

While these composite films are clearly relatively stable during one bend cycle, it is important to ascertain their stability over many bend cycles. Shown in Figure 5.13 B is the mean sheet resistance per cycle plotted versus cycle number for the same films examined in Figure 5.13 A. It is clear that the sheet resistance of the Iljin-based films varied by <1 % over ~130 cycles. Similarly, the HiPCO-based composite subjected to tensile bending was also extremely stable. However, as before, the compressively bent HiPCO-based composite films were relatively unstable, undergoing increases in resistance of ~30 % over 200 cycles. Note that none of these composites failed during these measurements. The number of cycles was limited by time constraints. For comparison, the cyclic test data for an ITO / PET film is shown in the inset of Figure 5.13 B. In this case, to avoid immediate failure, the film was tested at low curvature, with minimum bend radius of 20 mm on each cycle. In stark contrast to the composite films, the sheet resistance of this film increased by a factor of 8 before failing around cycle 150. These results can be compared to previously published results for (lower conductivity) PEDOT : PSS / SWNT films whose resistance increased by ~8 % after 1800 bending cycles.[32]

5.3.4 Conclusion

The preparation of thin composite films based on PEDOT:PSS doped with two different types of SWNTs was demonstrated. The spatial uniformity of the optical transmittance of these films is exceptional. The optical transmittance and sheet resistance as a function of both mass fraction and film thickness was measured. While the optical properties of both composite types are similar, composites based on arc discharge tubes (Iljin Nanotech.) are significantly more conductive than those based on HiPCO tubes, reaching conductivities of 1.65 x 10^5 S/m. In both cases, the ratio of DC to optical conductivity was maximised for mass fractions of 55 – 60 wt%. The highest value found was σ_{DC}/σ_{Op} = 15, which was observed for an 80 nm thick film containing 60 wt% Iljin (arc discharge) SWNTs. This film has transmittance and sheet resistance values of T = 75% and R_s = 80Ω/□. Electromechanical testing showed both composites to be extremely stable under flexing and cycling. In particular, the Iljin-based composites displayed sheet resistances which varied by less than 1 % over 130 bend / release cycles. With moderate improvement such composites could be suitable for use as flexible electrodes in applications such as solar cells or displays.

5.4 References

1 Evelyn M. Doherty, Sukanta De, Philip E. Lyons, Aleksey Shmeliova, Peter N. Nirmalraj, Vittorio Scardaci, Jerome Joimel, Werner J. Blau, John J. Boland, and Jonathan N. Coleman, "The spatial uniformity and electromechanical stability of transparent, conductive films of single walled nanotubes," Carbon **47**, 2466-2473 (2009).

2 Philip E. Lyons, Sukanta De, Fiona Blighe, Valeria Nicolosi, Luiz Felipe C. Pereira, Mauro S. Ferreira, and Jonathan N. Coleman, "The relationship between network morphology and conductivity in nanotube films," Journal of Applied Physics **104** (044302) (2008).

3 Zhuangchun Wu, Zhihong Chen, Xu Du, Jonathan M. Logan, Jennifer Sippel, Maria Nikolou, Katalin Kamaras, John R. Reynolds, David B. Tanner, Arthur F. Hebard, and Andrew G. Rinzler, "Transparent, Conductive Carbon Nanotube Films," Science **27** (1273) (2004).

4 Virginia A. Davis, Lars M. Ericson, A. Nicholas, G. Parra-Vasquez, Hua Fan, Yuhuang Wang, Valentin Prieto, Jason A. Longoria, Sivarajan Ramesh, Rajesh K. Saini, Carter Kittrell, W. E. Billups, W. Wade Adams, Robert H. Hauge, Richard E. Smalley, and Matteo Pasquali, "Phase Behavious and Rheology of SWNT's in Superacids," Macromolecule **37** (1), 154-160 (2004).

5 Sivarajan Ramesh, Lars M. Ericson, Virginia A. Davis, Rajesh K. Saini, Carter Kittrell, Matteo Pasquali, W. E. Billups, W. Wade Adams, Robert H. Hauge, and Richard E. Smalley, "Dissolution of Pristine Single Walled Carbon Nanotubes in Superacids by Direct Protonation," The Journal of Physical Chemistry B **108** (26), 8794-8798 (2004).

6 G. S. Duesberg, M. Burghard, J. Muster, and G. Philipp, "Separation of carbon nanotubes by size exclusion chromatography," Chemical Communications **435** (1998).

7 Jonathan N. Coleman, Alexander Fleming, Stefanie Maier, Sean O'Flaherty, Andrew I. Minett, Mauro S. Ferreira, Stefan Hutzler, and Werner J. Blau, "Binding Kinetics and SWNT Bundle Dissociation in Low Concentration Polymer–Nanotube Dispersions," The Journal of Physical Chemistry B **108** (11), 3446-3450 (2004).

8 A. B. Dalton, C. Stephan, J. N. Coleman, B. McCarthy, P. M. Ajayan, S. Lefrant, P. Bernier, W. J. Blau, and H. J. Byrne, "Selective Interaction of a Semiconjugated Organic Polymer with Single-Wall Nanotubes," The Journal of Physical Chemistry B **104** (43), 10012-10016 (2000).

9 Zhenyu Sun, Valeria Nicolosi, David Rickard, Shane D. Bergin, Damian Aherne, and Jonathan N. Coleman, "Quantitative Evaluation of Surfactant-stabilized Single-walled Carbon Nanotubes: Dispersion Quality and Its Correlation with Zeta Potential," the Journal of Physical Chemistry C **112** (29), 10692-10699 (2008).

10 Shane D Bergin, Valeria Nicolosi, Silvia Giordani, Antoine de Gromard, Leslie Carpenter, J Werner J Blau, and onathan N Coleman, "Exfoliation in ecstasy: liquid crystal formation and concentration-dependent debundling observed for single-wall nanotubes dispersed in the liquid drug γ -butyrolactone," Nanotechnology **18** (45) (2007).

11 Silvia Giordani, Shane D. Bergin, Valeria Nicolosi, Sergei Lebedkin, Manfred M. Kappes, Werner J. Blau, and Jonathan N. Coleman, "Debundling of Single-Walled Nanotubes by Dilution: Observation of Large Populations of Individual Nanotubes in Amide Solvent Dispersions," The Journal of Physical Chemistry B **110** (32), 15708-15718 (2006).

12 S. Reich, C. Thomsen, and P. Ordejón, "Electronic band structure of isolated and bundled carbon nanotubes," Physics Review B **65** (155411) (2002).

13 Hong-Zhang Geng, Dae Sik Lee, Ki Kang Kim, Gang Hee Han, Hyeon Ki Park, and Young Hee Lee, "Absorption spectroscopy of surfactant-dispersed carbon nanotube film: Modulation of electronic structures," Chemical Physical Letters **455**, 275-278 (2008).

14 B. Ruzicka, L. Degiorgi, R. Gaal, L. Thien-Nga, R. Bacsa, J. P. Salvetat, and L. Forro, "Optical and dc conductivity study of potassium-doped single walled carbon nanotube films," Physical Review B **61** (4) (2000).

15 David Hecht, Liangbing Hu, and George Grüner, "Conductivity scaling with bundle length and diameter in single walled carbon nanotube networks," Applied Physics Letters **89** (133112) (2006).

16 Hong-Zhang Geng, Ki Kang Kim, Kang Pyo So, Young Sil Lee, Youngkyu Chang, and Young Hee Lee, "Effect of Acid Treatment on Carbon Nanotube-Based Flexible Transparent Conducting Films," Journal of the American Chemical Society **129**, 7758-7759 (2007).

17 L. Hu, D. S. Hecht, and G. Gruner, "Percolation in Transparent and Conducting Carbon Nanotube Networks," Nano Letters **4** (12) (2004).

18 T. M. Barnes, J. van de Lagemaat, D. Levi, G. Rumbles, T. J. Coutts, C. L. Weeks, D. A. Britz, I. Levitsky, J. Peltola, and P. Glatkowski, "Optical characterization of highly conductive single-wall carbon-nanotube transparent electrodes," Physics Review B **75** (235410) (2007).

19 Gregory P. Crawford (ed), *Flexible flat panel displays*. (John Wiley & Sons, Ltd, 2005).

20 Sukanta De, Philip E. Lyons, Sophie Sorel, Evelyn M. Doherty, Paul J. King, Werner J. Blau, Peter N. Nirmalraj, John J. Boland, Vittorio Scardaci, Jerome Joimel, and Jonathan N. Coleman, "Transparent, Flexible, and Highly Conductive Thin Films Based on Polymer Nanotube Composites," American Chemical Society Nano **3** (3), 714-720 (2009).

21 E. S. Snow, J. P. Novak, M. D. Lay, E. H. Houser, F. K. Perkins, and P. M. Campbell, "Carbon nanotube networks: Nanomaterial for macroelectronic applications," Journal of Vacuum Science & Technology B: Microelectronics and Nanometer Structures **22** (4), 1990-1994 (2004).

22 Dmitriy A. Dikin, Sasha Stankovich, Eric J. Zimney, Richard D. Piner, Geoffrey H. B. Dommett, Guennadi Evmenenko, Son Binh T. Nguyen, and Rodney S. Ruoff, "Preparation And Characterization of Graphene Oxide Paper," Nature **448**, 457-460 (2007).

23 Y. Leterrier, L. Médico, F. Demarco, J. -A. E. Månson, U. Betz, M. F. Escolà, M. Kharrazi Olsson, and F. Atamny, "Mechanical integrity of transparent conductive oxide films for flexible polymer-based displays " Thin Solid Films **460** (1-2), 156-166 (2004).

24 Zhong Chen, Brian Cotterell, and Wei Wang, "The fracture of brittle thin films on compliant substrates in flexible displays " Engineering Fracture Mechanics **69** (5), 597-603 (2002).

25 Wolfgang Bauhofer and Josef Z. Kovacsa, "A review and analysis of electrical percolation in carbon nanotube polymer composites," Composites Science and Technology **69** (10), 1486-1498 (2008).

26 F. M. Blighe, Y. R. Hernandez, W. J. Blau, and J. N. Coleman, "Observation of Percolation-like Scaling – Far from the Percolation Threshold – in High Volume Fraction, High Conductivity Polymer-Nanotube Composite Films," Advanced Materials **19** (24), 4443-4447 (2007).

27 Huina Guoa, T.V. Sreekumara, Tao Liua, Marilyn Minusa, and Satish Kumar, "Structure and properties of polyacrylonitrile/single wall carbon nanotube composite films," Polymer **46** (9), 3001-3005 (2005).

28 J. S. Moon, J. H. Park, T. Y. Lee, Y. W. Kim, J. B. Yoo, C. Y. Park, J. M. Kim, and K. W. Jin, "Transparent conductive film based on carbon nanotubes and PEDOT composites," Diamond and Related Materials **14**, 1882-1887 (2005).

29 Wei Wang, K. A. Shiral Fernando, Yi Lin, Mohammed J. Meziani, L. Monica Veca, Li Cao, Puyu Zhang, Martin M. Kimani, and Ya-Ping Sun, "Metallic Single-Walled Carbon Nanotubes for Conductive Nanocomposites," Journal of the American Chemical Society **130**, 1415=1419 (2008).

30 Tero Mustonen, Krisztián Kordás, Sami Saukko, Géza Tóth, Jari S. Penttilä, Panu Helistö, Heikki Seppä, and Heli Jantunen, "Inkjet printing of transparent and conductive patterns of single-walled carbon nanotubes and PEDOT-PSS composites," Physica Status Solidi (b) **244** (11), 4336-4340 (2007).

31 Hyeong Taek Ham, Yeong Suk Choi, Mu Guen Chee, Myoung Hwan Cha, and In Jae Chung, "PEDOT-PSS/Singlewall Carbon Nanotubes Composites," Polymer Engineering and Science **48**, 1-10 (2008).

32 Guang-Feng Wang, Xiao-Ming Tao, and Rong-Xin Wang, "Flexible organic light-emitting diodes with a polymeric nanocomposite anode," Nanotechnology **19** (145201) (2008).

33 S. Garreau, G. Louarn, J. P. Buisson, G. Froyer, and S. Lefrant, "In Situ Spectroelectrochemical Raman Studies of Poly(3,4-ethylenedioxythiophene) (PEDT)," Macromolecules **32** (20), 6807-6812 (1999).

34 X. Crispin, F. L. E. Jakobsson, A. Crispin, P. C. M. Grim, P. Andersson, A. Volodin, C. van Haesendonck, M. Van der Auweraer, W. R. Salaneck, and M. Berggren, "The Origin of the High Conductivity of Poly(3,4-ethylenedioxythiophene)-Poly(styrenesulfonate) (PEDOT PSS) Plastic Electrodes," Chemical Materials **18**, 4354-4360 (2006).

35 B. E. Kilbride, J. N. Coleman, J. Fraysse, P. Fournet, M. Cadek, A. Drury, S. Hutzler, S. Roth, and W. J. Blau, "Experimental observation of scaling laws for alternating current and direct current conductivity in polymer-carbon nanotube composite thin films," Journal of Applied Physics **92** (4024) (2002).

36 Dmitriy A. Dikin, Sasha Stankovich, Eric J. Zimney, Richard D. Piner, Geoffrey H. B. Dommett, Guennadi Evmenenko , Son Binh T. Nguyen, and Rodney S. Ruoff, "Preparation and characterization of graphene oxide paper," Nature **448**, 457-460 (2007).

Chapter 6 : Silver nanowire networks as flexible, transparent, conducting films: Extremely high DC to optical conductivity ratios[1]

6.1 Introduction and background

The main problem with implementing nanostructure networks as transparent electrodes has been achieving transmittance and sheet resistance values routinely achievable with ITO. The best results for graphene-based films[2] have been σ_{DC}/σ_{OP}=116,[3] while for nanotubes,[4] σ_{DC}/σ_{OP}=25 has been demonstrated. Thin films of metallic nanowires may bridge this gap. Lee *et al.* Have pioneered this method by preparing networks of silver nanowires (AgNWs) for which we calculate σ_{DC}/σ_{OP} = 150. In this chapter, a method is demonstrated to produce thin films of silver nanowires with σ_{DC}/σ_{OP}=500, similar to that required to match ITO. These films have DC conductivity of up to 5 x 10^6 Sm^{-1}, 8 % of the value for bulk silver. Films with R_s = 13Ω/□ coupled with T=85% were prepared. These films are stable under flexing for at least 1000 cycles.

6.2 Experimental procedure

Silver nanowires were purchased from Seashell Technologies (www.seashelltech.com) as suspensions in isopropylalcohol (C=12.5mg/mL as measured by thermogravimetric analysis, Perkin-Elmer Pyris). A small volume of the dispersion was diluted down to 0.1 mg/mL with Millipore water. This was subjected to half an hour low power sonication in a sonic bath (Model Ney Ultrasonic). The dispersion was further diluted down to a concentration C = 0.002 mg/mL with Millipore water and sonicated for a further 30 minutes. Silver nanowire films were prepared by vacuum filtration of the above dispersions using porous mixed cellulose ester filter membranes (MF-Millipore membrane, mixed cellulose esters, hydrophilic, 0.2 μm, 47 mm). A range of films with varying thickness was prepared by filtering different dispersion volumes, giving different deposited masses. These films were characterised by their deposited mass per unit area, M/A. The deposited films were transferred to a polyethylene terephthalate (PET) substrate using heat and pressure.[5] The PET was placed on a hot plate at 100 °C. The AgNW film/membrane was placed on the PET with the AgNWs in contact with the PET. A 3kg weight was then placed on top for 2 hours. The cellulose filter membrane was then removed by treatment with acetone vapour and subsequent acetone liquid baths followed by a methanol bath.[5] The film area was 36mm in diameter. Thin silver films were prepared using an Edwards S Auto 306 evaporator. Commercially available ITO was purchased from UQG Optics Ltd. Transmission scans were made using an Epson Perfection V700 photo flat-bed transmission scanner with a bit depth of 48bits per pixel and a spatial resolution of 6400 dpi. The numerical output of the scanner was calibrated by scanning a range of neutral density filters. The resultant calibration curve was used to transform the output to represent transmittance. This results in a transmittance map with a transmittance value for every pixel. Transmission maps were transformed into absorbance maps by applying $A = -\log T$ to each pixel. The mean and standard deviations of the transmittance or absorbance were

calculated from the entire data set (i.e., from the entire set of pixel values). Scanning electron microscopy measurements were made using a Hitachi S-4300 field emission scanning electron microscope. Charging was avoided by transferring the nanowire film from cellulose membrane to a glass substrate coated with a thin gold/palladium film. Atomic force microscope images were obtained using a Dimension V AFM.[a] In order to extract the topography and conductance data simultaneously, the microscope was operated in the conductance imaging mode (C-AFM).[a] In this technique, the AFM tip acts like a mobile probe on the surface and is held at ground potential and a DC bias is applied to the sample. The *z* feedback signal is used to generate a normal contact mode AFM topographic profile, and the current passing between the tip and the sample is measured using a pre-amplifier to generate the conductance image. A bias voltage of 0.2 mV up to 1 V is applied to the electrode on the surface that drives current through the wires. A current range of 2 pA to1 μA can be detected by the pre-amplifier in the C-AFM module. For this purpose, a Cr/Pt-coated conductive tip with a force constant of 3 N/m and a resonant frequency of 75 kHz was employed. In all cases, the loading force employed during measurement was approximately 15 nN. (The tips were purchased f[l]rom Budget Sensors, ElectriMulti 75.) Optical transmission spectra were recorded using a Cary Varian 6000i, with a sheet of PET used as the reference. Sheet resistance measurements were made using the four-probe technique with silver paste electrodes of dimensions and spacings typically of ~ millimetre in size and a Keithley 2400 sourcemeter. Electromechanical measurements were made using a Zwick Z0.5 Proline tensile tester.[b] The AgNW film on PET was bent into a semi-circle, which was constrained by the grips of the tensile tester. The film was connected via two electrodes (attached to the grips) to a Keithley KE 2601. The bend radius was then defined by the distance between the grips. The inter-grip distance was then oscillated

[a] The AFM and C-AFM measurements were performed by Dr. Peter Nirmalraj of the School of Chemistry, Trinity College Dublin.

[b] The electromechanical measurements were performed by Evelyn Doherty of the School of Chemistry, Trinity College Dublin and Jerome Joimel of Hewlett Packard DIMO, Liffey Park Technology Campus, Barnhall Road, Leixlip, Co Kildare, Ireland.

typically between 15 and 5 mm over many cycles. LabVIEW software recorded film resistance, inter-grip distance, and cycle number.

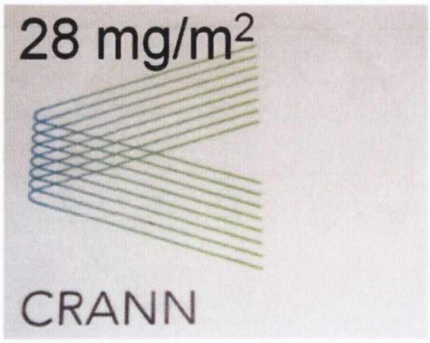

Figure 6.1 *Photograph of a film of AgNWs on PET covering the CRANN logo.*

6.3 Results and discussion

Shown in Figure 6.1 is a photograph of a nanowire film on a PET substrate. This was prepared by depositing 28 mg/m^2 of AgNWs onto a cellulose membrane by vacuum filtration. It is clear from this image that the film appears to be of very high optical quality. While this is generally true, it is noted that the films appear very slightly milky due to light scattering from the nanowires.[6] The optical uniformity of the film was tested by taking a transmission scan of the deposited film. This involves measurement of the local white light transmittance with a spatial resolution of 4μm, measured over an area of 2 mm x 2 mm. The uniformity of the transmittance was characterised by calculating the standard deviation of the transmittance over all pixels, ΔT. This worked out to be ΔT = 1.8 % for the film shown in Figure 6.1 demonstrating the optical quality of these films. When normalized to transmittance, this gives $\Delta T/\langle T \rangle$ = 2.1 %. This technique will be used below to investigate the film uniformity as a function of film thickness.

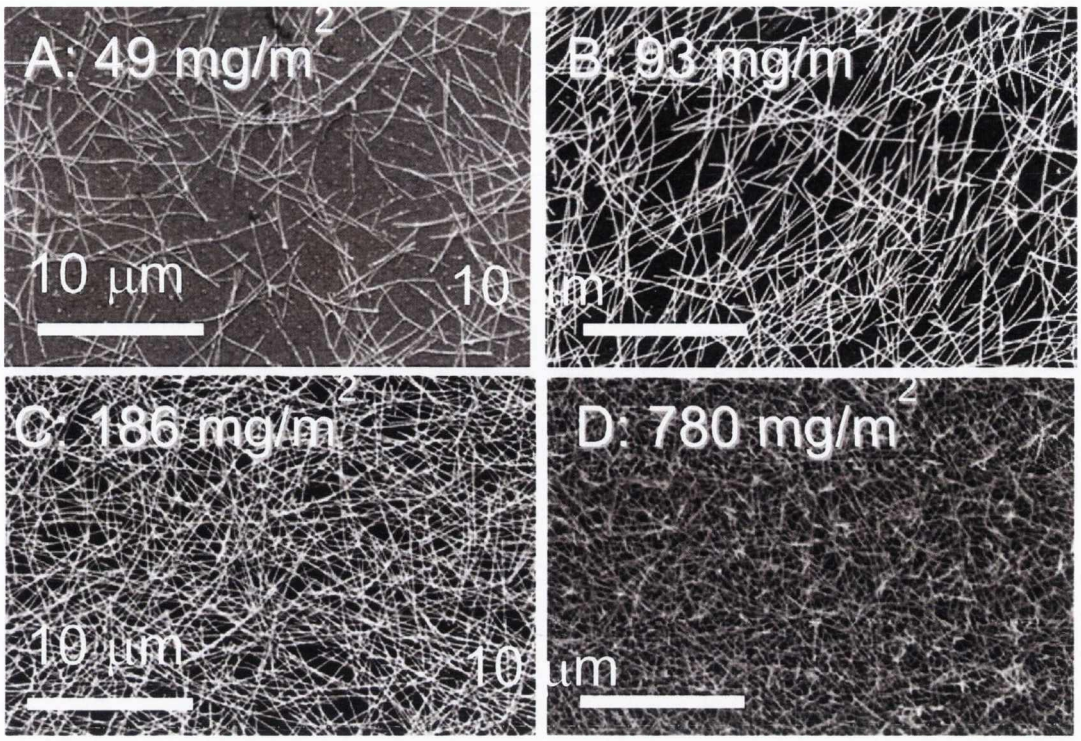

Figure 6.2 *SEM images of the surfaces of films of increasing thickness, 46 ≤ M/A ≤ 780 mg/m^2.*

The nature of these films was investigated using scanning electron microscopy as shown in Figure 6.2 A-D. To facilitate SEM analysis, the films were transferred onto Au/Pd-coated glass after filtration. Shown in Figure 6.2 A is an SEM image for an *M/A* = 46 mg/m^2 film. This image shows a network of nanowires that, while clearly above percolation, can be considered sparse. As a result, there is significant non-uniformity, with holes in the network (where the substrate is visible) of sizes ranging from 2-6 μm in diameter. In Figure 6.2 B-D, successive images for films of increasing thickness (*M/A* increasing from 93 to 780 mg/m^2) are shown. It is clear from these images that, as the thickness is increased, the networks become less sparse with the substrate appearing less frequently.

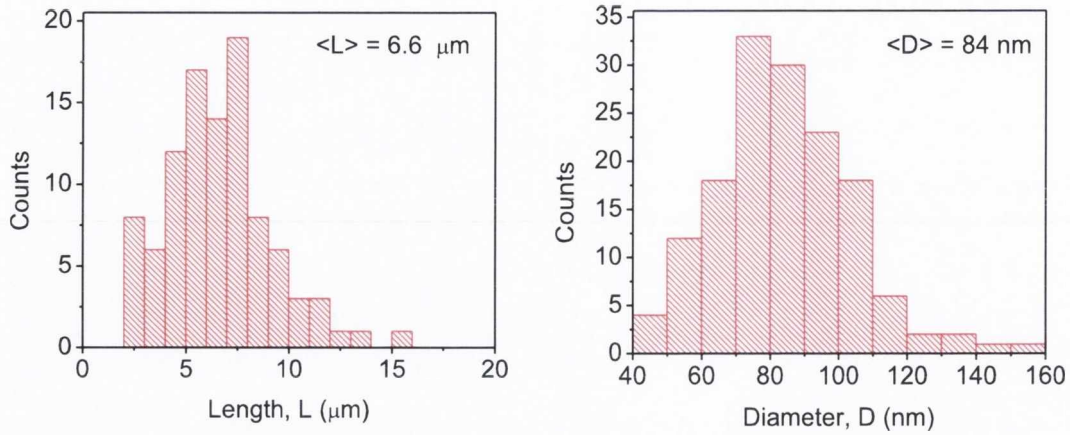

Figure 6.3 *Statistics relating to the length and diameter of the individual nanowires*

In addition, the films appear more uniform; by 780 mg/m^2, the substrate cannot be seen at all and the network appears spatially homogeneous. From images such as the one shown in Figure 6.2 A, the length and diameter of the nanowires can be measured. These data are shown in Figure 6.3 in the form of histograms. The length varies from 2.5 to 15 μm with a mean of 6.6 μm. The diameter varies from 50 to 150 nm with a mean of 84 nm. These lengths are larger than those found for most carbon nanotubes, while the diameters are almost an order of magnitude larger than that usually found for carbon nanotube bundles in thin films.

The transmittance spectra in the visible region were measured for all films studied, as shown in Figure 6.4. The spectra were reasonably featureless, although those representing very thin films displayed a number of weak, broad peaks. From these spectra, the transmittance at 550nm, T, was measured and the sheet resistance, R_s, was calculated for all the films studied in this work, as shown in Figure 6.5. For the thinnest films (M/A = 28 mg/m^2), T approaches 92 % for sheet resistance approaching 100 Ω/□. For thick films (M/A = 230 mg/m^2), T approaches 32 % for R_s = 0.5 Ω/□. In the middle range, which is of most interest for electrode applications, the film with M/A = 70 mg/m^2 displays T = 75 % and R_s = 3.4 Ω /□, for example.

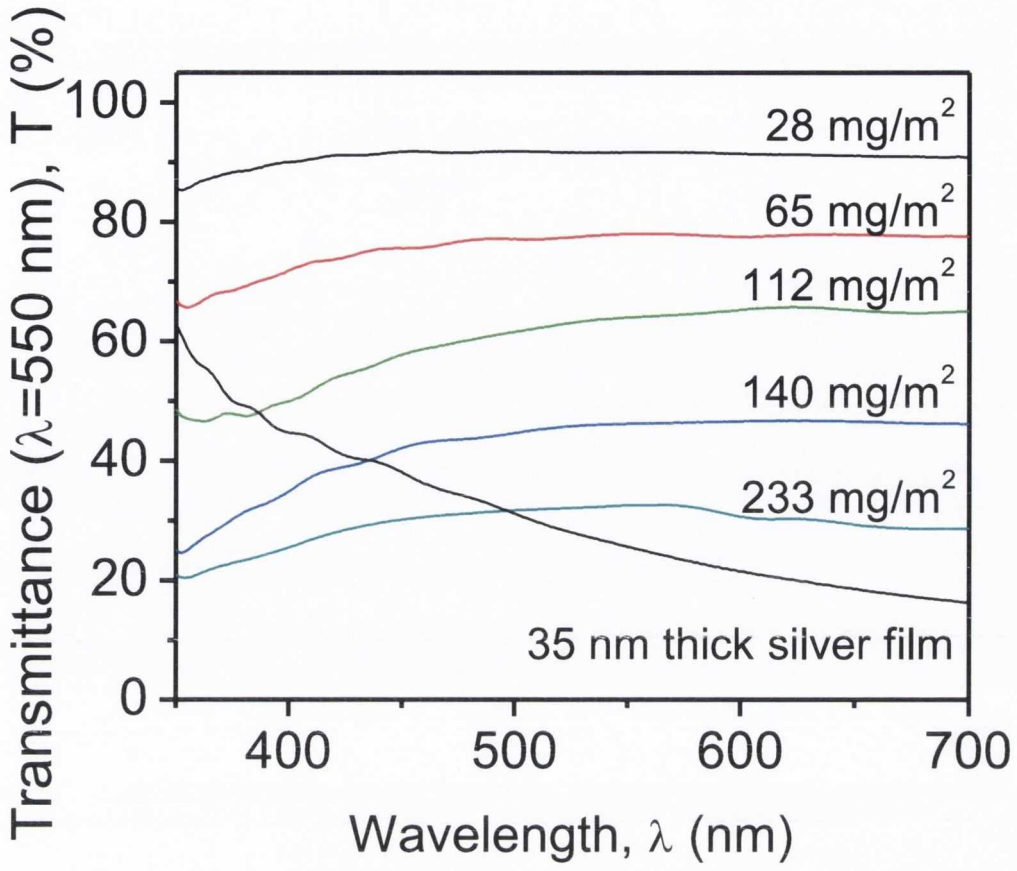

Figure 6.4 *Film transmittance spectra for selected AgNW films at a range of thicknesses. Also shown is the spectrum of a 35 nm thick evaporated silver film.*

In general, the transmittance and sheet resistance for thin metallic films are related by Equation 2.68 which has previously been shown to accurately describe films of both carbon nanotubes[4] and polymer nanotube composites.[7] This expression has been fitted to the data in Figure 6.5 and provides a reasonable fit for $M/A > 70$ mg/m^2. It is clear from Figure 6.2 A that films with $M/A \sim 70$ mg/m^2 are quite sparse and perhaps should be considered as 2D networks rather than 3D films. With this in mind, a network to film transition occurring at $M/A \sim 70$ mg/m^2 can be imagined.

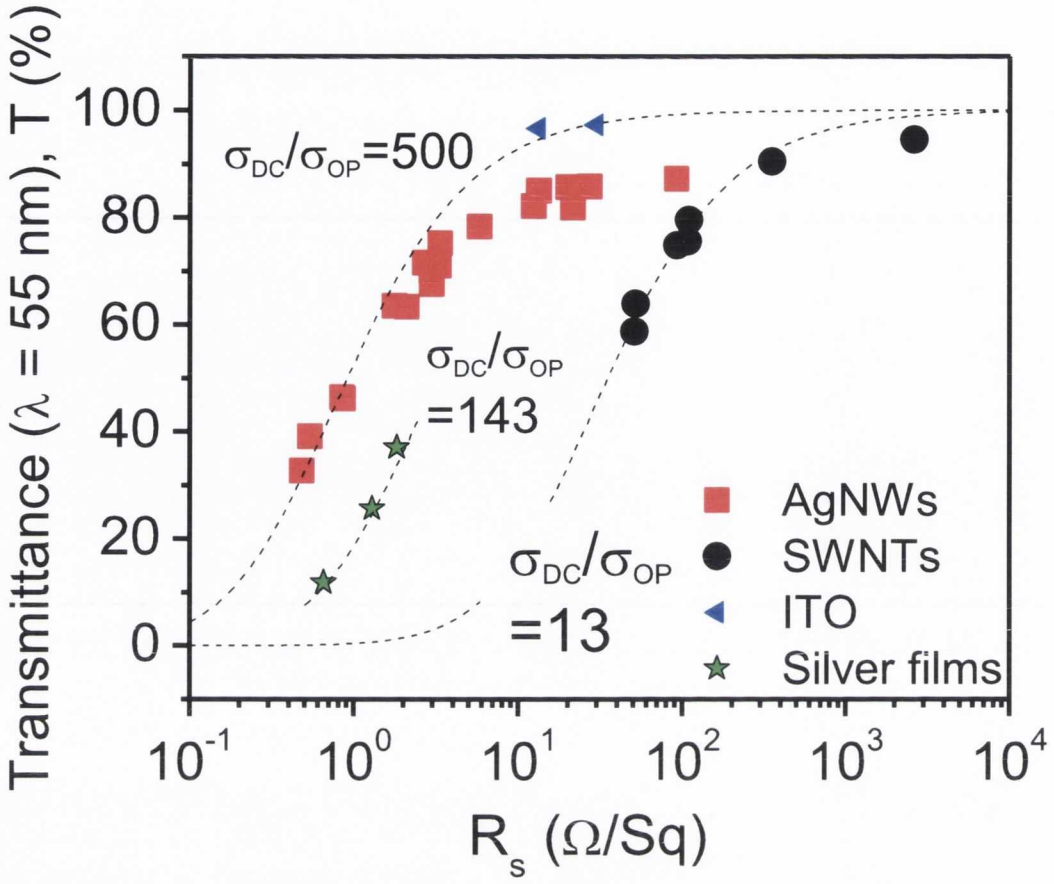

Figure 6.5 *Transmittance (λ=550nm) plotted as a function of film sheet resistance for the films studied in this work. The solid symbols represent films of AgNWs. For context, data is also given for films of evaporated silver, commercial ITO and single wall carbon nanotubes.*

The fit to Equation 2.68 shown in Figure 6.5 is described completely by σ_{DC}/σ_{Op}=500. This ratio can be considered as a figure of merit for thin conducting films. A value of σ_{DC}/σ_{Op}=500 is extremely large for a nanostructured thin film. Previous work has demonstrated a maximum value of σ_{DC}/σ_{Op} = 25 for acid-treated films of SWNTs.[4] This is illustrated by plotting on Figure 6.5 data measured in our lab for near state-of-the-art nanotube films (Iljin Nanotech, no post-treatment[8]). These data are described by σ_{DC}/σ_{Op} =

13, significantly worse than that displayed by the AgNW films. This transmittance-sheet resistance data is superior to all data found in the literature for nanostructured thin films. In addition, the values presented in Figure 6.5 are slightly better than data recently reported for metallic grids.[9]

To put these sets of data in context, thin silver films with thicknesses of 25, 35, and 50 nm were prepared by evaporation (thinner films oxidized, rapidly rendering them quite resistive). The transmittance (see Figure 6.4) and sheet resistance was found to vary in the ranges 10 % < T< 40 % and 0.7 Ω/□ < R_s < 1.8 Ω /□ as shown in Figure 6.5. These data are well described by Equation 2.68 with σ_{DC}/σ_{Op} = 143, far below that measured for AgNW films. In addition, T and R_s were measured for two films of commercially available ITO. These films had T ~ 97% and R_s ~ 15-30Ω/□, giving σ_{DC}/σ_{Op} = 400-800, slightly better than that measured for the AgNW films. It is clear from this graph that the AgNW films in this work are significantly better than solid silver films but slightly inferior to ITO. This will be discussed in more detail below.

In order to measure bulk film properties such as by σ_{Op} and σ_{DC}, the M/A must be related to the film thickness, t .To do this, a relatively thick film with M/A = 780 mg/m^2 was prepared. This film was thick enough to measure its thickness by SEM, giving t = 1800 nm. Knowing the thickness and mass per unit area allows the film density to be calculated from $M/A = \rho t$, giving ρ = 435 kg/m^3. From this the porosity was calculated to be 96 %. Assuming the film density is invariant with M/A (an assumption that is probably less valid at lower thickness), an average film thickness for all films can be calculated. Such thickness values should be treated with scepticism for M/A < 70 mg/m^2 (160 nm) below which the films should be considered 2D networks.

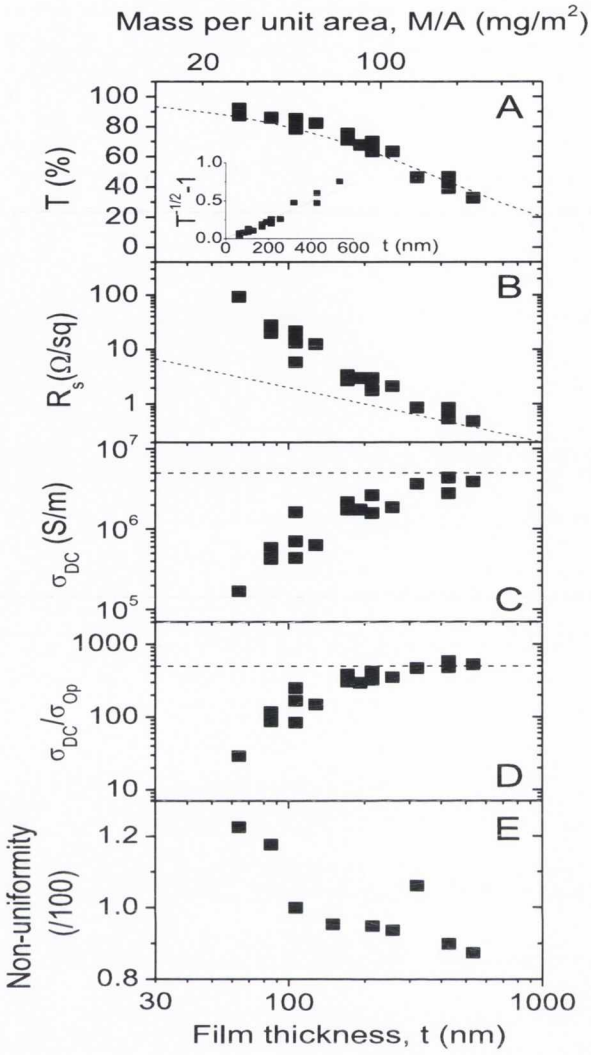

Figure 6.6 *Properties of AgNW films as a function of film thickness, t. For completeness the deposited mass per unit area is shown on the top axis. A) Optical transmittance, measured at 550 nm. The dotted line is a fit to equation 2.67., consistent with an optical conductivity of 6472 Sm^{-1}. B) Sheet resistance. The dotted line represents bulk-like behaviour as given by $R_s = 1/\sigma_{DC}t$, where $\sigma_{DC}=5\times10^6$ Sm^{-1} is the DC conductivity. C) DC conductivity, calculated from $R_s = 1/\sigma_{DC}t$. The dotted line illustrates a DC conductivity of 5×10^6 Sm^{-1}. D) Ratio of DC to optical conductivity as calculated from the T and R_s data. The dotted line illustrates conductivity ratio of 500. E) Local non-uniformity of films, defined as the standard deviation of the local absorbance measured with a pixel size of 4 microns.*

Shown in Figure 6.6 A is a graph of transmittance (550 nm) as a function of film thickness. The transmittance, T, scales with thickness, t, according to Equation 2.67. That Equation 2.67 is appropriate for these networks is emphasised by the inset, which shows that the data is fitted extremely well by this model when appropriately linearised. This equation has been fit to the data in Figure 6.6 A over its whole range, yielding a value of σ_{Op} = 6472 Sm^{-1}. This value is surprisingly low and compares with σ_{Op}=1.75×10^5 Sm^{-1} as measured for our thin evaporated silver films. This is lower than the reported value of 9.4 × 10^6 Sm^{-1} for bulk silver.[10] In any case, it is unclear why these AgNW networks should display such low values of σ_{Op}. The measured value is just 0.07 % of the value for bulk silver, a factor that cannot be explained solely by the high film porosity. In addition, the optical conductivity is lower than values measured for thin nanotube films (1.5-2 × 10^4 Sm^{-1}, λ = 550 nm).[11-13]

Shown in Figure 6.6 B is the sheet resistance data as a function of film thickness. It can be seen that this data does not scale inversely with thickness as would be expected for a bulk material (illustrated by the dashed line). This can be seen more clearly by plotting the data as DC conductivity versus thickness using $\sigma_{DC} = 1/(R_s t)$ as shown in Figure 6.6 C. The DC conductivity is not thickness invariant but increases with increasing thickness from ~2 × 10^5 Sm^{-1} for the 60 nm thick film up to ~5 × 10^6 Sm^{-1} for the 600 nm thick film. The conductivity appears to approach saturation for thicknesses greater than 160 nm (M/A < 70 mg/m^2) i.e. above the network to bulk transition. These conductivities are extremely high with the maximum values approaching 8% of bulk silver (6.3 × 10^7 Sm^{-1}). This fraction (8%) is close to the fractional volume of film filled by nanowires (4%). It is also worth noting that the conductivity of the evaporated silver films was measured to be 2.6 × 10^7 Sm^{-1}. We attribute the difference between this value and the bulk value to the presence of a thin oxide layer. These AgNW films also display conductivities much higher than the

highest conductivity observed for a nanotube films; ~6×10^5 Sm^{-1}.[5] As the conductivity of nanostructured films such as these is limited by the presence of inter-wire bundles,[14] we suggest that the effective junction resistance in these AgNW films is exceptionally low. Previously,[15] computational studies have suggested junction resistances of ~1 Ω. This is extremely low compared with estimates of nanotube-nanotube junction resistances of ~50 kΩ.[16]

Equation 2.68 can be used to calculate the conductivity ratio, σ_{DC}/σ_{Op}, as a function of film thickness as shown in Figure 6.6 D. Unsurprisingly, this data resembles the DC conductivity data with σ_{DC}/σ_{Op} increasing with increasing thickness from ~ 25 for the 60 nm thick film up to ~ 500 for the 600 nm thick film. In addition, like the DC conductivity, σ_{DC}/σ_{Op} begins to saturate above the network to bulk transition. These conductivity ratios are exceptionally high compared with other systems. Bulk silver[10] has been reported to show σ_{DC}/σ_{Op} ~ 7 although a value of σ_{DC}/σ_{Op} = 143 was measured for the evaporated thin silver films. In comparison, the highest value recorded for nanotube films[11] has been σ_{DC}/σ_{Op} ~ 25. Only doped metal oxides such as ITO have comparable values (σ_{DC}/σ_{Op} ~ 400-800).

As mentioned above, the DC conductivity and conductivity ratio tend to fall off for thicknesses below the network to film transition. This transition can be explored in more detail by measuring the local non-uniformity of the films as a function of thickness. This was done by recording transmission scans (pixel size 4 μm) of a number of the films discussed above. The resulting transmission maps were transformed into absorbance (A) maps using $A = -logT$. By the Beer-Lambert law, the absorbance is proportional to the number of absorbing objects per unit area. This means the absorbance map is a measure of the spatial distribution of nanowires per 4 μm pixel. For purposes required here, the non-uniformity is defined as the standard deviation of absorbance as measured over a 2 mm × 2

mm grid (500 × 500 pixels). A large degree of non-uniformity is associated with a high standard deviation. The data for non-uniformity as a function of film thickness is shown in Figure 6.6 E. It is clear that the non-uniformity is reasonably constant for thicker films but increases significantly for film with thickness below 150 nm. This is very close to the estimated network to film transition thickness of 160 nm (M/A < 70 mg/m^2). In fact Figure 6.6 B-E are all similar in that in all cases the data shown deviates strongly from the high thickness value for thicknesses below ~ 150-170 nm, emphasising the presence of a network to film transition.

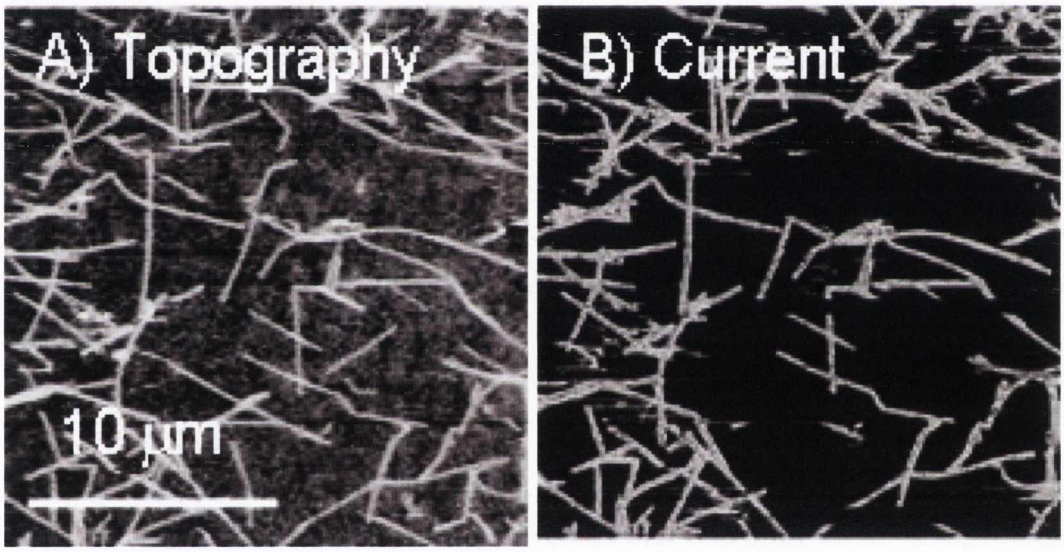

Figure 6.7 *A) Topographic AFM image of a sparse (M/A=10 mg/m^2) AgNW film. B) C-AFM current map taken of the same section of film.*

An additional condition for a thin film to act as an electrode is that current can effectively flow out of the plane of the film as well as through it. To test this, conductive AFM (C-AFM) measurements were performed. Shown in Figure 6.7 A is an AFM topographical image of the surface of a sparse AgNW network (M/A = 10 mg/m^2). All AFM images recorded show a network of straight, well defined nanowires, lying in the

plane of the film. While the vast majority of wires are connected to the network, a small number are isolated. Shown in Figure 6.7 B is a conductive-AFM current map of the same area of the network shown in Figure 6.7 A.

The current map is very similar to the topographical map and clearly shows a nanowire network. This map unambiguously shows that current can flow out of the plane of the film from the wire sidewalls to the AFM tip. This is important as it shows that current can be gathered uniformly from all areas of the surface of these films – a critical property for any material with potential for use as an electrode. We note that none of the nanowires in the network are orientated out of the plane of the film. The current is collected from the sidewall of the wires.

As mentioned above, these films have optical and electrical properties close to those measured for ITO. However, to surpass ITO as a flexible electrode these films need to remain transparent and conducting under flexing. Such a material is of considerable interest as an electrode in applications such as e-paper. To test this, AgNW films on PET were prepared at a number of thicknesses. In each case, the sheet resistance during bending was monitored with the AgNW film in compression and in one case in tension. The films were bent from an initial radius of curvature of 7.5 mm to a final radius of 2.5 mm before being relaxed. This was repeated over many bend cycles. Shown in Figure 6.8 A-C is the mean sheet resistance per cycle plotted versus cycle number for three AgNW films of different thickness.

The thinnest film (M/A = 39 mg/m^2, t = 90 nm) showed reasonably stable sheet resistance over the first 200 cycles. However, at this point the film began to fail, with the sheet resistance increasing by two orders of magnitude over the next 2000 cycles. In contrast, the sheet resistance of the thicker films was virtually unchanged over ~ 2000 cycles with a deviation of < 2% around the mean. For the M/A = 79 mg/m^2 film (t = 180

nm), the sheet resistance for both compressive and tensile bending was measured, as shown in Figure 6.8 C.

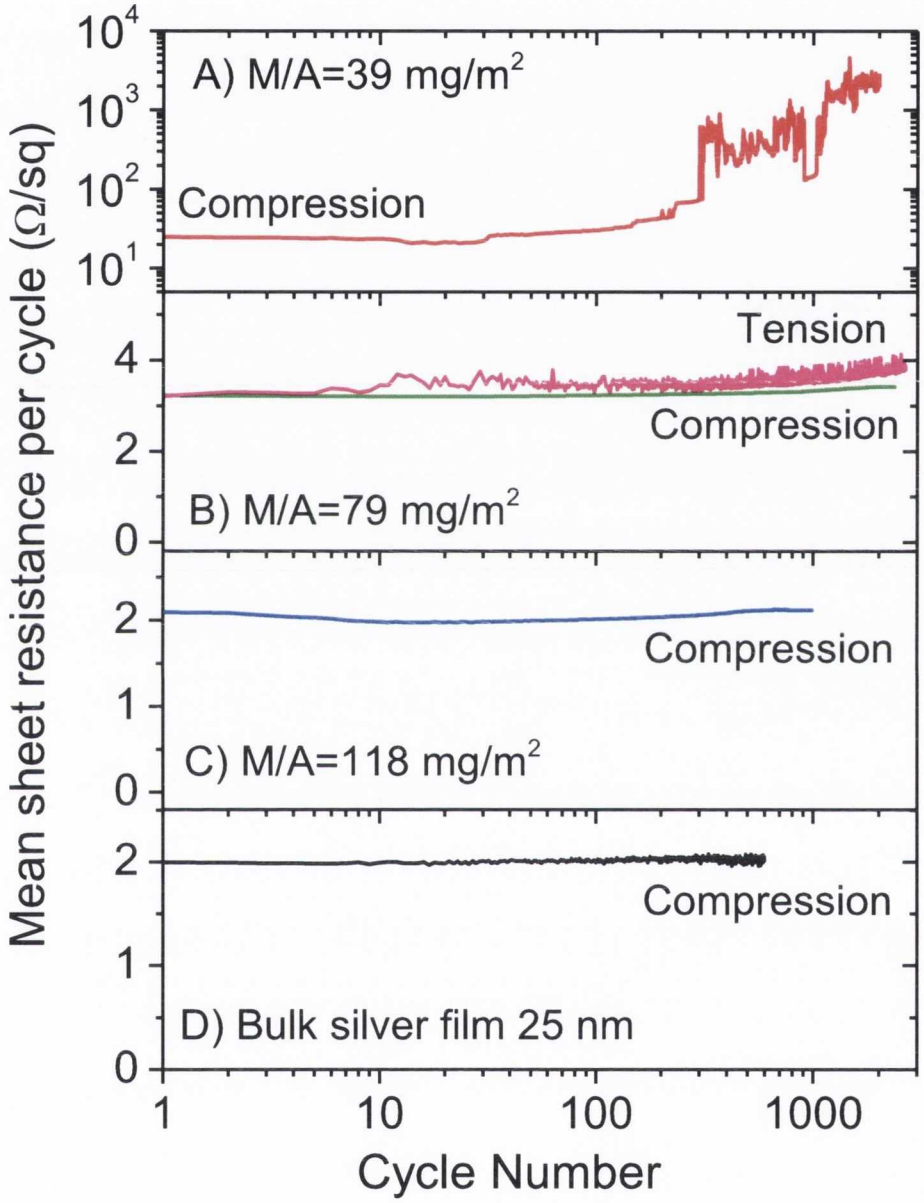

Figure 6.8 *Sheet resistance as a function of cycle number for AgNW films of three different thicknesses; A) M/A=39 mg/m² (t=90nm), M/A=79 mg/m² (t=182nm), M/A=118 mg/m² (t=271nm). Note all films were measured in compression while the film in B) was also measured in tension.*

Both data sets showed little variation in resistance although the results of the tensile test were slightly noisier. For comparison, the electromechanical stability of a solid silver film with thickness 25 nm was measured (shown in Figure 6.8 D). Here the sheet resistance was as stable as the thicker AgNW films. This is in stark contrast to thin ITO films which have been reported to fail catastrophically after only 160 bend cycles.[17] Note that none of the films studied in this work failed during these measurements. In each case, the number of cycles was limited by time constraints.

However, one problem with these materials is their adhesion to PET. Scotch tape tests were performed on AgNW films with thicknesses of 150 nm and 430 nm on PET. Unlike carbon nanotube films, both AgNW films failed the test, being completely removed from the substrate. While this is a problem, it may not be a fatal one as it is likely that PET can be chemically treated to improve the adhesion. Further study should address technical problem.

It is prudent to note that above the network to bulk transition, these AgNW films display a figure of merit (σ_{DC}/σ_{Op}) of ~ 500, slightly lower than that measured for ITO (σ_{DC}/σ_{Op} ~ 400 - 800). Unlike ITO,[17-19] these films are electromechanically robust under flexing. However, transmittance and sheet resistance values matching ITO cannot be simultaneously attained. To reach transmittance greater than 90%, reasonably thin films must be prepared. Unfortunately, such films have thicknesses below the network to film transition and as such have reduced values of σ_{DC}/σ_{Op} and so reduced σ_{DC}. The best results achieved were R_s = 13Ω/□ for T = 85% (M/A = 47 mg/m^2, t = 107 nm). This film is below the network to film transition and as such displays significant non-uniformity as illustrated in Figure 6.8. This non-uniformity will pose a significant problem for real applications. These issues could be resolved simply by forcing the network to film transition to occur at lower thicknesses. This could be done simply by using AgNWs with lower diameter as the

transition thickness is probably defined by some multiple of the wire diameter. A similar transition has been observed in films of single wall nanotube bundles (diameter ~ 20 nm) to occur at t = 40 nm.[13] In this work the transition was observed at t ~ 160 nm for wires with D = 84 nm. In both cases, the transition occurs for film thicknesses of approximately twice the nanowire diameter. In order to achieve $T > 90$ % coupled with $\sigma_{DC}/\sigma_{Op} > 400$, the network to film transition needs to be shifted below 50 nm (see Figure 6.6). If the transition occurs for thicknesses of twice the wire diameter, this means wires with diameters below 25 nm are required. In addition to improving T, using such low diameter wires should have an additional effect. It has recently been shown that the conductivity of networks of nanowires increases as the wire diameter decreases.[14,20] This means that using lower diameter nanowires may result in further increases in σ_{DC}/σ_{Op}, as well as reduction in the transition thickness. Recently gold nanowires have been reported with diameters as low as 6 nm.[21]Using such wires should result in high work-function, spatially uniform, flexible electrodes with high transmittance and extremely high DC conductivity.

6.4 Conclusions

In conclusion, thin transparent, conductive films from silver nanowires have been prepared. For thicknesses below ~160 nm, these films act like a 2D network while thicker films are more bulk-like. The optical transmittance decreases with increasing thickness as described by an optical conductivity of σ_{Op} = 6472 Sm^{-1} (550 nm). The DC conductivity increases with thickness from ~ 2×10^5 Sm^{-1} for low thicknesses, saturating close to 5×10^6 Sm^{-1}, 8% of the bulk silver value. This results in films with sheet resistance < 10 Ω/□ as long as the thickness is > 100 nm. In addition the ratio, σ_{DC}/σ_{Op} increases with increasing thickness, saturating close to 500 for thicknesses > 200nm. The best film had

R_s=13Ω/□ for T=85%. In addition, these films are stable under flexing with the sheet resistance varying by < 2% over more than 1000 bend cycles.

Such films hold great promise as flexible, transparent electrodes. This is especially true if they could be fabricated from low diameter nanowires as this would result in better uniformity and better results for very thin films. As these films can be prepared from the liquid phase, large area electrodes by spraying could be realised. Such a large area, low cost deposition method is ideal for industry and may be widely implemented should the cost of these materials decrease sufficiently.

6.5 References

1 Sukanta De, Thomas M. Higgins, Philip E. Lyons, Evelyn M. Doherty, Peter N. Nirmalraj, Werner J. Blau, John J. Boland, and Jonathan N. Coleman, "Silver Nanowire Networks as Flexible, Transparent, Conducting Films : Extremely High DC to Optical Conductivity Ratios," American Chemical Society Nano **3** (7), 1767-1774 (2009).

2 Xuan Wang, Linjie Zhi, and Klaus Müllen, "Transparent, Conductive Graphene Electrodes for Dye-Sensitized Solar Cells," Nano Letters **8** (1), 323-327 (2008).

3 Sukang Bae, Hyeongkeun Kim, Youngbin Lee, Xiangfan Xu, Jae-Sung Park, Yi Zheng, Jayakumar Balakrishnan, Tian Lei, Hye Ri Kim, Young Il Song, Young-Jin Kim, Kwang S. Kim, Barbaros Ozyilmaz, Jong-Hyun Ahn, Byung Hee Hong, and Sumio Iijima, "Roll-to-roll production of 30-inch graphene films for transparent electrodes," Nat Nano **5** (8), 574-578 (2010).

4 Hong-Zhang Geng, Dae Sik Leea, Ki Kang Kima, Gang Hee Hana, Hyeon Ki Parka, and Young Hee Lee, "Absorption spectroscopy of surfactant-dispersed carbon nanotube film: Modulation of electronic structures " Chemical Physics Letters **455** (4-6), 275-278 (2008).

5 Zhuangchun Wu, Zhihong Chen, Xu Du, Jonathan M. Logan, Jennifer Sippel, Maria Nikolou, Katalin Kamaras, John R. Reynolds, David B. Tanner, Arthur F. Hebard, and Andrew G. Rinzler, "Transparent, Conductive Carbon Nanotube Films," Science **305** (5688), 1273-1276 (2004).

6 Jung-Yong Lee, Stephen T Connor, Yi Cui, and Peter Peumans, "Solution-Processed Metal Nanowire Mesh Transparent Electrodes," Nano Letters **8** (2), 689-692 (2008).

7 Sukanta De, Philip E. Lyons, Sophie Sorel, Evelyn M. Doherty, Paul J. King, Werner J. Blau, Peter N. Nirmalraj, John J. Boland, Vittorio Scardaci, Jerome Joimel, and Jonathan N. Coleman, "Transparent, Flexible, and Highly Conductive Thin Films Based on Polymer−Nanotube Composites," American Chemical Society Nano **3** (3), 714-720 (2009).

8 Evelyn M. Doherty, Sukanta De, Philip E. Lyons, Aleksey Shmeliov, Peter N. Nirmalraj, Vittorio Scardaci, Jerome Joimel, Werner J. Blau, John J. Boland, and Jonathan N. Coleman, "Transparent, Conductive Films from Single Walled Nanotubes: Film Morphology, Uniformity and Electromechanical Stability," Carbon **47** (10), 2466-2473 (2009).

9 Myung-Gyu Kang, Myung-Su Kim, Jinsang Kim, and L. Jay Guo, "Organic Solar Cells Using Nanoimprinted Transparent Metal Electrodes," Advanced Materials **20** (23), 4408-4413 (2008).

10 A. J. de Vries, E. S. Kooij, H. Wormeester, A. A. Mewe, and B. Poelsema, "Ellipsometric study of percolation in electroless deposited silver films," Journal of Applied Physics **101** (5), 053703 (2007).

11 H. Z. Geng, D. S. Lee, K. K. Kim, G. H. Han, H. K. Park, and Y. H. Lee, "Absorption spectroscopy of surfactant-dispersed carbon nanotube film: Modulation of electronic structures," Chemical Physics Letters **455** (4-6), 275-278 (2008).

12 B. Ruzicka, L. Degiorgi, R. Gaal, L. Thien-Nga, R. Bacsa, J. P. Salvetat, and L. Forro, "Optical and dc conductivity study of potassium-doped single-walled carbon nanotube films," Physical Review B **61** (4), R2468-R2471 (2000).

13 E.M. Doherty, S. De, L. Lyons, A. Shmelov, P.N. Nirmalraj, V. Scardaci, W.J. Blau, J.J. Boland, and J.N. Coleman, "Transparent, conductive films from single walled nanotubes: Film morphology, uniformity and electromechanical stability," Carbon **47**, 2466-2473 (2009).

14 P.E. Lyons, S. De, F. Blighe, V. Nicolosi, L.P.C. Pereira, M.S. Ferreira, and J.N. Coleman, "The relationship between network morphology and conductivity in nanotube films," Journal of Applied Physics **104**, 044302 (2008).

15 J. Y. Lee, S. T. Connor, Y. Cui, and P. Peumans, "Solution-processed metal nanowire mesh transparent electrodes," Nano Letters **8** (2), 689-692 (2008).

16 H. Stahl, J. Appenzeller, B. Lengeler, R. Martel, and Ph Avouris, "Investigation of the inter-tube coupling in single-wall nanotube ropes," Materials Science and Engineering: C **15** (1-2), 291-294 (2001).

17 S. De, P.E. Lyons, S. Sorrel, E.M. Doherty, P.J. King, W.J. Blau, P.N. Nirmalraj, J.J. Boland, V. Scardaci, J. Joimel, and J.N. Coleman, "Transparent, flexible, and highly conductive thin films based on polymer-nanotube composites " ACS Nano **3**, 714-720 (2009).

18 Zhong Chen, Brian Cotterell, and Wei Wang, "The fracture of brittle thin films on compliant substrates in flexible displays " Engineering Fracture Mechanics **69** (5), 597-603 (2002).

19 Y. Leterrier, L. Médico, F. Demarco, J. -A. E. Månson, U. Betz, M. F. Escolà, M. Kharrazi Olsson, and F. Atamny, "Mechanical integrity of transparent conductive oxide films for flexible polymer-based displays " Thin Solid Films **460** (1-2), 156-166 (2004).

20 D.H. Shin, H.C. Shim, J-W. Song, S. Kim, and C-S. H, "Conductivity of films made from single-walled carbon nanotubes in terms of bundle diameter," Scripta Materialia **60**, 607-610 (2009).

21 C. Wang, Y. J. Hu, C. M. Lieber, and S. H. Sun, "Ultrathin Au nanowires and their transport properties," Journal of the American Chemical Society **130** (28), 8902-8903 (2008).

Chapter 7 : Conclusions and future work

7.1 Summary of results

The factors controlling the conductivity in carbon nanotube networks were studied. A large range of single wall, double wall and functionalised carbon nanotubes were processed from aqueous dispersions into relatively thick films. The films were characterized by Raman spectroscopy, scanning electron microscopy, density and resistance measurements. The conductivity of these films ranged between 2.08 x 10^2 Sm^{-1} and 2.62 x 10^5 Sm^{-1}. The film conductivity was shown to be dependent on the nanotube structural purity, with highly crystalline nanotubes exhibiting the highest values. An increase in mean bundle diameter and film porosity corresponded to a decrease in the conductivity. This was associated with a decrease in the network connectivity. Computer modelling showed that the conductivity of a network of conducting rods scales linearly with inter-rod junction density. An expression for number of inter-nanotube junctions *per* nanotube and the number density of junctions was derived from the porosity and mean bundle diameter. The conductivity scaled reasonably well with the junction number density measured for the prepared films. The specific conductivity, calculated using idealised network parameters, of each nanotube type was shown to a scale strongly with the Raman G/D ratio.

Single walled carbon nanotubes were exfoliated extensively and deposited as very thin, transparent films. A method of transferring such thin films to a transparent and flexible polymer substrate was perfected. Arc-discharge nanotube films with a range of

thicknesses were prepared using sodium dodecyl sulphate as the stabilizing surfactant. These films were characterized optically by visible region absorption spectrometry, showing very good transmittance which scaled well with film thickness. The film conductivity was constant (~2×10^5 Sm^{-1}) for thickness' down to 40 nm, at which point the spatial uniformity and hence network connectivity decreases, resulting in a higher resistance. For a thickness of 40 nm the films displayed a transmittance and sheet resistance of T=80% and R_s=110 Ω/□. This corresponds to a value of the conductivity ratio σ_{DC}/σ_{Op}=13.0. Furthermore, these films were shown to be electromechanically stable. The films experienced a very small change (~2-5 %) in resistance over more than 2000 bend cycles.

The conductive polymer PEDOT:PSS, was incorporated into nanotube networks. PEDOT:PSS was combined with varying mass fractions of arc-discharge and HiPCO produced nanotubes to prepare thin composite films. These films where optically characterized, showing high spatial uniformity and good transmittance. Arc-discharge nanotube composites showed the highest conductivity of 1.65×10^5 Sm^{-1}. However, the ratio of DC to optical conductivity was seen to have a maximum in both cases, at a mass fraction of 55-60 wt%. This peaked at a value of σ_{Op}/σ_{DC}=15, corresponding to T=75% and R_s=80 Ω/□, for an 80 nm thick, 60 wt% arc-discharge composite. Both types of composites showed extremely high electromechanical stability with the sheet resistance of the arc-discharge nanotube composite films displaying less than 1 % change over 130 cycles.

Silver nanowires, which do not experience large junction resistances, were used to prepare thin, transparent, flexible and conductive films with a range of thicknesses. These films exhibited a saturated conductivity of 5×10^6 Sm^{-1} for thick samples, which decreased below ~160 nm to from ~2×10^5 Sm^{-1}. The saturated conductivity is extremely high, with a sheet resistance of <10 Ω/□ for thicknesses above 100 nm. The transition from bulk-like to

2-Dimensional network is similar to that observed for carbon nanotube networks, but the higher transition point reflects the larger mean silver nanowire diameter. The visible region transmittance produced flat and relatively featureless spectra that scaled well for all thicknesses giving an optical conductivity of σ_{Op}=6472 Sm^{-1} (550 nm). The conductivity ratio σ_{DC}/σ_{Op} was shown to increase with thickness and above 200 nm the ratio saturated at ~ 500. The film most suitable as a flexible display electrode exhibited a sheet resistance and transmittance of 13 Ω/□ and 85 % respectively. The films in this work were cycled more than 1000 times in tension and compression and exhibited a variation in sheet resistance of < 2 %.

7.2 Conclusions

The intent of the thesis was to demonstrate and investigate the applicability of thin networks of quasi 1-Dimensional metallic nanostructures as transparent, flexible electrodes. These results conclusively show that, in order to maximise the film conductivity, the constituent nanotubes must be defect free and arranged into a dense network of very thin nanotube bundles. Not only should this result in high conductivities but also in very homogenous and smooth films which are two properties beneficial for incorporation into devices. The pure SWNT thin films displayed very high conductivity accompanied by reasonable visible region optical transmission, close to the values required for application as transparent electrodes. Even so, there are a few issues to be addressed in order to optimise the performance of any device in which they are incorporated. As mentioned previously, surface roughness is important to any multiple-layer devices. Not only does the incorporation of PEDOT:PSS result in one of the most conductive composites reported, it also reduces the surface roughness of the film while at the same time filling the porous structure inherent to a network of 2-dimensional tubes. This edges

these PEDOT:PSS/SWNT composite films closer to being employed as flexible transparent electrodes.

The resistance associated with the junctions between carbon nanotubes was measured to be very large and, assuming ideal network morphology, there would still exist a substantial barrier to the flow of current due to this junction resistance. Networks of silver nanowires experience very small junction resistances and hence show very promising properties, with transmittance and sheet resistance values matching that of some Indium Tin Oxide films. Their 2-diemsnional structure and rigid nature results in very large porosities and large surface roughnesses. However, this does not offset the benefits arising from very simple processing and extremely low junction resistance. It can be imagined that the porosity and surface roughness issues could be solved with novel fabrication methods, opening the way for flexible and robust transparent electrodes.

It is the hope that this thesis will usefull in the implementation of nanostrucutres as flexible and tranaparent electred as the information unearthed in this research definitevly points the way to increases in electrical and optical properties of nanostructured films.

7.3 Future work

As shown in this work, the conductivity of a network of randomly positioned rods should have a conductivity that is related to the junction density, which is dependent on the rod length and diameter. In the case of nanotubes, the effect of bundle length was neglected as a measurement of bundle length *in* a network is unfeasible. Silver nanowires do not experience such a high level of aggregation and the length and diameter of the constituent wires in a network should be easily measured. Through this a scaling relationship between the morphology controlling factors (wire length, L, diameter, D), and

conductivity is expected to take the form LD^n where $-2 \leq n \leq -4$. Such a scaling law would allow the conductivity of a film to be contolled by tailoring the wire length and diameter, a very advantageous ability when implementing a material in electronics.

Silver nanowires prepared using liquid phase processes tend to have a very large length distribution. By reducing this distribution the networks hould be more uniform, with a higher connectivity and a lower surface roughness. This would prove to a valuable and simple method of improving these films for electrode purposes.

Another positive property of silver nanowires is the ability to prepare aqueous phase dispersions, allowing large scale depsoition via spraying and other techniques. This is very attractive for industrial applications as it allows a relativley easy, low cost, large scale processing, which in the future will be required for all visual display technology platforms.

As the field of nanostructure sysnthesis advances, a host of 1- and 2-Dimensional nanostructures are available for implementation in networks. As there is so many possible applications for flexible electrodes it is prudent to investigate the various advantages and drawbacks of each material. To this end, recent work in this group has concentrated on exfoliation of graphene in the liquid phase and through this, deposition of graphene films in the hope of taking advantage of graphenes amazing electrical and mechanical properties. Also being investigated is the viablility of preparing composites in which two types of nanostrucutres, for example carbon nanotubes and graphene, are combined in order to attain beneficial properties.

The final aim of this research is to be able to incorporate networks of quasi 1-dimensional nanostructures as transparent electrodes. Although the main focus has been on electrodes for display purposes, transparent electrodes are of interest in other technologically relevant areas including transparent and flexible circuitry. Even the most

basic of electronic circuits require components such as capacitiors, resistors, transistors, diodes and indcutors. One of the most important components are capacitors which are used in power storage and certain sensing applications. It would be interesting to prepare transparent and flexible capacitors using SWNT thin films as the parallel electrode plates and observing how the device characteristics vary, if at all, upon bending. This would be a good start to SWNT based flexible circuits.

Of obvious interest is to incorporate thin films of both single walled carbon nanotubes and silver nannowires into devices. To this end we have started collaborating with memebrs of the optoelectronics group in the Cavendish Laboratory, University of Cambridge. Silver nanowire thin films were incorporated into photovolatic devices such as hybrid solar cells. Although the results are promising, problems arise from the AgNW film surface roughness, which creates shorts in the devices. As mentioned earlier, addressing this issues and further study of the resultant device characterisitics is of high importance. We have also begun collaboration with researchers in the Photovoltaics and thin film electronics laboratory in École Polytechnique Fédérale de Lausanne, Switzerland. Silver nanowire films were used as the front contact in solar cells showed quite good results, although with a lower current collection capacity than the reference Indium tin Oxide electrodes. Both sets of initial results demonstrate that AgNW network thin films could, with some improvement, be used as transparent electrodes in solar cell devices which are one of the hottest research topics in the age as people strive for an efficient and sustainable energy source.

Chapter 8 : Appendix

8.1 List of Publications

P. E. Lyons[1,3], S. De[1,3], F. Blighe[1], V. Nicolosi[1], L. F. C. Pereira[1,3], M. S. Ferreira[1,3], and J. N. Coleman[1,3] "The relationship between network morphology and conductivity in nanotube films". Journal of Applied Physics 104, 044302 (2008)

F. M. Blighe, P.E. Lyons, S. De, W. J. Blau[1,3], and J. N. Coleman "On the factors controlling the mechanical properties of nanotube films". Carbon, 46, 41-47 (2008).

J. Amiran[1], V. Nicolosi[1], S. D. Bergin[1], U. Khan[1], P.E. Lyons, and J. N. Coleman "High Quality Dispersions of Functionalized Single Walled Nanotubes at High Concentration". Journal of Physical Chemistry C, 112, 10, 3519-3524 (2008).

E. M. Doherty[1,3], S. De, P.E. Lyons, A. Shmelov[1], P. N. Nirmalraj[2,3], V. Scardaci[3,4], J. Joimel[3,4], W. J. Blau, J. J. Boland[2,3], and J. N. Coleman "The spatial uniformity and electromechanical stability of transparent, conductive films of single walled nanotubes". Carbon, 47, 2466-2473 (2009).

S. De, P.E. Lyons, S. Sorel[1,3], E. M. Doherty, P. J. King[1,3], W. J. Blau, P. N. Nirmalraj, J. J. Boland, V. Scardaci, J. Joimel, and J. N. Coleman "Transparent, Flexible, and Highly Conductive Thin Films Based on Polymer?Nanotube Composites". ACS Nano, 3, 3, 714-720 (2009).

S. De, T. M. Higgins[5], P.E. Lyons, E. M. Doherty, P. N. Nirmalraj, W. J. Blau, J. J. Boland, and J. N. Coleman "Silver nanowire networks as flexible, transparent, conducting films: Extremely high DC to optical conductivity ratios". ACS Nano, 3, 7, 1767–1774 (2009)

P. N. Nirmalraj, P.E. Lyons, S. De, J. N. Coleman, and J. J. Boland "Electrical Connectivity in Single-Walled Carbon Nanotube Networks". Nano Letters, 9, 3890 (2009)

[1] School of Physics, Trinity College Dublin, University of Dublin, Dublin 2, Ireland.

[2] School of Chemistry, Trinity College Dublin, University of Dublin, Dublin 2, Ireland.

[3] Centre for Research on Adaptive Nanostructures and Nanodevices, Trinity College Dublin, University of Dublin, Dublin 2, Ireland.

[4] Hewlett Packard DIMO, Liffey Park Technology Campus, Barnhall Road, Leixlip, Co. Kildare, Ireland.

[5] School of Chemistry, University of Wollongong, Wollongong, NSW2522. Australia.